University of Belgrade,
Faculty of Physics

University of Turin,
Physics department

Lazar Markovic

Measurement of triple self-coupling of the Higgs boson in the four lepton decay channel with the CMS experiment

Doctoral dissertation

Belgrade/Turin, 2026

Univerzitet u Beogradu,
Fizički fakultet

Univerzitet u Torinu,
Departman za fiziku

Lazar Marković

Merenje trostruke samointerakcije Higsovog bozona u kanalu raspada na četiri leptona eksperimentom CMS

Doktorska disertacija

Beograd/Torino, 2026

Thesis Supervisors

Dr. Predrag Milenović
Associate professor
University of Belgrade, Faculty of physics

Dr. Roberto Covarelli
Associate professor
University of Turin, Physics departments

Thesis defense committee:

Dr. Vukašin Milošević
Associate professor
University of Belgrade, Faculty of physics

Dr. Nikola Konjik
Associate professor
University of Belgrade, Faculty of physics

Dr. Nicola Amapane
Associate professor
University of Turin, Physics department

Dr. Roberto Covarelli
Associate professor
University of Turin, Physics department

Date of the defense

_____

Abstract

This doctoral dissertation presents the research performed in the are of development of detector technologies and of the measurement of the Higgs boson self-coupling.

A study of Ultra Fast Silicon Detectors was carried out to support future detector upgrades. In particular, the inter-pad region was studied in order to optimize the design in view of inter-pad width and fill factor. It was found that Inter-pad width of ~ 25 μm is achievable for certain type design. Further,a novel measurement, dubbed elastomer measurement was carried out to measure the leakage current and the guard ring current. Complementary measurements at different temperatures were carried out. All together, trend of the expected curves is reproduced well, although with a less precision for sensors with a deeper implant.

The Higgs boson fiducial cross section of the $H \rightarrow ZZ \rightarrow 4l$ decay channel at 13.6 TeV was measure using data collected by the CMS detector during 2022 (early Run 3 data taking period). The measured fiducial cross section value is consistent with the value predicted by the standard model within uncertainties, thereby validating the analysis strategy applied throughout the thesis.

The central analysis of this doctoral dissertation determines the expected sensitivity to the Higgs-boson self-coupling modifier κ_λ in the $H \rightarrow ZZ \rightarrow 4l$ decay channel. The study employs the EFT framework, categorizing events into untagged, VBF, and VH topologies to enhance discrimination. The resulting likelihood scans yield the following expected intervals:

$$
\begin{aligned}
\text{untagged category:} \quad & -19.258 < \kappa_\lambda < 21.488, \\
\text{VBF category:} \quad & -25.410 < \kappa_\lambda < 23.273, \\
\text{VH category:} \quad & -32.367 < \kappa_\lambda < 34.256, \\
\text{combined categories:} \quad & -18.537 < \kappa_\lambda < 19.644.
\end{aligned}
\tag{1}
$$

Contents

Introduction

The Standard Model (SM) of particle physics represents a quantum field theory that successfully describes all known elementary particles and three of the four known fundamental interactions. Built upon the principles of quantum field theory and local gauge invariance, the SM has been scrutinized for roughly five decades, constantly testing its predictions against experimental data. Even though it provides precise predictions, it remains an incomplete theory, namely it does not provide a quantum description of gravity, nor does it explain the origin of dark matter or dark energy, nor account for the observed matter–antimatter asymmetry of the Universe. These are some of the open questions to be answered by modern physics, or perhaps by new models.

One of the pillars of the SM is the so called Higgs mechanism, a mechanism responsible for the spontaneous breaking of electroweak symmetry and the generation of particle masses. The discovery of the Higgs boson in 2012 by the ALTAS and CMS collaborations marked a turning point in understanding of the properties of the SM. As of then, scientific community has devoted its attention to measuring properties of the Higgs boson, like mass, spin, parity, coupling to other particles, various decay rates and production cross section. One of the equally important properties of the Higgs boson is its self-coupling, a parameter of the SM which governs the tri- and -quartic Higgs boson interaction, but also the shape of the Higgs potential and the value of the vacuum expectation value. Therefore, measuring this parameter is an essential test of the SM and it provides a powerful probe of new physics effects. Measuring any deviation of the Higgs boson self-coupling from the predicted value by the SM potential may reveal further structure of the scalar sector or new physics at higher energy scales.

Precision cross-section and Higgs boson couplings measurements represent one of the key steps in testing the predictive power and validity of the SM. The Higgs-boson-to-four-lepton decay channel ($H \rightarrow ZZ \rightarrow 4l$), the so called *golden channel*, characterized by low background and a fully reconstructible final state, provides a window for such measurement. These measurements not only provide a verification of theoretical predictions at high orders in perturbation theory, but also offer possibilities to interpret the measurements within an Effective Field Theory (EFT) framework. In the $H \rightarrow ZZ \rightarrow 4l$ channel, the Higgs boson self-coupling appears in loop corrections, which enables probing for this coupling and setting constraints on it, which is the main topic of this thesis. As the Higgs boson can be produced on- and off-shell, it offers two complementary approaches for studying properties of this particle, especially the Higgs boson self-coupling. In the off-shell region, at high masses of the propagating Higgs boson, the Higgs boson self-coupling effects become more pronounced compared to the Higgs boson on-shell production.

The ability to measure the Higgs boson self-coupling relies on advancements of accelerator and detector technologies. The Large Hadron Collider, which is the world's most powerful particle accelerator, is situated at CERN. At the begin of its operation, the so called Run 1, in 2011 (2012), the LHC operated at center-of-mass energy of 7 TeV (8 TeV). During the three year period of 2016-2108, known as Run 2, the LHC operated at center-of-mass energy of 13 TeV. As of 2022, marking the beginning of Run 3, the LHC operates at center-of-mass energy of 13.6 TeV. Following the end of

Run 3 data taking period, the LHC will undergo a shutdown and upgrade period, resulting in the High-Luminosity Large Hadron Collider. This new and improved accelerating system, with the experiments also upgraded, is expected to start colliding protons in 2029-2030, and is expected to collect data corresponding to integrate luminosity of $3000 - 4000$ fb^{-1}. With the new dataset it will be possible to perform more precise measurements and probe for rare processes, especially in relation to the Higgs boson. However, with increased proton-proton collision rate not only does the increase in integrate luminosity come, but also a new experimental challenge. In particular, the number of simultaneous interactions per bunch (of proton) crossing will increase from current's $40 - 60$ on average to about $140 - 200$ on average.

One of the key technologies which will be used to face this newly coming challenge is the Ultra-Fast Silicon Detector (UFSD) technology that is based on Low-Gain Avalanche Diode technology. UFSDs are characterized by a high spatial granularity with extraordinary time resolution $\sim 30 - 40$ ps allowing for four dimensional reconstruction of tracks and vertices (compared to present day three dimensional which relies on spatial information alone). These novel sensors will be integrated into CMS Minimum Ionizing Particle Timing Detector (CMS MIP TD, CMS MTD) which will serve a crucial purpose of maintaining tracking performances under harsh working conditions of HL-LHC. The research presented in this thesis includes inter-pad region optimization of UFSD and a novel elastomer-based measurement of UFSD sensors.

This thesis combines complementary lines of research, detector development, extension and validation of theory predictions and Higgs boson data analysis, within the context of the CMS experiment at the LHC. The thesis is presented in several chapters. Chapter 1 gives a description of the Large Hadron Collider and the CMS experiment. Next, Chapter 2 discusses upgrades for the HL-LHC, focusing on the design optimization of the UFSD interpad region and on the UFSD sensor characterization via a novel elastomer measurement method. In Chapter 3 a overview of the SM is given. Chapter 4 discusses the Higgs boson self-coupling measurements, introduces the SMEFT framework and discusses inclusion of the $\mathcal{O}_6$ operator in the SM and its effect on the Higgs boson self-coupling. Chapter 5 presents the experimental analysis: (i) cross section calculation up to NNLO in perturbation theory the $pp \to ZZ$ process, (ii) the Higgs boson fiducial cross section measurement with early Run 3 data, and (iii) the Higgs boson self-coupling study in the off-shell regime of production. Lastly, Chapter 6 provides a discussion of results.

Chapter 1

The Compact Muon Solenoid experiment at the Large Hadron Collider

1.1   The Large Hadron Collider

The European Organization for Nuclear Research (CERN) is one of the world's largest centers for scientific research. It is located on the border between France and Switzerland and operates as an international collaboration. At the moment, CERN has 25 member states but also a large number of non-member states with international cooperation agreements. At CERN, research is specifically focused on fundamental particle physics, i.e. its primary mission is to explore the fundamental constituents of matter and the forces governing their interactions. As such, CERN has always stood at the frontier of scientific and technological advancements, with the most advanced system built being the Large Hadron Collider (LHC) [1], the world's most powerful particle accelerator to date. Built within a tunnel originally constructed for the Large Electron-Positron Collider (LEP) [2], the LHC is a build-up of decades of research for which several Nobel prizes were awarded for theoretical and experimental advancements in the area of particle physics.

The LHC is housed in a circular tunnel with a circumference of ~ 27 km, situated at an average depth of ~ 100 m. The accelerator ring is comprised of eight arcs connected by eight straight sections known as insertion regions (IR). Four of these regions host major experimental facilities (ATLAS at IR1, ALICE at IR2, CMS at IR5, and LHCb at IR8), while the remaining regions manage critical beam operations such as acceleration (IR4), beam collimation (IR3 and IR7), and beam dumping (IR6). Proton acceleration to the final collision energies is conducted in several, carefully orchestrated stages. Protons are initially produced by ionizing hydrogen gas in a Duoplasmatron device. Then, they are subsequently accelerated through multiple stages. First, protons are injected into the linear accelerator LINAC2 where they reach 50 MeV (LINAC4 replaced LINAC2 after Run 2). Next, protons enter the Proton Synchrotron Booster (PSB) (or simply BOOSTER), composed of four stacked synchrotron rings. Until 2018 (until the end of Run 2 data taking period), the Booster accelerated protons to 1.4 GeV, whilst after 2018 protons are accelerated to 2 GeV. From the PSB, protons proceed to the Proton Synchrotron (PS), which accelerates them up to 26 GeV. Here, protons are structured into bunches, each bunch typically containing around 1.15×10^{11} protons with spacing of 25 ns. Following the PS, bunches are transferred to the Super Proton Synchrotron (SPS), where protons are further accelerated to the energy of 450 GeV. Finally, proton bunches are injected into the main LHC ring, where they undergo acceleration via radiofrequency (RF) cavities installed at IR4. Sixteen RF cavities, each capable of achieving peak voltages of about 2 MV, incrementally accelerate the beams from 450 GeV to their final energy (currently 6.8 TeV per beam in Run 3). An overview of CERN's

accelerator complex is shown in Figure 1.1.
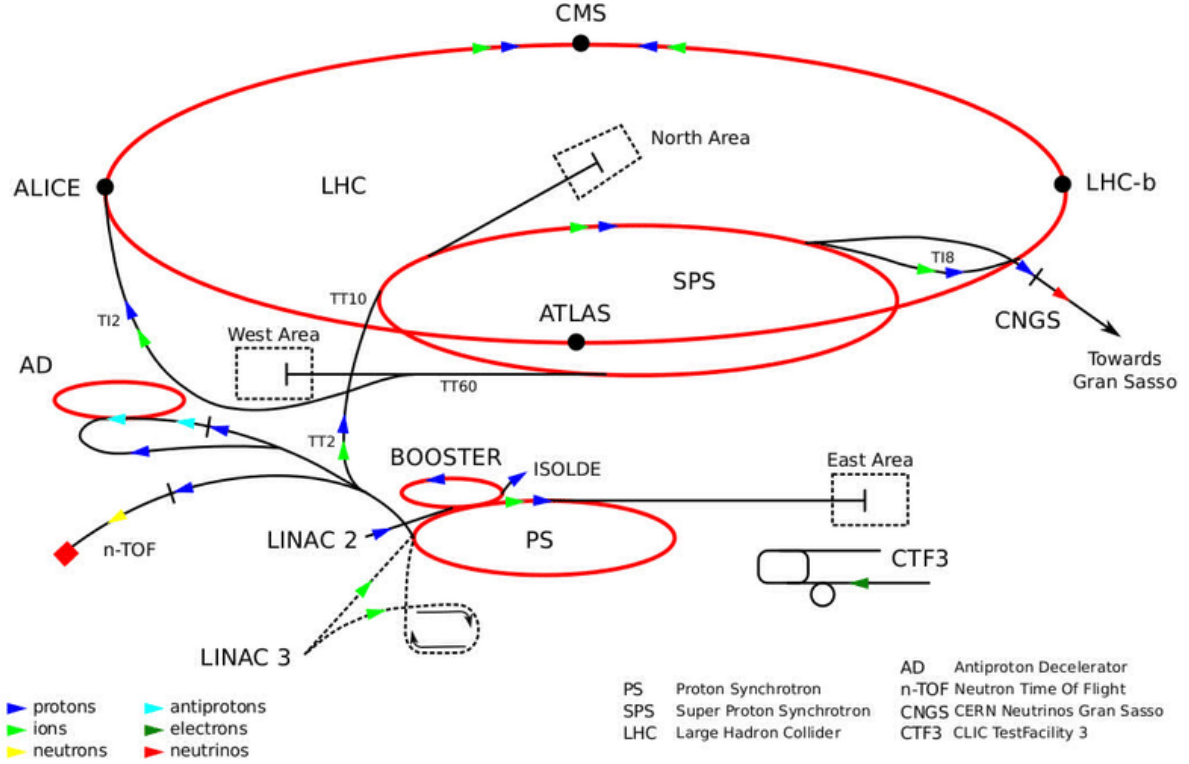
Figure 1.1. Schematic view of the CERN accelerator complex. The blue arrow represents the protons, which follow the path LINAC2 → BOOSTER → PS → SPS → LHC, with BOOSTER, PS, SPS and LHC being highlighted in red. Figure taken from Ref. [3].

Precise beam control within the LHC is vital to ensure the safety, integrity, and efficiency of the experimental programs. Beam manipulation involves guiding beams along a circular path, focusing, collimation, and controlled beam dumping. Guiding beams along a circular path is achieved by using strong dipole magnets which produce a magnetic field of ~ 8.33 T. Quadrupoles are used to focus the beam in horizontal and vertical directions, maintaining precise beam trajectories and ensuring tight control over beam sizes. Beam collimation, a critical procedure performed primarily at IR3 and IR7, employs multiple stages of collimators and absorber which remove stray protons that deviate significantly from the ideal beam path. Lastly, beam dumping conducted at IR6 is essential to safely dispose of high-energy proton beams.

Since the beginning of LHC's operations, the center-of-mass (COM) energy of the colliding protons (ions) was gradually increased striving for the originally desired value of 14 TeV. Work period of LHC is divided into three distinct phases, which in most differ by COM energy, commonly referred to as Run 1 (2009-2013), Run 2 (2015-2018) and Run 3 (2022-ongoing till 2026). During Run 1, the maximal achieved COM energy of proton-proton (p-p) collisions was 8 TeV, with an integrated luminosity of ~ 25 fb^{-1}. During Run 2, COM energy was increased to 13 TeV, with an integrated luminosity of ~ 150 fb^{-1}. The ongoing Run 3 is operating at a collision energy of 13.6 TeV, with an integrated luminosity aiming to surpass previous achievements while standing at ~ 220 fb^{-1} (June 2025). The LHC's sophisticated beam acceleration and manipulation systems represent remarkable feats of engineering, essential for the precise control of ultra-high-energy collisions. These systems have aided and led to remarkable discoveries, continuously expanding fundamental understanding of

the universe. Probably the CERN's most notable scientific achievement is the discovery of the Higgs boson in 2012 by the ATLAS [4] and the CMS [5] collaborations. The ongoing Run 3 research, among other topics, aims to further probe and measure properties of the Higgs boson, the Spontaneous Symmetry Breaking mechanism and search for new physics beyond the Standard Model which will bring our view of the universe to a new height of understanding.

After the end of the Run3 data taking period, the LHC will be temporarily shut down and upgraded, thus entering the new era of High-Luminosity LHC (HL-LHC) [6]. Scheduled upgrade is foreseen to end by 2029 and will result in tenfold increase of integrated luminosity with COM energy of 14 TeV. Increased luminosity will vastly improve the statistics, resulting in deeper studies of particle physics, but also it can possibly open the door for new physics phenomena to be observed and studied.

## 1.2   The Compact Muon Solenoid Experiment

The LHC accelerator ring hosts four major experiments (detectors), one of which is the Compact Muon Solenoid (CMS) detector [7]. The CMS detector is a general-purpose detector, meaning it is built to handle a wide range of measurements in high-energy physics (HEP). It serves both in the search for new particles and phenomena beyond the Standard Model, and in delivering high-precision measurements of already known processes.

The CMS detector possesses a cylindrical geometry with azimuthal symmetry around the beam axis. At its heart lies a powerful solenoid magnet [8], a cylindrical coil made from superconducting cable which generates a magnetic field of 3.8 T along the beam direction (beam line). Keeping the cylindrical geometry in mind, the coordinate system is defined as follows. The origin is located at the nominal interaction point, which is at the center of the detector. The y-axis points vertically upward, the x-axis extends horizontally toward the center of the LHC ring, and the z-axis follows the direction of the beam, oriented toward the Jura mountains. As is usually the case, the azimuthal angle ϕ is measured in the x-y plane as a measure of angular distance from positive direction of the x-axis, while the polar angle θ is a measure of angular distance from the positive direction of the z-axis. In HEP, however, instead of using θ it is more common to use quantity called pseudorapidity which itself is a function of θ , defined as $\eta = -\ln\tan(\frac{\theta}{2})$. In the ultra-relativistic limit pseudorapidity becomes what is know as rapidity and is defined as $y = \frac{1}{2}\ln\frac{E+p_z}{E-p_z}$. It is important to highlight that the rapidity difference is Lorentz invariant. Besides the angular quantities mentioned here, p_T and E_T are also used in HEP, i.e. transverse momentum and transverse energy respectively. Using η, p_T, ϕ and mass of the particle m one can construct a four-momentum vector.

The detector is composed of multiple subsystems arranged concentrically around the beamline, as schematically illustrated in Figure 1.2. From the beamline outward, the sub-detectors are arranged as follows: the tracking system [9], the Electromagnetic Calorimeter (ECAL) [10], the Hadronic Calorimeter (HCAL) [11], the superconducting magnet [8], and finally the muon detection stations [12]. The tracker reconstructs trajectories of charged particles by exploiting the curvature of the trajectory induced by the magnetic field. The ECAL and HCAL measure energy deposits of photons and (anti)electrons (ECAL) and hadrons (HCAL). The outermost system is designated for tracing the paths of muons, which are typically the most penetrating particles produced in collisions. As each of these sub-detectors plays a distinct role, it is only when the combined information provided by every subsystem is analyzed that the underlying event can be reconstructed. However, the reasoning should be taken with a caveat, not every detector works with a 100% efficiency for a number of reasons. Namely, it is not always the case that it is possible to catch every particle within the effective volume

(geometrical efficiency) of a detector, secondly it is not always the case that the caught particle can be exactly reconstructed (reconstruction efficiency). Reconstruction efficiency itself is governed by the efficiencies of each of the subsystems and by the efficiency of the reconstruction algorithm.
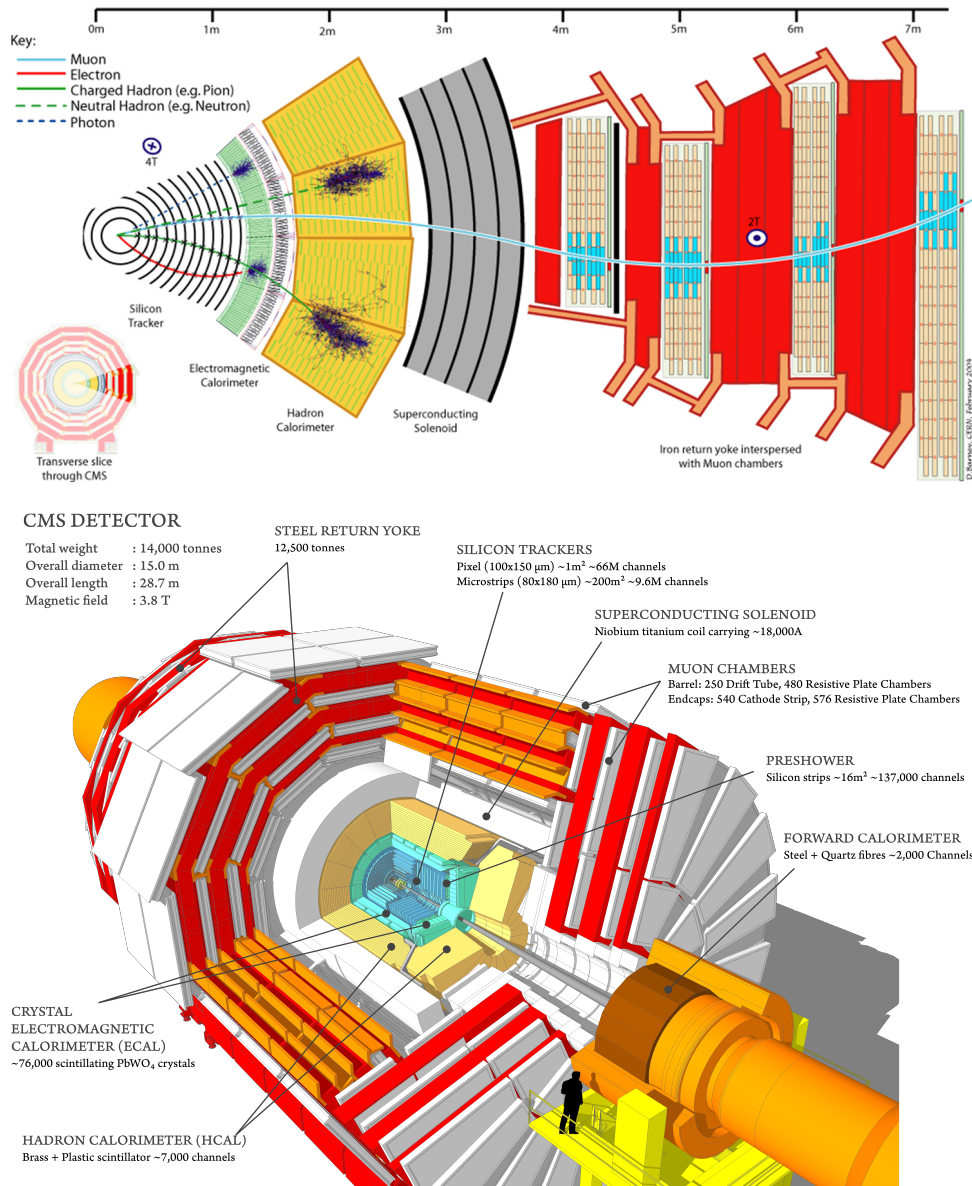
Figure 1.2. Top: Schematic transverse overview of CMS's subsystems with an exemplary signature shown for photon, electron, pion, neutron and muon (taken from Ref. [13]). Bottom: Overview of the CMS detector in whole with each subsystem marked (taken from Ref. [14]).

The design of the CMS detector was governed by the extreme demands imposed by the LHC's operating conditions. With about 2800 bunches circulating in each beam and crossing every 25 ns, the LHC was designed for a collision rate of roughly 40 million interactions per second. When looking at a single crossing of the bunches, about $40 - 60$ (on average) interactions (the so called pile-up interactions) happen, with each giving a myriad of particles. In case an event which is significant for the study occurs, it will be masked by a large number of particles which can cause an overlap in tracks and energy deposits, thus making the reconstruction of the main event harder. These high rates result in dense bursts of particles, requiring the detector to record events with very fine temporal and spatial

resolution, even more so when signals from different collisions overlap. Particles produced in these collisions often carry momenta of several GeV or higher. To accurately trace and reconstruct their paths, a strong uniform magnetic field is necessary to curve their trajectories and enable charge and momentum measurements. To reliably detect every particle produced in collisions the detector must be as hermetic as possible so that no significant energy escapes undetected (except for neutral weakly interacting particles). Overall, the CMS detector represents a remarkable feat of ingenuity with the main design requirements being excellent time resolution and a highly efficient trigger system, high spatial granularity across all subsystems, a strong and stable magnetic field, broad geometric coverage, high momentum resolution for charged particles, high energy resolution, accurate measurement of muon momentum and their identification, reliable reconstruction of missing transverse energy, low wear-out over time and high resistance to radiation.

1.2.1 Tracker

The CMS tracker [9] is the innermost sub-detector of the CMS experiment and is positioned closest to the beamline. Its primary purpose is to record the impacts of charged particles with minimal perturbation to their paths. Recorded information is then used to reconstruct the trajectories of charged particles with high spatial resolution. As charged particles traverse the detector volume, they experience a strong magnetic field of 3.8 T, which forces charged particles to move along curved trajectories, thus introducing separation between close tracks and enabling measurement of their momenta and aids in track reconstruction. In essence, particles with higher transverse momentum follow less curved paths, while lower-momentum particles exhibit greater curvature. By sampling these trajectories at multiple key locations, the tracker enables precise momentum measurements.

Beyond trajectory reconstruction, the tracker provides crucial information about the particle's origin by identifying primary and secondary (decay) vertices and displaced tracks, making it possible to detect particles from secondary decays. A primary vertex refers to the point where a p-p collision occurs, i.e., the origin of the hard scattering event. It is reconstructed using tracks from charged particles that are consistent with originating from a common spatial point. A secondary vertex is the decay point of a particle that has a mean lifetime long enough to traverse a measurable distance from the primary vertex before it undergoes a decay. Secondary vertices are reconstructed using displaced tracks, i.e. those that do not point back to the primary vertex. Additionally, at very low momenta the system allows for indirect estimation of particle mass through energy loss measurements.

The CMS tracking system is composed of two main parts: an inner pixel detector and an outer silicon strip tracker, which is depicted in Figure 1.3. As particles traverse these layers, they generate electric signals which are subsequently amplified and digitized.

At the center of the tracker lies the silicon pixel detector, which is designed to withstand the highest particle flux, as it is closest to the beam line. It consists of three/four concentric barrel layers, supplemented by two forward endcaps on either side. Each endcap is comprised of two disks. The pixel detector contains approximately 66 million pixels, enabling fine-grained measurements essential for vertex reconstruction and for resolving multiple closely spaced tracks in high-pile-up environments.

Surrounding the pixel system is the silicon strip tracker, which spans a surface area of nearly 198 m^2 and includes around 9.3 million individual strips. It is divided into four main subsystems: the Tracker Inner Barrel (TIB), Tracker Inner Disks (TID), Tracker Outer Barrel (TOB), and Tracker Endcaps (TEC). TIB and TOB are structured as concentric barrel layers, with four and six layers respectively. TID is composed of three parallel disks on each end. TEC are composed of 9 parallel disks with each of them being segmented into several concentric rings.

The CMS tracker provides full coverage for pseudorapidities up to $|\eta| < 2.5$. It is capable of
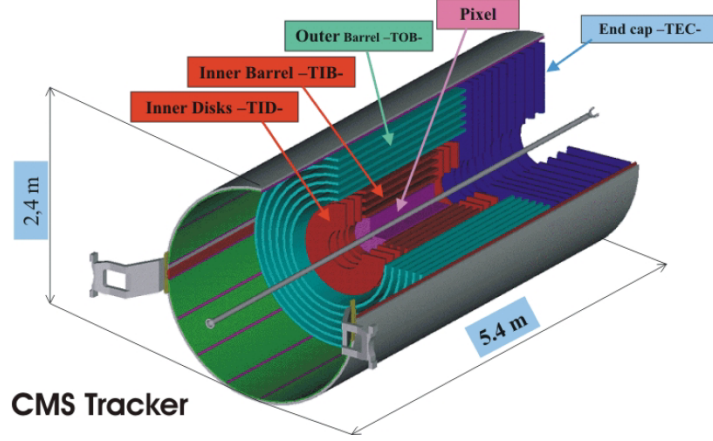
Figure 1.3. Schematic view of the CMS Tracker with its components (Pixel, TEC, TOB, TIB, TID) marked. Pixel Tracker is at the very core, surrounded by Strip Tracker (TIB, TID, TEC, TOB). The entire system is ~ 2.4 m tall and ~ 5.4 m long. Figure taken from Ref. [15].

reconstructing tracks for particles with transverse momentum as low as 0.1 GeV. The tracker system has proved to be very efficient [16], with reconstruction efficiencies of charged leptons close to 100%, while the position resolution of the reconstructed primary vertices is $10 - 12 \ \mu$m along all three axis (x, y, z).

1.2.2 ECAL

Following the tracker system in the radial layout of the CMS detector, next in line is the Electromagnetic Calorimeter (ECAL) [10]. A precise measurement of particle energies is essential for reconstructing the full picture of p-p collision events. In particular, the accurate detection of electrons and photons is critical for identifying and studying key processes such as Higgs boson decays into two photons ($H \rightarrow \gamma\gamma$) and into four leptons via intermediate Z bosons ($H \rightarrow ZZ \rightarrow 4l$). As such, the ECAL is optimized to measure the energy of photons and (anti)electrons with high precision.

The ECAL is a homogeneous, scintillating calorimeter built from lead-tungstate ($PbWO_4$) crystals. The energy of a traversing photon or electron is measured based on a phenomenon of electromagnetic showering. When a charged particle enters a lead-tungstate crystal, it initiates a shower, thus emitting a cascade of secondary particles. These particles excite the crystal lattice which then produces scintillation light. The emitted light is collected with photodetectors, which are mounted at the back of each crystal, and are converted into electrical signals for further processing. The small radiation length ($X_0 = 0.89$ cm) and Molière radius ($R_M = 2.2$ cm) of $PbWO_4$ allow for the construction of a compact and finely segmented calorimeter. This is crucial for separating nearby electromagnetic showers, particularly in environments with high particle multiplicities.

The ECAL is divided into three major components (as shown in Figure 1.4): The ECAL Barrel (EB) (covering the region $|\eta| < 1.479$), the ECAL Endcaps (EE) (extending coverage to $|\eta| < 3.0$), and the Preshower Detector (ES) installed in front of the endcaps in the range $1.653 < |\eta| < 2.6$.

The Preshower Detector plays a crucial role in the endcap region, where particles (e.g. π^0) decaying into two photons can mimic single high-energy photon signatures. At high pseudorapidities, the angular separation between the two photons becomes small enough that the showers they produce in the ECAL might overlap, which complicates their identification. To solve this issue, the ES system consists of two layers of lead absorbers followed by silicon strip sensors. These layers induce electromagnetic showers, which allows for accurate determination of the shower's position. In practice,
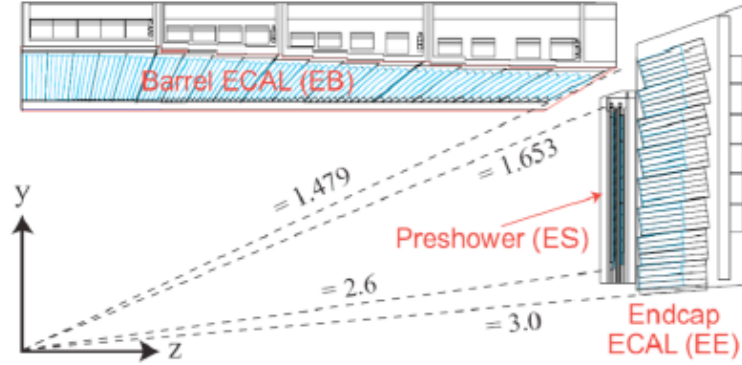
Figure 1.4. Overview of a longitudinal quarter of the ECAL with its components (EB, ES, EE) marked. Figure taken from Ref. [17].

when the energy is observed in the EE region, its origin is traced back to the interaction point. If corresponding energy deposits are also observed in the ES, the combined energy and shape information help determine whether the signal corresponds to a single photon or a pair.

Performance-wise, the ECAL demonstrates exceptional energy resolution. Based on the data collected during LHC's operation in 2010 and 2011 at a COM energy of $\sqrt{s} = 7$ TeV [18], for electrons from Z boson decays, the energy resolution is better than 2% in the central region of the barrel ($|\eta| < 0.8$) and typically ranges between $2 - 5\%$ in the outer barrel and endcap regions. For photons from $H \rightarrow \gamma\gamma$ decays at 125 GeV, the resolution varies across the barrel from 1.1% to 2.6%, and between 2.2% and 5% in the endcaps. Based on the data collected during LHC's operation in 2015-2018 at a COM energy of $\sqrt{s} = 13$ TeV [19], for electrons from Z boson decays with low bremsstrahlung (for the inclusive sample), the energy resolution was better than $1.8\,(2.0)\%$ in the central barrel, $3.0\,(4.0)\%$ in the outer barrel, and $4.5\,(5.0)\%$ in the endcaps region. These performance figures are critical for reconstructing narrow invariant mass peaks, such as the Higgs boson, and for ensuring high sensitivity in searches for new physics involving final states which include photons and electrons.

1.2.3 HCAL

The Hadronic Calorimeter (HCAL) [11] is the next major sub-detector layer after the ECAL and is responsible for measuring the energy of hadrons (e.g. neutrons, etc.). It plays a key role in reconstructing jets, which are cone-shaped collimated sprays of hadrons resulting from quarks and gluons undergoing QCD showering and hadronization. Additionally, HCAL contributes significantly to the determination of missing transverse energy (MET). When the total measured energy in the transverse plane from both the ECAL and HCAL does not balance to zero, this is interpreted as missing transverse energy. Reason for apparent MET could be that the detector performances are suboptimal, or it could be that an undetectable or weakly interacting particles escaped the volume of a detector. For example, these could be Standard Model neutrinos or hypothetical beyond the Standard Model [3] particles such as dark matter candidates.

The HCAL is divided into four main components, as shown in Figure 1.5: the Barrel Hadronic Calorimeter (HB) (covering $|\eta| < 1.3$), the Endcap Hadronic Calorimeter (HE) (spanning $1.3 < |\eta| < 3.0$), the Forward Hadronic Calorimeter (HF) (covering the very forward region of $2.8 < |\eta| < 5.0$, the Outer Hadronic Calorimeter (HO) which is placed outside the solenoid and is covering the range of

$|\eta| < 1.3$. The HCAL ensures nearly full coverage in pseudorapidity up to $|\eta| < 5$, which corresponds the polar angle approaching $\theta = 180°$. This wide angular coverage maximizes the likelihood of detecting all particles produced in a collision.
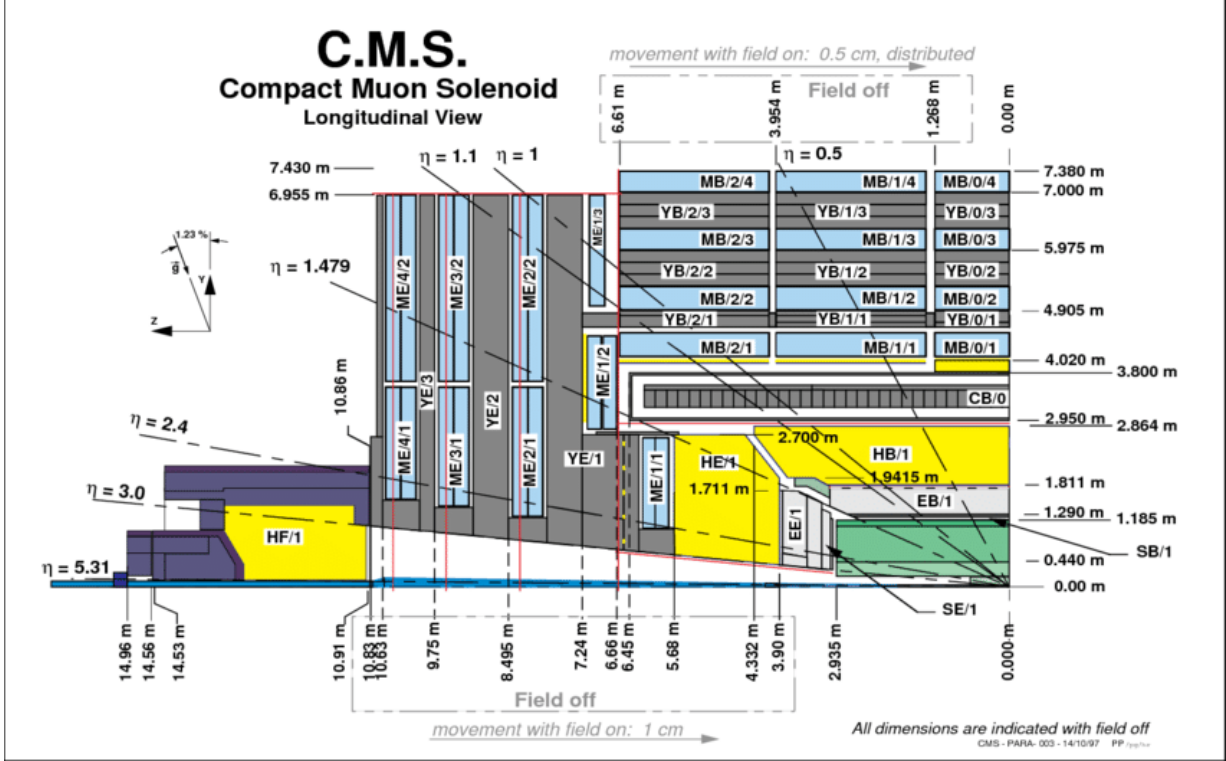
Figure 1.5. Schematic overview of the upper half of the CMS detector's longitudinal cross section, in the range of $|\eta| < 5.31$. Elements filled in with the color yellow are HE, HB, HF and HO (positioned above HE and HB, outside of solenoid). Figure taken from Ref. [20].

The HB, HE, and HO calorimeters are constructed as sampling calorimeters, composed of alternating layers of dense absorber material and plastic scintillator tiles. The absorbers induce hadronic showers when struck by incoming hadrons (similar to the electromagnetic showering). The accompanying scintillator emits scintillation light as the particles traverse it. Each scintillator tile is coupled with wavelength-shifting fibers (WSFs), which absorb the initial blue-violet scintillation light and re-emit it in the green spectral range. This light is then transferred via optical fibers to photodetectors for processing. The Outer Hadronic Calorimeter (HO) is uniquely positioned outside the solenoid. Its purpose is to capture any energy that may leak from the HB, thus improving the hermeticity and overall energy resolution of the calorimeter system in the central region.

The HFs are located at each end of the detector, specifically designed to detect particles emerging at shallow angles with respect to the beamline. These particles are typically highly energetic and more numerous, placing significant demands on detector radiation tolerance. As a result, the HF adopts a distinct design from the other HCAL components. Instead of scintillators, the HF uses quartz fibers embedded in steel absorbers to exploit the Cherenkov effect. When a charged particle travels through quartz at a speed exceeding that of light in that same medium, it emits Cherenkov photons. These photons are detected and processed, allowing the HF to operate efficiently even under extreme radiation levels. This makes it an essential component for forward energy measurement and for reducing MET uncertainty.

The HCAL is a vital subsystem of CMS, enabling precise hadronic energy measurements and playing a central role in jet reconstruction, particle flow algorithms, and missing energy calculations.

When information from both HCAL and ECAL are combined, the energy resolution measured in a pion test beam is $\sigma/E \approx 110\%/\sqrt{E[\text{GeV}]} + 9\%$ [21].

1.2.4 Muon chambers

The CMS muon system [12] is located outside the solenoid and spans a pseudorapidity range of $|\eta| < 2.4$. It comprises multiple layers of gaseous detectors embedded within the steel flux-return yoke of the magnet. The return yoke serves a dual purpose: it provides the mechanical support structure and acts as a path for the magnetic field lines to close, significantly impacting the curvature of muon trajectories outside the solenoid. This design enables multiple spatial measurements of traversing muons, essential for accurate track reconstruction.

The system incorporates three types of gaseous ionization detectors: Drift Tube Chambers (DTs), Cathode Strip Chambers (CSCs), and Resistive Plate Chambers (RPCs). DTs are placed in the barrel region ($|\eta| < 1.2$), where the background radiation from neutrons and the overall muon rate are relatively low. In the endcap region ($1.2 < |\eta| < 2.4$), CSCs are used due to their superior performance in high radiation and high-rate environments. RPCs complement both DTs and CSCs by providing excellent time resolution as they are installed in both the barrel and endcap regions.

A schematic layout of the muon system is shown in Figure 1.6, illustrating the positioning of DTs, RPCs, and CSCs within the detector.
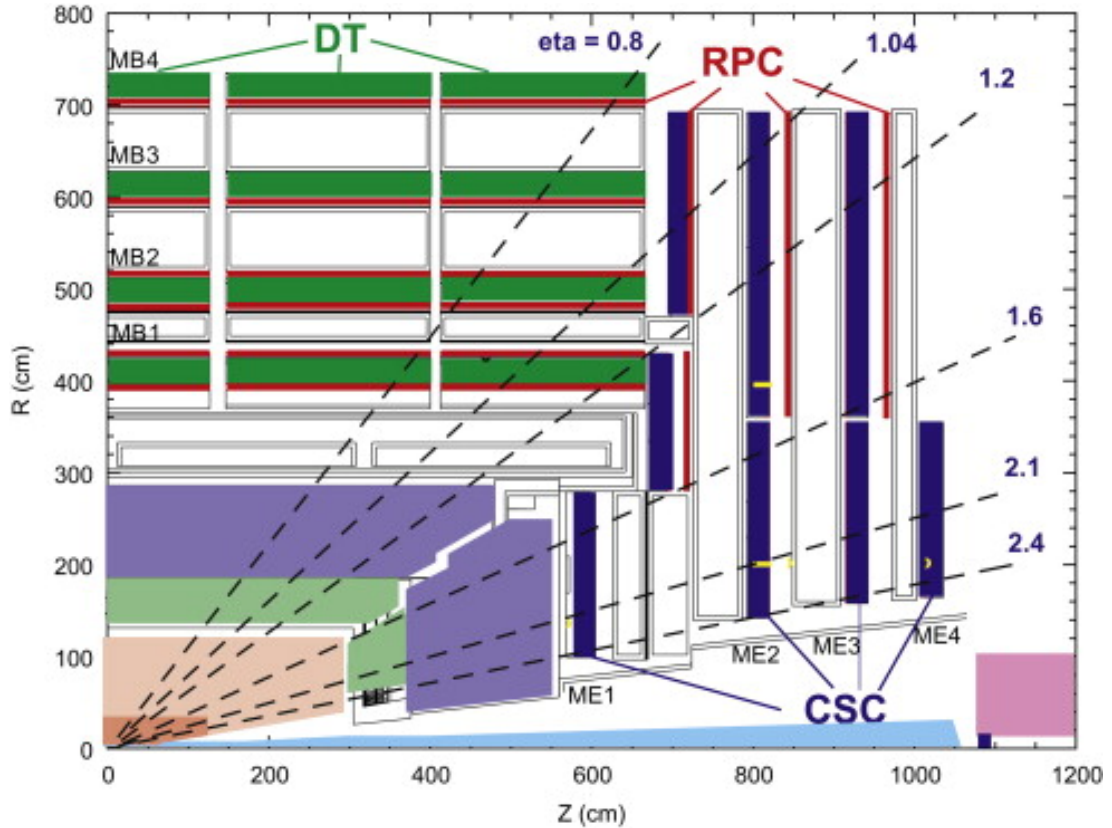
Figure 1.6. Schematic overview of the upper half of the muon system's longitudinal cross section, in the range $|\eta| < 2.4$. The rest (not shown) of the detector is symmetric due to the cylindrical symmetry of the detector. Figure taken from Ref. [22].

The muon system is designed for robust reconstruction and high identification efficiency. According to Run 2 performance studies [23], the muon reconstruction and identification efficiency exceeds

96% across the full pseudorapidity range.

1.2.5   Data acquisition

The LHC is designed to deliver proton bunch crossings every 25 ns, corresponding to a 40 MHz collision rate. It is technically unfeasible to record all these events, as each raw CMS event is approximately 1 MB in size. To reduce the data flow to a manageable $\sim$ kHz output rate, CMS employs a two-level trigger system [24]: the hardware-based Level-1 Trigger (L1) and the software-based High-Level Trigger (HLT).

The Level-1 Trigger, implemented in custom electronics, receives data from the calorimeters and muon systems at the full 40 MHz rate. It identifies high-energy physics objects, such as electrons, photons, muons, and jets, on certain thresholds. This information is processed through separate calorimeter and muon trigger paths and merged in the Global Trigger, which applies selection algorithms. To tackle large collision rate and hence information processing requirements, the data are held in pipeline buffers. Events not selected are discarded, while those passing the L1 logic are forwarded to the DAQ system. This stage reduces the rate from 40 MHz to approximately 100 kHz.

The HLT further processes events using a large computing farm. It reconstructs detector-level objects, applies sophisticated algorithms to refine object identification and isolate specific event topologies. The HLT itself is running in two stages, where the first one is commonly called Level-2 trigger which utilizes information from calorimeters and muon stations. The second stage is known as Level-3 trigger and here algorithms utilize information from the tracker as well. The end result is a reduction of the rate down to $1-7$ kHz.

This two-tiered system allows CMS to retain the most relevant events for physics analyses, reducing the raw data volume by more than five orders of magnitude while preserving sensitivity to rare processes.

1.2.6   Particle reconstruction algorithm

The Particle Flow (PF) [13] algorithm in CMS performs a global event reconstruction by optimally combining information from all sub-detector systems (tracker, ECAL, HCAL, and muon detectors). Unlike traditional methods that treat calorimeter and tracking information separately, PF correlates every track and calorimeter deposit to identify the complete list of final-state particles (photons, electrons, muons, charged and neutral hadrons). This global approach yields a superb event description. In practice, PF provides the best possible measurement of each particle's direction, momentum and type, leveraging CMS's high ECAL granularity, hermetic HCAL coverage, and strong magnetic field. Once all PF candidates are formed, composite objects like jets and missing energy are built from them. Foundation of the algorithm lies within track reconstruction and calorimeter clusters.

Charged tracks are reconstructed using an iterative Combinatorial Track Finder (CTF) based on Kalman filtering [25, 26]. Firstly, tracker hits are grouped into hit-clusters, then the pattern recognition is performed iteratively. Lastly, using least-squares methods, best-fit values are extracted from track parameters.

The calorimeter signal reconstruction begins with pulse shape fitting using template functions to suppress out-of-time pileup. For the HCAL, distinct algorithms were used in 2016–2017 for HLT and offline processing, while the MAHI algorithm was adopted universally in 2018. The PF algorithm identifies local energy maxima as seeds, grows topological clusters from neighboring cells above noise thresholds, and applies a Gaussian mixture model to iteratively reconstruct PF clusters by sharing cell energies based on proximity to each seed.

The heart of PF is the linking stage, which associates tracks and clusters to form individual particle candidates. Once all tracks and calorimeter clusters are available, the algorithm proceeds in several steps. The first one is extrapolation of tracks. Through a careful procedure, each charged track from the tracker is projected outward to the calorimeters. If it intersects PF clusters in ECAL or HCAL, these elements are linked to that track. This connects a track's track (momentum) to corresponding energy deposits. Once a track is matched to calorimeter energy, the calorimeter contributions from that track are then removed from further consideration. This is crucial to avoid double counting. Any calorimeter cluster not linked to a track is considered to originate from a neutral particle (photon or neutral hadron).

PF then classifies each candidate by type. A charged hadron candidate is formed by a track with matching calorimeter clusters. Its momentum is primarily given by the track, and its energy is refined by adding ECAL/HCAL deposits. These are the bulk of particles in jets. A PF photon is identified as an ECAL cluster with no associated track and an electromagnetic shower shape, taking into account ECAL energy, as well as the ratio between HCAL and ECAL energy. Only photons isolated from other tracks and calorimeter clusters are retained. Bremsstrahlung photons radiated by electrons are recovered by linking additional ECAL clusters to nearby Gaussian Sum Filter (GSF) [27] tracks. An electron candidate arises when a track is linked to an ECAL supercluster (with little to no HCAL energy), resulting in one PF electron object. A muon candidate is a track that extends out to and is matched with hits or tracks in the muon chambers. Muons deposit negligible energy in the calorimeters, so their momentum is taken essentially from the tracker . Any HCAL (or ECAL+HCAL) cluster without a track is treated as a neutral hadron (e.g. K_L^0, neutrons).

After this linking and classification, the event is described by a list of PF candidates: charged hadrons, neutral hadrons, photons, electrons, muons, and taus. Jets are then reconstructed by clustering the charged and neutral hadron candidates (after removing those from pileup) using the anti-k_T algorithm [28]. Missing transverse energy (MET) is computed as the negative vector sum of all PF candidates' transverse momenta, giving an accurate measure of invisible momentum, i.e. the momentum carried away from the detector without it being detected.

Finally, each PF object is calibrated and corrected to match detector performance. For example, electron energies are calibrated using $Z \to ee$ events, i.e. scale factors and Gaussian smearing are applied so that the reconstructed Z mass peaks align between data and MC. Similarly, muon momenta are calibrated with data-driven corrections derived from fits to the $Z \to \mu\mu$ mass peak. All leptons also carry identification and trigger scale factors from tag-and-probe studies to correct efficiency differences between data and simulation. Neutral hadrons and photons receive calorimeter energy corrections, from test beams and physics samples. Jets formed from PF particles receive the standard jet-energy corrections. In practice, PF yields superior performance: because charged hadrons are measured by the precise tracker and photons by ECAL, CMS achieves much finer jet and MET resolution than with calorimeters alone. Overall, the PF algorithm's detailed clustering, linking and particle-by-particle reconstruction enables CMS to fully exploit its detector capabilities for precision physics analyses.

Chapter 2

# Upgrade of the CMS detector for the High-Luminosity LHC

2.1 The High-Luminosity LHC

The LHC will enter its third long shutdown period as of 2026 and will last till 2029 when Run 4 (and later runs) is planned to begin. During the shutdown period, the LHC systems and detectors/experiments (among which CMS) situated along the LHC will be upgraded as a preparation for the future runs. This upgrade of the LHC is known as the High-Luminosity LHC (HL-LHC) [29]. The timeline of the LHC and HL-LHC eras is shown in Figure 2.1. The main goal of the HL-LHC is the increase in instantaneous luminosity, which will result in an increase of the $p-p$ collisions rate. The total integrated luminosity of the HL-LHC phase is planned to reach about $3000-4000$ fb^{-1} [29], over a period of about ten years.

The main motivation behind the HL-LHC is to perform more accurate measurements, which would path the way for precision tests of the SM, as well as search for rare processes, new phenomena and new particles (e.g. dark matter particles). As there is a number of parameters to be measured more precisely and a plethora of hypothesis extending the SM to be tested, a large data sample of about 3000 fb^{-1} added to the so far collected data will be of great importance. Here the considerations of HL-LHC's impact on CMS's physics analysis program is limited to measurements centered around the Higgs boson, more specifically to the Higgs boson self-coupling to which more sensitivity will be gained with the increase in data sample. The Higgs boson self-coupling can be measured (see Chapter 4 for more details) in single-, di- and tri-Higgs boson production processes by measuring the production cross section which is sensitive to the mentioned coupling. An example of di-Higgs final state is $pp \rightarrow HH \rightarrow b\bar{b}b\bar{b}$, which is a rare process characterized by a small production cross section. However, despite the rarity of the process, it is an important channel as it is sensitive not only to the Higgs boson self-coupling, but also to the couplings of the Higgs boson to the gauge bosons through the VBF production mode (see Section 3.3.1). Another approach to the Higgs boson self-coupling measurement is through exploitation of quantum loops where Higgs boson appears, for example in the $pp \rightarrow H \rightarrow ZZ \rightarrow 4\ell$ process. Precisely determining the value of the mentioned couplings will put the SM to a closure test and possibly pave the way for new physics.

With increase in luminosity a consequent increase in pile-up is expected. Comparing the beam conditions of LHC to those of the HL-LHC, pile-up will increase from 40-60 (on average) per bunch crossing to about $140-200$ which will pollute the signal originating from the hard scattering event, i.e. the process of interest). This increase degrades trigger performance and event reconstruction.

Considering first the ill effects on trigger performance, a higher event multiplicity will increase
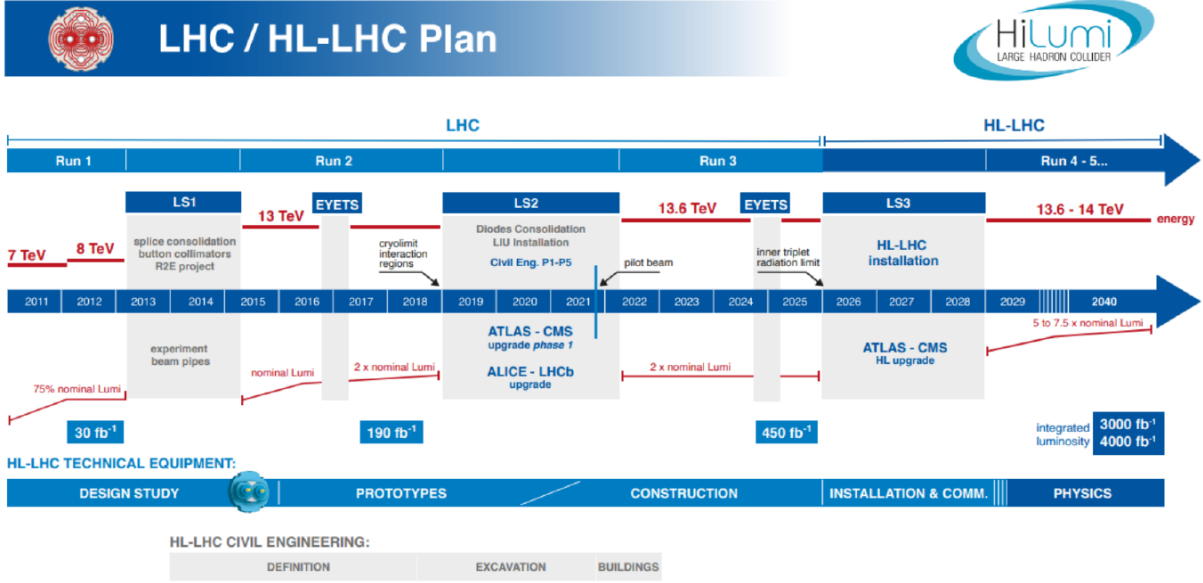
Figure 2.1. Projected timeline for LHC and HL-LHC era. Figure taken from Ref. [30].

the detector occupancy: jets and energy deposits originating from pile-would make disentangling between background and underlying hard scattering difficult, which leads to higher trigger rates. One possible way of mitigating such effects is to simply tighten the trigger thresholds. However, this means that events where hard scattering occurred might be lost due to tight constraints from the trigger side. When it comes to the event reconstruction, large number of vertices per bunch crossing and hits in the tracker, originating from pile-up, result in an overlap of tracks and calorimeter energy deposits. These overlaps from unrelated collisions are superimposed to the hard scattering event making event reconstruction challenging. Without a proper solution to the problems posed by high pile-up not only is the event reconstruction difficult, but also data from consecutive collisions may be merged during reconstruction due to trigger performance, buffers, processing speed, etc. Another important consideration which governs the upgrade is the resistance under extreme radiation conditions. Specifically, the highest fluences are expected in the Endcap region which is closest to the beam line.

High pile-up and extreme radiation conditions together govern and condition upgrades to the detectors along the LHC. In particular, in order to maintain its current performance in object reconstruction efficiency and resolution, the CMS detector is undergoing a "Phase-2 upgrade" which is planned to result also in tolerance to higher radiation levels. Undergoing upgrade involves work on several sub-detector systems as well as addition of completely new subsystems.

Tracking sub-detector system will be replaced in its entirety with a new tracker of higher granularity and higher radiation hardness. Enhanced granularity will be achieved by shortening the silicon strips and by using smaller and thinner pixels, which will result in a granularity increase by a factor of ~ 4. Also, the coverage in pseudorapidity will be increased, extending to $|\eta| \sim 4$. Comprehensive reports on CMS Phase 2 upgrade plans for all subsystems can be found in the following Refs. for: Tracker [31], Endcap Calorimeter (HGCAL) [32], Barrel Calorimeter [33], Muon Stations [34], L1 Trigger [35] and CMS Data Acquisition and High Level Trigger [36].

In the following section the Endcap Timing Layer MIP (Minimum Ionizing Particle) Timing Detector (ETL MTD) [37] will be discussed.

2.2 The MIP Timing Detector

As mentioned above, increased number of pile-up interactions (to $140 - 200$ per bunch crossing) poses a significant challenge for optimal performance of the detector as is. Due to increased pile-up performances of all CMS subsystems are affected. Constraining the discussion here to tracker system, the most notable challenge is to disentangle the myriad of overlapping vertices and tracks which makes particle, hence event, reconstruction extremely difficult. In the Phase 1 (Run 1, Run 2 and Run 3) of the CMS, vertices and tracks are reconstructed in three dimensions which in high pile-up conditions would make track association suboptimal, as can be seen in Figure 2.2. Simulation studies [37] show that including time information reduces the number of vertices merged in spatial dimension. In particular, using a MTD of resolution ~ 30 ps will allow to effectively split the bunch crossing (characterized by an RMS of $\sim 180 - 200$ ps) in time into smaller exposures of about $30 - 40$ ps. By doing so, the number of pile-up interactions would drop from a total of $\sim 140 - 200$ to a $\sim 40 - 60$ per exposure, which corresponds to current CMS performance conditions. Based on simulations, with inclusion of timing information in the tracker, for $\sim 140 - 200$ pile-up interactions the fraction of merged vertices is reduced from about 15% down to 1% whilst the number of pile-up tracks incorrectly assigned to the primary vertex is reduced by half.
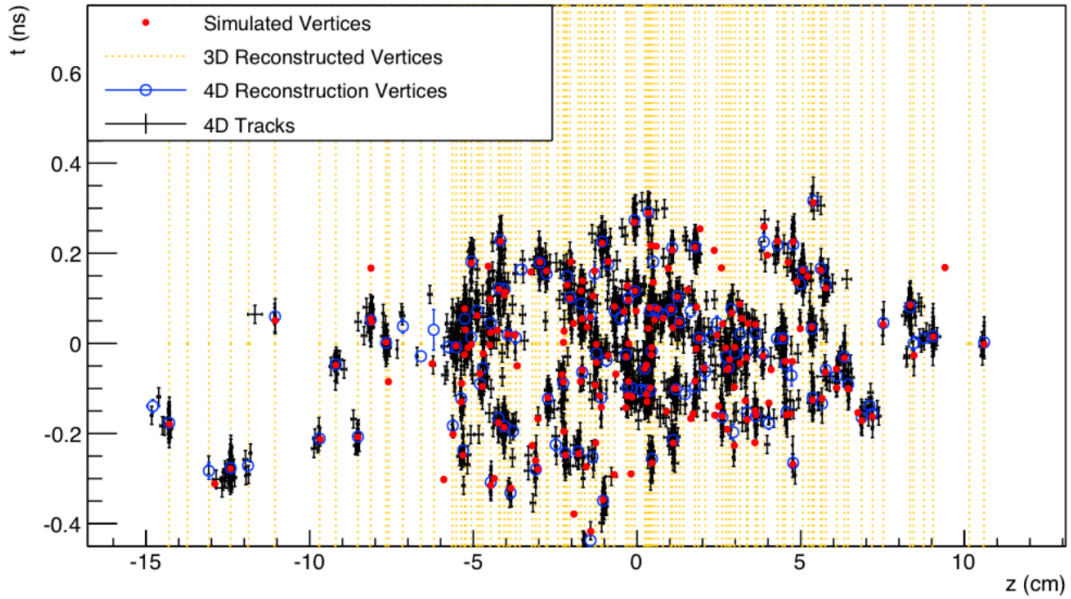
Figure 2.2. Simulated and reconstructed vertices in a bunch crossing with 200 pileup interactions assuming a MIP timing detector with ~ 30 ps ps time resolution covering the barrel and endcaps. The horizontal axis is the z position along the beam line, where the "0" is the center of the IR. The vertical axis is the time with "0" being the point in time when the beams completely overlap in z. The simulated vertices are the red dots. The vertical yellow lines indicate 3D-reconstructed (i.e. no use of timing information) vertices, with instances of vertex merging visible throughout the display. The black crosses and the blue open circles represent tracks and vertices reconstructed using a method that includes the time information and is therefore referred to as "4D". Many of the vertices that appear to be merged in the spatial dimension are clearly separated when time information is available. Figure taken from Ref. [37].

The MTD is designed as a thin detector layer which will be placed between tracker and calorimeters with the purpose of providing timing information of charged particle with resolution of $\sim 30 - 40$ ps at the start of HL-LHC era and due to radiation damage degrading to $\sim 50 - 60$ps by the end of HL-LHC era. The coverage of MTD extends to $|\eta| < 1.45$ in the Barrel Timing Layer (BTL) and

to $1.6 < |\eta| < 3.0$ in ETL. BTL and ETL cover different regions of the CMS detector which places constraints on their design. Several factors were considered when designing MTD. Namely, BTL will be inaccessible during the Phase 2 and less time was allocated to the development and construction of BTL which limits the technologies used to low time consuming R&D with well established production. Due to placement of the ETL it will be accessible for any potential repairs and upgrades. As the ETL will be installed in the high $|\eta|$ region it will be exposed to harsher conditions due to higher radiation levels which can be seen in Table 2.1 where expected radiation levels of different parts of BTL and ETL are summarized. Since the ETL will be exposed to higher radiation levels when compared to BTL, it had to be designed to be more radiation tolerant. BTL part of MTD will have about 2.5 times higher surface area than ETL. One more important aspect in consideration when designing the detector was economical availability. Based on these considerations it was decided that these two distinct parts of MTD, ETL and BTL, will be instrumented with different technologies.

Table 2.1. Expected radiation fluences and doses in different MTD regions after an exposure to integrated luminosity of 3000 fb^{-1}. Table taken from Ref. [37].

| Region	$|\eta|$ range	r [cm]	z [cm]	Φ [n$_{eq}$/ cm^2]	Dose [kGy]
Barrel	0.0	116	0	1.65×10^{14}	18
Barrel	1.15	116	170	1.8×10^{14}	25
Barrel	1.45	116	240	1.9×10^{14}	32
Endcap	1.6	127	303	1.5×10^{14}	19
Endcap	2.0	84	303	3.0×10^{14}	50
Endcap	2.5	50	303	7.5×10^{14}	170
Endcap	3.0	31.5	303	1.6×10^{15}	450

The BTL was designed as a cylindrical detector which will be installed inside the Tracker Support Tube (TST). Its active length will be about 5 m along the beamline, and its radial design will assume inner radius of 114.8 cm and outer radius of 118.8 m with a maximum thickness of 4 cm . The detector will be instrumented with LYSO:Ce scintillating crystal [38], coupled to and ready out by Silicon Photo Multipliers (SiPMs) [39]. Both of these components have been proven to be radiation tolerant to fluences up to 2×10^{14} n$_{eq}$/cm and to radiation doses of several tens of kGy [39]. The BTL will be read out by Time of Flight High Rate (TOFHIR) chip [40].

The ETL will be placed on both sides of the interaction region, between CE and Tracker, as shown in Figure 2.3. Each ETL will be comprised of two large disks which are designed to have radial coverage from 315 mm to 1200 mm which corresponds to previously mentioned pseudorapidity coverage of $1.6 < |\eta| < 3.0$. Along the beamline the ETL takes up 45 mm and its active surface per Endcap is ~ 7.2 m (both disks) while the fill factor (fraction of area sensitive to MIPs) is above 85%. Each disk will be covered on both sides with Ultra Fast Silicon Detectors (UFSDs) which are based on the highly radiation tolerant Low Gain Avalanche Diode (LGAD) technology [41]. LGAD are characterized by a moderate internal gain (about $10-30$), low noise, low jitter and fast rising pulses. For optimal performances LGAD are require to also have small capacitance which limits their size. A 16×16 module (in MTD TDR [37] a different design was reported, which was improved upon) of 256 pads, each with surface are of 1.3×1.3 mm^2 giving the total module surface are of 21×21 mm^2 (Figure 2.4), will be used to optimally instrument total surface are of ETL. Each module will be read out by dedicated Endcap Timing Read Out Circuit (ETROC) ASIC [42, 43]. With two disks per Endcap region, the ETL aims to maintain resolution of $30 - 40$ ps. up to the end of HL-LHC era. This means that bump-bonded ETROC+UFSD system must have resolution of ~ 50 ps per single hit, where with two hits (on average 1.7) per track the resolution is given by $\sigma_{track} = \sigma_{hit}/\sqrt{n}$, where n

is the number of hits. As ETL will be exposed to large radiation it is designed to be accessible for potential repairs and upgrades. To make it accessible the two disks on Endcap side occupy thermally isolated volume, and each disks is split down vertically into two segments. In depth description of the MTD and its components, their integration and design can be found in Ref. [37].
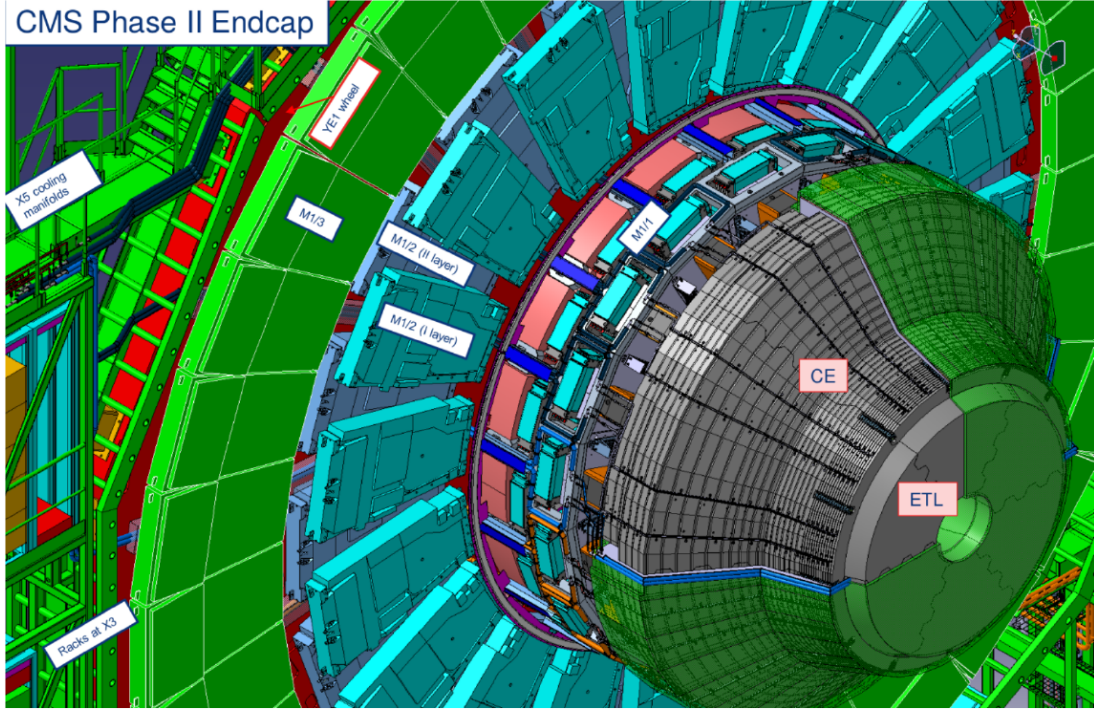
Figure 2.3. Schematic overview of the upgraded "nose" of the CMS's calorimeter. The ECAL is positioned in front of CE. Figure taken from Ref. [44].
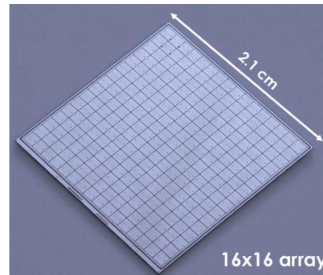
Figure 2.4. A prototype design of 16×16 pad matrix. Figure taken from Ref. [45].

2.3   UFSD sensors

UFSD is technology based on LGAD which is a semiconductor based diode. A regular PIN diode operated under reverse bias is comprised of a p^{++} (p doped silicon) and n^{++} (n doped silicon) electrodes, and a intrinsic bulk. Diodes characterized by a lightly p doped bulk are often also considered PIN diodes in literature, as will be the case here. When a reverse bias is applied to such a device, i.e. when a negative external voltage is applied to the p^{++} electrode while leaving n^{++} electrode at ground, the pn junction is inversely polarized which creates a large depleted volume. When a charged particle

traverses the sensor it creates electron-hole $(e-h)$ pairs which move towards electrodes under influence of the electric field. The moving charges induce charges on the electrodes, i.e. current signal, where the current induced on the k electrode is given by the Shockley-Ramo's theorem [46, 47]:

$$i_k(t) = -q\vec{v} \cdot \vec{E_w}, \tag{2.1}$$

where q is the charge of particle which induced current, $\vec{v}$ is its drift velocity and $\vec{E_w}$ is weighting field which has the same dependence on geometry as an electric field between parallel electrode plates where the read-out electrode is numerically set to 1 whilst the other is set to 0. Numerically it is equal to $1/d$, where d is thickness of the sensor. If the weighting field is constant, the induced current depends on drift velocity, which depends on the temperature and the electric field (formed in the depletion region). It can be seen that the drift velocity determines how quickly the signal is formed. Saturating the drift velocity at room temperature requires electric field of ~ 30 kV/cm in case of electrons (holes), whilst for holes it is considered as constant above $\sim 50 - 100$ kV/cm.

If the electric field is higher than ~ 300 kV/cm, electrons on their mean free path acquire sufficient energy to produce secondary charged pairs upon impact [48] with silicon atoms. As mean free path of holes is larger than that of electrons, the electric field can be tuned so that only electron induce charge multiplication. Assuming only electrons induce charge multiplication, the electron mean free path $\alpha_n(E, T, \Phi)$ is constant across the high-field region (d_{High}) and generation of next generation charged particles is negligible, the number of generated secondary charges can be written as:

$$N_{e-h}(d, E, T, \Phi) = N_{0,e-h} \cdot E^{\alpha_n(E,T,\Phi)d_{High}}, \tag{2.2}$$

where $N_{0,e-h}$ is number of charged pairs generated by the impinging particle, E is the electric field, T is temperature and Φ is fluence. Ratio of $N_{e-h}(d, E, T, \Phi)/N_{0,e-h}$ is defined as gain G. Applying high enough voltage to induce charge multiplication within PIN diode would achieve high gain values, which would result in a larger current and make the signal detection easier. However, the sensors would enter breakdown due to high fields, hence a different approach has to be taken.

The Low-Gain Avalanche Diodes (Figure 2.5) are silicon based diodes that utilize a narrow $(0.5 - 1$ μm) p^+ doped layer, gain layer, directly beneath the n^{++} electrode $(0.5 - 2$ μm). Applying a reverse bias voltage to LGAD sensor depletes the gain layer which results in formation of high enough electric field for the electrons to induce charge multiplication close to the pn junction. Once a charged particle passes through LGAD sensors it creates $e-h$ pairs which drift towards the n^{++} (e) and p^{++} (h) electrodes. On their way to the n^{++} electrode, electrons enter the gain layer, where charge multiplication happens. As the charge multiplication occurs in the vicinity of the n^{++} electrode, secondary electrons are collected quickly, whilst secondary holes have to traverse the entire bulk of the LGAD sensor before being collected on the p^{++} electrode which is the why the induced current is dominate by current generated by holes.

In order to achieve excellent timing performances several aspects have to be considered. The weighting field has to be uniform which is achieved if the electrodes are much larger than the thickness. Electric field in the depletion region must be high enough to saturate the drift velocity of electrons as the signal rise time is governed by the electron drift time. Sensors need to be thin and achieve a high fill factor and fine segmentation. Lastly, UFSD sensors must be as radiation hard as possible. Effects of radiation are leakage current (current that flows through the sensor when a reverse bias is applied to pn junction) increase which is controlled by thickening the sensor and keeping the operational temperature low, variation of the doping concentration via donor and acceptor removal (solution discussed in Refs. [49–52], and charge trapping which is related to high drift times and radiation fluence. Interestingly, considering even the highest fluences, shape of the signal does not change dramatically [53].
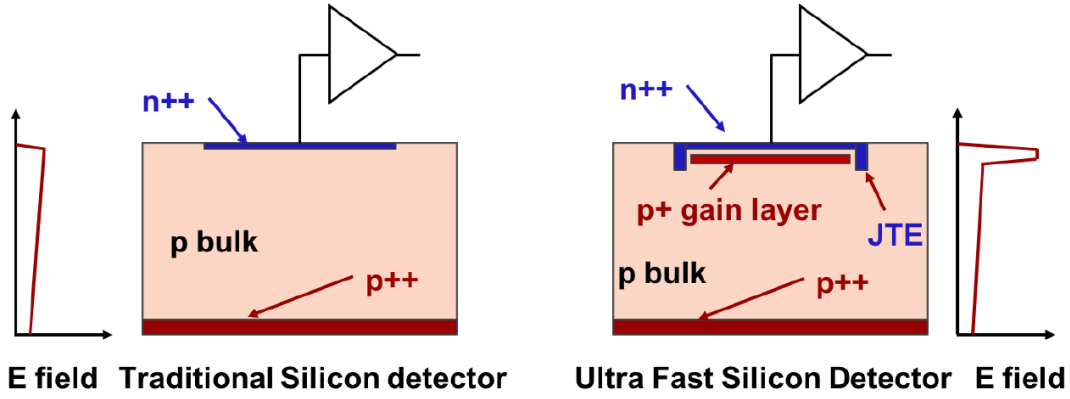
Figure 2.5. Cross-sectional diagrams comparing a standard silicon detector and a UFSD with an additional p implant providing the larger electric field needed for charge multiplication. Figure taken from Ref. [37].

The time resolution of UFSD sensors is governed by several factors [37, 53], listed here without in-depth discussion. Due to presence of the noise on top of the signal, firing time of the comparator (fires when preamplifier reaches given voltage threshold) is shifted, which can result in either delayed or earlier firing, an effect know as jitter which is tackled by keeping the sensor's noise lower than the electronic noise and by increasing the signal slew rate. Comparing large and smaller signals, large signals cross the given voltage threshold earlier than the small signals, which is an effect know as time walk and is tackled by using adequate Constant-Fraction-Discriminator (CFD). Third term which contributes to the total time resolution is the Landau noise term, a term that accounts for (non)-uniformity of the energy deposition which follows a Landau distribution. Non-uniformity of drift velocity and/or weighting field introduce distortions in the signal which can be controlled by large electric field and by using electrodes which are much larger than the thickness of the sensor. Flow of electrons over the pn junctions introduces a fluctuation of the current, which is called the shot noise. The shot noise is increased due to random nature of multiplication process, which means the number of secondary charges differs from G (on average it is G). The last term that contributes to time resolution of UFSD sensors is related to digitization of comparator's output, specifically usage of Time-to-Digital-Converter (TDC) which has its own time resolution which is in HEP $\sim$ 10 ps. With this in mind, in case of geometry that is like that of parallel plate capacitor, where electrodes are much larger than the thickness and if electronic's noise is the dominant source of noise, the time resolution can be expressed as:

$$\sigma_{\text{t}} = \sqrt{\sigma_{\text{jitter}}^2 + \sigma_{\text{Landau}}^2}. \tag{2.3}$$

where the Landau noise term is the dominant source of the noise in a well-designed system.

Properties of UFSD sensors were studied extensively, and can be found for example in Refs. [54–57]. Here a inter-pad region design and optimization [58] and novel elastomer measurement is presented.

2.4 Inter-pad region design and optimization

Achieving fine segmentation and high fill factor is done by grouping as much UFSD sensors as possible in as small area as possible. However, there are certain limitations here. Design of inter-pad region, which is a no-gain region, determines the fill factor. This region separates two adjacent pads (also referred to as a pixels) and is not equipped with a gain layer. Reducing its width would increase

the fill factor. A sketch of a UFSD multi-pad design with a key components marked is shown in Figure 2.6. The guard-rings are designed to gradually decrease the voltage (its absolute value) from the edge of the sensor which is biased to the first read-out pad which is grounded. Junction Termination Extension (JTE) is designed to prevent $e - h$ pairs produced by a traversing charged particle from reaching the gain layer as this would delay the signal. JTE designed as a n^{++} implant equipped with a metal field plate. In the region between JTEs of two neighboring pads a p-stop implant (p^{++} doped) is placed. its purpose is to prevent shortening of all n^{++} implants which would happen due to creation of inversion layer at the $Si - SiO_2$ interface(trapped positive charges). Design and optimization of the inter-pad region are presented in Ref. [58], from which a part will be presented here, specifically the study of sensors from the UFSD3.1 production manufactured by Fondazione Bruno Kessler (Italy).
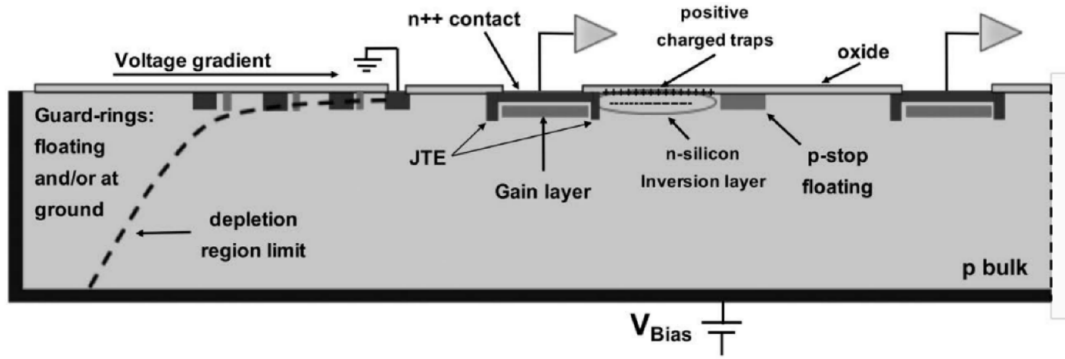
Figure 2.6. Cross section schematic view of a UFSD multi-pad design with components marked. Figure taken from Ref. [53].

UFSD3.1 production explores a range of inter-pad region designs and p-stop doping. Wafers of UFSD3.1 production are produced with different doping of p-stop, expressed in arbitrary units where the reference point is that of UFSD2 and UFSD3 production: W12 has p-stop doping of 0.02, W13 has p-stop doping of 0.05, W14 has p-stop doping of 0.1, W16 has p-stop doping of 0.15, W17 has p-stop doping of 0.2 and W18 has p-stop doping of 1. Different design of inter-pad region are presented in Figure 2.7, with specifics given in Table 2.2.

Table 2.2. Inter-pad region design of the UFSD3.1 arrays. Table taken from Ref. [58].

Type	Interpad region width [μm]	Region A/B design	Region A area [a.u.]	Region B area [a.u.]
1	16	*Grid*	A	2B
2	20.5	*Full*	100A	10B
3	20.5	*Full*	10A	B
4	23.5	*Grid*	2A	2B
5	25	*Full*	20A	2B
6	27.5	*Full*	10A	B
7	27.5	*Full*	20A	2B
8	27.5	*Grid 2*	2A	2B
9	38	*2 p-stops*	/	/
10	49	*Grid guard-ring*	/	/
11	25	*Empty*	100A	10B

Biasing the sensor and measuring its leakage current it can be seen how p-stop doping affects at which bias voltage the breakdown occurs. Figure 2.7 showcases how leakage current for type 2 design for different wafers, with different p-stop doping between them, increases as the bias increases up to a certain point where a breakdown occurs (abrupt change in trend). It is observed that sensors

with higher p-stop doping undergo premature breakdown, whilst sensors with lower p-stop doping reach the expected breakdown voltage which is around $360 - 380$ V. In the case when p-stop doping was kept fixed while different design type was used it was observed that sensors characterized by larger region A/B surface undergo breakdown earlier than sensors characterized by lower region A/B surface. Sudden change in trend of I(V) curves is explained by existence of the high electric field in the inter-pad region. This electric filed arises at the pn junction between the inversion layer and the p-stop [59]. Doping concentration of the p-stop governs how high the electric field is, i.e. higher doping leads to a higher values of electric field. Also, the inter-pad width and sensor thickness contribute to the arising electric field. As the p-stop is floating its potential is determined by the applied bias voltage and the ground of adjacent pixels. In thin sensors, the p-stop potential will float closer to the values of applied bias voltage resulting in a higher electric filed which can cause early breakdown of sensors characterized with narrow inter-pad region.
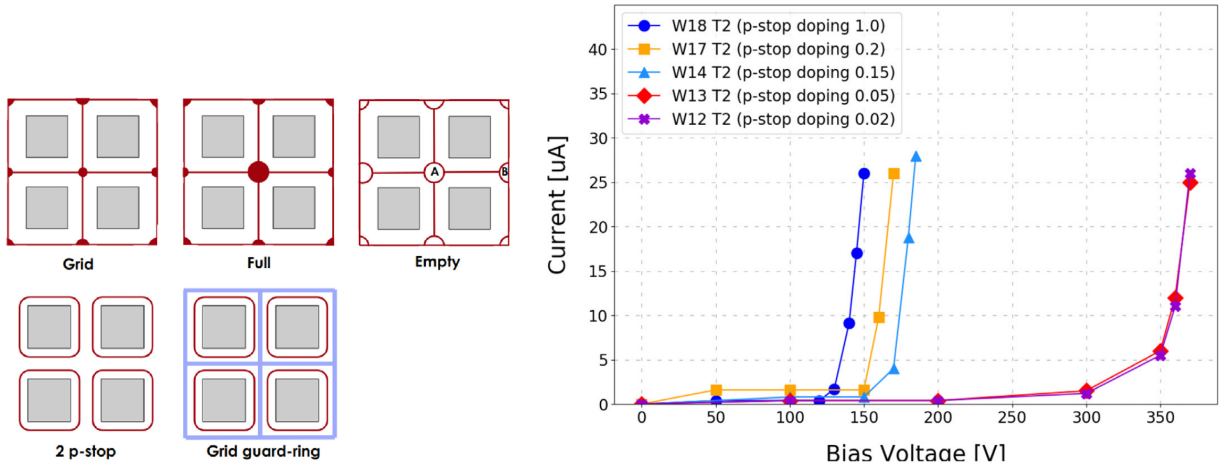
Figure 2.7. Sketch (left) of of the structures present in the inter-pad region of the UFSD3.1 design, where the p-stops are shown in maroon, and the guard-ring is in blue. I(v) characteristic of devices with different p-stop doping having the same inter-pad design (Type 2). Figures taken from [58].

Based on measurements performed on UFSD3.1 campaign it can be concluded that low p-stop doping and small region A/B surface are the optimal characteristics to avoid early breakdown of a sensor. Inter-pad width of ~ 25 μm is achievable, e.g. type 4 (Table 2.2). Measuring procedure of inter-pad width, study of effects of micro discharges, effect of floating pads and grid guard-ring design done for UFSD3 and UFSD3.1 production are discussed in detail in Ref. [58].

2.5 Elastomer measurement

A pioneering measurement, the elastomer setup measurement, was developed in the Laboratory of Innovative Silicon Sensors (Dept. of Physics, Univ. of Torino and INFN Torino). The measurement is focused on contacting all single pads of a multi-array pad system with an elastomer-based material, doped with silver to ensure conductivity. The goal of this study is to assess the potential usefulness of this kind of setup, where all pads are contacted at the same time with a non-metallic material which allows for a measurement of a collective leakage current, and paving a way for a future precise measurement in which, by contacting all 256 pads, a faulty sensors can be detected right away. Also, the usefulness lies in the fact that a collective leakage current (or in general, a current) can be measured easily at low cost. An additional aspect is the uniformity of measurement, which can be achieved by

contacting all of the single pads at the same time in the same way with the same material/read-out component.

Several different measurements of UFSD4 16×16 sensors characteristics were performed, namely the leaking current, the guard ring current and the behavior under change of temperature for a fixed value of the reverse bias. Besides the development of a new experimental technique, for which the work presented here serves as a basis, the measurements presented provide a baseline comparison to some of the characteristics measured by FBK. This provides a baseline check through which the validity of the elastomer measurement can be validated and used for further development of the technique.

2.5.1 UFSD4 production

The UFSD4 is the latest production series of ultra-fast silicon detectors made by FBK. It consists of 18 6-inch wafers. Several different pad arrays were included in the UFSD4 production series, 1×2, 2×2, 5×5 and 16×16. The inter-pad region adopts the type 9 and type 10 designs, with 5 different guard rings design, GR3_0, GR3_1, GR3_2, GR5_1, GR5_STD. The wafer layout is shown in Figure 2.8. Gain layer doses (Boron, expressed as doses relative to UFSD2 production) vary across wafers, as well as carbon implants doping, diffusion type. Also, the design features shallow and deep gain layers. The details of the production are given in Table 2.3. Sensors of the UFSD4 production are 50 μm thick. Considering 16×16 sensors, a standard guard ring design is adopted, where the guard ring loops around a 16×16.

Table 2.3. UFSD4 wafer characteristics. CH-BL stands for carbon diffusion at high thermal load, followed by boron diffusion at low thermal load (and analogous for CL-BL). Table taken from Ref. [60].

Wafer	DI	Gain-layer dose	Carbon dose	Diffusion
1	Shallow	0.96	0.8	CH–BL
2	Shallow	1.00	1.0	CH–BL
3	Shallow	0.98	1.0	CH–BL
4	Shallow	0.98	0.8	CH–BL
5	Shallow	0.98	0.8	CH–BL
6	Shallow	0.98	0.8	CH–BL
7	Shallow	0.98	0.8	CH–BL
8	Shallow	0.98	0.8	CH–BL
9	Shallow	0.98	0.8	CH–BL
10	Shallow	0.98	0.8 + CS0.6	CH–BL
11	Shallow	0.98	0.8 + CS0.6	CH–BL
12	Deep	0.75	0.6	CL–BL
13	Deep	0.77	0.6	CL–BL
14	Deep	0.77	0.6	CL–BL
15	Deep	0.77	0.6	CL–BL
16	Deep	0.77	0.6	CL–BL
17	Deep	0.79	0.6	CL–BL
18	Deep	0.79	0.6	CL–BL

2.5.2 Experimental setup

The characterization of UFSD4 16×16 pad arrays (hereafter sensors) was performed by measuring the I(V) characteristic curve, i.e. the leakage current as a function of bias voltage. The leakage current is
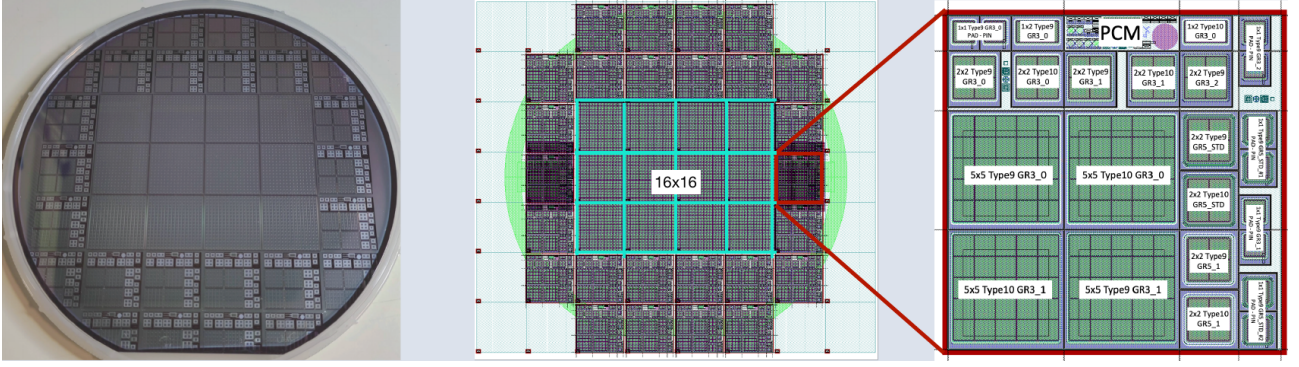
Figure 2.8. UFSD4 wafer (left) and reticle (middle and right) layout. In cyan a matrix of 16×16 sensors is marked, whilst in red smaller pad arrays are marked. The right figure show positioning and characteristics of smaller pad arrays. Figure taken from Ref. [45].

measured in the absence of traversing ionizing particles and for these purposes the measuring devices are placed in a black box. The current-voltage characteristic was measured with a probe station, equipped with a Keysight B1505 power device analyzer [61]. The probe station features a metal plate, referred to as the *chuck*, on which the sensor is placed and held in place by a vacuum pump-based system. The chuck is negatively biased, while the tungsten-rhenium needles which contact specific points of the sensor's front face are grounded. The needles used as contact to the sensor are equipped with micrometer screws which ensures fine manipulation of the needles. The probe station is also equipped with an optical microscope with different magnification levels.

Using a PRUSA® printer and a PLA prusament printing (non conductive) material, a dedicated mask was printed to hold the sensor in place. The mask consists of three pieces, two of them contacting and covering opposite sides (back and front) of the sensor, with the front mask designed to cover the sensor edge-to-edge while leaving some space to contact the guard rings. The third part, which is a mask cover, is equipped with a copper tape and contacts the elastomer through the opening on the front mask. A clamp was also 3D-printed to press and hold the mask around the sensor tightly. The bottom side of sensor is contacted with a copper tape by elastomer interlaid between the tape and back of the sensor, while the entire surface of the top side (through the opening) was contacted with an elastomer material doped with silver (conductive elastomer) to enable sensor biasing. The mask pieces are shown in Figure 2.9. As sensors are fragile, a mat resistant to static electricity is used to cover the work area, which ensures a proper handling of the sensors avoiding any potential damages due to static discharge. This configuration enables controlled ramping of the reverse bias while monitoring the leakage current, breakdown behavior, and the onset of gain-layer depletion.

In cases where the guard ring current (or the current of a single pad) is measured, the probe station was used with its needles and chuck to contact the sensors and enable the biasing, whilst for the elastomer measurement needles and chuck are not needed, as biasing is achieved with a system of cables contacting the copper tape.

For an I(V) measurement at varying temperatures, voltage was gradually increased to a value which corresponds to 8 fc of collected charge. The voltage value differs between wafers with different sensors design (see Table 2.3). Before enclosing a sensor in the mask, and after performing a measurement, all of the sensors were subjected to optical inspection using the probe station's microscope.
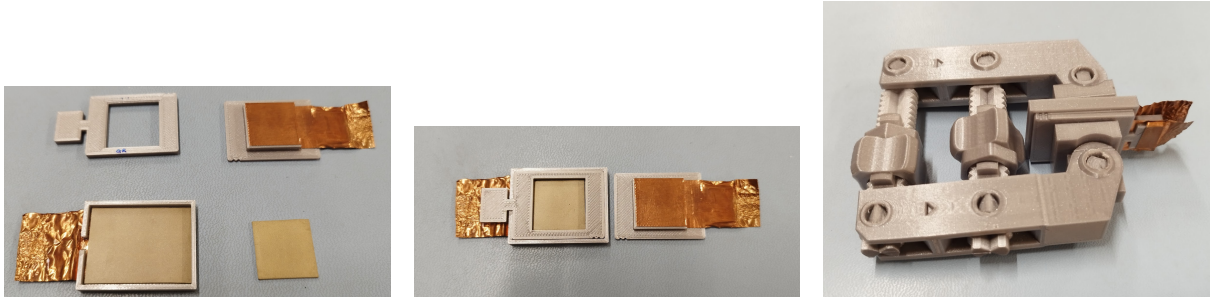
Figure 2.9. Left picture shows pieces (three) of the sensor's mask with a small elastomer cutout that tightly fits the opening on the top mask. Middle picture shows the top and bottom mask pieces fit together with elastomer cutout fit within the opening (it covers the sensor). Right picture shows the clamp tightened and holding the mask with copper tapes sticking out to ensure enough space for wires to be attached to.

2.5.3 Leakage current and guard ring current scan

A baseline measurement of the leakage current of UFSD4 16×16 sensors at room temperature was performed using the elastomer setup and was compared to measurements made by FBK. Leakage current is read out from the back of the sensor, dubbed I_{BACK}. In total 45 sensors were tested, where a selection across different wafers was made. The labeling, present in each of the plots below, is adopted as Wafer_Column-Row, where column and row are read out from the wafer layout grid shown in the middle of Figure 2.8. For each of the I(V) scans an upper limit on current, i.e. compliance, was set thus avoiding sudden offset of charge multiplication.

Every sensor was investigated using a microscope before and after measurement. The setup itself does not damage the sensors as the used elastomer material does not have sharp edges and it soft, although it may happen that due to the nature of the setup, i.e. frequent opening of the mask, the sensor gets dirty. Dust particles can creep into between the mask and sensor under test. Adding to matter "contaminating" the space between elastomer and the sensor, the elastomer material itself has fiber-like structure on the surface that can shed sometimes and make the sensors dirty, however this does not damage the sensors. It could also be the case that these fibers are from an outside source, present on the work station or in the air.

There is an important remark on the handling of the sensors. Scratches were observed in some cases, which cause the sensor breakdown. These scratches can come from two sources, handling with tweezers or contacting the sensors with the needles of the probe station. In case of tweezers, plastic ones are preferred, and so the ones with smooth edges and flat tips instead of the point tweezers. Another contributing factor to the precision of performed measurement is the level of tightness of the clamp used to press down elastomer material and hold the mask (and sensors) in place. Elastomer material is soft and elastic enough not to tear and break under the stress of the tightening clamp. However, the lack of proper scale to indicate the level of tightness contributes to the precision, or the lack thereof. On the other hand, the silicon sensors are resilient to stress in the geometry of the setup, and the clamp can be tightened to its maximum making sure the sensors was contacted by elastomer uniformly and over all pads. In all of the results presented here the I_{BACK} current is displayed as positive.

Here two scans are shown, with representatives of a good and a suboptimal scan. On Figure 2.10(a) a scan of selected sensors from wafer 10 is shown, whilst on Figure 2.10(b) a scan of selected sensors from wafers 8 and 9 is shown. From Figure 2.10 it can be seen that the trend of the I(V) curve is replicated well, however the FBK and elastomer curves do not match exactly, rather

elastomer measurement tends to be positioned higher, i.e. tends to exhibit higher current values. Analyzing measurements of selected sensors from wafers 8 and 9, again the same behavior is observed, i.e. the elastomer measurement shows a slightly higher leakage current. Sensors W8_2-3 and W9_2-5 when measured with elastomer setup go into charge increase $50 - 100$ V sooner than what FBK measured. This behavior might indicate the sensor breakdown, or in fact the setup might be faulty, as there is a number of variables that may affect the measurement. Optical inspection shows that sensors W9_2-5 W8_2-3 had the same surface damages in the form of scratches prior and after the measurement. In this case the elastomer setup didn't cause extra damages, meaning they may have happened during some prior handling.

Looking at sensors W9_3-3 and W9_4-5, it can be safely concluded that the sensors are broken and inoperable as the same trend was measured with elastomer setup and by FBK. For these sensors they are characterized by rapid onset of current increase. Measurement performed on all the other sensors are shown in Appendix A, where similar trends and results are observed, hinting about the usefulness of the elastomer setup. Optical inspection indicates surface damages of these sensors.

(a)   (b)
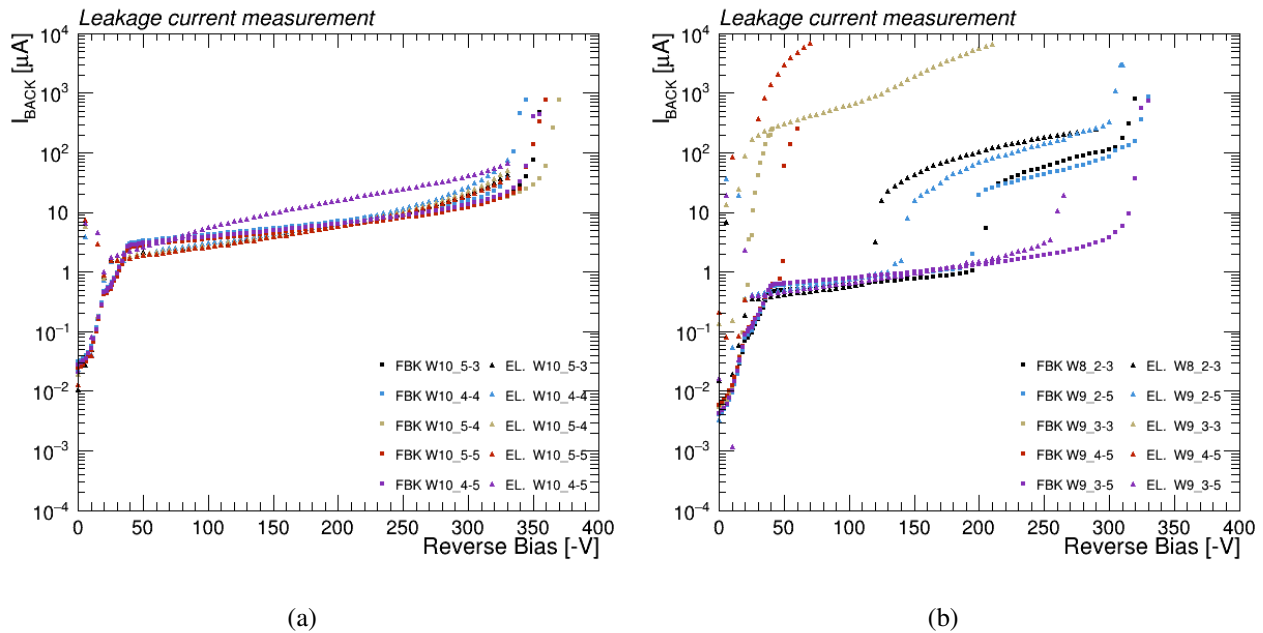
Figure 2.10. Leakage current scan, measured on sensors selected from wafer 10 (a) and wafers 8 and 9 (b), as a function of reverse bias. Elastomer measurements are labeled with triangles and the FBK measured values are labeled with squares.

For each of the 45 tested sensors, the guard ring current was also measured and compared to the one reported by FBK. The guard ring current is measured using the probe station, by contacting the guard ring with a needle and by keeping the back of a sensor reverse biased. Measurements performed on the same batches of sensors as reported above, is also reported here. Guard ring current measurement of sensors selected from wafer 10 is shown in Figure 2.11(a) and of sensors from wafers 8 and 9 is shown in Figure 2.11. Just as in the case of leakage current scan, the guard ring current scan of wafer 10 selected sensors shows (Figure 2.11) good agreement with the FBK measurement, while for W8 and W9 there is agreement to some extent. What is observed is a higher current than measured by FBK, and earlier current increase, except in the broken sensors. Results of measurement performed on remaining sensors are shown in Appendix A.

Further tests were done on a different batch of sensors to inspect their behavior under temperature

27
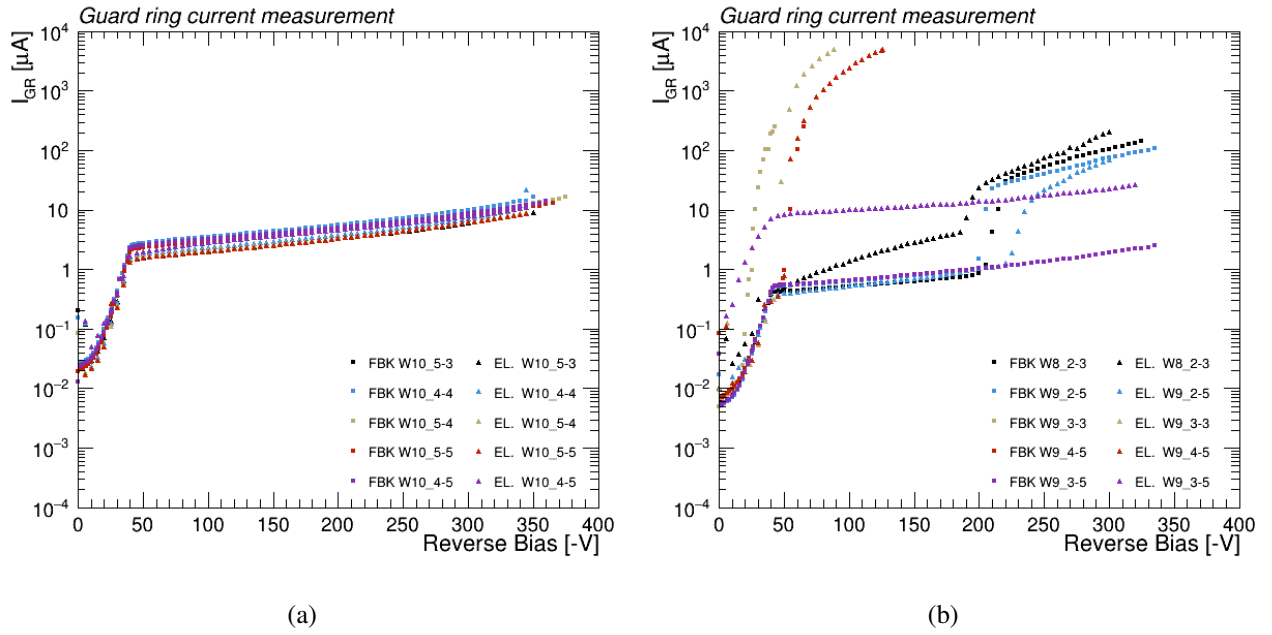
Figure 2.11. Guard ring current scan, measured on sensors selected from wafer 10 (a) and wafers 8 and 9 (b), as a function of reverse bias. Elastomer measurements are labeled with triangles and the FBK measured values are labeled with squares.

change, namely how does the leakage current change when sensors are exposed to different temperatures set to a reverse bias which corresponds to 8 fC of collected charge. The temperature was varied from $20°$ C (first measurement) to, $0°$ C, $-25°$ C and again to $20°$ C (last measurement), while also adjusting the voltage level to correspond to 8 fC of collected charge. After every temperature change, we waited for 40 mins for temperature, voltage and overall the system to settle, then the measurement was made. A difference between the first and last measurements (at the same temperature, and reverse bias) is visible, indicating a mild hysteresis effects. For four sensors, the observed effect is shown in Table 2.4.

Table 2.4. Comparison of the first and last measured leakage current values for selected UFSD4 sensors, measured with the elastomer setup. Measurements were performed at $20°C$, at the indicated reverse bias voltage.

Sensor	Bias [V]	I_{first} [μA]	I_{last} [μA]
W2_4-4	250	-59.3	-310
W7_3-4	250	-4.9	-4.49
W9_3-4	250	-21.2	-36.8
W17_4-3	175	-123.9	-170

One possible explanation of this effect is a possible change in contact pressure. If the clamp is not sufficiently tight a small fluctuations in contact and the resistance can arise due to the elastomer contraction and relaxation due to temperature change. The clamp itself may exhibit the same behavior, loosening the grip on the sensors as the temperature changes.

Chapter 3

The Standard Model of particle physics

The Standard Model (SM) [62–64] of particle physics is a quantum field theory (QFT) [65–67] that successfully describes all known elementary particles (point-like objects, no substructure) and three of the four fundamental forces of nature (electromagnetic, weak, and strong) in a single unified framework. The cornerstones of the SM are QFT formalism, gauge group formalism, symmetry formalism, Lagrangian formalism, renormalization [68], spontaneous symmetry breaking [69–72] and relativistic quantum mechanics. The SM symmetry group is expressed as a product of gauge symmetry group and space-time symmetry group: $\mathcal{G} = G \times P$, where P is the Poincaré symmetry group and the SM local gauge symmetry group G is defined as $SU(3)_C \times SU(2)_L \times U(1)_Y$ (expressed via Lie groups), which incorporates the principles of local gauge invariance. Each gauge symmetry group is associated with one fundamental interaction, as will be discussed.

As described by the SM, everyday matter (excluding dark matter) is constituted of fundamental particles (fermions) which interact by exchanging gauge bosons, i.e. the force carriers. Fermions of the SM are further grouped into two categories, quarks and leptons. Each gauge boson of the SM is associated with a certain interaction, i.e. a gauge symmetry group. In addition to gauge bosons, the SM includes one more boson, the Higgs boson which is a scalar particle associated with the Higgs field. The Higgs field itself is associated with the electroweak symmetry breaking (EWSB), also referred to as spontaneous symmetry breaking (SSB), a mechanism by which particles gain mass.

The quarks and leptons are further organized into three families (generations), where all families are characterized by the increasing mass. Each generation contains two quarks (with electric charges $+\frac{2}{3}$ and $-\frac{1}{3}$ in units of the elementary charge $|e|$) and two leptons (one charged -1 and one neutral). The first generation is comprised of the up (u) and down (d) quarks, the electron (e^-) and the electron neutrino (ν_e). The second generation contains the charm (c) and strange (s) quarks, the muon (μ^-) and muon neutrino (ν_μ), and the third generation contains the top (t) and bottom (b) quarks, the tau lepton (τ^-) and tau neutrino (ν_τ). In total there are 12 fermions, where for each fermion there exists an associated antiparticle characterized by the same mass and opposite charge. In terms of interactions, the main difference between leptons and quarks is that quarks interact via strong force, while leptons do not. The gauge bosons of the SM are the force carriers, as will be discussed: the electromagnetic interaction is mediated by the photon γ, the weak interaction by the charged W^+, W^- bosons and the neutral Z boson, and the strong interaction is mediated by eight gluons g. Elementary particles in the SM are listed in Table 3.1.

Table 3.1. Fermions (leptons and quarks) and bosons (gauge and Higgs) of the SM

Leptons	Quarks	Gauge bosons	Higgs boson
$\begin{pmatrix} \nu_e \\ e \end{pmatrix}$	$\begin{pmatrix} u \\ d \end{pmatrix}$	g (gluon)	H
$\begin{pmatrix} \nu_\mu \\ \mu \end{pmatrix}$	$\begin{pmatrix} c \\ s \end{pmatrix}$	γ (photon)	
$\begin{pmatrix} \nu_\tau \\ \tau \end{pmatrix}$	$\begin{pmatrix} t \\ b \end{pmatrix}$	$W^\pm, Z$	

3.1 Quantum Chromodynamics

The strong interaction is described by the theory of Quantum Chromodynamics (QCD) [73]. It is a non-Abelian gauge theory based on the $SU(3)_C$ color symmetry group which provides a description of how quarks and gluons interact. Quarks carry a color charge, which is a charge of the strong interaction, with three color states conventionally denoted as red (R), green (G) and blue (B). Gauge bosons of QCD, i.e. particles which mediate the force between color-charged particles, are the gluons. As there are 8 generators of the $SU(3)_C$ group, there is a total of 8 gluons, each one carrying a combination of color–anticolor charge. Conventionally, generators of the $SU(3)_C$ group are represented via the Gell-Mann matrices in the triplet representation, $T_a = \frac{1}{2}\lambda_a$ ($a = 1, \ldots, 8$).

The QCD Lagrangian for a single quark flavor q, invariant under $SU(3)_C$ transformations, is written as (mass term is introduced later on):

$$\mathcal{L}_{\text{QCD}} = \bar{q}\Big(i\gamma^\mu D_\mu\Big)q - \frac{1}{4}G^a_{\mu\nu}G^{a,\mu\nu} \tag{3.1}$$

where D_μ is the $SU(3)_C$ covariant derivative, $G^a_{\mu\nu}$ is the gluon field strength tensor, and sum over three colors for the quark field and over $a = 1, \ldots, 8$ for gluon fields is implicit. The interaction between quarks and gluons is introduced via the QCD covariant derivative:

$$D_\mu q = (\partial_\mu - ig_s T^a G^a_\mu)q, \tag{3.2}$$

where g_s is the strong coupling constant, T^a are the $SU(3)$ generators in the fundamental representation and the field strength tensor is defined as

$$G^a_{\mu\nu} = \partial_\mu G^a_\nu - \partial_\nu G^a_\mu + g_s f^{abc}G^b_\mu G^c_\nu, \tag{3.3}$$

where f^{abc} are the structure constants of $SU(3)_C$. The first term of Eq. (3.1) is the kinetic term for the quark field $q(x)$, while the second term is the gluon field kinetic term which contains self-interactions and propagation terms. Because of the non-Abelian $SU(3)$ symmetry, gluons can interact with one another resulting in triple and quartic self-interaction terms.

The observed particles in nature (hadrons) are color-neutral bound states of quarks and/or anti-quarks. Color neutrality is realized as a certain combination of (anti)color charges which results in an object that is referred to as "white". Namely, if a bound state is comprised of quark-antiquark pair (mesons), the anti-particle would have to carry the opposite color of the one carried by the particle in that bound state, e.g. $R\bar{R}$. Examples include the pions $\pi^{\pm,0}$ and kaons K, as well as the heavier quarkonia (e.g. $J/\psi = c\bar{c}$, $\Upsilon = b\bar{b}$). Another way of achieving neutrality, in the sense of color, is

through a bound state of three quarks (baryons), where the combination of all three colors ensures neutrality, i.e. RGB state is color neutral. Examples include proton (uud) and neutron (ddu). Worth mentioning here are states of a more exotic nature, tetraquarks and pentaquarks, represented as certain combinations of four and five quarks and antiquarks respectively.

Interestingly, only these bound states of (anti)quarks are observed in nature, i.e. no free quark or gluon has ever been observed in nature by itself, a phenomenon called quark confinement. This phenomenon, a feature of QCD, is a result of the running coupling, where the coupling strength and consequently the interaction strength increase as the distance between the color-charged objects increases. This would mean that when the energy is put into separating quarks, if it is high enough, quarks would not separate, rather a quark-antiquark pair would be created where the particles would bind together between themselves in a process known as hadronization. Hadronization process is non-perturbative as the coupling strength is not small anymore, rather it grows which in turn makes analytic calculations difficult. On the other hand, at very short distances quarks behave as if they were free and weakly interacting, a property known as asymptotic freedom.

In the SM, quark masses are not intrinsic parameters of QCD, i.e. the mass term can't be forced into the Eq. (3.1) as it would violate the $SU(2)_L \times U(1)_Y$ symmetry. Masses are introduced, or generated, through Yukawa interactions with the Higgs field in the electroweak sector (see below) which preserves said symmetry.

3.2 Electroweak sector

Both quarks and charged leptons interact via electromagnetic and weak interactions, although with one key difference between the nature of the two interactions: the weak interaction violates parity, whilst the electromagnetic does not. Because of this fact, a description via states of left-handed and right-handed chirality is adopted, providing also a different treatment of left and right chiral states. The electroweak (EW) theory [74–76], based on the direct product of Lie groups $SU(2)_L \times U(1)_Y$, unifies the electromagnetic and weak interactions in a single gauge framework first proposed by S. L. Glashow [74]. Said group product has four generators which gives four gauge bosons in total. Before the $SU(2)_L \times U(1)_Y$ EW symmetry is broken down to $U(1)_Q$ electromagnetic gauge symmetry, the gauge fields are the weak isospin triplet W_μ^a ($a = 1, 2, 3$) corresponding to $SU(2)_L$ and the weak hypercharge field B_μ corresponding to $U(1)_Y$. The fundamental fermions form left-handed doublets and right-handed singlets, where each lepton and quark component is classified by three quantum numbers: weak isospin I, the third component of the weak isospin I_3 and the weak hypercharge Y, with the connection between them expressed by Gell-Mann–Nishijima formula:

$$Q = I_3 + \frac{Y}{2}. \tag{3.4}$$

Here Q is the electromagnetic charge (or just charge) of the particle. All left-handed fermions transform as $SU(2)_L$ doublets, while right-handed fermions transform as singlets. This structure reflects the maximal parity violation observed in weak interactions, i.e. only left-handed fermions (and right-handed antifermions) participate in the charged-current weak force. Specifically, fields are grouped as:

$$\begin{pmatrix} \nu_e \\ e \end{pmatrix}_L, \quad \begin{pmatrix} \nu_\mu \\ \mu \end{pmatrix}_L, \quad \begin{pmatrix} \nu_\tau \\ \tau \end{pmatrix}_L, \quad e_R, \quad \mu_R, \quad \tau_R,$$
$$\begin{pmatrix} u \\ d \end{pmatrix}_L, \quad \begin{pmatrix} c \\ s \end{pmatrix}_L, \quad \begin{pmatrix} t \\ b \end{pmatrix}_L, \quad u_R, \quad d_R, \quad c_R, \quad s_R, \quad t_R, \quad b_R, \tag{3.5}$$

where the third component of the weak isospin is 0, 1/2 or $-1/2$ for right-handed, upper or lower members of left-handed doublet fields, respectively, while the hypercharge Y is assigned such that the formula $Q = I_3 + Y/2$ reproduces the correct electric charge.

The electroweak part of the Lagrangian before EWSB, i.e. invariant under $SU(2)_L \times U(1)_Y$ transformations, is written as

$$\mathcal{L}_{\text{EW}} = \mathcal{L}_{\text{gauge}} + \mathcal{L}_{\text{fermion}} + \mathcal{L}_{\text{Higgs}} + \mathcal{L}_{\text{Yukawa}}. \tag{3.6}$$

The gauge field part $\mathcal{L}_{\text{gauge}}$ contains the kinetic terms for the W^a and B fields:

$$\mathcal{L}_{\text{gauge}} = -\frac{1}{4} W^a_{\mu\nu} W^{a,\mu\nu} - \frac{1}{4} B_{\mu\nu} B^{\mu\nu}, \tag{3.7}$$

where $W^a_{\mu\nu}$ and $B_{\mu\nu}$ are the field strength tensors associated to $SU(2)_L$ and $U(1)_Y$ groups respectively:

$$\begin{aligned} W^a_{\mu\nu} &= \partial_\mu W^a_\nu - \partial_\nu W^a_\mu + g_2 \epsilon_{abc} W^b_\mu W^c_\nu, \\ B_{\mu\nu} &= \partial_\mu B_\nu - \partial_\nu B_\mu, \end{aligned} \tag{3.8}$$

It can be observed that there are no explicit mass terms for the gauge bosons in $\mathcal{L}_{\text{gauge}}$ because such terms $(\sim M^2 W_\mu W^\mu)$ would violate the gauge symmetry, hence all electroweak gauge bosons are massless prior to EWSB.

The fermionic part $\mathcal{L}_{\text{fermion}}$ includes the kinetic terms and gauge interactions of quarks and leptons

$$\mathcal{L}_{\text{fermion}} = \sum_j \overline{\psi}^j_L i\gamma^\mu D^L_\mu \psi^j_L + \sum_{j,\sigma} \overline{\psi}^j_{R\sigma} i\gamma^\mu D^R_\mu \psi^j_{R\sigma}. \tag{3.9}$$

The fermionic part of the Lagrangian is expressed in terms of a left-handed doublet and a right-handed singlet

$$\psi^j_L = \begin{pmatrix} \psi^j_{L+} \\ \psi^j_{L-} \end{pmatrix}, \quad \psi^j_{R\sigma}, \tag{3.10}$$

where index j runs over three generations $j = 1, 2, 3$, $\sigma = \pm$, where the "$+$" sign stands for neutrinos and (u, c, t) quarks, while the "$-$" sign stands for electrically charged leptons and (d, s, b) quarks. The coupling to the gauge fields is achieved through the covariant derivative

$$D^{L,R}_\mu \psi_{L,R} = \left(\partial_\mu - ig_2 T^{L,R}_a W^a_\mu - ig_1 \frac{Y}{2} B_\mu \right) \psi_{L,R} \tag{3.11}$$

where g_2 and g_1 are the $SU(2)_L$ and $U(1)_Y$ coupling constants, respectively, $T^L_a = \frac{1}{2}\sigma_a$ and $T^R_a = 0$. As with the gauge bosons, explicit fermion mass terms of the form $m\overline{\psi}_L \psi_R$ are forbidden by electroweak gauge symmetry. This is a crucial point, where bare masses for quarks and leptons are not allowed in the unbroken theory, and all masses must arise from the Higgs mechanism (EWSB).

3.2.1 Spontaneous symmetry breaking and the Higgs mechanism

At first, a spontaneous symmetry breaking mechanism for a global $U(1)$ Abelian group was proposed by J. Goldstone in 1961 [69, 70]. Following the work done here, later in 1964, P. Higgs [71], and F. Englert and R. Brout [72] extended the description to the case of local Abelian gauge theory. Some time after, in 1967, A. Salam and S. Weinberg further extended the model of the Higgs mechanism to the non-Abelian local gauge symmetry of the EW model [75, 76] proposed by Glashow [74]. They

showed that it is possible to break the electroweak symmetry $SU(2)_L \times U(1)_Y$ down to the electromagnetic $U(1)_Q$ symmetry, where a complex scalar field is introduced. The scalar part (also referred to as the Higgs part) of the EW Lagrangian is then written as:

$$\mathcal{L}_{Higgs} = (D_\mu \Phi)^\dagger (D^\mu \Phi) - V(\Phi), \tag{3.12}$$

where the covariant derivative (of the EW sector) is:

$$D_\mu \Phi = \left(\partial_\mu - i g_2 \frac{\sigma_a}{2} W_\mu^a - i \frac{g_1}{2} B_\mu \right) \Phi. \tag{3.13}$$

i.e. the complex scalar field $\Phi(x)$ is an $SU(2)_L$ doublet of weak hypercharge $Y = +1$ and weak isospin $I = \frac{1}{2}$:

$$\Phi(x) = \begin{pmatrix} \phi^+(x) \\ \phi^0(x) \end{pmatrix}, \tag{3.14}$$

The most general renormalizable scalar potential ($V(\Phi)$) consistent with gauge invariance is

$$V(\Phi) = -\mu^2 (\Phi^\dagger \Phi) + \lambda (\Phi^\dagger \Phi)^2, \tag{3.15}$$

with μ^2 and λ being real parameters. If $\mu^2 > 0$, the potential is of the famous "Mexican hat" shape and has a continuous set of degenerate minima at $\Phi^\dagger \Phi = \frac{\mu^2}{2\lambda} \equiv \frac{v^2}{2}$, lying along a flat bottom. The choice $\langle \Phi \rangle \neq 0$ in one of these minima will spontaneously break the symmetry. Choice of the vacuum expectation value is arbitrary, hence a choice can be made such that only the neutral component acquires a nonzero Vacuum Expectation Value (VEV):

$$\langle \Phi \rangle = \frac{1}{\sqrt{2}} \begin{pmatrix} 0 \\ v \end{pmatrix}, \tag{3.16}$$

with $v = \sqrt{\frac{\mu^2}{2\lambda}} \approx 246$ GeV, which is determined from the Fermi constant in μ-decay. This particular vacuum is invariant under electromagnetic $U(1)_Q$ transformations, but it is not invariant under the full electroweak transformation group. Thus $SU(2)_L \times U(1)_Y \rightarrow U(1)_Q$ breaking is achieved.

By choosing to work in unitary gauge [77], the scalar field can be parametrized around the vacuum as

$$\Phi(x) = \frac{1}{\sqrt{2}} \begin{pmatrix} 0 \\ v + H(x) \end{pmatrix}, \tag{3.17}$$

where three of the four initial scalar degrees of freedom are transformed away, i.e. they become the longitudinal polarization components of the massive $W^\pm$ and Z bosons. Here $H(x)$ is a real scalar field, the Higgs field, representing physical fluctuations about the vacuum. Gauge boson fields can be transformed to introduce the physical gauge boson fields

$$\begin{aligned} W_\mu^\pm &= \frac{1}{\sqrt{2}} \left(W_\mu^1 \mp i W_\mu^2 \right), \\ Z_\mu &= W_\mu^3 \cos\theta_W + B_\mu \sin\theta_W, \\ A_\mu &= -W_\mu^3 \sin\theta_W + B_\mu \cos\theta_W, \end{aligned} \tag{3.18}$$

where θ_W is the Weinberg angle (also called the weak mixing angle) and is defined by

$$\sin\theta_W = \frac{g_1}{\sqrt{g_1^2 + g_2^2}}, \quad \cos\theta_W = \frac{g_2}{\sqrt{g_1^2 + g_2^2}}. \tag{3.19}$$

Plugging Eq. (3.17) and Eq. (3.18) into Eq. (3.12), it transforms into:

$$\mathcal{L}_{Higgs} = \frac{1}{2}(\partial_\mu H)(\partial^\mu H) - \mu^2 H^2 - \lambda v H^3 - \frac{\lambda}{4}H^4 + \frac{\mu^4}{4\lambda} + $$
$$(v + H)^2 \left(\frac{g_2^2}{4} W_\mu^- W^{+\mu} + \frac{g_1^2 + g_2^2}{8} Z_\mu Z^\mu \right). \tag{3.20}$$

Analyzing terms which are quadratic in fields ($\sim H^2, W_\mu^- W^{+\mu}, Z_\mu Z^\mu$) it is clear that the spontaneous breaking of the electroweak symmetry generates masses of the weak gauge bosons, whilst the photon (A_μ, identified as the gauge field of $U(1)_Q$) and gluon (G_μ) remain massless. The weak boson masses are $m_W = \frac{g_2 v}{2}$, $m_Z = v\sqrt{g_1^2 + g_2^2}/2$ and the Higgs boson mass is $m_H = \mu\sqrt{2} = v\sqrt{2\lambda}$. The Higgs field's self-interactions are also obtained, they are H^3 and H^4 interaction terms with strengths proportional to λ. The generation of W and Z masses through the Higgs mechanism was a major triumph of the electroweak theory by Weinberg, Salam and Glashow [74–76]. It explained why the weak force is short-ranged (due to massive W, Z bosons) whereas the electromagnetic force is long-ranged (with massless photon), all within a unified gauge theory. Also, after symmetry breaking, the massive W and Z gauge bosons can interact with the Higgs field. Expanding the Higgs part of the Lagrangian yields interaction terms of the form

$$\mathcal{L}_{HVV} = g_{HVV} H V_\mu V^\mu + g_{HHVV} H^2 V_\mu V^\mu, \tag{3.21}$$

with $V = W, Z$, it is easy to find the coupling constant (coupling strength) for the single Higgs interaction with a pair of W and Z bosons, and they are given as $g_{HWW} = \frac{M_W^2}{v}$ and $g_{HZZ} = 2\frac{M_Z^2}{v}$. As it can be seen here, these couplings are proportional to the gauge boson masses squared, a direct consequence of the Higgs mechanism. In fact, it is a general case that the coupling of the Higgs boson to any elementary particle is a function of the particle's mass. It implies, for instance, that interactions of the Higgs are stronger with the heavier Z than with the lighter W bosons, and a massless photon has no $H\gamma\gamma$ tree-level coupling at all.

3.2.2 Fermion masses

Prior to electroweak symmetry breaking, all SM fermions are massless as noted above. Mass terms are generated through Yukawa interactions in $\mathcal{L}_{\text{Yukawa}}$, as implemented by Weinberg [76]. For a single generation, the Yukawa terms can be written as:

$$\mathcal{L}_{\text{Yukawa}} = -y_\ell \overline{L}_L \Phi \ell_R - y_d \overline{Q}_L \Phi d_R - y_u \overline{Q}_L \widetilde{\Phi} u_R + \text{h.c.}, \tag{3.22}$$

with the fields defined as

$$L_L = (\nu_L, l_L)^T, \quad Q_L = (u_L, d_L)^T, \quad \widetilde{\Phi} = i\sigma_2 \Phi^* = (\phi^{0*}, -\phi^-)^T. \tag{3.23}$$

Here y_ℓ, y_d, y_u are generation-dependent Yukawa coupling constants for the charged lepton (e, μ, τ), down-type quark (d, s, b), and up-type quark (u, c, t), respectively. Field $\widetilde{\Phi}$ is the isospin-conjugate Higgs field (with hypercharge -1) used to give an $SU(2)_L$ invariant coupling to up-type quarks. After symmetry breaking, by substituting Eq. (3.17) in Eq. (3.22), the linear terms in H then generate fermion masses

$$m_f = \frac{y_f v}{\sqrt{2}}, \tag{3.24}$$

for each charged fermion $f = \ell, u, d$. At the same time, the Yukawa interactions also predict a direct coupling of the physical Higgs boson, to fermion–antifermion pairs, of strength y_f

$$-\frac{m_f}{v} H \bar{f} f. \tag{3.25}$$

When extending Eq. (3.22) to all three generations, one must consider the fact that the Yukawa couplings y_u, y_d, y_ℓ become 3×3 matrices in generation space. The mechanism described above works in a similar way for quarks and leptons, the main difference between them being flavor mixing in the quark sector. This comes from the fact that the weak quark-interaction eigenstates do not coincide with mass eigenstates. After symmetry breaking and after changing to quark mass eigenstates by utilizing unitary transformations, masses of quarks are obtained. Also, as a consequence of changing to quark mass eigenstates, the charged-current weak interaction Lagrangian takes a special from which is discussed in the following chapter. Finally the Yukawa Lagrangian $\mathcal{L}_{\text{Yukawa}}$ now reads

$$\mathcal{L}_{\text{Yukawa}} = -\sum_f m_f \overline{\psi}_f \psi_f - \sum_f \frac{m_f}{v} \overline{\psi}_f \psi_f H, \tag{3.26}$$

where f goes over all fermions (modulo neutrinos) in the SM, i.e. quarks and leptons. It can be seen that the Higgs boson couples to fermions proportionally to their masses, so heavy fermions (e.g. t quark) have large Yukawa couplings and interact with the Higgs field much more strongly than light fermions (e.g. electrons). Neutrinos in the SM do not acquire mass because there are no right-handed neutrino fields ν_R to write Yukawa terms with. However, neutrinos are known to oscillate between flavors [78, 79], which implies they have nonzero masses and mix in a lepton-flavor mixing matrix analogous to the CKM matrix (see bellow). Solving the problem of explaining the origin of neutrino masses involves Beyond the SM (BSM) models [80, 81], where for an example the proposed solutions are a see-saw mechanism or adding an effective dimension-5 operator to the Lagrangian of the SM which would generate Majorana masses after symmetry breaking. Here neutrinos as treated as massless particles.

3.2.3 Electroweak currents and interactions

After electroweak symmetry breaking, Lagrangian of the SM also describes the interactions between the SM fermions and physical gauge bosons, as well as interaction between the gauge bosons themselves. These interactions are achieved through the covariant derivatives present in Eq. (3.9) and Eq. (3.7). Expressing the Lagrangian in terms of the physical fields ($W^{\pm}$, Z, γ, and the mass-eigenstate fermions) and grouping fermionic interaction terms together, interactions between fermions and gauge bosons are written as

$$\mathcal{L}_{\text{FG}} = J^{\mu}_{\text{em}} A_{\mu} + J^{\mu}_{\text{NC}} Z_{\mu} + J^{\mu}_{\text{CC}} W^{+}_{\mu} + J^{\mu\dagger}_{\text{CC}} W^{-}_{\mu}, \tag{3.27}$$

where the currents read:

$$\begin{aligned}
J^{\mu}_{\text{em}} &= -e \sum_{f=l,q} Q_f \overline{\psi}_f \gamma^{\mu} \psi_f, \\
J^{\mu}_{\text{NC}} &= \frac{g_2}{2\cos\theta_W} \sum_{f=l,q} \overline{\psi}_f (g_V \gamma^{\mu} - g_A \gamma^{\mu} \gamma_5) \psi_f, \\
J^{\mu}_{\text{CC}} &= \frac{g_2}{\sqrt{2}} \left(\sum_{i=1,2,3} \overline{\nu}^i \gamma^{\mu} \frac{1-\gamma_5}{2} e^i + \sum_{i,j=1,2,3} \overline{u}^i \gamma^{\mu} \frac{1-\gamma_5}{2} V_{ij} d^j \right),
\end{aligned} \tag{3.28}$$

where index f runs over SM fermions and the indices i, j run over the three families of fermions. Coupling of the currents to gauge bosons is reflected through coupling constants: Q_f (charge) for

the electromagnetic current (J_{em}^μ), g_2 for the charged current (J_{CC}^μ) and g_V and g_A together with g_2 comprise the coupling for the neutral current (J_{NC}^μ). Values of g_V and g_A are dictated by the charge Q_f and isospin I_3^f of f_L:

$$
\begin{aligned}
g_V &= I_3^f - 2Q_f \sin^2\theta_W, \\
g_A &= I_3^f.
\end{aligned}
\tag{3.29}
$$

The first term in $\mathcal{L}_{\text{FG}}$ exhibits vector-like structure, and describes how the photon (A_μ) couples to any charged particle with strength eQ_f. The neutral-current (NC) interactions are mediated by the Z boson and couple to any fermion f, both left- and right-handed components, though with different strengths. The structure of NC interaction term is described via terms which transform as vector and axial vectors (commonly denoted as V-A), pointed out by the vector (g_V) and axial-vector (g_A) couplings of the Z to fermion f. The charged-current (CC) interactions are mediated by $W^\pm$ and couple exclusively to left-handed fermions. The charged-current weak interaction contains a quark mixing matrix known as the Cabibbo–Kobayashi–Maskawa (CKM) matrix V_{ij} [82, 83], where i, j are generation indices. The off-diagonal elements of V_{ij} ($i \neq j$) allow a W boson to convert one quark flavor into another. For example, a W^+ can induce $u \to d$, $u \to s$, or $u \to b$ transitions with different amplitudes given by V_{ud}, V_{us}, V_{ub}. Empirically, the CKM matrix is nearly diagonal, meaning the transitions within the same generation are most probable. The CKM matrix can be parametrized using three mixing angles and one complex phase. The complex phase in the CKM matrix accounts for CP violation in weak interactions (observed in certain meson decays), a triumph of the SM explanation of CP-violating phenomena in the quark sector [82].

As mentioned above, the gauge sector also contains self-interactions. The self-interactions between the gauge bosons and their form are a direct consequence of the $SU(2)$ non-Abelian symmetry (as was the case with $SU(2)_C$ in case of the gluons) and would not be present in a purely Abelian theory like QED. Grouping the gauge boson self-interaction terms together, the interactions are written as

$$
\begin{aligned}
\mathcal{L}_{G,\text{self}} = {} & e[(\partial_\mu W_\nu^+ - \partial_\nu W_\mu^+)W^{-\mu}A^\nu + W_\mu^+ W_\nu^- F^{\mu\nu} + h.c.] \\
& + e\cot\theta_W[(\partial_\mu W_\nu^+ - \partial_\nu W_\mu^+)W^{-\mu}Z^\nu + W_\mu^+ W_\nu^- Z^{\mu\nu} + h.c.] \\
& - e^2/(4\sin^2\theta_W)[(W_\mu^- W_\nu^+ - W_\nu^- W_\mu^+)W_\mu^+ W_\nu^- + h.c.] \\
& - e^2/4(W_\mu^+ A_\nu - W_\nu^+ A_\mu)(W^{-\mu}A^\nu - W^{-\nu}A^\mu) \\
& - e^2/4\cot^2\theta_W(W_\mu^+ Z_\nu - W_\nu^+ Z_\mu)(W^{-\mu}Z^\nu - W^{-\nu}Z^\nu) \\
& e^2/2\cot\theta_W(W_\mu^+ A^\nu - W_\nu^+ A_\mu)(W^{-\mu}Z^\nu - W^{-\nu}Z^\mu) + h.c.,
\end{aligned}
\tag{3.30}
$$

where $F_{\mu\nu} = \partial_\mu A_\nu - \partial_\nu A_\mu$, $Z_{\mu\nu} = \partial_\mu Z_\nu - \partial_\nu Z_\mu$.

With the above ingredients, the SM Lagrangian is complete. The theory contains a total of 19 free parameters: 3 gauge couplings (g_1, g_2, g_s), 2 parameters in the Higgs potential (μ^2 and λ, often traded for v and m_H), 9 Yukawa couplings for the charged fermions (3 charged leptons + 6 quarks), 4 parameters for the CKM matrix (3 mixing angles + 1 CP-violating phase), and 1 QCD vacuum angle (the θ-parameter which is empirically tiny, related to the strong CP problem). The values of these parameters are not calculated within the SM, rather they must be determined from experiment.
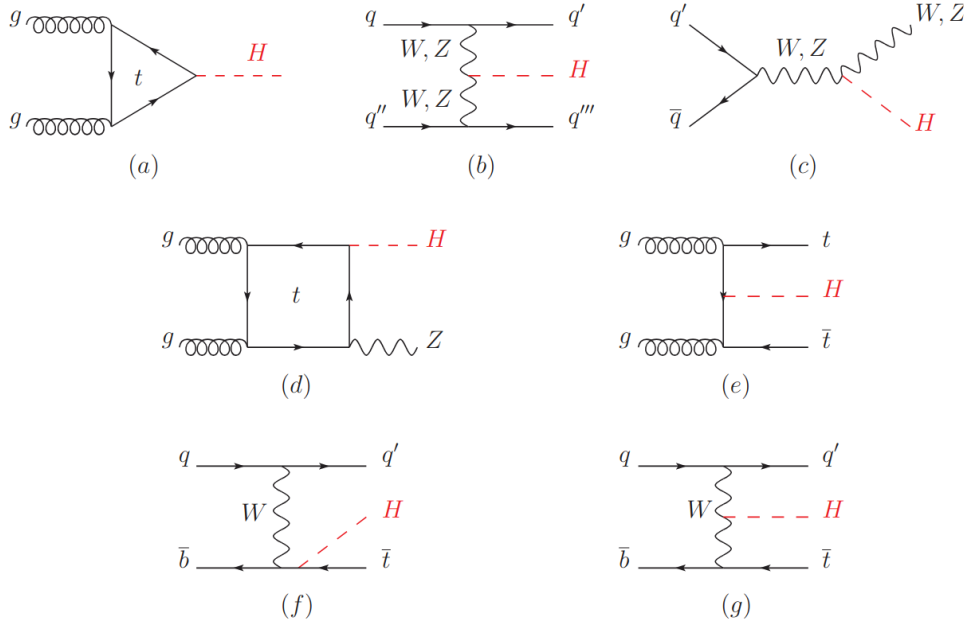
3.3 The Higgs boson

The Higgs boson is a central part of the electroweak theory, being the particle associated with the Higgs field which permeates the universe. Its nonzero vacuum expectation value $v \approx 246$ GeV is what

gives masses to the W and Z bosons and to fermions (via Yukawa couplings). It carries neither electric and nor color charges, hence is not directly subject to electromagnetic or strong forces. However, it couples to all massive SM particles: its couplings to gauge bosons and fermions are proportional to M_V^2 and m_f respectively (as described above). Therefore, the Higgs boson provides a unique window into the generation of mass and has distinctive production and decay modes that have been the focus of extensive experimental studies since its discovery.

3.3.1 Production of the Higgs boson at the LHC

Higgs boson production depends on several factors with the most important being which particles interact to produce the Higgs boson and at what energies. At the LHC, as protons are being collided, the Higgs boson is produced via quark-(anti)quark and gluon-gluon initiated processes. The four main production processes in proton–proton collisions at $\sqrt{s} = 13$ TeV, as shown in Figure 3.1, are gluon-gluon fusion (ggF), vector boson fusion (VBF), associated production with W or Z boson (radiation of a Higgs boson, or Higgsstrahlung, VH) and top quark associated production ($t\bar{t}H$), which can be seen from the cross section values [84] shown in Table 3.2.

Figure 3.1. The main modes of production of the Higgs boson at the LHC, shown in figures a (ggF), b (VBF), c (VH) and e ($t\bar{t}H$). Diagram presented in (d) shows Higgs and Z boson production via gluon gluon fusion through a square loop. Diagrams presented in (f) and (g) show Higgs boson production, where the Higgs boson is radiated from a $\bar{t}$ quark or a through a W boson fusion, where one of the initial state quarks is the b quark. Figure taken from [84].

In ggF, Figure 3.1(a), two gluons from the incoming protons fuse into a Higgs boson through a loop of heavy quarks. Given the sizable Yukawa couplings of heavy quarks and the large gluon flux in high energy p-p collisions, the cross section for this channel has the largest contribution to the Higgs boson production.

In the case of a quark-initiated process, both quarks can emit a weak boson (W or Z), Figure 3.1(b), which then fuse into a Higgs boson. A typical signature of VBF are two jets from the scattered initial-state quarks in the forward regions. This mode of production has the second largest cross section and offers a possibility to study HVV couplings directly.

Table 3.2. The cross section values at different COM energies ($\sqrt{s}$) for the most contributing modes of production of the Higgs boson at the LHC. The four main channels are ggF, VBF, VH and $t\bar{t}H$. Table taken from Ref. [85].

	Production cross section (in pb) for $m_H = 125$ GeV					
$\sqrt{s}$ (TeV)	ggF	VBF	WH	ZH	ttH	total
1.96	$0.95^{+17\%}_{-17\%}$	$0.065^{+8\%}_{-7\%}$	$0.13^{+8\%}_{-8\%}$	$0.079^{+8\%}_{-8\%}$	$0.004^{+10\%}_{-10\%}$	1.23
7	$16.9^{+5.5\%}_{-7.6\%}$	$1.24^{+2.2\%}_{-2.2\%}$	$0.58^{+2.2\%}_{-2.3\%}$	$0.34^{+3.1\%}_{-3.0\%}$	$0.09^{+5.6\%}_{-10.2\%}$	19.1
8	$21.4^{+5.4\%}_{-7.6\%}$	$1.60^{+2.1\%}_{-2.1\%}$	$0.70^{+2.1\%}_{-2.2\%}$	$0.42^{+3.4\%}_{-2.9\%}$	$0.13^{+5.9\%}_{-10.1\%}$	24.2
13	$48.6^{+5.6\%}_{-7.4\%}$	$3.78^{+2.1\%}_{-2.1\%}$	$1.37^{+2.0\%}_{-2.0\%}$	$0.88^{+4.1\%}_{-3.5\%}$	$0.50^{+6.8\%}_{-9.6\%}$	55.1
14	$54.7^{+5.6\%}_{-7.4\%}$	$4.28^{+2.1\%}_{-2.1\%}$	$1.51^{+1.8\%}_{-1.9\%}$	$0.99^{+4.1\%}_{-3.7\%}$	$0.61^{+6.9\%}_{-9.8\%}$	62.1

If, however, the initial state consists of a same-flavor (different-flavor) quark-antiquark pair, this can fuse into a virtual Z (W) boson, as shown in Figure 3.1(c). In either case the fusion into a weak boson is followed by an emission of a Higgs boson.

The least contributing process (out of the four process with the most significant contributions), $t\bar{t}H$, is shown in Figure 3.1(e). In gluon-gluon collisions it is possible for a pair of top-antitop quarks to be produced, where a Higgs boson is radiated. The $t\bar{t}H$ process is a fertile ground for top-Yukawa coupling y_t measurements.

3.3.2 Higgs boson decays

The Higgs boson has a wide range of decay modes as it couples with all particles which have mass. It can directly decay (tree level diagrams) to $H \rightarrow WW^*, ZZ^*$ (bosonic modes) and $H \rightarrow f\bar{f}$ (fermionic modes) where f can be $e, \mu, \tau, u, d, c, s, b$, while the decay $H \rightarrow t\bar{t}$ is excluded due to the top quark's large mass. Also, Higgs boson can also undergo decay via higher-order loops into gauge bosons gg, $\gamma\gamma$, $Z\gamma$. Calculating the partial decay width Γ_i for a given process and dividing by the total Higgs boson decay width Γ_H, one finds the branching ratio (Br). Branching ratios are dependent on SM parameters such as coupling constants and masses of relevant particles. The Higgs boson branching ratios as a function of the Higgs boson's mass m_H are shown in Figure 3.2. These ratios are calculated [84, 86] for a fairly wide range of Higgs boson's mass including $m_H = 125$ GeV which is presented in Table 3.3.

Table 3.3. Values [84, 86] of branching ratios for the most dominant decay modes of the Higgs boson of a mass $m_H = 125$ GeV. Table taken from Ref. [84].

Decay channel	Branching ratio	Rel. uncertainty
$H \rightarrow \gamma\gamma$	2.27×10^{-3}	2.1%
$H \rightarrow ZZ$	2.62×10^{-2}	$\pm 1.5\%$
$H \rightarrow W^+W^-$	2.14×10^{-1}	$\pm 1.5\%$
$H \rightarrow \tau^+\tau^-$	6.27×10^{-2}	$\pm 1.6\%$
$H \rightarrow b\bar{b}$	5.82×10^{-1}	$^{+1.2\%}_{-1.3\%}$
$H \rightarrow c\bar{c}$	2.89×10^{-2}	$^{+5.5\%}_{-2.0\%}$
$H \rightarrow Z\gamma$	1.53×10^{-3}	$\pm 5.8\%$
$H \rightarrow \mu^+\mu^-$	2.18×10^{-4}	$\pm 1.7\%$

It can be seen that the most dominant decay mode is to the heaviest kinematically allowed fermion pair $H \rightarrow b\bar{b}$ with $Br \approx 58\%$. Second largest Br is for $H \rightarrow W^+W^-$, standing roughly at $Br \approx 21\%$. The $H \rightarrow ZZ^*$ channel has a Br of about 2.6% which is small in itself, but the importance of
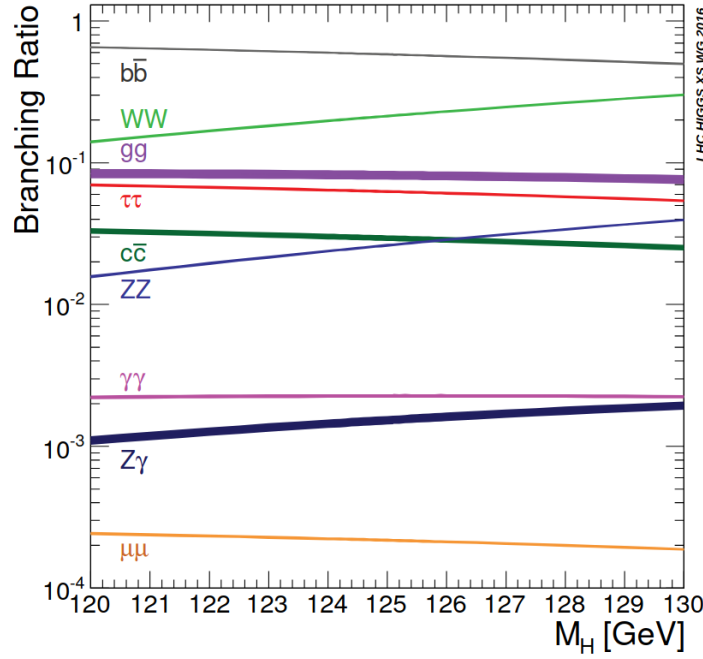
Figure 3.2. Branching ratios for different decay modes of the Higgs boson shown as a function of Higgs boson's mass. Figure taken from Ref. [84].

this channel is far greater, as it allows for precise measurements due to the small contamination from other processes with the same final state (background); i.e. $H \to ZZ^* \to 4l$ channel is characterized by the highest signal-to-background ratio. The total width Γ_H of the Higgs boson is predicted by SM to be $\Gamma_H \approx 4.1$ MeV [84, 86]. Unfortunately, this is below the CMS experimental mass resolution, therefore the total width of the Higgs boson cannot be directly measured. However, its value can be inferred by means of indirect measurements.

3.3.3 Higgs boson discovery and properties measurement

Measurements of the Higgs boson are designed to exploit a set of observables which are sensitive to Higgs boson properties. Some examples of these measurements are invariant mass of the system of final state particles measurement [5, 87], cross sections measurements [5, 88], differential cross sections [88] and Simplified Template Cross Sections (STXS) measurements [89]. Each measurement of the final state's kinematic variables, such as invariant mass or transverse momentum, is a counting experiment.

In *differential* cross section measurements, instead of counting the total number of Higgs events (which yields the total cross section), experiments measure yields in binned variables such as the Higgs transverse momentum (p_T^H), the number of associated jets, etc. These differential cross sections provide a more detailed test of the theory as certain new physics effects could alter the kinematic distributions of the Higgs boson.

When presenting results of a measurement, experiments often quote *fiducial* cross sections. A fiducial cross section is defined as a cross section within specific kinematic cuts. These cuts closely match the detector acceptance and analysis selections which aims to minimize the noise (background processes, background) and allow for a better signal extraction.

Owing to the abundant QCD-induced processes (i.e. large QCD background), even though certain decay modes of the Higgs boson are dominant, from an experimental point of view they are not

straightforward to detect. For instance, the $H \to b\bar{b}$ decay is dominant but there's a very large QCD background associated with b-jets which makes this channel challenging for Higgs boson searches and measurement of its properties (although it is directly sensitive to the y_b coupling). There's a delicate trade-off to be considered between how much a channel is dominant in terms of its signal yields and how large of a background comes with it. Most dominant decay channels in fact come with a large background. On the other hand subdominant decays, even though they are less probable to happen, may be polluted by a smaller background which results in a large enough purity for the physics studies.

One of the most important decay channels, commonly referred to as the "golden channel," is the Higgs-to-four-lepton decay channel $H \to ZZ^* \to \ell^+\ell^-\ell'^+\ell'^-$ ($\ell = e, \mu$) [5, 87]. Even though it is characterized by a very small branching ratio, this channel's final state (four charged leptons) is fully reconstructible with small background contamination. Another, as important, decay channel is $H \to \gamma\gamma$, which results in a narrow peak in the diphoton invariant mass distribution, visible above the diphoton background [4, 5]. Both of these channels are characterized by a very precise mass resolution, as opposed to $H \to W^+W^-$, $H \to \tau^+\tau^-$ and $H \to b\bar{b}$ channels which are also included in the analysis that resulted in the Higgs boson discovery by the CMS [5] and ATLAS [4] collaborations.

At first, using Run 1 $\sqrt{s} = 7$ TeV dataset which corresponds to an integrated luminosity of ~ 4.7 fb^{-1}, the CMS collaboration reported excesses of events at around $119, 126, 320$ GeV in $H \to ZZ$ decay channel [90]. Reuslts from CMS $H \to \gamma\gamma$ decay channel analysis of Run 1 $\sqrt{s} = 7$ TeV dataset, which corresponds to an integrated luminosity of ~ 4.8 fb^{-1}, show an excesses of events at around ~ 124 GeV with a $3.1\,\sigma$ local significance [91]. Doing a measurement on combined CMS Run 1 $\sqrt{s} = 7$ TeV and Run 1 $\sqrt{s} = 8$ TeV datasets [5], with integrated luminosities of up to 5.1 and 5.3 inverse femtobarns respectively, the local significance in $H \to \gamma\gamma$ decay channel was increased above $4\,\sigma$, whilst in $H \to ZZ$ decay channel it was increased to above $3\,\sigma$ at around 125 GeV. Further, when a combined analysis of all five channels ($H \to ZZ$, $H \to \gamma\gamma$, $H \to W^+W^-$, $H \to \tau^+\tau^-$, $H \to b\bar{b}$) was done, the local significance went up to $5\,\sigma$ (Figure 3.4 with a claim of the Higgs boson discovery.

The ATLAS collaboration published their findings in the same year, independently of the CMS collaboration. Individual analysis of $H \to ZZ$, $H \to \gamma\gamma$ and $H \to W^+W^-$ at $\sqrt{s} = 8$ TeV ($L \sim 5.8$ fb^{-1}) are combined with results of previous studies of $H \to ZZ$, $H \to \gamma\gamma$, $H \to W^+W^-$, $H \to \tau^+\tau^-$, $H \to b\bar{b}$ at $\sqrt{s} = 7$ TeV ($L \sim 4.8$ fb^{-1}) which resulted in excess of events at around 125 GeV with a significance of $5.9\,\sigma$ (Figure 3.4), thus claiming a discovery of the Higgs boson [4].

In July 2012, both the ATLAS and CMS collaborations had independently observed clear excess of events at around 125 GeV, particularly in the four-lepton and diphoton mass distributions. Figure 3.3 displays reconstructed invariant four-lepton mass (m_{4l}) distributions by ATLAS and CMS, within carefully selected fiducial phase spaces by ATLAS [4] and CMS [5]. A peak at around ~ 125 GeV is clearly visible above the m_{4l} background distribution. The local p-value of combined measurements of all five above mentioned channels by ATLAS and CMS with which the discovery of the Higgs boson came is shown in Figure 3.4.

Following the Higgs boson discovery, measurement of the Higgs boson properties became the focus of the ATLAS and CMS collaborations. These include measurements of production and decay rates, couplings to other particles, self-coupling (see Chapter 4), mass and width, spin and parity.

When measuring production and decay rates in specific modes, the usual practice is to define the *signal strength* for production μ_i and the signal strength for decay μ^f as the ratio of measured production (decay) rate to its SM prediction:
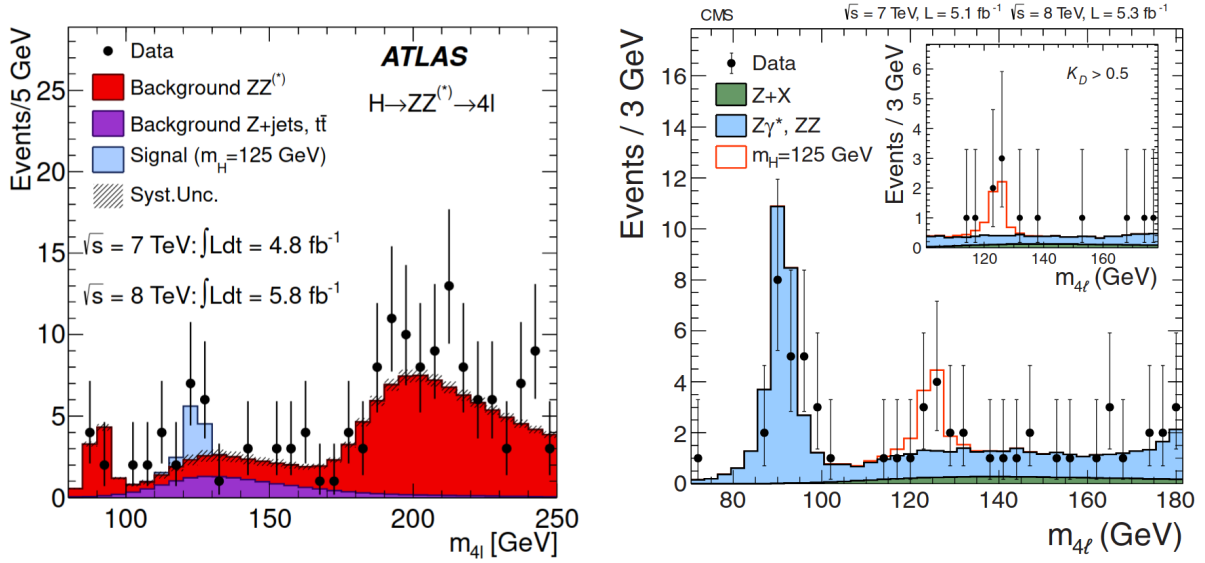
Figure 3.3. Invariant mass of the four-leptons as reconstructed by ATLAS (left) and CMS (right). Figures taken from Refs. [4, 5].

$$\mu_i = \frac{\sigma_i}{(\sigma_i)_{SM}}, \quad \mu^f = \frac{Br^f}{(Br^f)_{SM}}. \tag{3.31}$$

The signal strength for a given process $i \rightarrow H \rightarrow f$ is then defined as:

$$\mu_i^f = \frac{\sigma_i \times Br^f}{(\sigma_i)_{SM} \times (Br^f)_{SM}}. \tag{3.32}$$

Combined analyses of ATLAS and CMS data from Run 1 [92], combined CMS analyses of Run 2 [93–95], and combined ATLAS analyses of Run 2 [96, 97] consistently show excellent agreement with the SM prediction of 1 for the various signal strengths. The mass of the Higgs boson is measured to be $m_H = 125.04 \pm 0.12$ GeV [98] which is the most precise measurement of the Higgs boson mass up to date. Measurement of the Higgs boson's spin and parity [95, 97, 99–103] determined that the Higgs boson is a scalar particle with positive parity $J^P = 0^+$, as described by the SM. As it is challenging to directly measure the width Γ_H of the Higgs boson due to detector resolution limitations, indirect constraints [98, 104–106] point to a width predicted by the SM (~ 4 MeV). Couplings to gauge bosons and a subset of elementary fermions (t, b, τ, μ), often expressed as a ratio to the SM predicted value (quantifying deviations), were measured and all found to be in line with the SM predictions [95, 97].

However, as precise and yielding as these measurements seem to be, the Higgs boson self-coupling is less precisely determined. An overview of the measurements, and more, are discussed in the following chapter, chapter [ref].

3.4 Successes and shortcomings of the SM

The SM has been shown to be extremely successful in explaining a wide range of experimental results over the past few decades. It successfully predicted the existence of W and Z boson, discovered in 1983. It also predicted the existence of the top quark, where the top quark was discovered in
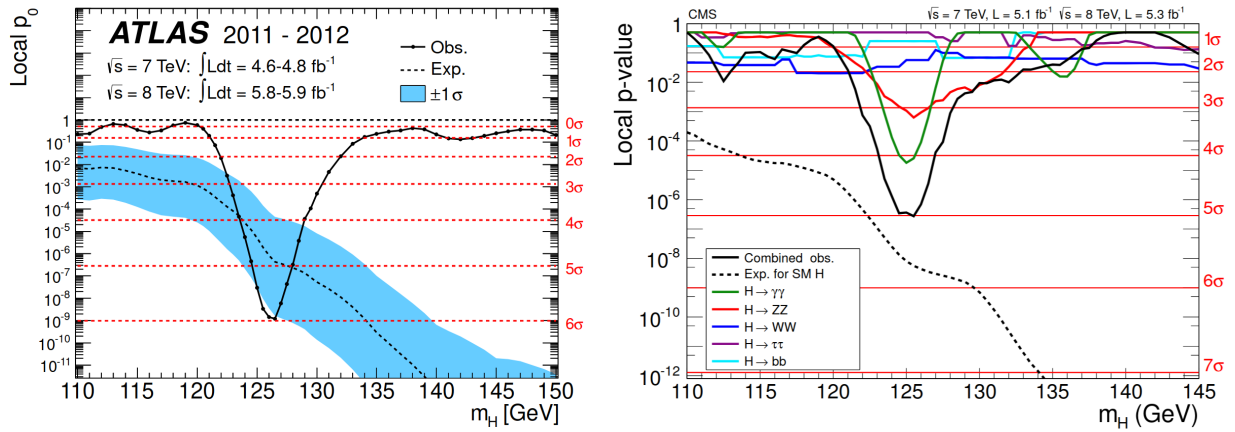
Figure 3.4. The local p value measured at around ~125 GeV based on the combined analysis of channels $H \rightarrow ZZ$, $H \rightarrow \gamma\gamma$, $H \rightarrow W^+W^-$, $H \rightarrow \tau^+\tau^-$, $H \rightarrow b\bar{b}$ by ATLAS (left) and CMS (right) collaborations. Figures taken from Refs. [4, 5].

1995. Perhaps the most astonishing achievement is the Higgs boson discovery by CMS [5] and ATLAS [4] in 2012. This discovery confirms how the particles acquire their mass by means of EWSB and confirms the minimal shape of the scalar potential. Detailed measurements have been made in the electroweak and the QCD sector, which all consistently match the SM predictions. These measurements, which span several decades, include couplings of various particles, signal strengths, ratios of certain parameters, masses, and many more.

However, despite being such a successful theory, the SM is known to lack a description of several observed phenomena. Firstly, it doesn't provide a suitable description of gravity (not quantized yet) and it does not account for dark energy which is measured to amount to $\sim 69\%$ of energy density of the Universe. Also, the SM lacks a viable dark matter candidate (which amounts to $\sim 25\%$ of energy density of the Universe). Although there are models which contain a candidate for a dark matter particle, they were not proven to be correct. Looking at $\mathcal{L}_{\text{Yukawa}}$ it can be seen that the neutrinos are massless according to the SM, a fact which has been proven not to be true. In fact, neutrinos were observed to exhibit flavor oscillations [78, 79] which implies that neutrinos have small but nonzero masses. Looking at the predicted matter to antimatter asymmetry, the SM's prediction does not hold well and is unable to explain the dominance of matter over antimatter. The list of open problems goes on, entailing also the hierarchy problem, CP symmetry violation in QCD, the reasons why do SM fermions exhibit growing mass across generations and why are there exactly three fermion generations, or why the coupling constants and all of the SM particle's masses have their observed value.

Also, a big task still left to do is to precisely measure the Higgs boson self-coupling constant, which governs the shape of the scalar potential and plays an important role in the EWSB mechanism. The lack of theoretical description of these phenomena strongly suggest that the SM is an incomplete theory which can be viewed as a low-energy effective theory of a more complete framework. These considerations are a topic of the following chapter.

Chapter 4

The Higgs boson self-coupling in an Effective Field Theory approach

The shape of the scalar field potential is governed by two parameters, μ and λ. After EWSB, the Higgs boson self-coupling constant λ parametrizes the Higgs field potential V as can be seen from Eq. (3.20):

$$V = \frac{m_H^2}{2}H^2 + \lambda v H^3 + \frac{\lambda}{4}H^4, \tag{4.1}$$

where the constant term in Eq. (3.20) was omitted as it just introduces an overall shift. The second and third term of Eq. (4.1) describe the Higgs boson triple and quartic self-interaction respectively. The scalar field potential shown above is the minimal one allowing for the symmetry to be broken in a way that gives rise to the masses of W, Z and H bosons, whilst leaving the photon and gluons massless. In this context, the Higgs boson self-coupling parameter λ is of great importance as it governs the shape of the Higgs field potential, determines the Higgs field VEV and is associated with the mechanism of EWSB. Precise measurements and their interpretation within an Effective Field Theory (EFT) approach would allow for better understanding of the role which the self-coupling plays in the SM, as is discussed in the following sections.

4.1 Higgs boson self-coupling measurements

The Higgs boson self-coupling parameter can be measured via two complementary approaches, directly and indirectly. Viewed from the κ-framework point of view [107], the Higgs boson self-coupling modifier is defined as the ratio of the Higgs boson self-coupling to the value predicted by SM, $\kappa_\lambda = \lambda/\lambda_{SM}$. A precise measurement of κ_λ is the key to understanding the mechanism of EWSB, where a significant deviation from 1 would point to a direction of BSM physics.

4.1.1 Indirect measurements: Single Higgs boson production

Indirect measurements rely on single Higgs boson production processes and self-coupling constraints are inferred from high-precision measurements of these processes. Looking at tree-level diagrams, none of the single-Higgs production processes depend on λ. However, at higher orders (Next-to-Leading Order, NLO) in EW perturbation theory, quantum-loop corrections involving the Higgs boson self-coupling give a contribution. Although these contributions are numerically small, they can impact distributions of kinematic variables, thus making their impact meaningful. Such loops may appear in

production, propagation and the decay of the Higgs boson. Feynman diagrams involving one loop with the Higgs boson in it are shown in Figure 4.1.
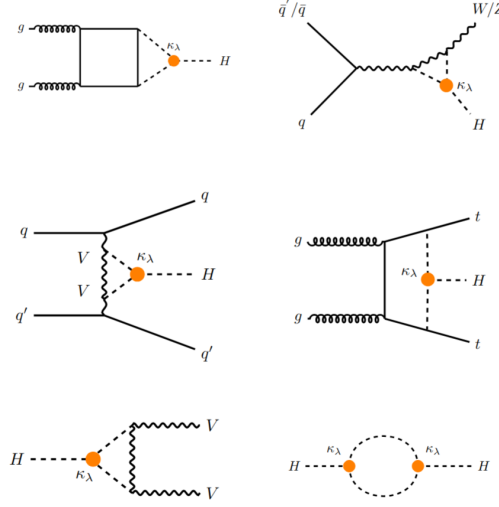
Figure 4.1. NLO EW Feynman diagrams corresponding to κ_λ corrections to the main Higgs boson production modes (top two rows), to the $H \to VV$ decay (bottom left) and to the Higgs boson propagator (bottom right). Figure taken from Refs. [108].

Considering for example corrections to ggF, one can see that the two Higgs bosons produced by a square loop of t (b) quarks are fused together in a single Higgs boson through a vertex which contains the self-coupling. Overall, these diagrams modify the behavior of ggF kinematics which can be observed by measuring distributions of variables such as transverse momentum of the Higgs boson $p_T(H)$. Also, as there are multiple Higgs bosons participating in the diagram, the Higgs off-shell region is of interest; in particular, in the far off-shell region where the mass of the virtual Higgs boson is twice or more the pole mass, some deviation in κ_λ can be probed more easily. However, the off-shell region remains unexplored in this context.

CMS and ATLAS performed extensive measurements of κ_λ in the combination of single-boson production processes. Focusing on the $H \to ZZ \to 4l$ channel in its on-shell region, κ_λ was probed by examining the Higgs p_T distribution where constraints at the 95% CL [87] are extracted from the maximum likelihood scan, as is shown in Figure 4.2:

$$-5.4 < \kappa_\lambda < 14.9 \tag{4.2}$$

4.1.2   Direct measurements: di-Higgs boson production

Direct measurements of the Higgs boson self-coupling are particularly challenging as processes where multiple Higgs bosons are produced have to be observed and studied. The challenge here is that such processes, like di-($pp \to HH$) and tri- ($pp \to HHH$) Higgs boson production, are extremely rare due to the smallness of the production cross section, which is a variable directly sensitive to the self-coupling parameter. Specifically, the SM di-Higgs production cross section for $m_H = 125$ GeV is calculated to be $\sigma_{HH} = 32.4^{+2.0}_{-6.8}$ fb [86], which is three orders of magnitude smaller than the single Higgs boson production cross section. The tri-Higgs boson production cross section is even smaller and even more challenging to observe and study.

As both the di-Higgs boson production cross section and the final state kinematics are directly sensitive to the self-coupling, an optimal analysis relies on the most sensitive channels, i.e. those
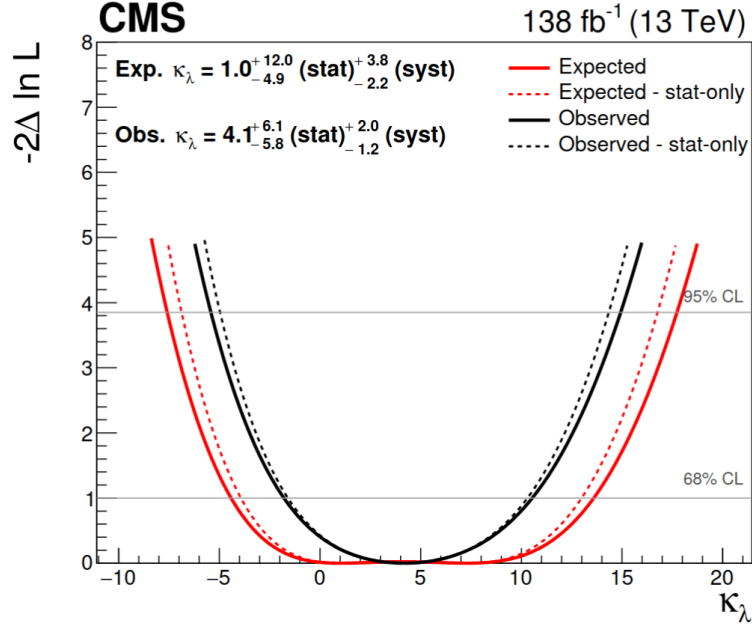
Figure 4.2. Likelihood scan as a function of κ_λ. The scan is shown with (solid line) and without (dashed line) systematic uncertainties profiled in the fit. Figure taken from Ref. [87].

with a high Br and/or clean signature. As the branching fraction of $H \to b\bar{b}$ is the largest, it is a common practice to require one of the Higgs bosons produced to decay to a pair of $b\bar{b}$. A second Higgs boson is required to decay to a $b\bar{b}$, $\tau^+\tau^-$, $\gamma\gamma$, or leptons from W and Z decays. Processes which contribute to the di-Higgs boson production at the LHC are shown in Figure 4.3. The self-coupling (κ_λ) appears in ggF process Figure 4.3(b) and VBF process Figure 4.3(c). Other diagrams shown in Figure 4.3 also show production of a Higgs boson pair: even though they are unaffected by κ_λ they are important for the analysis as they interfere with the diagrams where the self-coupling appears, since these processes have the same initial and final state. Depending on the κ_λ value, these diagrams can interfere destructively (as in the SM) but also constructively. As presented in [95,109], were κ_λ to be different from 1, the cross section is a non-monotonic function of κ_λ: it exhibits a dip (Figure 4.4) around the SM value of κ_λ, which is a consequence of destructive interference between the diagrams contributing to $pp \to HH$ [95]. For $|\kappa_\lambda| \gg 1$, the resulting interference between the contributing processes becomes constructive, resulting in higher production cross section values which would have been measured already. This makes certain κ_λ values easier to exclude.

4.1.3 Combinations and summary

A combination of single- and di-Higgs boson production processes, i.e. indirect and direct measurements, brings the most information to the analysis and improves the overall fit. Both the CMS and ATLAS collaborations have placed constraints on the Higgs boson self-coupling (κ_λ) through a combined analysis of single- and di-Higgs boson production channels using the Run2 dataset. The CMS collaboration reports the observed likelihood scan in Figure 4.5, where the combination of single-Higgs boson production channels results in $-1.8 < \kappa_\lambda < 12.0$ at 95% CL, the combination of di-Higgs boson production channels yields $-1.7 < \kappa_\lambda < 7.0$ and the combination of both single- and di-Higgs boson production channels yields $-1.2 < \kappa_\lambda < 7.5$, under the assumption that the other Higgs boson couplings are fixed to their SM predictions. Loosening this assumption, κ_λ is constrained to $-1.4 < \kappa_\lambda < 7.8$ at 95% CL. A similar combination from the ATLAS collaboration is
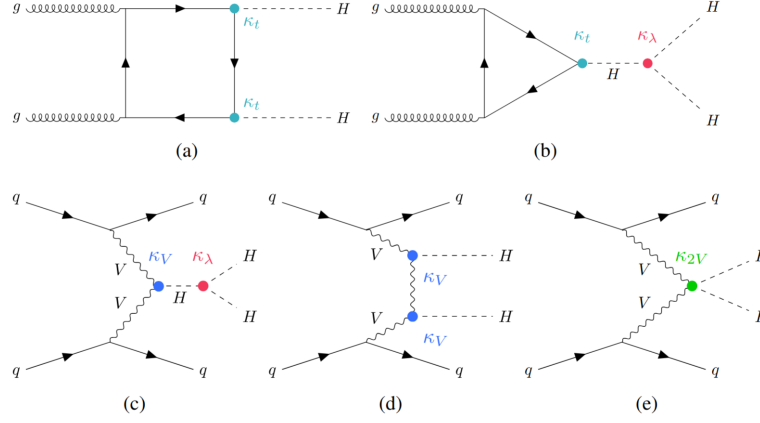
Figure 4.3. Examples of leading-order Feynman diagrams for Higgs boson pair production: for ggF production (diagrams a and b), VBF production (diagrams c, d and e). Figure taken from Ref. [109].
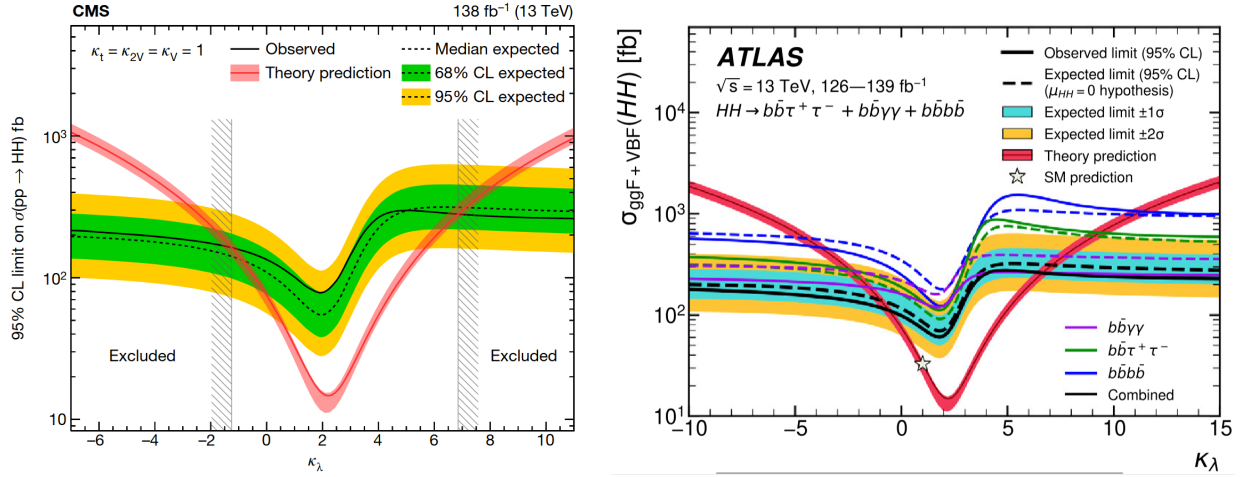

Figure 4.4. Expected and observed 95% CL upper limits on the HH production cross section for different values of κ_λ presented by CMS (left) and ATLAS (right). Figures taken from Ref. [95](left) and Ref. [109](right).

shown in Figure 4.5, where the Higgs boson self-coupling modifier is constrained to $-0.4 < \kappa_\lambda < 6.3$ at 95% CL, again under the assumption that the other Higgs boson couplings are fixed to their SM predictions. If the Higgs boson couplings are left as floating parameters of the fit, the Higgs boson self-coupling modifier is constrained to $-1.4 < \kappa_\lambda < 6.1$ at 95% CL. A summary of the individual decay channels contributing to each combination is presented in Table 4.1 and Table 4.2.

In summary, indirect measurements of the Higgs boson self-coupling exploit single Higgs boson production processes where quantum loops involving the Higgs self-coupling appear. Eventually, the self-coupling measured indirectly was shown to be less constrained when compared to the results of direct measurements. However, the measurements from single- and di-Higgs boson searches should be viewed as complementary, as each of them exploits a different approach in order to measure the same coupling.

So far the Higgs boson self-coupling was measured in processes where the Higgs boson is produced on-shell. In the context of Higgs boson self-coupling, the off-shell region remains unexplored either by ATLAS or CMS. Recent phenomenological studies [137] propose a way of modeling potential deviations of the Higgs boson self-coupling (from the SM predicted value) in the off-shell region, using the Effective Field Theory approach which is the topic of following sections.
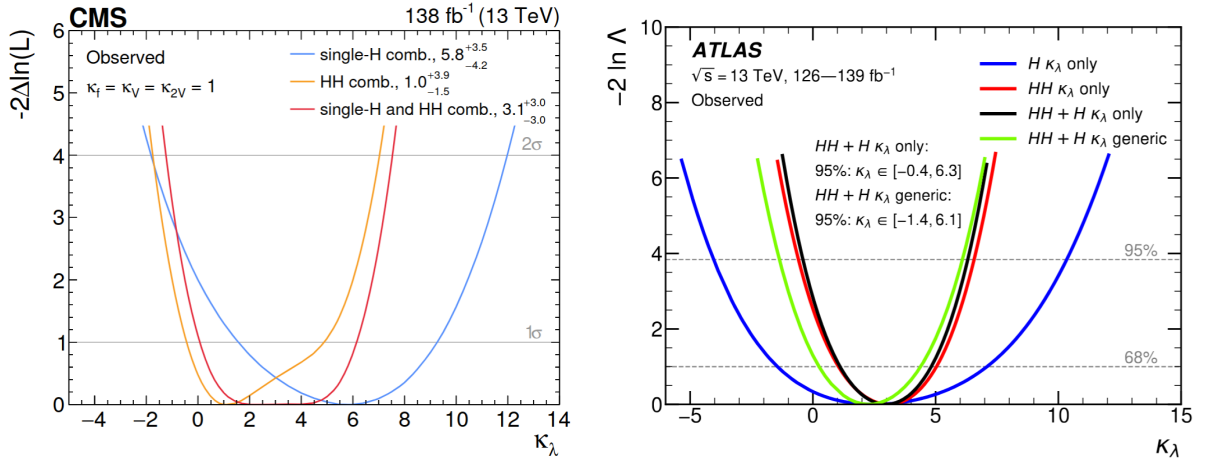
Figure 4.5. Observed profile likelihood scans of κ_λ parameter by CMS (left) [108] and ATLAS (right) [109]. On the left plot the results from the combinations of only single-H (blue), only HH (yellow) and the combination of single-H and HH (red) channels, with all other coupling modifiers fixed to unity, are presented. Similarly, on the right plot the results from the combinations of only single-H (blue), only HH (red) and the combination of single-H and HH (black) channels, with all other coupling modifiers fixed to unity, are presented. The combined result for the generic model, i.e. where the Higgs boson couplings to other particles are treated as free floating parameters, is superimposed (green curve). Figures taken from Ref. [108](left), Ref. [109](right).

Table 4.1. Summary of CMS single- and di-Higgs analyses used in the combination [108]. Table taken from Ref. [108].

Analysis	Integrated luminosity (fb^{-1})	Targeted H/HH production modes	References
H $\rightarrow 4\ell$	138	ggF, VBF, VH, ttH	[110]
H $\rightarrow \gamma\gamma$	138	ggF, VBF, VH, ttH, tH	[111, 112]
H $\rightarrow$ WW	138	ggF, VBF, VH	[113]
H $\rightarrow$ leptons (ttH)	138	ttH	[114]
H $\rightarrow$ bb (ggF)	138	ggF	[115]
H $\rightarrow$ bb (VH)	77	VH	[116]
H $\rightarrow$ bb (ttH)	36	ttH	[117]
H $\rightarrow \tau\tau$	138	ggF, VBF, VH	[118]]
H $\rightarrow \mu\mu$	138	ggF, VBF	[119]
HH $\rightarrow \gamma\gamma b\bar{b}$	138	ggF and VBF	[120]
HH $\rightarrow \tau\tau b\bar{b}$	138	ggF and VBF	[121]
HH $\rightarrow b\bar{b}b\bar{b}$	138	ggF, VBF, and VHH	[122–124]
HH $\rightarrow$ leptons	138	ggF	[125]
HH $\rightarrow$ WW$b\bar{b}$	138	ggF and VBF	[126]

4.2 Effective Field Theories

Effective Field Theories (EFTs) [138–141] are a powerful tool used in theoretical physics, which provides a way to describe and study low-energy phenomena without requiring complete knowledge of high-energy dynamics. The key idea is that the scales of lower- and higher-energy dynamics can be separated. Specifically, if phenomena exhibited by a physical system involve a rather large mass (energy) scale M and a significantly smaller scale $E \ll M$, it is possible to formulate an EFT valid for scales E by integrating-out explicit degrees of freedom related to the scale M. A direct consequence of this construction is that low-energy states are effectively independent of states at high

Table 4.2. Summary of ATLAS single- and di-Higgs analyses used in the combination [109]. Table taken from Ref. [109].

Analysis channel	Integrated luminosity (fb^{-1})	References
$H \to \gamma\gamma$	139	[127]
$H \to ZZ^* \to 4\ell$	139	[128]
$H \to \tau^+\tau^-$	139	[129]
$H \to WW^* \to e\nu\mu\nu$ (ggF, VBF)	139	[130]
$H \to b\bar{b}$ (VH)	139	[131]
$H \to b\bar{b}$ (VBF)	126	[132]
$H \to b\bar{b}$ (ttH)	139	[133]
$HH \to b\bar{b}\gamma\gamma$	139	[134]
$HH \to b\bar{b}\tau^+\tau^-$	139	[135]
$HH \to b\bar{b}b\bar{b}$	126	[136]

energies, i.e. the lower- and higher-energy dynamics are decoupled. As it holds that $E/M \ll 1$, this ratio can be used as an expansion parameter enabling for a construction of a effective Lagrangian in form of a series of operators. These operators are constructed based on several rules: firstly the EFT symmetries must be consistent with the well established symmetries of a system; all relevant degrees of freedom must be taken into account; and at low energies the constructed EFT must provide the same description as the theory based on which it was established (underlying theory). Constructed operators obeying these rules are ordered by their canonical dimension which shows how much they are suppressed in terms of $1/M$. With this construction the decoupled physics phenomena which appear at higher energies are manifested in the description through inclusion of higher-dimensional operators, where to each operator a coefficient is associated, the so called *Wilson coefficient* ($C_i^{(d)}$) which is suppressed by appropriate powers of the cutoff scale $\Lambda \sim M$. If $\mathcal{L}_{\mathrm{LE}}$ is the Lagrangian of the lower energy dynamics, the Lagrangian of an EFT can be written as:

$$\mathcal{L}_{\mathrm{EFT}} = \mathcal{L}_{\mathrm{LE}} + \sum_{i,d} \frac{C_i^{(d)}}{\Lambda^{d-D}} \mathcal{O}_i^{(d)}, \tag{4.3}$$

where the sum runs over all operators of the canonical dimension d in line with the symmetries and the field content of the underlying theory. and D is set as a general space-time dimension. Let the operators $\mathcal{O}_i^{(d)}$ have units of E^d, then the order of the i-th term in Eq. is

$$C_i^{(d)}(E/\Lambda)^{d-D}. \tag{4.4}$$

Expanding the sum in Eq. (4.3) one finds:

$$\mathcal{L}_{\mathrm{EFT}} = \mathcal{L}_{d \leq D} + \mathcal{L}_{d=D+1} + \mathcal{L}_{d=D+2} + \cdots, \tag{4.5}$$

where each summand is finite. The first term contains term of $d \leq D$, and is renormalizable [68, 142, 143]. All of the others terms contain a finite number of terms and make the Lagrangian non-renormalizable. By performing calculations order-by-order ($1/\Lambda$ expansion) an EFT can in principle be predictive. At a fixed d, a finite number of higher-dimensional operators appear and, when taking equations of motion and field redefinitions into careful consideration, a basis set of operators can be constructed.

A possible method to obtain an EFT is the top-down procedure, where the theory inherits symmetries (not all of them necessarily) from the high-energy (UV) theory and contains only relevant, light, degrees of freedom. An example of top-down construction would be Fermi's theory of weak

interaction [144] (beta decay) which is obtained from the SM by removing (integrating out) the W boson at energy scales below M_W. The absence of the W boson is manifested in the existence of local four-fermion operator $(\bar{q}\gamma^\mu q)(\bar{\ell}\gamma_\mu \nu)$, suppressed by $1/M_W^2$, which result in a four-fermion vertex. On the other hand, in the bottom-up approach the underlying UV theory is a priori not known, rather an effective Lagrangian truncated at a certain canonical dimension d is constructed by supplementing the Lagrangian of the IR theory with operators consistent with the symmetries and the field content. The bottom-up approach relies on symmetry (gauge invariance, Lorentz invariance, global symmetries, etc.) and naturalness considerations in order to constrain any possible Lagrangian candidates.

In practice the EFT Lagrangian is usually truncated at the few lowest orders which are relevant for the studied phenomena. This results in a simplified theory characterized by a finite number of free parameters. With this, any general observables can be represented as a power series in E/Λ. For example, a scattering amplitude can be written as

$$\mathcal{M} = \mathcal{M}_{(0)} + \sum_{d \geq D+1} \frac{\mathcal{M}_{(d)}}{\Lambda^{d-D}}, \tag{4.6}$$

where $\mathcal{M}_{(0)}$ comes from the renormalizable part of the Lagrangian ($d \leq D$) and $\mathcal{M}_{(d)}$ and the sum stands for all of the higher dimension terms. In case E is significantly smaller than Λ, the $\mathcal{M}_{(0)}$ term dominates, and $\mathcal{M}_{(d)}$ is a set of small correction. Truncation at a certain d has to be done carefully so as to introduce only a small uncertainty from corrections above a certain d, which are omitted from calculation. Generally, the smaller the ratio E/Λ, the fewer terms are needed for a given precision. As long as the series is dominated by a few terms and the experimental inputs are enough to fix the Wilson coefficients, the predictivity of the constructed EFT is preserved.

Effective field theories should be used with caution as there are limitations to them. They are effective only below a certain cutoff Λ above which new physics phenomena occur where the high energy dynamics is decoupled from the lower energy dynamics. Approaching, and exceeding the cut-off scale makes the EFT non predictable, i.e. the description will no longer match the actual dynamics of the system, as new phenomena not included in the EFT are now accessible. However, if the cutoff Λ is very high then the high energy phenomena, reflected through higher dimensional operators, will be unobservable (even if their effect is small at low energies) as the effects of higher operators are suppressed. Even though caveats exist, EFT can provide model independent framework allowing for a parameterization of any possible BSM effects also showing which experimental measurements offer most sensitivity to BSM effects of interest. The effective field theory approach is a powerful tool in high energy physics where the Standard Model Effective Field Theory is widely adopted as a base for description of the potential BSM effects in a model agnostic way.

4.3   Introduction to SMEFT and the SILH basis

When the EFT framework is applied to the SM, one obtains the Standard Model Effective Field Theory (SMEFT) [145]. The SMEFT is based on the assumption that the SM is a valid theory up to some new physics scale Λ, assuming UV effects are decoupled (or nearly decoupled). Above this threshold new physics phenomena appear, i.e. new fields (particles) and/or interactions. Using the ratio E/Λ (E being the energy scale of the interactions) as an expansion parameter, the BSM effects are described by supplementing the SM Lagrangian with every higher-dimensional term built from SM field content - assuming no additional light degrees of freedom are present - whilst respecting the well established symmetries of the SM (e.g. local gauge, Poincaré, baryon and lepton number conservation). In this way, structured as a tower of operators, SMEFT establishes a model-independent parameterization of

BSM effects.

The SMEFT Lagrangian [145] is:

$$
\mathcal{L}_{SMEFT} = \mathcal{L}_{SM} + \mathcal{L}^{(5)} + \mathcal{L}^{(6)} + \mathcal{L}^{(7)} + \mathcal{L}^{(8)} + \ldots,
$$
$$
\mathcal{L}^{(d)} = \sum_{i=1}^{n_d} \frac{C_i^{(d)}}{\Lambda^{d-4}} Q_i^{(d)} \quad \text{for } d > 4,
\tag{4.7}
$$

where $C_i^{(d)}$ are the Wilson coefficients and the operators $Q_i^{(d)}$ are suppressed by the $d-4$ power of the cutoff scale Λ. The first term ($\mathcal{L}_{SM}$) is the renormalizable SM Lagrangian. Each higher dimensional $d \geq 5$ term is a sum of $Q^{(d)}$ independent operators of canonical mass dimension $d \geq 5$ where to each operator a corresponding Wilson coefficient $C^{(d)}$ is assigned. Viewing all of the terms $d \geq 5$ as corrections to the SM Lagrangian, the expansion is dominated by those terms which have the weakest suppression by powers of Λ. Symmetry considerations constrain the term of $d = 5$ to a single operator [146] (up to hermitian conjugation and flavor change):

$$
Q_{\nu\nu} = (\tilde{\Phi}^\dagger l_p)^\dagger \mathcal{C}(\tilde{\Phi}^\dagger l_r),
\tag{4.8}
$$

where $l_{r,p}$ are leptonic doublets of r, p-th generation, $\mathcal{C}$ is the charge conjugation operator and $\tilde{\Phi}$ was defined in Eq. (3.23). This term, first written by Weinberg in 1979, proposes an explanation as to why the neutrino masses are so small $m_\nu \sim C^{(5)} v^2 / \Lambda$. Asides from giving rise to the neutrino masses, it violates the lepton number conservation and as such is omitted in the following considerations.

The next-to-leading order corrections of BSM effects to the SM Lagrangian appear at $d = 6$. Operators appearing here are of particular importance for SMEFT as they are numerous and they introduce corrections to all observables, for example the Higgs boson couplings. Dimension $d \geq 7$ terms are suppressed by $1/\Lambda^{\geq 3}$ and can be excluded from analysis on the base of being highly suppressed corrections. Adopting the truncated expansion at $d = 6$, a manageable set of operators is obtained which is characterized by a finite set of Wilson coefficients $C_i^{(6)}$:

$$
\mathcal{L}_{SMEFT} = \mathcal{L}_{SM} + \mathcal{L}_6 = \mathcal{L}_{SM} + \sum_{i=1}^{n_6} \frac{C_i^{(6)}}{\Lambda^2} Q_i^{(6)}.
\tag{4.9}
$$

The first complete set of operators was found by Grzadkowski [147] in 2010, where 2499 operators in total are organized in 59 families of operators which account for flavor and CP structure, implicitly summing over three generations of fermions (and flavors). These 59 operators which are non-redundant and gauge-invariant constitute the Warsaw basis [147] and are classified based on the fields they are built from. There are in total 15 purely bosonic operators, 19 operators built with 2 fermion fields and 25 of four-fermionic operators which give contact interactions. The Warsaw basis is shown in Table 4.3. An important remark here is that the Warsaw basis is renormalized at one-loop level [148–152]. Following the notation previously introduced, $l_{p,r,s,t}^j$ ($q_{p,r,s,t}^j$) stands for a left-handed doublet of leptonic (quark) fields where the index $j = 1, 2$ runs over isospin components and indices p, r, s, t run over three generations. Color indices of quarks are suppressed in the notation. Fields $e_{p,r,s,t}$, $u_{p,r,s,t}$, $d_{p,r,s,t}$ denote right-handed chiral charged lepton (e, μ, τ), up type quark (u, c, t) and down type quark (d, s, b) fields respectively. Indices i, j, k appearing in relation to bosonic field operators run over $1, 2, 3$, indices a, b, c run over colors and the Gell-Mann matrices are introduced via $T^a = \lambda^a / 2$. Index i which appears in relation to σ^i matrices runs over the Pauli matrices ($\sigma^{1,2,3}$). Left- and right-handed fermions are in general denoted with L and R. The covariant derivative $D_\mu \Phi$ was introduced in Eq. (3.13). Denoting with $X^{\mu\nu}$ the field strength tensor of either $G^{\mu\nu}$, $W^{\mu\nu}$ or $B^{\mu\nu}$, its dual field strength tensor is defined as:

$$\widetilde{X}^{\mu\nu} = \frac{1}{2}\epsilon^{\mu\nu\rho\sigma}X_{\rho\sigma}. \tag{4.10}$$

Covariant derivatives $\overleftrightarrow{D}_\mu$ acting on the scalar field are given as

$$\Phi^\dagger i\overleftrightarrow{D}_\mu\Phi = \Phi^\dagger(iD_\mu\Phi) - (iD_\mu\Phi^\dagger)\Phi, \tag{4.11}$$

$$\Phi^\dagger i\overleftrightarrow{D^i}_\mu\Phi = \Phi^\dagger\sigma^i(iD_\mu\Phi) - (iD_\mu\Phi^\dagger)\sigma^i\Phi. \tag{4.12}$$

Lastly, the $\sigma^{\mu\nu}$ term is the commutator of Pauli matrices:

$$\sigma^{\mu\nu} = \frac{i}{2}[\gamma^\mu, \gamma^\nu]. \tag{4.13}$$

In addition to these 59 B conserving operators, there are 4 B violating operators,

$$Q_{duq} = \varepsilon^{\alpha\beta\gamma}\varepsilon_{jk}\left[\left(d_p^\alpha\right)^T Cu_r^\beta\right]\left[\left(q_s^{\gamma j}\right)^T C\ell_t^k\right], \tag{4.14}$$

$$Q_{qqu} = \varepsilon^{\alpha\beta\gamma}\varepsilon_{jk}\left[\left(q_p^{\alpha j}\right)^T Cq_r^{\beta k}\right]\left[(u_s^\gamma)^T Ce_t\right], \tag{4.15}$$

$$Q_{qqq} = \varepsilon^{\alpha\beta\gamma}\varepsilon_{jn}\varepsilon_{km}\left[\left(q_p^{\alpha j}\right)^T Cq_r^{\beta k}\right]\left[(q_s^{\gamma m})^T C\ell_t^n\right], \tag{4.16}$$

$$Q_{duu} = \varepsilon^{\alpha\beta\gamma}\left[\left(d_p^\alpha\right)^T Cu_r^\beta\right]\left[(u_s^\gamma)^T Ce_t\right]. \tag{4.17}$$

One important thing to note is that the choice of operator basis is not unique. Different operator bases are related by equations of motion, integration by parts or by Fierz identities [153]. Besides the popular Warsaw basis, another widely used basis is the Strongly-Interacting Light Higgs (SILH) basis [154, 155].

The SILH basis was constructed as tool to use for parameterization of the new strong-sector effects on the Higgs boson and EW physics. Namely, in composite Higgs boson models, the Higgs boson is a pseudo-Goldstone boson (i.e. light bound state) of a strong interaction which is characterized by mass of the heavy resonance m_ρ and by the coupling strength g_ρ of this resonance. The Warsaw basis and the SILH basis are related by fields redefinitions and equations of motion and substitution of certain operators in one basis with a combination of operators from the other basis [156]. Concerning the Higgs boson, the effective SILH Lagrangian $\mathcal{L}_{\text{SILH}}$ is written as:

$$
\begin{aligned}
\mathcal{L}_{\text{SILH}} = {} & \frac{c_H}{2f^2}\partial^\mu(\Phi^\dagger\Phi)\,\partial_\mu(\Phi^\dagger\Phi) + \frac{c_T}{2f^2}\left(\Phi^\dagger\overleftrightarrow{D^\mu}\Phi\right)\left(\Phi^\dagger\overleftrightarrow{D}_\mu H\right) \\
& - \frac{c_6\lambda}{f^2}(\Phi^\dagger\Phi)^3 + \left(\frac{c_y y_f}{f^2}\Phi^\dagger\Phi\,\bar{f}_L\Phi f_R + \text{h.c.}\right) \\
& + \frac{ic_W g_2}{2m_\rho^2}\left(\Phi^\dagger\sigma^i\overleftrightarrow{D^\mu}\Phi\right)(D^\nu W_{\mu\nu})^i + \frac{ic_B g_1}{2m_\rho^2}\left(\Phi^\dagger\overleftrightarrow{D^\mu}\Phi\right)(\partial^\nu B_{\mu\nu}) \\
& + \frac{ic_{HW} g_2}{16\pi^2 f^2}(D^\mu\Phi)^\dagger\sigma^i(D^\nu\Phi)W_{\mu\nu}^i + \frac{ic_{HB} g_1}{16\pi^2 f^2}(D^\mu\Phi)^\dagger(D^\nu\Phi)B_{\mu\nu} \\
& + \frac{c_\gamma g_1^2}{16\pi^2 f^2}\frac{g_2^2}{g_\rho^2}\Phi^\dagger H B_{\mu\nu}B^{\mu\nu} + \frac{c_g g_s^2}{16\pi^2 f^2}\frac{y_t^2}{g_\rho^2}\Phi^\dagger\Phi G_{\mu\nu}^a G^{a\mu\nu},
\end{aligned} \tag{4.18}
$$

where $f = m_\rho/g_\rho$, $y_{f,t}$ are fermionic and top Yukawa couplings, and c_X are Wilson coefficients ($X = H, T, 6, y, W, B, HW, HB, \gamma, g$).

Table 4.3. Baryon number conserving operators in the Warsaw basis [147], categorized into eight classes $\mathcal{L}_6$

$\mathcal{L}_6^{(1)} - X^3$	$\mathcal{L}_6^{(6)} - \psi^2 X H$	$\mathcal{L}_6^{(8b)} - (\bar{R}R)(\bar{R}R)$
$Q_G = f^{abc}G_{\mu\nu}^a G^{b\nu\rho}G_\rho^{c\mu}$	$Q_{eW} = (\bar{l}_p \sigma^{\mu\nu}e_r)\sigma^i H W_{\mu\nu}^i$	$Q_{ee} = (\bar{e}_p\gamma_\mu e_r)(\bar{e}_s\gamma^\mu e_t)$
$Q_{\widetilde{G}} = f^{abc}\widetilde{G}_{\mu\nu}^a G^{b\nu\rho}G_\rho^{c\mu}$	$Q_{eB} = (\bar{l}_p \sigma^{\mu\nu}e_r)\Phi B_{\mu\nu}$	$Q_{uu} = (\bar{u}_p\gamma_\mu u_r)(\bar{u}_s\gamma^\mu u_t)$
$Q_W = \epsilon^{ijk}W_\mu^{i\nu}W_\nu^{j\rho}W_\rho^{k\mu}$	$Q_{uG} = (\bar{q}_p \sigma^{\mu\nu}T^a u_r)\widetilde{\Phi} G_{\mu\nu}^a$	$Q_{dd} = (\bar{d}_p\gamma_\mu d_r)(\bar{d}_s\gamma^\mu d_t)$
$Q_{\widetilde{W}} = \epsilon^{ijk}\widetilde{W}_\mu^{i\nu}W_\nu^{j\rho}W_\rho^{k\mu}$	$Q_{uW} = (\bar{q}_p \sigma^{\mu\nu}u_r)\sigma^i \widetilde{\Phi} W_{\mu\nu}^i$	$Q_{eu} = (\bar{e}_p\gamma_\mu e_r)(\bar{u}_s\gamma^\mu u_t)$
$\mathcal{L}_6^{(2)} - \Phi^6$	$Q_{uB} = (\bar{q}_p \sigma^{\mu\nu}u_r)\widetilde{\Phi} B_{\mu\nu}$	$Q_{ed} = (\bar{e}_p\gamma_\mu e_r)(\bar{d}_s\gamma^\mu d_t)$
$Q_\Phi = (\Phi^\dagger\Phi)^3$	$Q_{dG} = (\bar{q}_p \sigma^{\mu\nu}T^a d_r)\Phi G_{\mu\nu}^a$	$Q_{ud}^{(1)} = (\bar{u}_p\gamma_\mu u_r)(\bar{d}_s\gamma^\mu d_t)$
$\mathcal{L}_6^{(3)} - \Phi^4 D^2$	$Q_{dW} = (\bar{q}_p \sigma^{\mu\nu}d_r)\sigma^i \Phi W_{\mu\nu}^i$	$Q_{ud}^{(8)} = (\bar{u}_p T^a\gamma_\mu u_r)(\bar{d}_s\gamma^\mu T^a d_t)$
$Q_{\Phi\Box} = (\Phi^\dagger\Phi)\Box(\Phi^\dagger\Phi)$	$Q_{dB} = (\bar{q}_p \sigma^{\mu\nu}d_r)\Phi B_{\mu\nu}$	
$Q_{\Phi D} = (\Phi^\dagger D^\mu\Phi)^*(\Phi^\dagger D_\mu\Phi)$		

$\mathcal{L}_6^{(4)} - X^2\Phi^2$	$\mathcal{L}_6^{(7)} - \psi^2\Phi^2 D$	$\mathcal{L}_6^{(8c)} - (\bar{L}L)(\bar{R}R)$
$Q_{\Phi G} = \Phi^\dagger\Phi G_{\mu\nu}^a G^{a\mu\nu}$	$Q_{\Phi l}^{(1)} = (\Phi^\dagger i\overleftrightarrow{D}_\mu\Phi)(\bar{l}_p\gamma^\mu l_r)$	$Q_{le} = (\bar{l}_p\gamma_\mu l_r)(\bar{e}_s\gamma^\mu e_t)$
$Q_{\Phi\widetilde{G}} = \Phi^\dagger\Phi \widetilde{G}_{\mu\nu}^A G^{A\mu\nu}$	$Q_{\Phi l}^{(3)} = (\Phi^\dagger i\overleftrightarrow{D}_\mu^i\Phi)(\bar{l}_p\sigma^i\gamma^\mu l_r)$	$Q_{lu} = (\bar{l}_p\gamma_\mu l_r)(\bar{u}_s\gamma^\mu u_t)$
$Q_{\Phi W} = \Phi^\dagger\Phi W_{\mu\nu}^i W^{i\mu\nu}$	$Q_{\Phi e} = (\Phi^\dagger i\overleftrightarrow{D}_\mu\Phi)(\bar{e}_p\gamma^\mu e_r)$	$Q_{ld} = (\bar{l}_p\gamma_\mu l_r)(\bar{d}_s\gamma^\mu d_t)$
$Q_{\Phi\widetilde{W}} = \Phi^\dagger\Phi \widetilde{W}_{\mu\nu}^i W^{i\mu\nu}$	$Q_{\Phi q}^{(1)} = (\Phi^\dagger i\overleftrightarrow{D}_\mu\Phi)(\bar{q}_p\gamma^\mu q_r)$	$Q_{qe} = (\bar{q}_p\gamma_\mu q_r)(\bar{e}_s\gamma^\mu e_t)$
$Q_{\Phi B} = \Phi^\dagger\Phi B_{\mu\nu} B^{\mu\nu}$	$Q_{\Phi q}^{(3)} = (\Phi^\dagger i\overleftrightarrow{D}_\mu^i\Phi)(\bar{q}_p\sigma^i\gamma^\mu q_r)$	$Q_{qu}^{(1)} = (\bar{q}_p\gamma_\mu q_r)(\bar{u}_s\gamma^\mu u_t)$
$Q_{\Phi\widetilde{B}} = \Phi^\dagger\Phi \widetilde{B}_{\mu\nu} B^{\mu\nu}$	$Q_{\Phi u} = (\Phi^\dagger i\overleftrightarrow{D}_\mu\Phi)(\bar{u}_p\gamma^\mu u_r)$	$Q_{qu}^{(8)} = (\bar{q}_p\gamma_\mu T^a q_r)(\bar{u}_s\gamma^\mu T^a u_t)$
$Q_{\Phi WB} = \Phi^\dagger\sigma^i\Phi W_{\mu\nu}^i B^{\mu\nu}$	$Q_{\Phi d} = (\Phi^\dagger i\overleftrightarrow{D}_\mu\Phi)(\bar{d}_p\gamma^\mu d_r)$	$Q_{qd}^{(1)} = (\bar{q}_p\gamma_\mu q_r)(\bar{d}_s\gamma^\mu d_t)$
$Q_{\Phi\widetilde{W}B} = \Phi^\dagger\sigma^i\Phi \widetilde{W}_{\mu\nu}^i B^{\mu\nu}$	$Q_{\Phi ud} + \text{h.c.}$	$Q_{qd}^{(8)} = (\bar{q}_p\gamma_\mu T^a q_r)(\bar{d}_s\gamma^\mu T^a d_t)$

$\mathcal{L}_6^{(5)} - \psi^2\Phi^3$	$\mathcal{L}_6^{(8a)} - (\bar{L}L)(\bar{L}L)$	$\mathcal{L}_6^{(8d)} - (\bar{L}R)(\bar{L}R)$
$Q_{e\Phi} = (\Phi^\dagger\Phi)(\bar{l}_p e_r\Phi)$	$Q_{ll} = (\bar{l}_p\gamma_\mu l_r)(\bar{l}_s\gamma^\mu l_t)$	$Q_{ledq} = (\bar{l}_p^j e_r)(\bar{d}_s q_t^j)$
$Q_{u\Phi} = (\Phi^\dagger\Phi)(\bar{q}_p u_r\widetilde{\Phi})$	$Q_{qq}^{(1)} = (\bar{q}_p\gamma_\mu q_r)(\bar{q}_s\gamma^\mu q_t)$	$Q_{quqd}^{(1)} = (\bar{q}_p^j u_r)\epsilon_{jk}(\bar{q}_s^k d_t)$
$Q_{d\Phi} = (\Phi^\dagger\Phi)(\bar{q}_p d_r\widetilde{\Phi})$	$Q_{qq}^{(3)} = (\bar{q}_p\gamma_\mu\sigma^i q_r)(\bar{q}_s\gamma^\mu\sigma^i q_t)$	$Q_{quqd}^{(8)} = (\bar{q}_p^j T^a u_r)\epsilon_{jk}(\bar{q}_s^k T^a d_t)$
	$Q_{lq}^{(1)} = (\bar{l}_p\gamma_\mu l_r)(\bar{q}_s\gamma^\mu q_t)$	$Q_{lequ}^{(1)} = (\bar{l}_p^j e_r)\epsilon_{jk}(\bar{q}_s^k u_t)$
	$Q_{lq}^{(3)} = (\bar{l}_p\gamma_\mu\sigma^i l_r)(\bar{q}_s\gamma^\mu\sigma^i q_t)$	$Q_{lequ}^{(3)} = (\bar{l}_p^j\sigma_{\mu\nu}e_r)\epsilon_{jk}(\bar{q}_s^k\sigma^{\mu\nu}u_t)$

Even though the choices of basis may differ, all choices are equivalent if all operators are considered. In this sense SMEFT allows for a parameterization of BSM effects through inclusion of

higher-dimensional operators to the SM Lagrangian. In principle, by comparing precision measurements to the SMEFT predictions it is possible to constrain Wilson coefficients. As SMEFT is built in a model-independent manner, a specific model can be mapped onto SMEFT by calculating it's contributions to the Wilson coefficients. Based on the set of experimental constraints it is possible to judge whether such a model is allowed or is excluded by the data having in mind the validity of the expansion. This is the basis for interpretation of the Higgs boson (or any other particle) measurements, especially when probing for subtleties such as the Higgs boson self-coupling.

4.4 EFT effects on Higgs boson self-coupling

The analysis presented in this thesis is based on the work done in [137], where a phenomenological study of the effects of $\mathcal{O}_6$ was performed in the ZZ off-shell region, giving predictions on the constraints at LHC and HL-LHC. Here the Higgs boson self-coupling deviations w.r.t. SM are modeled with introduction of one CP even operator from the SILH basis (found in the Warsaw basis as well):

$$\mathcal{L} = \mathcal{L}_{SM} + \frac{c_6}{v^2}\mathcal{O}_6, \tag{4.19}$$

where

$$\mathcal{O}_6 = -\lambda(\Phi^\dagger\Phi)^3 = -\lambda|\Phi|^6, \tag{4.20}$$

where c_6 is a dimensionless Wilson coefficient evaluated at the EW scale, $\mu = \mathcal{O}(v)$. It should be noted that in [137] the c_6 Wilson coefficient is denoted with $\bar{c}_6$, whilst here the bar is omitted.

After EWSB and canonical normalization, the Higgs field potential describing the self-interaction takes the form [137, 154]:

$$V \supset -\lambda(1 + c_6)vH^3. \tag{4.21}$$

Modified Higgs boson self-coupling introduces three types of corrections [137] to the SM LO process $gg \rightarrow H^* \rightarrow ZZ$ (Figure 4.6) which appear at NLO EW via quantum loops:

- corrections to ggF Higgs boson production: two-loop topologies and the wave-function renormalization of the Higgs boson field result in a renormalized ggF vertex (Figure 4.7, top)

- corrections to the Higgs boson propagator: wave-function renormalization of the Higgs field and corrections to the bare Higgs boson self-energy and the mass counterterm result in a renormalized contribution to the self-energy of the Higgs field (Figure 4.7, middle)

- corrections to the Higgs boson decay: loop contributions and a Higgs boson wave-function renormalization together give renormalized HZZ vertex (Figure 4.7, bottom)

It can be seen that sensitivity to the c_6 parameter in the process $gg \rightarrow H^* \rightarrow ZZ \rightarrow 4l$ arises through NLO EW corrections. Besides affecting Higgs production, propagation and decay, $\mathcal{O}_6$ affects the overall size of the cross section and the shape of kinematic distributions with m_{4l} playing a significant role [137]. The Higgs boson width is also affected by introduction of the operator $\mathcal{O}_6$ but the effect is minuscule in ggF production mode, henceforth it is omitted for the studies of ggF.
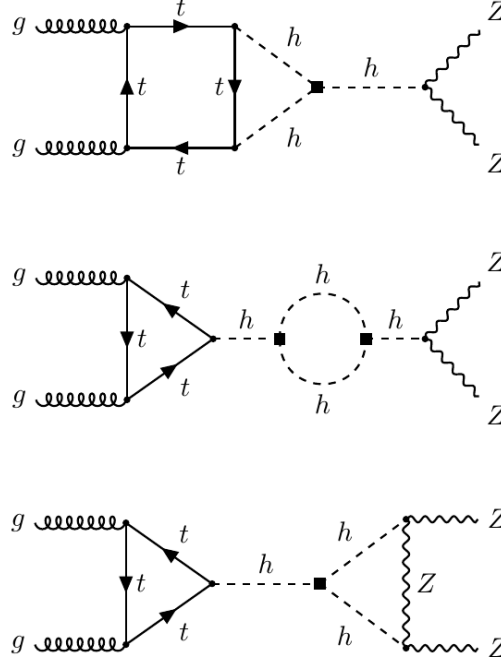
A summary of $\mathcal{O}(\lambda)$ corrections (Figure 4.7) to the SM LO process $gg \rightarrow H^* \rightarrow ZZ$ in the equation form and the related discussion, based on [137] (keeping the notation), is presented here.

The renormalized gluon-gluon fusion vertex that describes the Higgs boson production is given as:
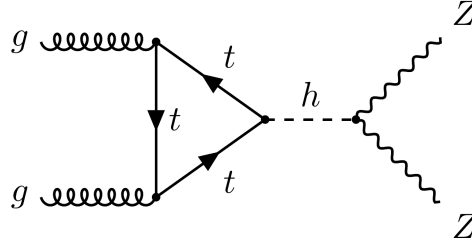
Figure 4.6. $gg \to H^* \to ZZ$ SM LO Feynman diagram. Figure taken from Ref. [137].

Figure 4.7. $\mathcal{O}(\lambda)$ correction to the $gg \to H^* \to ZZ$ production. Black squares represent modified triple Higgs boson vertex. Figure taken from Ref. [137].

$$\hat{\Gamma}_{ggF}^{\mu\nu}(p_1, p_2) = -\frac{\alpha_s \delta^{a_1 a_2}}{\pi v} \left(\eta^{\mu\nu} p_1 \cdot p_2 - p_1^\nu p_2^\mu\right) \left[\frac{\delta Z_h}{2} \mathcal{F}_1 + \frac{\lambda \bar{c}_6}{(4\pi)^2} \mathcal{F}_2\right], \tag{4.22}$$

where α_s denotes the strong coupling constant, a_1 and a_2 are color indices and $\eta^{\mu\nu}$ is the Minkowski metric. The one-loop correction to the Higgs boson wave function associated to insertions of the operator $\mathcal{O}_6$ [157, 158] is given as

$$\delta Z_h = N_h c_6 \left(c_6 + 2\right), \quad N_h = \frac{\lambda}{(4\pi)^2} \left(9 - 2\sqrt{3}\pi\right) \simeq -1.54 \cdot 10^{-3}, \tag{4.23}$$

and the one-loop triangle diagram with internal top quarks and mass of the top quark m_t is given as

$$\mathcal{F}_1 = \frac{m_t^2}{m_H^2} \left[2 - \left(m_H^2 - 4m_t^2\right) C_0(\hat{s}, 0, 0, m_t^2, m_t^2, m_t^2)\right]. \tag{4.24}$$

Here, $\hat{s} = 2p_1 \cdot p_2$ and the C_0 is a three-point Passarino-Veltman scalar integral [159]. The non-factorisable two-loop form factor $\mathcal{F}_2$ has been calculated analytically in [157, 160], To cover the off-shell range up to $\hat{s} = 1$ TeV, the numerical results for the non-factorisable two-loop form factor $\mathcal{F}_2$ [161, 162] are employed.

The Higgs boson propagator, as mentioned, also receives corrections from insertions of the operator $\mathcal{O}_6$. The resulting renormalized contribution to the self-energy of the Higgs is given as:

$$\hat{\Sigma}(\hat{s}) = \Sigma(\hat{s}) + (\hat{s} - m_H^2)\delta Z_h - \delta m_H^2, \tag{4.25}$$

where the bare Higgs boson self-energy and the mass counterterm in the on-shell scheme are given as:

$$\Sigma(\hat{s}) = \frac{\lambda c_6}{(4\pi)^2}(c_6 + 2)\, 9m_H^2\, B_0(\hat{s}, m_H^2, m_H^2), \tag{4.26}$$

$$\delta m_H^2 = \frac{\lambda c_6}{(4\pi)^2}(c_6 + 2)\, 9m_H^2\, B_0(m_H^2, m_H^2, m_H^2), \tag{4.27}$$

where B_0 is a two-point Passarino-Veltman scalar integral [159].

The Higgs boson decay $H \to ZZ$ receives a loop contribution of order $\mathcal{O}(\lambda)$ and a counterterm contribution involving Higgs boson wave-function renormalization. Following the notation of [163], the Higgs boson decay vertex describing the $H(p_1 + p_2) \to Z(p_1)Z(p_2)$ is given as:

$$\hat{\Gamma}_{hZZ}^{\mu\nu}(p_1, p_2) = \frac{2m_Z^2}{v}\left[\eta^{\mu\nu}\mathcal{G}_1 + p_1^\nu p_2^\mu \mathcal{G}_2\right], \tag{4.28}$$

where m_Z denotes the Z-boson mass. The $\mathcal{O}(\lambda)$ corrections to the form factors $\mathcal{G}_1$ and $\mathcal{G}_2$ are given by:

$$\begin{aligned}
\mathcal{G}_1 = \frac{\delta Z_h}{2} - \frac{\lambda c_6}{(4\pi)^2}\bigg[&12\Big(m_Z^2\, C_0\big((p_1 + p_2)^2, p_1^2, p_2^2, m_H^2, m_H^2, m_Z^2\big) \\
&- C_{00}\big((p_1 + p_2)^2, p_1^2, p_2^2, m_H^2, m_H^2, m_Z^2\big)\Big) + 3\, B_0\big((p_1 + p_2)^2, m_H^2, m_H^2\big)\bigg],
\end{aligned} \tag{4.29}$$

$$\begin{aligned}
\mathcal{G}_2 = \frac{\lambda c_6}{(4\pi)^2} \cdot 12\Big[&C_1\big((p_1 + p_2)^2, p_1^2, p_2^2, m_H^2, m_H^2, m_Z^2\big) + C_{11}\big((p_1 + p_2)^2, p_1^2, p_2^2, m_H^2, m_H^2, m_Z^2\big) \\
&+ C_{12}\big((p_1 + p_2)^2, p_1^2, p_2^2, m_H^2, m_H^2, m_Z^2\big)\Big]
\end{aligned} \tag{4.30}$$

where C_1, C_{00} and C_{11} are the tensor coefficients of the three-point Passarino-Veltman integrals [159, 163].

It should be noted that the wave-function renormalization term δZ_h exactly cancels between propagator corrections and the vertices corrections combined [137]. This leaves vertices with linear dependence of c_6. From Eqs. (4.22), (4.22) and (4.28) it can be seen that at the matrix element level, the highest contribution in terms of c_6 is quadratic. However, at amplitude level the dependence becomes that of a fourth order polynomial. This is a key feature which shapes how modeling and fitting strategies are developed.

4.4.1 Corrections to the Higgs boson EW production modes

Based on the c_6-dependent corrections to the ggF mode of Higgs boson production in literature [137], corrections to the EW Higgs boson production modes (VBF and VH) were introduced to the working framework. As the same decay channel is considered ($H \to ZZ \to 4l$), the corrections to propagator and decay adopt the same structure as those in case of ggF Higgs boson production.
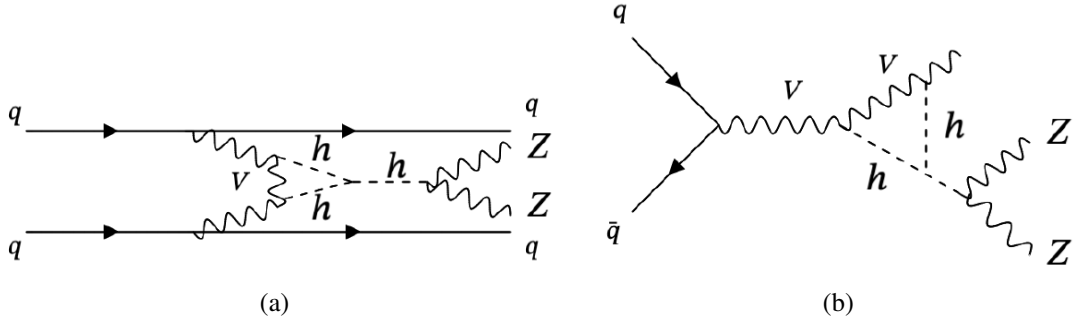
Figure 4.8. Corrections to the VBF (a) and VH (b) Higgs boson production vertices. Corrections to propagator and decay vertex of the Higgs boson are the same as in the case of ggF mode of Higgs boson production

However, the EW production vertex corrections are somewhat different than in the case of ggF. In fact, they have almost identical structure as the decay corrections of ggF, meaning they are introduce triangle loop formed by two Higgs boson and one electroweak boson, which is shown in Figure 4.8. The main difference between the two cases (EW and ggF) is that the in case of ggF production the loop is closed by a Z boson, whilst in case of EW production the loop can be closed by either Z or W boson. Thus, the EW production vertex corrections are written as:

$$\hat{\Gamma}^{\mu\nu}(p_1, p_2) = \frac{2m_{W/Z}^2}{v} \left[\eta^{\mu\nu} \mathcal{G}_1 + p_1^\nu p_2^\mu \mathcal{G}_2 \right], \tag{4.31}$$

where the coefficients $\mathcal{G}_1$ and $\mathcal{G}_2$ assume the form:

$$\mathcal{G}_1 = \frac{\delta Z_h}{2} - \frac{\lambda c_6}{(4\pi)^2} \left\{ 12 \left[m_{Z/W}^2 \, C_0 \big((p_1{+}p_2)^2, p_1^2, p_2^2, m_H^2, m_H^2, m_{Z/W}^2 \big) \right. \right.$$
$$\left. \left. - C_{00} \big((p_1{+}p_2)^2, p_1^2, p_2^2, m_H^2, m_H^2, m_{Z/W}^2 \big) \right] + 3\, B_0 \big((p_1{+}p_2)^2, m_H^2, m_H^2 \big) \right\}, \tag{4.32}$$

$$\mathcal{G}_2 = \frac{\lambda c_6}{(4\pi)^2} \, 12 \left[C_1 \big((p_1{+}p_2)^2, p_1^2, p_2^2, m_H^2, m_H^2, m_{Z/W}^2 \big) + C_{11} \big((p_1{+}p_2)^2, p_1^2, p_2^2, m_H^2, m_H^2, m_{Z/W}^2 \big) \right.$$
$$\left. + C_{12} \big((p_1{+}p_2)^2, p_1^2, p_2^2, m_H^2, m_H^2, m_{Z/W}^2 \big) \right]. \tag{4.33}$$

An important note here is that, even though the corrections to the EW production modes are structurally similar to ggF corrections, the δZ_H term does not cancel as it does in case of ggF. This is a consequence of different Z and W permutations present in VBF and VH processes. To simplify the model, the δZ_H contributions from production and decay are absorbed into the propagation term, since all three components scale with the same factor $c_6(c_6+2)$. As a result, the remaining production and decay terms scale linearly with c_6.

4.5 Implementation and validation of Monte Carlo simulations

The implementation of the aforementioned ggF effects in a Monte Carlo simulation is described in Ref. [137]: it relies on the MCFM code [164], where the c_6 corrections to the Higgs production via

gluon fusion, propagation and decay were incorporated for the process $gg \rightarrow H^* \rightarrow ZZ$. Here these corrections were tested and used for validation. At the matrix element level, the implementation includes all contributions up to $\mathcal{O}(\lambda^2)$, which encompasses both the BSM and LO SM $gg \rightarrow H^* \rightarrow ZZ$ Feynman diagrams.

Based on the modified version 8.0 of MCFM (hereafter referred to as MCFM8.0), the encoded amplitudes were first propagated to MCFM version 7.0.1 [165–168], which is integrated into the JHUGen MC generator framework [169–173], hereafter referred to as JHUGen-MCFM. Subsequently, the amplitudes were transferred to the MELA software package [169–173], enabling both event reweighting and the construction of matrix element-based discriminants.

For processes that share the same initial and final states, the MELA package allows reweighting of events from one hypothesis (native) to a different one (target). The underlying idea is to calculate matrix elements (of corresponding Feynman diagrams) for native and target hypothesis based on a native-hypothesis data sample (in this case MC- generated). Based on the ratio of these matrix elements a weight is found and the applied on an event-by-event basis to the native hypothesis, thus reweighting it to the target hypothesis. Therefore, distributions of observables, e.g. m_{4l}, can be rescaled from native hypothesis to represent the target hypothesis. This method efficiently saves computing resources, significantly reducing the number of MC samples needed for the analysis.

The matrix-element discriminant method uses the full LO matrix elements to calculate a discriminant, often in the form of a likelihood ratio, which is a single variable that quantifies how much an event is likely to belong to an event class (signal) with respect to another class (background). The calculation takes into account the full kinematics of the four-lepton final state, including angles and invariant masses.

Several validation steps of the code porting to JHUGen-MCFM and to MELA were performed, and are presented in the following sections. Firstly the generation of a MC sample that corresponds to a LHC energy of 14 TeV was performed with MCFM8.0, which allows for direct comparison to the results reported in Ref. [137]. Secondly, after integration of BSM matrix elements into the JHUGen-MCFM a test of cross section calculation was carried out, together with a test construction of discriminant D_S (as reported in [137]). Lastly, MELA reweighting was also tested, comparing the MC-generated target hypothesis m_{4l} distributions to target distributions obtained by reweighting one of the native hypothesis distributions.

4.5.1 Comparison to reported MC predictions

As a first test, a comparison of m_{4l} distributions for different c_6 hypothesis to the reported distributions in Ref. [137] was performed. It should be noted that $c_6 = 0$ hypothesis corresponds to the LO SM process. Distributions are from MC samples generated with MCFM8.0. The process under investigation is the full $gg \rightarrow ZZ \rightarrow 4l$ (labeled as #131 in MCFM), including the Higgs signal and background components and their interference.

SM parameters of the MCFM8.0 setup are taken from [137] as: $m_t = 173.0$ GeV, $m_b = 4.66$ GeV, $m_c = 1.2750$ GeV, $m_H = 125.0$ GeV. The anti-k_T jet algorithm and the CT14.NN [174] PDF set were used. Events are selected based on the phase space cuts taken from Ref. [137] and reported in Table 4.4. The employed cuts are applied to generator-level observables, i.e. to observables where detector effects are not considered.

Distributions are shown in Figure 4.9, showcasing the correct setup and usage of the MCFM8.0 code. Comparing the two plots, a good agreement is found. Because of the number of events which could be effectively generated in the test, in Figure 4.9(a) wider bins were used as opposed to Figure 4.9(b), which removes some features like the onset of the distribution in the very first

bins. The shift in the overall normalization, which can be observed for example in the region $220 < m_{4l} < 260$ GeV, is due to the fact that only the $2e2\mu$ final state was considered in Figure 4.9(a), whereas in Figure 4.9(b) all four-lepton final states were considered ($2e2\mu$, $4e$, 4μ). However the ratio plot confirms that the predicted behavior is well reproduced at least up to 700 GeV, where statistical fluctuations (smaller number of events in the high-tail region) are present.

Table 4.4. Generator level cuts used for event selection.

Lepton transverse momenta:	$p_{T,\ell_1} > 20$ GeV
	$p_{T,\ell_2} > 15$ GeV
	$p_{T,\ell_3} > 10$ GeV
	$p_{T,\ell_4} > 6$ GeV
Pseudorapidity:	$|\eta| < 2.5$
Four-lepton invariant mass:	220 GeV $< m_{4\ell} < 1000$ GeV
First Z candidate mass:	50 GeV $< m_{Z_1} < 106$ GeV
Second Z candidate mass:	50 GeV $< m_{Z_2} < 115$ GeV

(a)   (b)
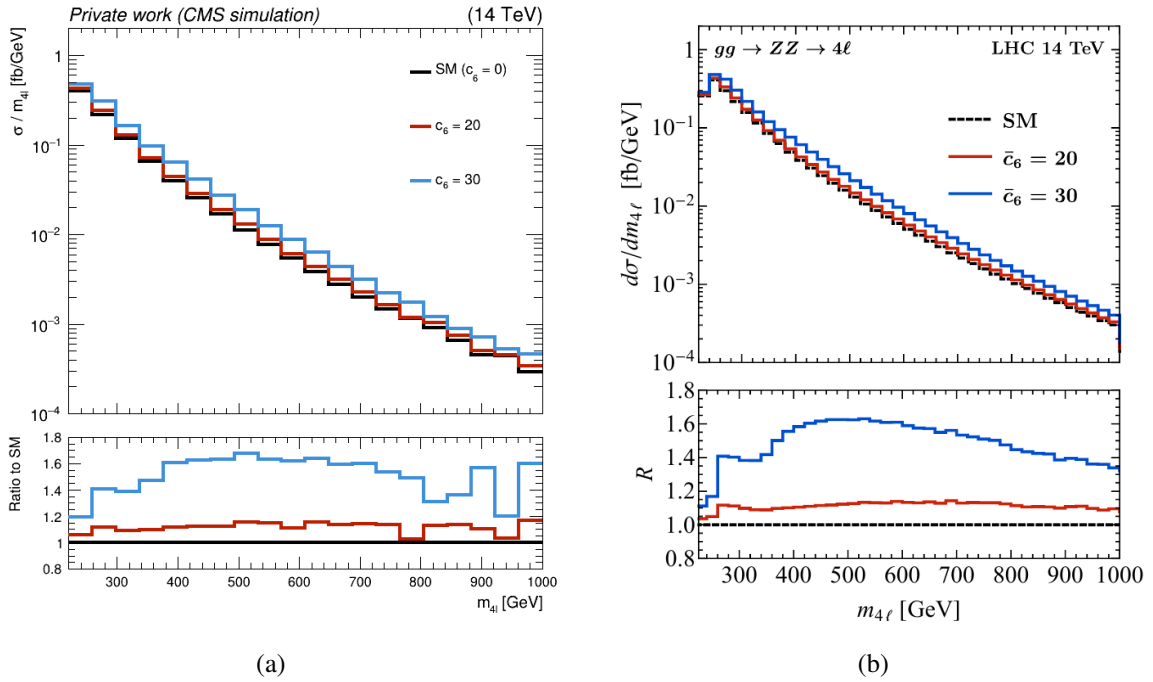
Figure 4.9. Generator-level m_{4l} distributions for the process $gg \to ZZ \to 2e2\mu$ (Higgs-boson contribution included): generated privately with MCFM8.0 (a) and reported in Ref. [137](b). Distributions correspond to the LO SM predictions (black), the BSM hypotheses $c_6 = 20$ (red) and $c_6 = 30$ (blue). Lower panels of present ratios of BSM m_{4l} distributions to the LO SM distribution.

4.5.2 BSM effects on reconstructed observables

Based on data samples generated for different c_6 values at COM energy of 13 TeV, using MCFM8.0, several reconstruction-level (events after showering, hadronization and simulated detector effects) observables were tested under change of the value of c_6 parameter in two different processes. Firstly

in the signal process $gg \to H^* \to ZZ \to 4l$ (Higgs signal only, numbered as #128 in MCFM8), secondly in the $gg \to ZZ \to 4l$ process which includes Higgs boson production as well as gluon-gluon induced background (numbered as #131 in MCFM8). In all of the figures presented the dominant $qqZZ$ background contribution has been scaled down to approximately match the area under the histogram that corresponds to $c_6 = 30$ hypothesis. Events were generated with the cuts reported in Table 4.4 and with the detector conditions corresponding to Run 2 2018 data taking period which also means the distributions were scaled to expected yield of Run 2018.

Based on the tested observables, it can be concluded that the most sensitivity to BSM effects is carried by the m_{4l} (four-lepton invariant mass), $p_T(l_1)$ (transverse momentum of leading lepton, i.e. lepton with the highest p_T), $p_T(l_2)$ (transverse momentum of a sub-leading lepton, i.e. lepton with the second highest p_T), $p_T(Z_1)$ (transverse momentum of a lepton pair with an invariant mass closest to the Z boson nominal mass) and $p_T(Z_2)$ distributions, which are shown in Figures 4.10, 4.11, 4.12, 4.13, 4.14, respectively.

(a)   (b)
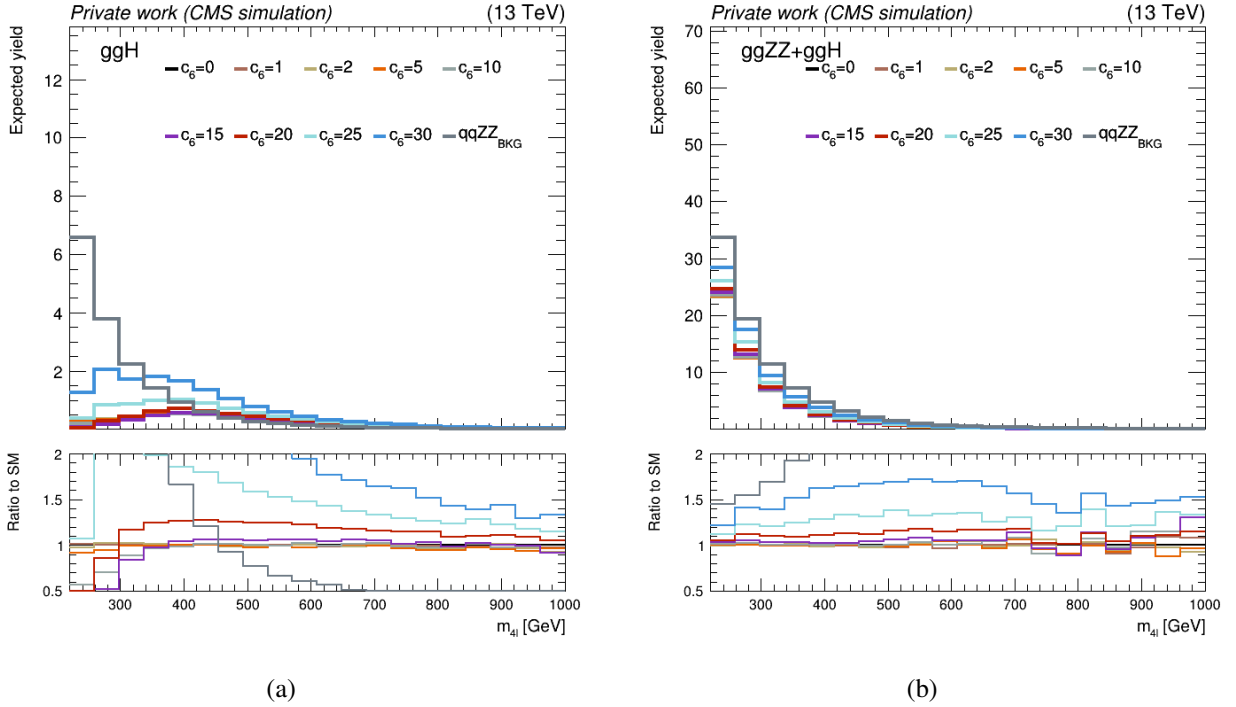
Figure 4.10. Reconstruction level m_{4l} distributions for the processes $gg \to H^* \to ZZ \to 4l$ (a) and $gg \to ZZ \to 2e2\mu$ where the Higgs boson contribution is included (b). Lower panels present ratios of BSM distributions ($c_6 \neq 0$) to the LO SM distribution ($c_6 = 0$).

While an appreciable change in the total cross-section is visible only for $c_6 \gtrsim 15$, the shape modification is clear in the ggF Higgs production process, while it is dampened as $ggZZ$ background and their interference are included in the analysis. More variables and results are shown in Appendix B.

4.5.3 Cross section comparison between MCFM8.0 and JHUGen-MCFM7.0

The second step in MC implementation and validation was encoding, of the matrix elements into the JHUGen-MCFM, enabling usage of the amplitudes within the larger-scope MELA framework. Each contribution to the BSM matrix element can be accessed and tested separately: Higgs boson production, propagation and decay.
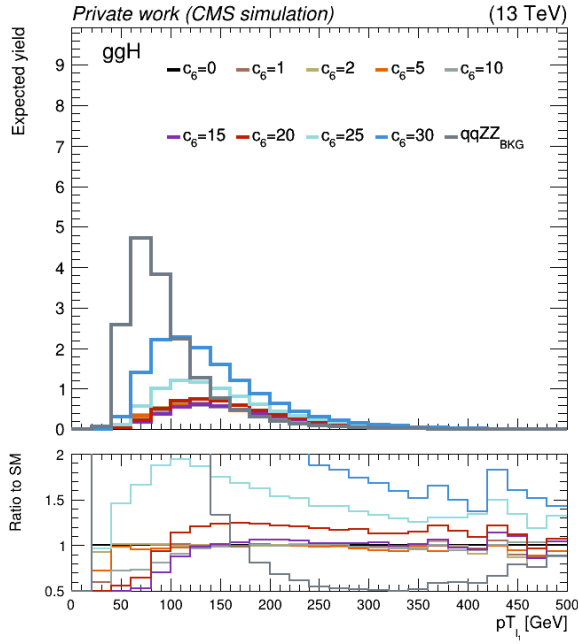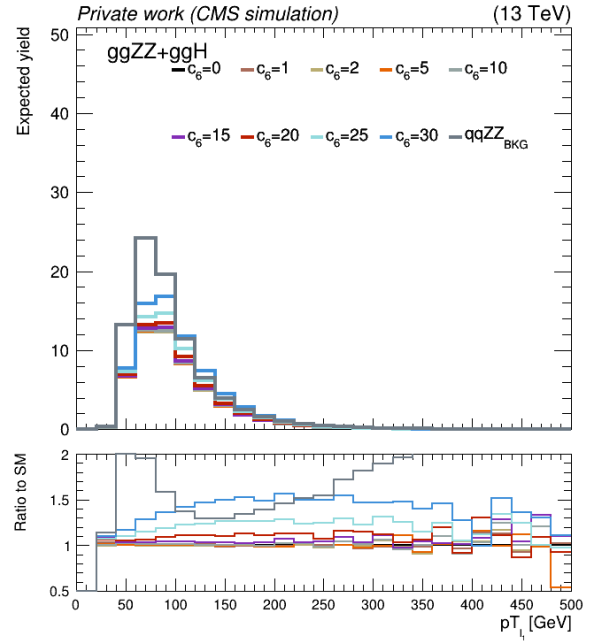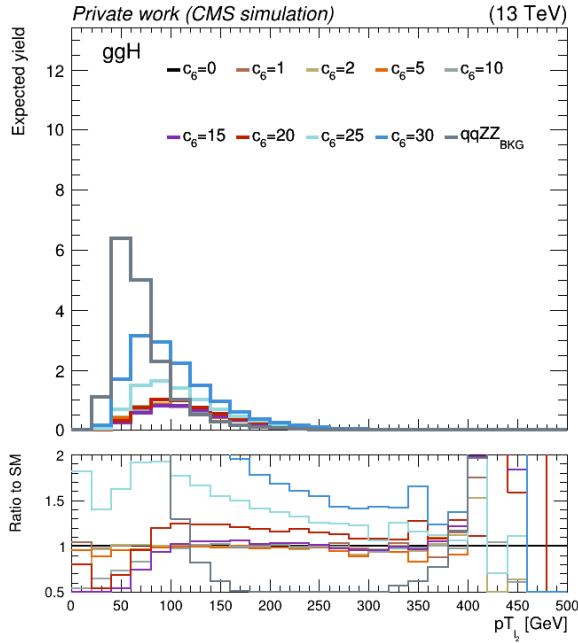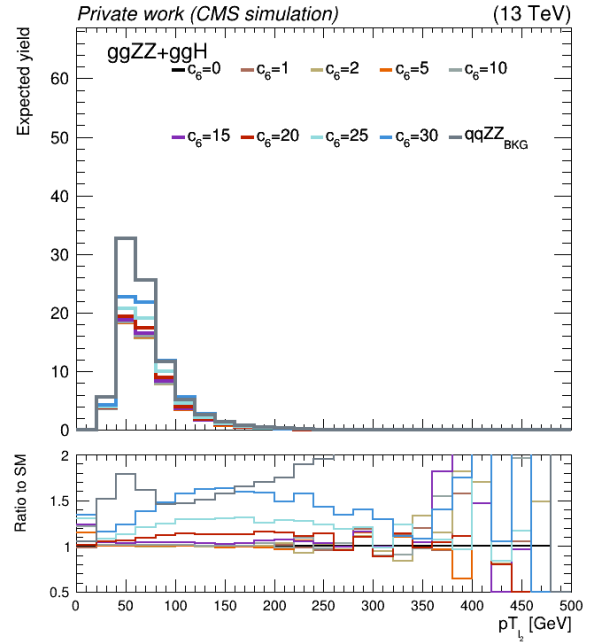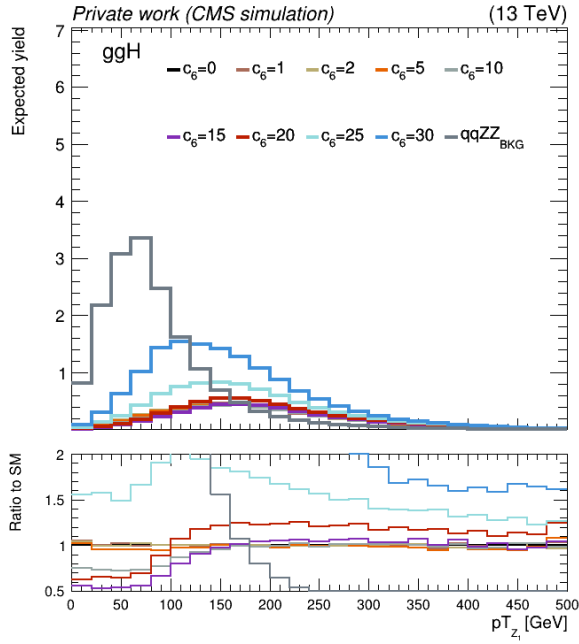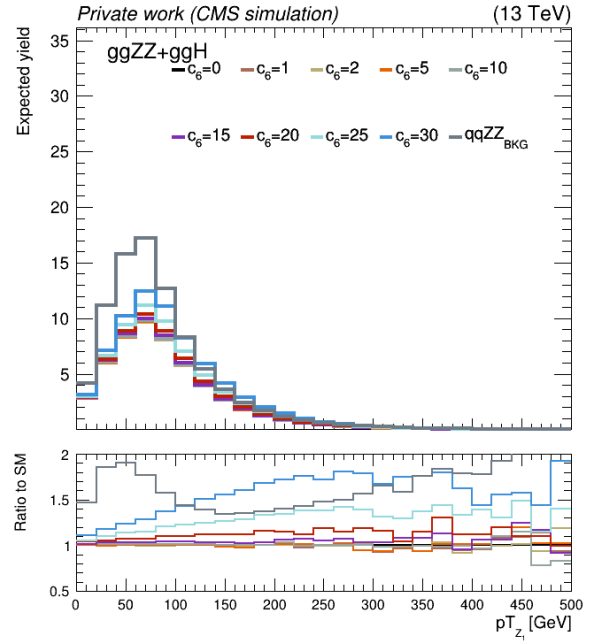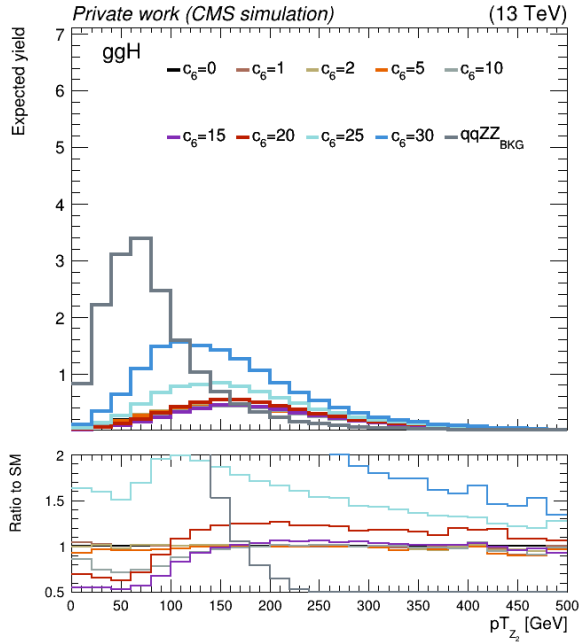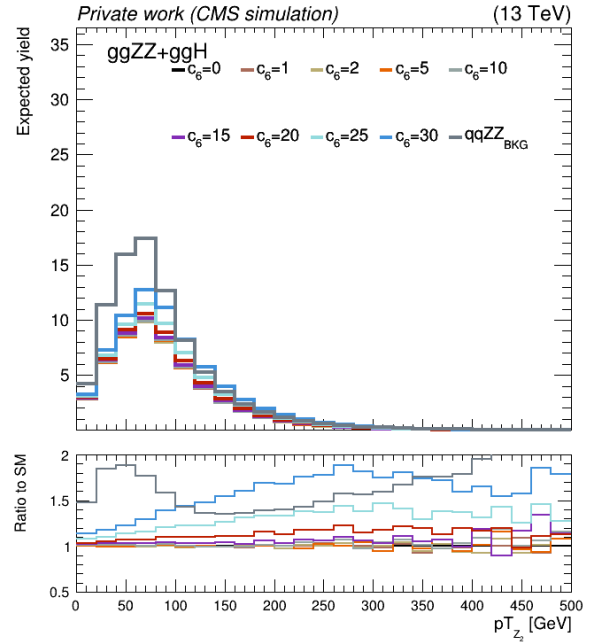
Figure 4.11. Reconstruction level $p_T(l_1)$ distributions for the processes $gg \rightarrow H^* \rightarrow ZZ \rightarrow 4l$ (a) and $gg \rightarrow ZZ \rightarrow 2e2\mu$ where the Higgs boson contribution is included (b). Lower panels present ratios of BSM distributions ($c_6 \neq 0$) to the LO SM distribution ($c_6 = 0$).

Figure 4.12. Reconstruction level $p_T(l_2)$ distributions for the processes $gg \rightarrow H^* \rightarrow ZZ \rightarrow 4l$ (a) and $gg \rightarrow ZZ \rightarrow 2e2\mu$ where the Higgs boson contribution is included (b). Lower panels present ratios of BSM distributions ($c_6 \neq 0$) to the LO SM distribution ($c_6 = 0$).

Figure 4.13. Reconstruction level $p_T(Z_1)$ distributions for the processes $gg \to H^* \to ZZ \to 4l$ (a) and $gg \to ZZ \to 2e2\mu$ where the Higgs boson contribution is included (b). Lower panels present ratios of BSM distributions ($c_6 \neq 0$) to the LO SM distribution ($c_6 = 0$).

Figure 4.14. Reconstruction level $p_T(Z_2)$ distributions for the processes $gg \to H^* \to ZZ \to 4l$ (a) and $gg \to ZZ \to 2e2\mu$ where the Higgs boson contribution is included (b). Lower panels present ratios of BSM distributions ($c_6 \neq 0$) to the LO SM distribution ($c_6 = 0$).

For validation purposes, each BSM contribution to the overall matrix element was turned on separately and the cross section was calculated for the process $gg \to ZZ \to 2e2\mu$ (including Higgs boson production $H^*_{\text{SM+BSM}}$ and the background). Selection cuts are different than in the previous subsection and entail $4\text{ GeV} < m_{2e/2\mu} < 13000\text{ GeV}$, $130\text{ GeV} < m_{4\ell} < 1000\text{ GeV}$, with the usage of the CTEQ6L1 [175] PDF set (internally available in MCFM). Focusing again on the off-shell, region, results of these calculations are presented in Table 4.5, where comparison between MCFM8.0 and JHUGen-MCFM can be seen. In these calculations the Higgs width was set to that of the SM and c_6 was set to 15.

Table 4.5. Contributions to cross section value for each BSM part of the matrix element calculated with MCFM8.0 and JHUGen-MCFM.

MCFM8.0				
BSM	Production	Propagation	Decay	All contributions
σ	70.3822 ± 0.0087 ab	177.317 ± 0.024 ab	71.3107 ± 0.0092 ab	86.922 ± 0.011 ab
JHUGen-MCFM				
σ	71.4484 ± 0.0082 ab	179.940 ± 0.021 ab	72.3839 ± 0.0083 ab	88.218 ± 0.012 ab

Comparing same BSM contribution between the two generators, as well as the SM cross section value, a slight discrepancy is found at the level of 1.5%. Nonetheless, the matrix element values were correctly retrieved and matched. The discrepancy is most likely attributed to compilers used, definition of SM parameters and their exact values between the two versions of the code, etc. and is anyway much smaller than theory uncertainties stemming e.g. from the choice of PDF sets or QCD renormalization and factorization scales. Taking this into account, it can be concluded that the BSM matrix elements were correctly propagated to JHUGen-MCFM, which allows for their further usage.

### 4.5.4 Testing of MELA reweighting features

With the BSM matrix elements available in MELA framework, a further testing of the reweighting feature itself was performed. As a base for reweighting, the $gg \to H^*_{\text{SM+BSM}} \to ZZ \to 2e2\mu$ ($c_6 = 25$) MC sample was chosen (generated with cuts reported in Table 4.4), reweighting it to the different BSM hypothesis (Figure 4.15(b)). Further, reweighted histograms were compared against MC data samples produced with MCFM8.0 (Figure 4.15(a)), comparing m_{4l} distributions to their counterparts, but also finding the ratio between two distributions for all given c_6 values. Such ratios are presented in Figure 4.15(c).

From Figure 4.15(c) it can be concluded that the reweighting of native hypothesis to itself gives the expected result of 1 across all bins. Apparent discrepancies are observed in the first bin, which can be attributed to the fact that the native hypothesis has a small number of events (Figure 4.15(a)). Past the 800 GeV value, statistical fluctuations due to low number of events again become relevant.

Another test was performed with MELA, whose goal was to reproduce the D_s distribution presented in Ref. [137]:

$$D_s = \log_{10}\left(\frac{P_h}{P_{gg} + c \cdot P_{q\bar{q}}}\right) \tag{4.34}$$

where P_h represents the squared ME for the $gg \to H^* \to ZZ \to 4l$ process, P_{gg} represents the squared ME for all gg-initiated channels (which includes the ggF Higgs boson production channel, $ggZZ$ background and their interference), $P_{q\bar{q}}$ is the squared ME for the $q\bar{q} \to ZZ \to 4l$ process

(a)

(b)

(c)
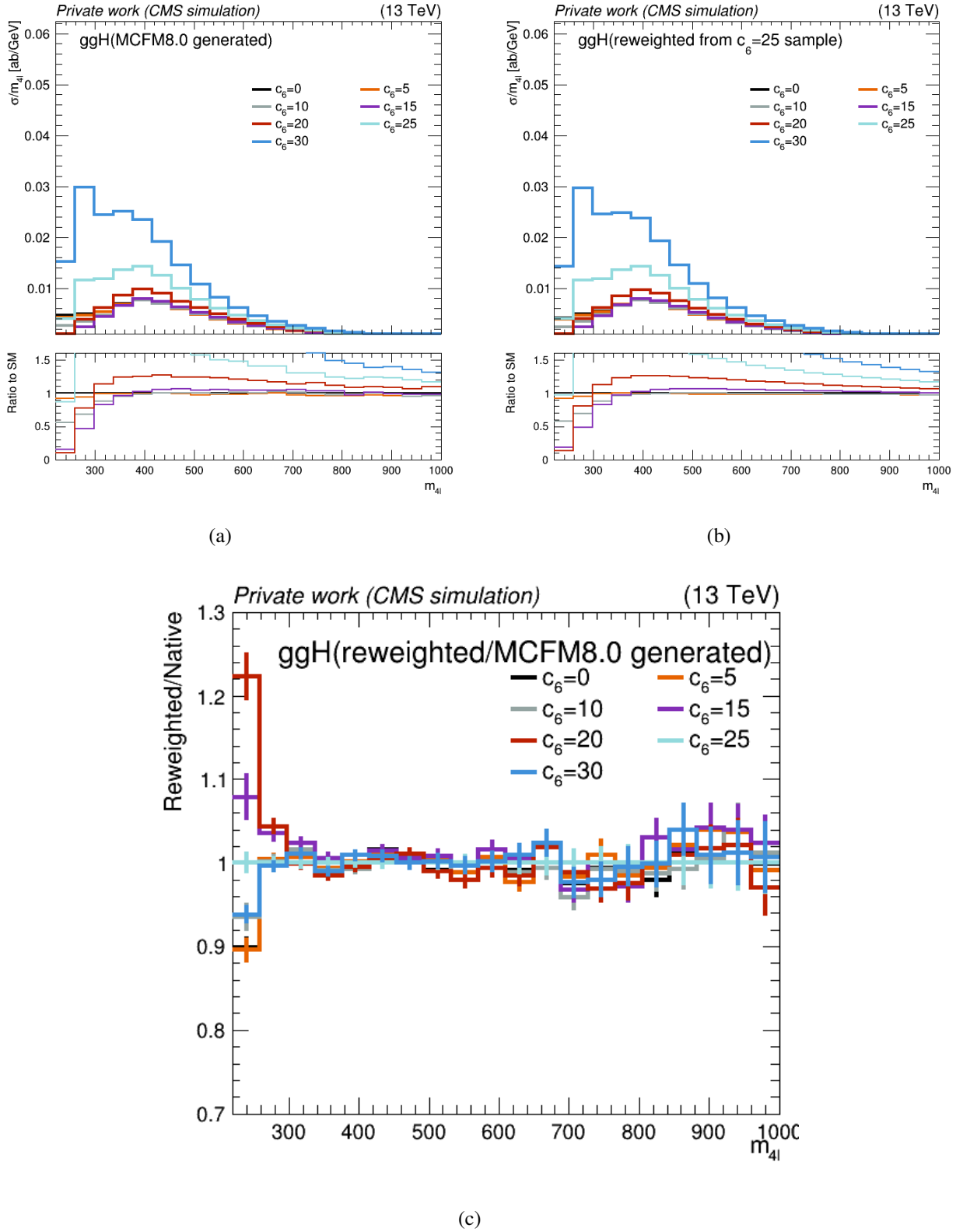
Figure 4.15. m_{4l} distributions and their ratio to the SM predicted distribution generated with MCFM8.0 (a), with reweighting (b) and the ration between the two approaches (c). Distributions show different c_6 hypotheses.

which is the dominant background to ggF, and constant c was set to 0.1, as reported in Ref. [137]. A

set of MC samples generated with MCFM8.0 for different values of c_6 was utilized. Using available matrix elements within MELA, the above mentioned matrix elements were calculated where c_6 was set to the value which was used in generation of a given sample. Results were compared to those of Ref. [137] and can be seen in Figure 4.16. It can be seen that the reproduced curves (Figure 4.16(a)) exhibit a similar behavior as the ones reported in Ref. [137] (Figure 4.16(a)). What is interesting to note is that, as the c_6 goes up in value, D_S starts shifting towards left of with respect to the SM case, after some value two peaks become evident and finally D_s start shifting towards right, where eventually the two peaks merge back into one.
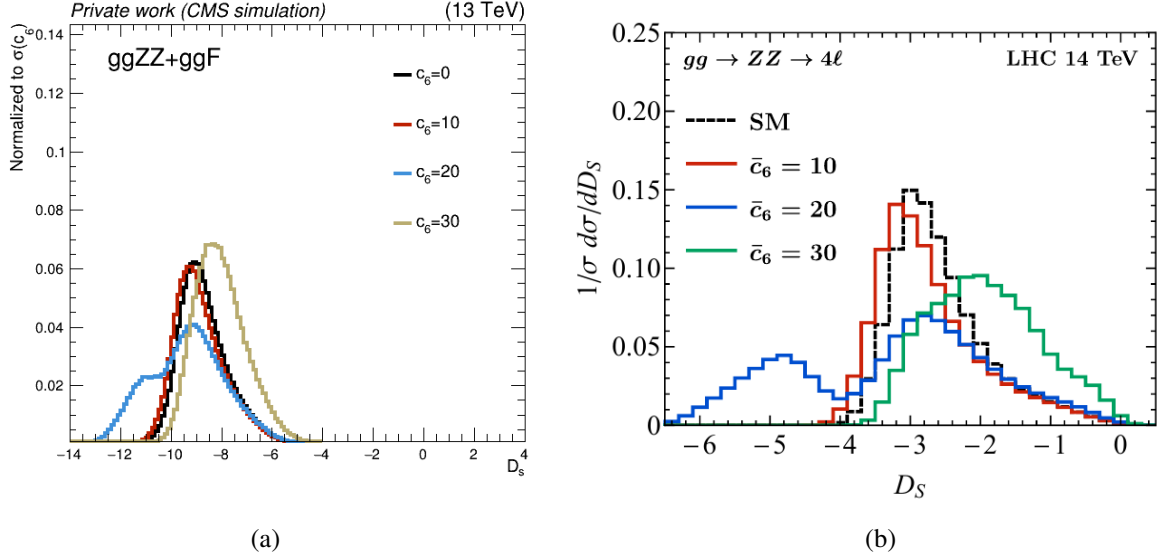
Figure 4.16. Generator-level D_s distributions for calculated for different c_6 hypothesis (a) and presented in Ref. [137]. The distributions were found for the process $gg \rightarrow ZZ \rightarrow 2e2\mu$ (Higgs-boson contribution included).

With an established theoretical, i.e. MC generator in a framework which includes effects of the dimension six operator $\mathcal{O}_6 = -\lambda|H|^6$, the Monte Carlo simulation infrastructure necessary for the measurement of c_6 (κ_λ) is set up.

Chapter 5

Measurements in the Higgs-boson-to-four-leptons benchmark decay channel

This chapter presents recent measurement of Higgs boson production and decay in the $H \rightarrow ZZ \rightarrow 4l$ channel, with emphasis on both on-shell and off-shell regimes of production. The $H \rightarrow ZZ \rightarrow 4l$ decay channel, often referred to as the golden channel, is of particular importance due to its exceptionally clean experimental signature, precise lepton reconstruction, and excellent mass resolution, which enables detailed studies of the Higgs boson properties and couplings.

Firstly an overview of the MATRIX computational framework which provides next-to-next-to-leading order (NNLO) predictions for the $pp \rightarrow ZZ$ process is presented. As this is the main irreducible background for the $H \rightarrow ZZ \rightarrow 4l$ and is therefore estimated from simulation, its precise estimation is a key ingredient for both on-shell and off-shell regimes of production. This work was entirely performed by the candidate.

The following sub-chapter describes the Run-3 measurements of inclusive and differential Higgs boson production cross sections in the on-shell $H \rightarrow ZZ \rightarrow 4l$ decay channel, based on the 2022 dataset collected by the CMS experiment. In this effort, the candidate was mainly involved in the definition and validation of simulated samples as well as in the $p_T(H)$ differential measurement.

Finally, the last sub-chapter reports results on how the Higgs boson self-coupling modifier κ_λ can be constrained through the off-shell Higgs boson production, where loop-induced effects offer indirect sensitivity to the Higgs boson self-coupling. These measurements need a larger amount of data, so the CMS Run-2 data are employed. They are the main topic of the candidate's PhD project.

5.1   NNLO diboson cross-section calculations using MATRIX

5.1.1   Introduction

The main background to the $H \rightarrow ZZ \rightarrow 4\ell$ channel is ZZ non-resonant production in p-p collisions. This is an irreducible background, featuring exactly the same final state as the signal, so it cannot be predicted from control regions in data and its estimate relies on simulation only. In general, as was the case with previous LHC's Runs (1 and 2), precise theoretical predictions for di-boson cross sections are of essential value for all Higgs-boson measurements. To this end, cross section for these production processes were calculated using state-of-the-art MC tools.

Starting with the Run 3, the p-p collision COM energy at LHC was increased to 13.6 TeV, so such

calculations need to be performed again. At the same time, more and more NNLO QCD calculations for colorless final states became available. The core tool of the calculation presented here is MATRIX ("Munich Automating qT subtraction and Resummation to Integrate X-sections") [176], a parton-level MC framework designed for high level precision fixed-order calculations of cross sections at the LHC. In particular, MATRIX allows for cross section calculation of $2 \to 1$, $2 \to 2$, and most recently $2 \to 3$ processes up to NNLO in QCD (+ ggNLO loop-induced) and NLO in EW perturbation theory. These processes include single Higgs boson or vector boson production ($pp/p\bar{p} \to H/W^{\pm}/Z$), vector boson pair production ($pp/p\bar{p} \to \gamma\gamma/Z\gamma/W^{\pm}\gamma/W^{\pm}/ZZ/W^{+}W^{-}$), on-shell top-pair production ($pp/p\bar{p} \to t\bar{t}$) and three-photon production ($pp/p\bar{p} \to \gamma\gamma\gamma$). Regarding the Z and $W^{\pm}$ bosons, all leptonic decay channels are included by accounting for all non-resonant and resonant diagrams, spin correlations and off-shell effects.

In the work presented here, using MATRIX versions v2.0.1 and v2.1.0., the $pp \to ZZ$ production cross section was computed in order to use it as a reference value for the 13.6 TeV $H \to ZZ \to 4\ell$ measurements. As this is useful for other studies in the CMS Collaboration, the cross-sections for the following processes were also calculated: $pp \to W^{\pm}$, $pp \to Z$, $pp \to W^{\pm}\gamma$, $pp \to Z\gamma$, $pp \to W^{+}W^{-}$, $pp \to W^{\pm}Z$, all with leptonic decays of $W^{\pm}$ and Z bosons.

5.1.2 Fixed order cross section calculation

MATRIX is built upon Munich ("MUlti-chaNnel Integrator at Swiss (CH) precision"), a parton-level MC integrator program which allows for computation of EW [177] and QCD [178] corrections at NLO accuracy for any SM process. Both tree-level and one-loop color- and spin-correlated amplitudes, which are a necessity for beyond LO calculation (QCD or EW), are provided via Open-Loops [179, 180]. OpenLoops relies on the Collier library [181, 182] for fast and stable tensor reduction, supported by CutTools [183] with OneLOop [184]. Employing the Catani–Seymour dipole subtraction method (for massless and massive partons) [185], to handle infrared (IR) divergences at NLO, the "Munich+OpenLoops" combination provides automated implementation of multi-channel MC integration which efficiently samples the phase space.

The computation of NNLO QCD cross sections requires evaluation of tree-level cross section with purely virtual contributions (two-loop amplitude), of one-loop contributions where one unresolved parton is present in the final state, and of tree-level amplitudes with up to two unresolved parton present in the final state. By incorporating the q_T-subtraction formalism [186] MATRIX framework is extended and reaches NNLO accuracy for cross section calculation of process with colorless final states. Two-loop amplitudes for off-shell massive vector-boson pair production [187] are sourced from the VVamp package [188].

Finally, MATRIX offers fiducial cuts for all final-state objects (jets, particles). In summary, MA-TRIX is a powerful tool enabling state-of-the-art fixed-order calculation of differential cross sections up to NNLO in QCD and up to NLO in EW for processes occurring at the LHC.

5.1.3 Combination of QCD and EW corrections

In a scenario where both EW and QCD corrections are large, mixed QCD-EW effects can become important. In general there are two ways to combine EW and QCD corrections. Based on the discussion in Ref. [189], *additive* and *multiplicative* schemes are considered here in order to estimate these higher-order effects. Firstly, higher-order effects are expressed by introducing a correction factor to the LO differential cross section $\mathrm{d}\sigma_{\mathrm{LO}}$:

$$d\sigma_{\mathrm{LO}} = d\sigma_{\mathrm{LO}}^{q\bar{q}} + d\sigma_{\mathrm{LO}}^{\gamma\gamma}, \tag{5.1}$$

where the first term denotes quark-induced processes and the second term denotes photon-photon induced processes. Higher-order QCD corrections are then written as:

$$d\sigma_{\mathrm{NNLO\_QCD}} = d\sigma_{\mathrm{LO}}\left(1 + \delta_{\mathrm{QCD}}\right) + d\sigma_{\mathrm{LO}}^{gg}, \tag{5.2}$$

where δ_{QCD} includes $q\bar{q}$, qg, $\bar{q}g$ channels at NLO QCD and gg and $q(\bar{q})q\prime$ channels at NNLO QCD, while $d\sigma_{\mathrm{LO}}^{gg}$ is the cross section of the loop-induced gg channel (which by itself is NLO in QCD) with LO correction applied to it (making it NNLO in QCD). Similarly, the NLO EW cross section can be written as

$$d\sigma_{\mathrm{NLO\_EW}} = d\sigma_{\mathrm{LO}}\left(1 + \delta_{\mathrm{EW}}\right), \tag{5.3}$$

where δ_{EW} accounts for all corrections in the $q\bar{q}$, $\gamma\gamma$ and $q\gamma$ (including $\bar{q}\gamma$ implicitly) channels.

The first prescription for combination of EW and QCD correction is a purely additive combination

$$d\sigma_{\mathrm{NNLO\_QCD+NLO\_EW}} = d\sigma_{\mathrm{LO}}\left(1 + \delta_{\mathrm{QCD}} + \delta_{\mathrm{EW}}\right) + d\sigma_{\mathrm{LO}}^{gg}, \tag{5.4}$$

where all terms of are simply summed.

In the other prescription, in order to approximate the effects of mixed QCD and EW higher-order corrections the EW correction factor is applied to the NNLO QCD cross section, with an exception of the loop-induced gg channel as the EW corrections are not applicable:

$$d\sigma_{\mathrm{NNLO\,QCD\times NLO\_EW}} = d\sigma_{\mathrm{LO}}\left(1 + \delta_{\mathrm{QCD}}\right)\left(1 + \delta_{\mathrm{EW}}\right) + d\sigma_{\mathrm{LO}}^{gg}. \tag{5.5}$$

Due to the how the EW corrections are applied to the NNLO QCD cross section, this scheme is known as the multiplicative scheme (in Ref. [189] denoted as factorized combination). The above expression can be rewritten in the form

$$d\sigma_{\mathrm{NNLO\,QCD\times NLO\_EW}} = d\sigma_{\mathrm{NNLO\,QCD+NLO\_EW}} + d\sigma_{\mathrm{LO}}\,\delta_{\mathrm{QCD}}\,\delta_{\mathrm{EW}}, \tag{5.6}$$

where it is easy to notice mixed QCD-EW corrections. If the dominant sources of EW and QCD are factorizable, the second term in Eq. (5.6) can be viewed as a fairly reasonable approximation of mixed QCD-EW effects.

With the additive and multiplicative schemes now defined, what remains is to set the notation for all cross section which were calculated and are presented in the subsection 5.1.5 and Appendix C:

- σ_{LO}: Cross section at leading order

- $\sigma_{\mathrm{NLO\_EW}}$: Cross section at NLO where first-order EW corrections are applied to σ_{LO}

- $\sigma_{\mathrm{NLO\_QCD}}$: Cross section at NLO where first-order QCD corrections are applied to σ_{LO}

- $\sigma_{\mathrm{NLO\_QCD+NLO\_EW}}$: Cross section at NLO where first-order QCD and EW corrections are applied additively to σ_{LO} (analogous to Eq. (5.4))

- $\sigma_{\mathrm{NLO\_QCD\times NLO\_EW}}$: Cross section at NLO where first-order QCD and EW corrections are applied multiplicatively to σ_{LO} (analogous to Eqs. (5.5) and (5.6))

- $\sigma_{\mathrm{LO\_gg}}$: Cross section of gg loop induced processes (NLO) where first-order QCD corrections are applied, making it a cross section at NNLO

- $\sigma_{\text{NLO\_gg}}$: Cross section of gg loop induced processes (NLO) where first- and second-order QCD corrections are applied, making it a cross section at NNNLO

- $\sigma_{\text{NNLO\_QCD}}$: Cross section at NNLO where first and second order QCD corrections are applied to σ_{LO} and then added with $\sigma_{\text{LO\_gg}}$ (if applicable)

- $\sigma_{\text{NNLO\_QCD+NLO\_EW}}$: Cross section at NNLO where first and second order QCD and first order EW corrections are applied additively to σ_{LO} (as in Eq. (5.4))

- $\sigma_{\text{NNLO\_QCD}\times\text{NLO\_EW}}$: Cross section at NNLO where first and second order QCD and first order EW corrections are applied multiplicatively to σ_{LO} (as in Eqs. (5.5) and (5.6))

- $\sigma_{\text{nNNLO\_QCD}}$: Cross section where first and second order QCD corrections are applied to σ_{LO} (NNLO) and then added with $\sigma_{\text{NLO\_gg}}$ if applicable

- $\sigma_{\text{nNNLO\_QCD+NLO\_EW}}$: Cross section where first and second order QCD and first order EW corrections are applied additively to σ_{LO} and then added with $\sigma_{\text{NLO\_gg}}$ (as in Eq. (5.4)) if applicable

- $\sigma_{\text{nNNLO\_QCD}\times\text{NLO\_EW}}$: Cross section where first and second order QCD and first order EW corrections are applied multiplicatively to σ_{LO} and then added with $\sigma_{\text{NLO\_gg}}$ (as in Eqs. (5.5) and (5.6)) if applicable

5.1.4   Running setup and process specific settings

Running cross section calculations up to NNLO in perturbation theory with MATRIX requires several external libraries and codes. These tools are: OpenLoops, which enables one-loop matrix element generation for a wide range of Standard Model processes; Collier which is a library for evaluation of one-loop integrals based on Denner–Dittmaier reduction techniques; CLN [190] and GiNaC [190] which are C++ libraries needed for the numerical evaluation of multivariate polynomials, algebras and special functions that appear in loop amplitudes; VVAMP which used for the computation of two-loop amplitudes (e.g. in diboson production).

One last crucial tool is the Les Houches Accord PDFs (LHAPDF) [191] which provides access to a number of results of different PDF-fitting groups, and as such it is viewed as a collection of PDF sets. In all of the cross section calculations presented below the version 6 of LHAPDF was used. The PDF set NNPDF31_nnlo_as_0118_luxqed [192] was used in the $pp \rightarrow ZZ$ validation described below. For cross section calculation at COM energy of $\sqrt{s} = 13.6$ TeV, depending on the process, two different PDF sets are used. In case of W^+W^- production ($pp \rightarrow e^-\mu^+\nu_\mu\bar{\nu}_e$ and $pp \rightarrow e^+e^-\nu_e\bar{\nu}_e$), owing to the top quark contamination, the 4 flavor scheme (4FS) ($m_b = 4.92$ GeV is non-vanishing) has the advantage as the bottom quark appears only in the final state. All partonic sub-processes with b quark in the final state are separately rendered finite due to b quark mass [193]. Thus, for W^+W^- production cross section calculation PDF set NNPDF31_nnlo_as_0118_nf_4_mc_hessian [194–196] was used, whilst for all other processes presented below PDF set NNPDF31_nnlo_as_0118_mc_hessian_pdfas [194–196] which employs 5FS ($m_b = 0$) was used. Throughout calculations photon induced contributions to the cross section are turned off.

MATRIX offers two modes of running the cross section calculation, cluster mode and multi-core mode. If running in cluster mode, the user has the option of choosing a batch service (cluster), then MATRIX will send sub-processes for integration to that specified cluster. Firstly, using the CMS collaboration's open-source environment of CMS SoftWare (CMSSW) [197] the MATRIX code was

compiled on the Linux Public Login User Service (LXPLUS) cluster, which is a file shared system. Then, a set of scripts which guide the proper execution of the MATRIX code were sent to CERN's batch service [198] based on HTCondor [199]. Here the user can request a machine with any number of cores, within reason, on which the code will be executed.

In case of all of the calculations, presented in the following subsection, the G_μ scheme [189] is employed alongside the complex-mass scheme where complex W- and Z-boson masses are used. Input widths and masses of particles are shown in Table 5.1.

Table 5.1. Values of widths and masses used in the G_μ scheme. The mass of the b quark is chosen based on whether a 4 flavor scheme (0) or 5 flavor scheme (4.92 GeV) is used. All fermions not explicitly mentioned in the table are treated as massless.

$$G_\mu = 1.16639 \times 10^{-5} \text{ GeV}^{-2}$$

$m_b = 0$ (4.92) GeV	$\Gamma_b = 0$
$m_t = 173.2$ GeV	$\Gamma_t = 1.44262$ GeV
$m_W = 80.385$ GeV	$\Gamma_W = 2.0854$ GeV
$m_Z = 91.1876$ GeV	$\Gamma_Z = 2.4952$ GeV
$m_H = 125$ GeV	$\Gamma_H = 4.07$ MeV

For all processes except for a single $W^\pm$ boson production, the CKM matrix is set to unity (see Ref. [189]). In that case of a single $W^\pm$ boson production the PDG SM values [200] are used. In case of the EW corrections to the $pp \to e^- \bar{\nu}_e$ and $pp \to e^+ \nu_e$, the one-loop diagrams with CKM matrix are not available within OpenLoops, hence only these one-loop EW corrections are approximated by employing a trivial CKM matrix, i.e. unity matrix.

5.1.5 Results

In order to validate the results obtained with MATRIX, a test run of calculating the production cross section for the process $pp \to ZZ$ was performed using MATRIX v.2.0.1. The setup follows from measurements of $pp \to ZZ$ production cross sections and constraints on anomalous triple gauge couplings at $\sqrt{s} = 13$ TeV [201]. Here well defined kinematic cuts were employed: di-lepton invariant mass was constrained to $60 \text{ GeV} < M_{\ell\ell} < 120$ GeV, mass of pair of any oppositely charged leptons was constrained to $m_{\ell^+\ell^-} > 4$ GeV and a requirement on lepton's transverse momentum was imposed $p_T^\ell > 5$ GeV. The last requirement is imposed due to the fact that leptons are treated as massless which leads to divergencies at low di-lepton mass. The PDF set NNPDF31_nnlo_as_0118_luxqed was used, as in Ref. [192], with the renormalization and factorization scales were set to $\mu_R = \mu_F = M_Z = 91.1876$ GeV. The rate of $Br(Z \to \ell^+\ell^-) = 0.03366$ [85] was used when extrapolating from $pp \to ZZ \to \ell^+\ell^-\ell'^+\ell'^-$ to $pp \to ZZ$. The $pp \to ZZ \to \ell^+\ell^-\ell'^+\ell'^-$ cross section was calculated according to the factorized cross section formula:

$$\mathrm{d}\sigma^{q\bar{q}}_{\text{NNLO\_QCD}\times\text{EW}} = \mathrm{d}\sigma^{q\bar{q}}_{\text{LO}}\left(1 + \delta^{q\bar{q}}_{\text{QCD}}\right)\left(1 + \delta^{q\bar{q}}_{\text{EW}}\right) + \mathrm{d}\sigma^{\gamma\gamma}_{\text{LO}}\left(1 + \delta^{\gamma\gamma/q\gamma}_{\text{EW}}\right) + \mathrm{d}\sigma^{gg}_{\text{NLO}} + \mathrm{d}\sigma^{aa}_{\text{NLO}}. \quad (5.7)$$

where $\delta^{q\bar{q}}_{EW}$ are corrections to the $q\bar{q}$ channel and $\delta^{q\bar{q}}_{QCD}$ is the same as δ_{QCD} in Eq. (5.2) but normalized to the $q\bar{q}$ channel LO cross section, and gg and $\gamma\gamma$ initiated contributions are applied additively. Results presented in Ref. [201] are shown in Figure 5.1. Validation results, which are compared to results of Ref. [201], are:

$$\sigma = 15.73^{+2.6\%}_{-2.5\%} \pm 0.08 \, \text{pb (at 13 TeV)}$$
$$\sigma = 17.05^{+3.0\%}_{-2.7\%} \pm 0.11 \, \text{pb (at 13.6 TeV)}$$

(5.8)
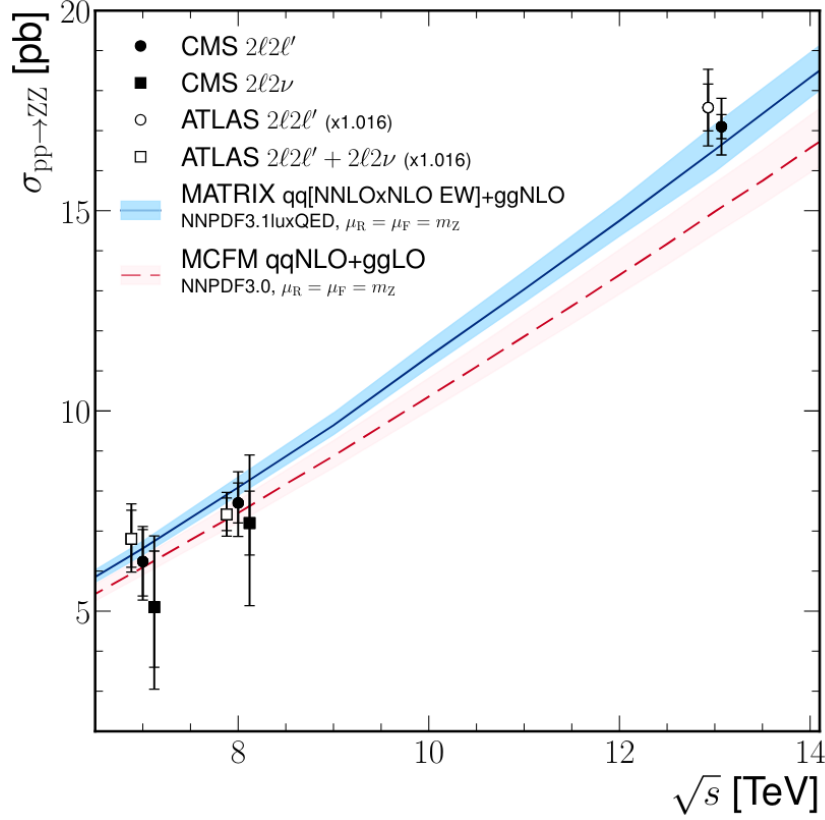
Figure 5.1. The total $pp \rightarrow ZZ$ cross section as a function of the proton-proton center-of-mass energy. The ATLAS measurements were performed with a slightly different M_Z mass window when compared to the measurement performed by the CMS, hence a correction factor of 1.6% is applied to account for the resulting difference in acceptance. The solid black line reflects MATRIX predictions, while the blue band around the MATRIX predictions reflects scale uncertainties. Measurements at the same COM energy were shifted slightly along the horizontal axis for clarity. Figure taken from [201].

A perfect match is not expected as, even though the same PDF set is employed between the two calculations, in Ref. [201] the envelope of all PDF replicas was taken, whilst here only the central replica of the PDF set was used. However, the numbers are in very good agreement, based on which can be concluded that the MATRIX setup works as expected and is reliable.

Cross sections for single vector boson V production ($V = W^{\pm}, Z$), vector boson plus photon production ($V\gamma$) and a vector bosons pair (VV) production have been calculated using two versions of MATRIX, MATRIX v.2.1.0 and v.2.0.1. Minimal kinematical cuts are selected and applied based on the MC production by the CMS collaboration. Each cross section value is obtained by taking the average value of a cross sections obtained with each of the PDF set replicas (103 for NPDF31_nnlo_as_0118_mc_hessian_pdfas, and 101 for NPDF31_nnlo_as_0118_nf_4_mc_hessian) and the PDF uncertainty is calculated as the standard deviation of the sample (the second one reported). The other, dominant, uncertainty estimates the impact of renormalization and factorization scales (the first one reported). It is found, for a fixed replica of the PDF set, as a envelope of seven-point scale variations, where both scales are independently varied of a factor 2 or 0.5 around a central

Table 5.2. Cross section values at different orders in perturbative expansion of QCD and EW and their combinations for $pp \rightarrow ZZ/W^+W^-$ production process at COM energy of 13.6 TeV

			Cross section values at 13.6 TeV [fb]		
σ_{ORDER}/process $pp \rightarrow$	$e^-\mu^-e^+\mu^+$	$e^-e^+e^-e^+$	$e^-e^+\nu_\mu\bar{\nu}_\mu$	$e^-\mu^+\nu_\mu\bar{\nu}_e$	$e^-e^+\nu_e\bar{\nu}_e$
σ_{LO}	$266.4^{+14.4\%}_{-14.6\%} \pm 0.2\%$	$120.2^{+12.0\%}_{-12.7\%} \pm 0.2\%$	$94.7^{+5.0\%}_{-5.9\%} \pm 0.1\%$	$1002^{+3.5\%}_{-4.3\%} \pm 0.1\%$	$1096^{+3.7\%}_{-4.4\%} \pm 0.1\%$
σ_{NLO_QCD}	$322.9^{+4.3\%}_{-7.1\%} \pm 0.3\%$	$144.8^{+3.6\%}_{-5.7\%} \pm 0.3\%$	$115.4^{+1.8\%}_{-2.2\%} \pm 0.2\%$	$1313^{+2.4\%}_{-2.0\%} \pm 0.1\%$	$1428^{+2.4\%}_{-2.0\%} \pm 0.1\%$
σ_{NLO_EW}	$262.9^{+14.6\%}_{-14.7\%} \pm 0.2\%$	$118.3^{+12.2\%}_{-12.8\%} \pm 0.2\%$	$93.3^{+5.2\%}_{-6.0\%} \pm 0.1\%$	$990.7^{+3.7\%}_{-4.4\%} \pm 0.1\%$	$1083^{+3.8\%}_{-4.5\%} \pm 0.1\%$
$\sigma_{NLO\_QCD+NLO\_EW}$	$319.4^{+4.3\%}_{-7.1\%} \pm 0.3\%$	$142.9^{+3.6\%}_{-5.7\%} \pm 0.3\%$	$114.0^{+1.8\%}_{-2.3\%} \pm 0.2\%$	$1303^{+2.4\%}_{-2.0\%} \pm 0.1\%$	$1415^{+2.4\%}_{-2.0\%} \pm 0.1\%$
$\sigma_{NLO\_QCD\times NLO\_EW}$	$318.7^{+4.4\%}_{-7.2\%} \pm 0.3\%$	$142.5^{+3.7\%}_{-5.8\%} \pm 0.3\%$	$113.7^{+1.9\%}_{-2.4\%} \pm 0.2\%$	$1299^{+2.4\%}_{-2.0\%} \pm 0.1\%$	$1411^{+2.4\%}_{-2.0\%} \pm 0.1\%$
σ_{NNLO_QCD}	$375^{+4.0\%}_{-5.0\%} \pm 0.9\%$	$160^{+2.6\%}_{-3.1\%} \pm 1.2\%$	$127.9^{+2.2\%}_{-1.9\%} \pm 0.6\%$	$1498^{+2.9\%}_{-2.5\%} \pm 0.9\%$	$1610^{+2.3\%}_{-2.0\%} \pm 0.7\%$
σ_{nNNLO_QCD}	$392^{+3.1\%}_{-4.5\%} \pm 0.9\%$	$166^{+2.7\%}_{-3.1\%} \pm 1.2\%$	$134.8^{+2.6\%}_{-2.3\%} \pm 0.6\%$	$1576^{+3.4\%}_{-2.9\%} \pm 0.8\%$	$1694^{+2.9\%}_{-2.5\%} \pm 0.7\%$
$\sigma_{nNNLO\_QCD+NLO\_EW}$	$388.6^{+3.1\%}_{-4.5\%} \pm 0.9\%$	$164^{+2.7\%}_{-3.0\%} \pm 1.2\%$	$133.3^{+2.7\%}_{-2.3\%} \pm 0.6\%$	$1565^{+3.5\%}_{-3.0\%} \pm 0.8\%$	$1681^{+3.0\%}_{-2.6\%} \pm 0.7\%$
$\sigma_{nNNLO\_QCD\times NLO\_EW}$	$387.0^{+3.1\%}_{-4.6\%} \pm 0.9\%$	$163^{+2.7\%}_{-3.2\%} \pm 1.2\%$	$132.7^{+2.6\%}_{-2.3\%} \pm 0.6\%$	$1559^{+3.4\%}_{-2.9\%} \pm 0.8\%$	$1674^{+2.9\%}_{-2.5\%} \pm 0.7\%$
σ_{LO_gg}	$27.3^{+32.7\%}_{-28.8\%} \pm 2.2\%$	$7.6^{+29.8\%}_{-21.8\%} \pm 0.6\%$	$6.9^{+21.7\%}_{-16.3\%} \pm 0.4\%$	$71.0^{+23.4\%}_{-17.2\%} \pm 0.7\%$	$75.9^{+23.3\%}_{-17.2\%} \pm 0.4\%$
σ_{NLO_gg}	$44.3^{+13.4\%}_{-16.1\%} \pm 4.1\%$	$13.3^{+18.3\%}_{-14.9\%} \pm 6.0\%$	$13.7^{+16.1\%}_{-13.1\%} \pm 1.4\%$	$150.7^{+18.4\%}_{-14.5\%} \pm 1.1\%$	$160.2^{+18.5\%}_{-14.5\%} \pm 0.8\%$

dynamic scale μ_0, where μ_0 was chosen as the transverse mass of the system. Throughout the calculation the photon induced processes were omitted from considerations.

Here the 4-lepton production cross section via ZZ/W^+W^- obtained using MATRIX v.2.1.0 is presented (Table 5.2), where only the cut on mass of opposite-sign-same-flavor lepton pair was imposed ($m_{\text{OSSF}} > 4$ GeV). From Table 5.2 it can be seen that the cross section for $pp \rightarrow e^-\mu^-e^+\mu^+$ production is about 2 times larger than the production cross section for $pp \rightarrow e^-e^+e^-e^+$, which is expected given identical particles and their permutations in the latter case. The third, fourth and fifth column are the cross section values for $pp \rightarrow ZZ$ (lepton flavor different than neutrino flavor), $pp \rightarrow W^+W^-$ (different leptonic decay between W bosons) and $pp \rightarrow ZZ/W^+W^-$ (same lepton flavor decay) respectively. It is important to stress out the importance of using 4FS in calculation of processes which include W^+W^- production as when 4FS is used the cross section is found to be around ~ 1500 fb compared to ~ 7500 fb in the 5FS case, as mentioned earlier.

One more important aspect of the calculation done here at different orders of perturbation theory is the possibility of calculating various K factors. These K factors are found as ratio of cross sections found in two consecutive orders of expansion in perturbation theory, e.g. $K_{\text{NLO}} = \sigma_{\text{NLO}}/\sigma_{\text{LO}}$. Usage of the K factors is helpful as they are applied as multiplicative factor (per bin, sometime dependent of a certain variable like mass) to generated distributions at a given order (e.g. m_{4l}) to bring them to a higher order.

The entire set of results obtained with the version MATRIX v.2.0.1 are presented in the Appendix C alongside the cross sections obtained with MATRIX v.2.1.0 for remainder of the processes. Comparing the results between the two releases of MATRIX it can be seen that MATRIX v2.1.0 exhibits better stability of calculation involving loops, and overall MATRIX offers cross section calculation at different orders of QCD and EW perturbative expansion where the uncertainty is governed majorly by variation of renormalization and factorization schemes in order to asses uncertainty associated to omission of higher-order effects.

There are a few notes to consider here if one wants to compare the cross section value obtained with MATRIX (for example for production of $W^+W^- \rightarrow l\nu l\nu$) to the one obtained with a different NLO MC generator, e.g. POWHEG. One would have to multiply the cross section value obtained with

MATRIX by an appropriate factor (in case of $W^+W^- \to l\nu l\nu$ this factor is 9, which accounts for all $l\nu l\nu$ combinations), as MATRIX does the calculation for just one flavor combination (as presented in Table C.10). Another important remark here is that the resonant production of a Higgs boson is included in the MATRIX calculation (where applicable), which gives slightly higher cross section value than if produced without inclusion of diagrams where a Higgs boson appears.

Overall MATRIX is a powerful state-of-the art MC tool for cross section calculation. Results obtained with MATRIX at COM energy of 13.6 TeV are used as a reference value for measurements and other theoretical predictions within the CMS collaboration, and as such they were subject to discussion and comparison to values obtained using different MC tools where an agreement was observed.

5.2 Measurements of Higgs boson fiducial cross sections at 13.6 TeV

Before studying the small off-shell effects affecting the tail of the $H^* \to ZZ \to 4l$ distribution, overall compatibility tests of the on-shell Higgs boson cross-section with the SM have been performed.

Here the Run-3 fiducial measurements are presented. Fiducial cross-section measurements are largely model-independent because they probe the production kinematics within a phase space that closely matches the experimental acceptance. Both ATLAS and CMS collaborations have measured the inclusive and fiducial cross section of $pp \to H \to ZZ \to 4l$ ($l = e, \mu$) at COM energy of $7, 8$ and 13 TeV [87, 88, 110, 202–204]. With the increase of COM energy to 13.6 TeV, the fiducial cross sections have to be measured again to further scrutinize the SM predictions.

5.2.1 Introduction

The first measurement of the Higgs boson production cross section in the four-lepton channel at a COM energy of 13.6 TeV using early Run 3 data collected by the CMS detector in 2022 is shown. Collected data correspond to an integrated luminosity of 34.7 fb^{-1} [205]. The analysis summarized here follows Ref. [206], where the details of the analysis can be found. The analysis is based on optimized methods that were developed for previous studies of the Higgs boson properties in the final state with four leptons [87, 88, 110]. The cross section values are obtained by performing an unbinned maximum likelihood fit to the observed four-lepton invariant mass distribution.

5.2.2 Data and MC samples

The dataset used in the analysis corresponds to proton–proton collisions delivered by the LHC and recorded by the CMS detector in 2022 [205].

Processes which contribute the most to the Higgs boson production at the LHC (see Section 3.3.1), i.e. ggF, VBF, VH, $t\bar{t}$H were simulated at NLO in QCD using POWHEG 2.0 [207–209]. Gluon-gluon fusion processes [210] were simulated including quark-mass effects [211], while simulation of remaining processes is based on work presented in the following Refs. for VBF [211], VH [212] and $t\bar{t}$H [213]. These processes are considered the signal processes in the analysis. In case of ggF simulated events, a dedicated weight was applied to each event in order to match the differential cross section at NNLO in QCD including parton shower matching (NNLOPS) [214] as a function of p_T^H and the jet multiplicity. The decay part, i.e. $H \to ZZ \to 4l$ is modeled with JHUGEN 7.0.2 [169–173].

All signal samples are generated with NNPDF_3.1_NNLO PDFs [194–196] and are normalized to the cross section values at $\sqrt{s} = 13.6$ TeV provided by the LHC Higgs Working Group [215].

For backgrounds two components have to be considered, irreducible and reducible ones. Irreducible background is a type of background which has the same final state as the process studied. Two processes contribute to irreducible background, ZZ production via quark-antiquark annihilation ($q\bar{q} \rightarrow ZZ$) and non-resonant gluon-gluon production ($gg \rightarrow ZZ$). The $q\bar{q} \rightarrow ZZ$ processes are modeled at NLO in QCD with POWHEG 2.0 [216] and, relying on computations of the NNLO cross sections (see previous section), are scaled to NNLO in QCD by a mass dependent $K(m_{ZZ})$ factor. A further factor which accounts for NLO EW corrections, based on calculation presented in Ref. [217], is applied as a function of m_{ZZ}. The $gg \rightarrow ZZ$ background samples were generated at LO using MCFM 7.0.1 [165–168]. Relying on soft-collinear approximation [218], the background and interference cross sections can be described equally well as signal. Therefore, based on work presented in Refs. [219–221], the same K factors for $gg \rightarrow H \rightarrow ZZ$ signal process and $gg \rightarrow ZZ$ background process are used. These K factors are approximately inherited from a previous analysis at $\sqrt{s} = 13$ TeV [222].

To simulate the parton showering and hadronization effects, the MC generators used are interfaced with PYTHIA 8.230 [223] using the CP5 underlying event tune [224]. Further, the CMS detector effects are subsequently simulated with GEANT4 [225, 226] and events are then reconstructed using the standard CMS reconstruction algorithm.

An additional component of the background is considered. This components stems from production of Z boson with associated jets, i.e. Z + jets. Jets or hadron decay products may be misreconstructed as leptons. Contribution of the reducible background is estimated from data based on a control-region method [110].

5.2.3 Event reconstruction and selection

The strategy for selection of events of interest closely follow that of Run 1 dataset analysis [99, 101] and Run 2 dataset analysis [110, 222, 227, 228], on which the presentation here is based on. Full explanation of the event reconstruction is given in Ref. [206].

Online selection is performed based on di-electron, di-muon and electron-muon HLT, but also based on triggers which require three leptons or a single lepton, where the trigger efficiency is determined as in Ref. [110]. All candidates events are constrained to have charged leptons which pass loose identification and isolation requirements [23, 229].

Muons within $|\eta| < 2.4$ and with transverse momentum $p_T > 5$ GeV are reconstructed by matching silicon-tracker tracks to muon chamber tracks [23]. Loose requirements are imposed on both tracker and muon-system tracks, and compatibility with small calorimeter deposits is taken into account. To discriminate between Z boson decay muons and hadron decay muons a relative isolation is constrained to $\mathcal{I}^\mu < 0.35$ [206].

Electrons within $|\eta| < 2.5$ and with transverse momentum $p_T > 7$ GeV are reconstructed by matching calorimeter cluster deposits to tracks, with identification performed using boosted-decision-tree [206].

Final State Radiation (FSR) photons, when selected, are used in invariant mass of the final state computations. PF photons within $|\eta| < 2.4$ are considered FSR photons if their transverse momentum satisfies $p_T > 2$ GeV and if their relative isolation is $\mathcal{I}^\gamma < 1.8$ [206]. Each photon is associated to the nearest lepton and is discarded if $\Delta R(\gamma, l)/(P_T^\gamma)^2 > 0.012$ GeV^{-2} and $\Delta R(\gamma, l) > 0.5$ where for a given lepton FSR photon with the minimal value of $\Delta R(\gamma, l)/(p_T^\gamma)^2$ is selected.

To suppress non-prompt leptons from hadron decays and photon conversions, the three-dimensional

impact-parameter significance with respect to the PV is required to be < 4.

The selection targets $H \to ZZ \to 4l$ decays with at least four well-identified and isolated leptons. The Z boson candidates are constructed from Opposite-Sign-Same-Flavor (OSSF) lepton pairs with a requirement on the invariant mass $12 < m_{ll} < 120$ GeV. The Z boson candidate with the mass closest to the nominal Z boson mass [230] is referred to as Z_1 whilst the other is referred to as Z_2 and they are combined to built the ZZ candidate.

Further requirements are imposed on the ZZ candidate in order to improve the sensitivity to the Higgs boson decays. All leptons pairs must satisfy $\Delta R(l_i, l_j) > 0.02$, the invariant mass of the Z_1 candidate is constrained to be $m_{Z_1} > 40$ GeV, all selected events must contain two leptons with $p_T > 10$ GeV and at least one lepton with $p_T > 20$ GeV. Related to $4e$ and 4μ channels specifically, the same leptons can be used for alternative pairing and hence to build alternative Z boson candidates, named $Z_a Z_b$ candidates. In the case of these categories, events are discarded if $m_{Z_b} < 12$ GeV and $|m_{Z_a} - m_Z| < |m_{Z_b} - m_Z|$. This removes events that originate from on-shell Z boson and a low-mass resonance decay. Further, the invariant mass of any oppositely charged lepton pair irrespective of the flavor is constrained to be $m_{l^+ l'^-} > 4$ GeV.

Lastly, the event is retained if the invariant mass of the four lepton final state system satisfies $m_{4l} > 70$ GeV. In case if more ZZ candidates satisfy the selection criteria the one with the higher $p_T(Z_2)$ is retained.

The fiducial phase space is defined so as to closely match the detector acceptance defined by the reconstruction-level selection. Definition of the fiducial phase space is adopted from previous analysis [110, 222], and is summarized in Table 5.3. Generator-level leptons are obtained by combining leptons with FSR photons, i.e. their four-momentum is combined, found within the cone of radius $\Delta R(\gamma, l) = 0.3$. Neutrinos, FSR and leptons are not considered when calculating the isolation sum in order to enhance the model independence of the measurement [88]. Electrons and muons originating from decays of tau leptons or hadrons are not included in the definition of the fiducial phase space region.

Table 5.3. Requirements used in the definition of the fiducial phase space for the $pp \to H \to ZZ \to 4l$ cross section measurement. Table taken from Ref. [87].

Lepton kinematics and isolation	
Leading lepton p_T	> 20 GeV
Next-to-leading lepton p_T	> 10 GeV
Additional electrons (muons) p_T	> 7 (5) GeV
Pseudorapidity of electrons (muons)	$|\eta| < 2.5$ (2.4)
p_T sum within $\Delta R < 0.3$ of each lepton	$< 0.35\, p_T^\ell$
Event topology	
At least two same-flavor, opposite-charge lepton pairs	
Inv. mass of the Z_1 candidate	$40 < m(Z_1) < 120$ GeV
Inv. mass of the Z_2 candidate	$12 < m(Z_2) < 120$ GeV
Distance between selected four leptons	$\Delta R(\ell_i, \ell_j) > 0.02$ for any $i \neq j$
Inv. mass of any opposite-sign lepton pair	$m(\ell^+ \ell'^-) > 4$ GeV
Inv. mass of the selected four leptons	$105 < m_{4\ell} < 160$ GeV
The selected four leptons must originate from the $H \to 4\ell$ decay	

5.2.4 Measurement strategy

The fiducial cross section is extracted from an unbinned maximum likelihood fit to the observed invariant four lepton mass distribution. For a given observable and for a given final state f, the

expected number of events in bin i can be written as:

$$N_{\text{obs}}^{i,f}(m_{4\ell}) = \sum_{j}^{\text{genBin}} \epsilon_{i,j}^{f} \left(1 + f_{\text{nonfid}}^{f,i}\right) \sigma_{\text{fid}}^{f,j} \mathcal{L} \mathcal{P}_{\text{res}}(m_{4l}) + N_{\text{nonres}}^{f,i} \mathcal{P}_{\text{nonres}}(m_{4l}) + N_{\text{bkg}}^{f,i} \mathcal{P}_{\text{bkg}}(m_{4l}), \quad (5.9)$$

where $\mathcal{P}_{\text{res}}(m_{4l})$, $\mathcal{P}_{\text{nonres}}(m_{4l})$, $\mathcal{P}_{\text{bkg}}(m_{4l})$ are probability density functions (pdf) corresponding to resonant, nonresonant and background contribution respectively. It is assumed that resonant fiducial signal and resonant nonfiducial signal obey the same probability density function.

Signal pdfs are are modeled in the following way. The resonant signal pdf, $\mathcal{P}_{\text{res}}(m_{4l})$, is modeled with a Double-sided Crystall Ball (DCB) function [231–233]. Parameters of the DCB are obtained from a fit of the m_{4l} distributions that correspond to a different of m_H in the range of $105 - 160$ GeV. This way the parameters of the fit retain dependence on the Higgs boson mass. This pdf is scaled by fiducial cross section and integrated luminosity $\mathcal{L}$. Pdfs of nonresonant signal is modeled with a Landau distribution. The reducible and irreducible background contributions are included as binned templates.

The resonant nonfiducial events originate from outside of fiducial phase space, but satisfy the selection criteria due to detector effects. This contribution is accounted for by introducing $f_{\text{nonfid}}^{f,i}$ parameter for each bin i and final state f. This parameter is estimated from simulated events. To take into account detector effects, i.e. the smearing (due to finite resolution) of generator-level observables (i.e. what is produced), the response matrix $\epsilon_{i,j}^{f}$ is introduced. The purpose of the response matrix is to unfold the number of expected events in bin i at the reconstruction-level to the number of expected events in bin j at the fiducial level. The terms $N_{\text{nonres}}^{f,i}(m_{4l})$ and $N_{\text{bkg}}^{f,i}(m_{4l})$ represent contributions to the overall number of observed events. The former encompasses events with more than four leptons coming from WH, ZH and $t\bar{t}H$ processes where one of the leptons originating from the Higgs boson decay is not selected or is lost, whilst the latter takes into account reducible and irreducible background contribution. The parameter of interest is the fiducial cross $\sigma_{\text{fid}}^{f,j}$ section in bin j, which is extracted from the fit.

The measurement is restricted to events inside the analysis fiducial phase space. Fiducial cross section is determined with the asymptotic approach [234] using a test statistic based on the profile likelihood ratio [235], whilst the systematic uncertainties enter the likelihood as nuisance parameters. All three categories , i.e. final states $(4e, 4\mu, 2e2\mu)$, and all bins of observables are fitted concurrently, where two additional parameters are included to regulate the mixture of different final states. These two parameters are left floating in the fit in order to increase the model independence of the measurement, as was previously implemented in Ref. [87,110]. To tackle the detector effects which introduce smearing of the generator-level observables, a likelihood-based unfolding is performed, which allows for simultaneous unfolding and extraction of the fiducial cross section [236].

Systematic uncertainties are closely related to those discussed in Ref. [87], and have been re-assessed to reflect the working performances of CMS detector during the year 2022, except for the K factors. Experimental uncertainties include uncertainty on integrated luminosity of the 2022 data taking period, uncertainty related to trigger performance, lepton reconstruction and selection, uncertainties related to lepton momentum scale and smearing are estimated, and also uncertainty due to background modeling. Theoretical uncertainties are related to the choice of PDFs, renormalization and factorization scales and K factors. The most pronounced uncertainty is relate to electron momentum scale, resolution, reconstruction and selection. All of the mentioned uncertainties are discussed in Ref. [206].

5.2.5 Results

The invariant mass distribution of the four lepton final state system is shown in Figure 5.2. The fiducial cross section is obtained by fitting Eq. (5.9) to the data, and for a Higgs boson mass of $m_H = 125.38$ GeV is:

$$\sigma_{\text{fid}} = 2.89^{+0.53}_{-0.49} \, (\text{stat})^{+0.29}_{-0.21} \, (\text{syst}) \, \text{fb}. \tag{5.10}$$

Results of fitting Eq. (5.9) to the data show good agreement with the SM prediction which is obtained by multiplying the cross section for the ggF production of the Higgs boson [86] and the branching ratio for the studied process [86] with the acceptance (ratio of event within fiducial phase space to the total number of signal events):

$$\sigma_{\text{expected}} = \sigma(pp \to H) \times Br(H \to ZZ \to 4l) \times \mathcal{A} = 3.09^{+0.27}_{-0.24} \, \text{fb}. \tag{5.11}$$
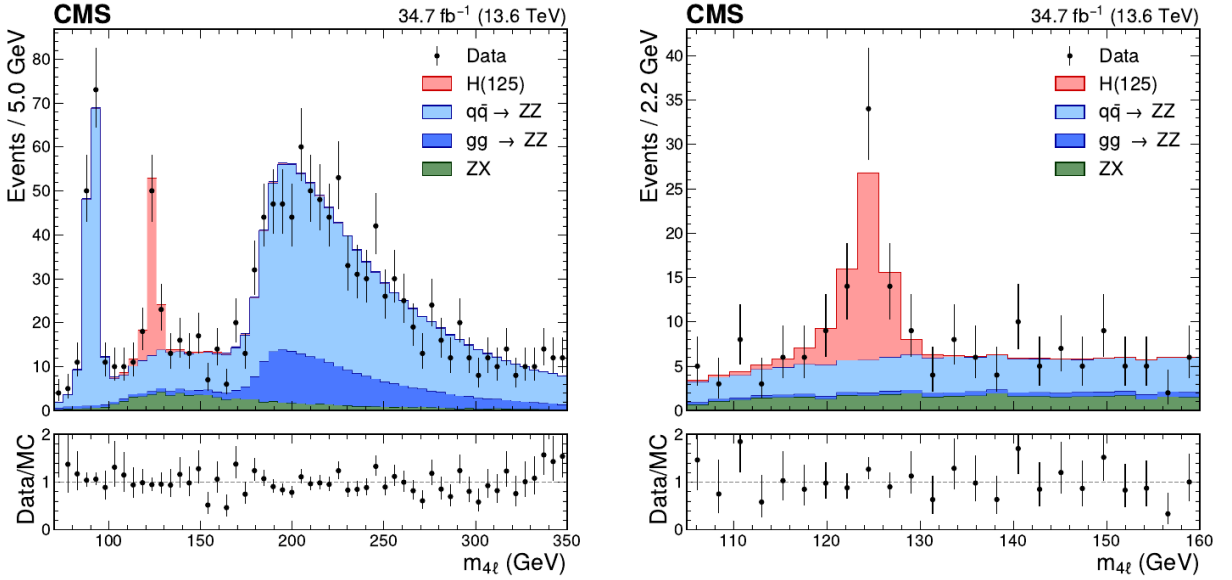
Figure 5.2. Distribution of the m_{4l} invariant mass in the ranges $70 - 350$ GeV (left), and $105 - 160$ GeV (right). The black points with error bars represent the data. The colored histograms show the signal (red histogram) and the background contributions. The post-fit normalization for all the processes is obtained from the measurement performed in the range $105 < m_{4l} < 160$ GeV. The bottom panels depict the ratio of the data to the post-fit MC distribution. Figure taken from Ref. [206].

Results of differential fiducial cross section measurements are presented and discussed in Ref. [206].

5.3 Higgs boson self-coupling analysis

5.3.1 Introduction

As discussed in Section 4, the Higgs boson self-coupling was probed directly and indirectly, but so far without exploring the off-shell regime of production. The main topic of the study present here is the Higgs boson self-coupling measurement in the $H \to ZZ \to 4l$ channel in the off-shell region. Measurements as such inherit a lot of infrastructure from the previous measurement of Higgs boson properties in the four lepton decay channel (including the off-shell regime of production) [98, 104,

105, 110, 222, 227, 228]. This includes MC samples and modeling, event selection, categorization and consideration regarding the systematic uncertainties. Here a general description of the infrastructure is given, while for more details it is advised to visit the most recent measurement of Higgs boson mass and width measurement [98].

5.3.2 Datasets and MC modeling

The dataset used in the analysis corresponds to the proton-proton collision delivered by LHC and recorded by the CMS detector during Run-2 data taking period that lasted in the period 2016-2018. Integrated luminosities collected per year are 36.3 fb^{-1} collected in 2016, 41.5 fb^{-1} collected in 2017 and 59.7 fb^{-1} collected in 2018. This brings to a total integrated luminosity, during the Run 2 data taking period at a proton-proton COM energy of 13 TeV, of 138 fb^{-1}.

Monte Carlo simulation is used to model signal processes, which involve the Higgs boson, and background processes in pp interactions at the LHC and their reconstruction in the CMS detector. Except for the different COM, most samples share the same configuration as in Section 5.2.2. Off-shell EW and ggF samples have a specific configuration following the studies performed in Chapter 4.

The JHUGEN 7.3.0 generator LO framework is used for modeling the vector boson scattering and triple-gauge-boson (VVV) background processes, the EW signal processes (VBF, VH) with either SM or anomalous couplings, and their interference, while relying on the MCFM matrix element for background processes. The SM simulation of the EW processes is also validated with the PHANTOM 1.3 [237] simulation. As NLO corrections are expected to be small, this simulation is used in its native form.

The inclusion of gluon-gluon fusion signal processes, with either SM or anomalous couplings, and its interference with the background is also included within the JHUGEN framework. The factorization and renormalization scales are chosen to be running as $m_{4l}/2$. In order to include higher order QCD corrections, LO, NLO, NNLO signal cross section calculations are performed using the MCFM and HNNLO 2 programs [186, 238, 239] for a wide range of Higgs masses, using a narrow width approximation. The NNLO K factors are used to reweight [86] the m_{4l} distributions from the MCFM and JHUGEN simulation at LO in QCD, and a uniform factor of 1.10 across all of the m_{4l} range is applied to normalize the cross section of the Higgs boson production via gluon fusion to the predictions for $m_{4l} \approx 125$ GeV at next-to-NNLO (N^{3}LO) in QCD [86]. In addition, gluon fusion production is simulated with the POWHEG 2 event generator at NLO in QCD. The simulated m_{4l} shapes or yields obtained from the POWHEG simulation of the gluon fusion process are corrected based on the above reweighted distributions.

While the NNLO K factor calculation is directly applicable to the signal contribution, it is approximate for the background and its interference with the signal. The NLO calculation with some approximations [219, 240–242] is available for the background and interference. Comparison with this calculation shows that while there is some increase of the NLO K factor for the interference close to the ZZ threshold, the NLO K factors for the background and interference are consistent with the signal within approximately 10% in the mass range $m_{4l} > 220$ GeV relevant for this analysis. Therefore, the background and interference contributions are multiplied by the same NNLO K factor and uniform N^{3}LO correction, both calculated for signal and including associated uncertainties, and introduce an additional unit factor with a 10% uncertainty for the background and the square root of this factor for the interference.

Cross-feed from on-shell to off-shell region is studied, i.e. whether there is a contribution to the overall off-shell yield stemming from on-shell production. The dominant process is the on-shell $Z(ll)H(2l + X)$ production which can end up reconstructed in the off-shell region. Estimation of the

cross-feed shows that $(ZH, H \rightarrow WW/ZZ)$ contributes to the overall yield with ~ 6.5 events.

The above mentioned samples, including the anomalous κ_λ couplings, were generated for a dedicated study and were repurposed by utilizing MELA package, i.e. the generated events were reweighted to fit the requirements of this analysis, thus saving time and resources in generation of a entirely new set of events (see Chapter 4 for details).

5.3.3 Event reconstruction and selection

The event selection, although similar to that of Section 5.2.3, is given here due to difference coming from the fact that the kinematic of on- and off-shell events is different.

As the events of interest are characterized by the presence of four leptons in the final state, a dedicated triggers are used for selection. Namely, the main triggers for the Run 2 dataset analysis are focused on selecting either a pair of electrons or muons, or an electron and a muon, which pass loose identification and isolation criteria. The transverse momentum (p_T) of the leading electron (muon) is required to be larger than 23 GeV (17 GeV), while that of the sub-leading lepton is required to be larger than 12 GeV (8 GeV). In order to maximize the signal acceptance additional trigger are used. One of these triggers requires presence of three leptons with lower p_T thresholds and no isolation requirements. Also, triggers based on isolated single-electron and single-muon with thresholds of 27 GeV and 22 GeV in 2016, and 35 GeV and 27 GeV in 2017 and 2018 is used. The overall trigger efficiency for simulated signal events that pass the full selection is larger than 99%.

Event reconstruction is based on the PF algorithm [13] which exploits information from all the CMS sub-detectors to identify and reconstruct individual particles in the event.

Electrons (muons) are reconstructed within the geometrical acceptance defined by a requirement on the pseudorapidity $|\eta| < 2.5$ ($|\eta| < 2.4$) and $p_T > 7$ GeV (5 GeV). The reconstruction algorithm combines information from both the tracker and the ECAL (muon system). Muons are selected by applying minimal requirements on the tracks reconstructed in muon system and the inner tracker system, and by considering the compatibility of tracks with small energy deposits in the calorimeters. In order to discriminate between Z boson decays and hadron decays, an isolation variable is calculated for electron and muons [110]. For muons an isolation requirement is constrained to $\mathcal{I}^\mu < 0.35$, while for electrons it is used to build a multivariate discriminant [110]. This discriminant includes observables sensitive to the presence of bremsstrahlung along the electron trajectory, the geometrical and momentum-energy matching between the electron trajectory and the associated cluster in the ECAL, the shape of the electromagnetic shower in the ECAL, and variables that discriminate against electrons originating from photon conversions. This discriminant also includes the isolation to suppress electrons originating from EW decays of hadrons within jets.

A dedicated algorithm is used to collect the final-state radiation of leptons [222]. Final State Radiation (FSR) photons, when selected, are used in invariant mass of the final state computations. PF photons within $|\eta| < 2.4$ are considered FSR photons if their transverse momentum satisfies $p_T > 2$ GeV and if their relative isolation is $\mathcal{I}^\gamma < 1.8$ [206]. Each photon is associated to the nearest lepton and is discarded if $\Delta R(\gamma, l)/(P_T^\gamma)^2 > 0.012$ GeV^{-2} and $\Delta R(\gamma, l) > 0.5$ where for a given lepton FSR photon with the minimal value of $\Delta R(\gamma, l)/(p_T^\gamma)^2$ is selected.

The jets are clustered using the anti-k_T jet clustering algorithm [28] with a distance parameter of 0.4. The jet momentum is determined as the vector sum of all particle momenta in the jet. Jets must satisfy $p_T > 30$ GeV and $|\eta| < 4.7$ and must be separated from all selected lepton candidates and any selected final-state radiation photons with a requirement on the distance parameter $\Delta R(\ell/\gamma, \text{jet}) > 0.4$, where $(\Delta R)^2 = (\Delta \eta)^2 + (\Delta \phi)^2$. Jets are b-tagged using the DeepCSV algorithm [243], which combines information about impact parameter significance, the secondary vertex, and jet kinematics.

The primary proton-proton interaction vertex is the reconstructed vertex with the largest value of p_T^2 summed over all jets clustered using anti-k_T jet clustering algorithm with the single tracks and associated missing transverse momentum (taken as the negative vector p_T sum of assigned jets) assigned to candidate vertices as inputs.

To suppress non-prompt leptons from hadron decays and photon conversions, the three-dimensional impact-parameter significance with respect to the PV is required to be < 4.

The selection targets $H \rightarrow ZZ \rightarrow 4l$ decays with at least four well-identified and isolated leptons, where three mutually exclusive final states are defined based on the lepton falvor: $2e2\mu$, $4e$, 4μ. The Z boson candidates are constructed from Opposite-Sign-Same-Flavor (OSSF) lepton pairs with a requirement on the invariant mass $12 < m_{ll} < 120$ GeV. The Z boson candidate with the mass closest to the nominal Z boson mass [230] is referred to as Z_1 whilst the other is referred to as Z_2 and they are combined to built the ZZ candidate. Further requirements are imposed on the ZZ candidate in order to improve the sensitivity to the Higgs boson decays. The invariant mass of the Z_1 candidate is constrained to be $m_{Z_1} > 40$ GeV, all selected events must contain two leptons with $p_T > 10$ GeV and at least one lepton with $p_T > 20$ GeV. Further, the invariant mass of any oppositely charged lepton pair irrespective of the flavor is constrained to be $m_{l^+l'^-} > 4$ GeV.

The off-shell region is in the following defined as $m_{4l} > 220$ GeV.

5.3.4 Event categorization and discriminants

Following the test of c_6 effects across a set of variables (including D_s) as discussed in Chapter 4, an optimal discriminant building is discussed here.

When considering the Higgs boson decay $H \rightarrow ZZ \rightarrow 4l$ there are 8 observables in total that fully characterize the event kinematics, as described in [169–171]. These 8 observables are $\vec{\Omega}^{H\rightarrow 4l} = \{\theta^*, \theta_1, \theta_2, \Phi, \Phi_1, m_{Z_1}, m_{Z_2}, m_{4l}\}$, with the angles being depicted in Figure 5.3 (right). The θ^* angle is defined in the rest frame of the Higgs boson as the angle between the beam axis and the direction of the Z_1 candidate. Angles Φ and Φ_1 are the azimuthal angles between the three planes constructed from the Higgs boson decay products and the decay products of the two Z bosons in the Higgs boson rest frame. The angles θ_1 and θ_2 are defined in the Z_1 and Z_2 rest frames, respectively, as the angles between the Z boson direction in the Higgs boson rest frame and the direction of the negative decay lepton. Considering the associated Higgs boson production (VBF and VH), there are 5 additional kinematical variables which define the process, namely the production side of the process $\vec{\Omega}^{H+jj} = \{\theta_1^{VBF}, \theta_2^{VBF}, \Phi^{VBF}, q_1^{2,VBF}, q_2^{2,VBF}\}$ (analogously for VH). These additional variables are shown in in blue (angels) and brown (q) in Figure 5.3 for VBF (left) and VH (middle) production modes.

It was seen in Section 4.5.2 and in Appendix B that there are some variables that exhibit shape changes as the c_6 coefficient changes value. Further, the D_s discriminant was tested, replicating well behavior reported in Ref. [137]. Although the study showed that D_s discriminant can be replicated, it was decided not to use it, as a discriminant agnostic to c_6 value is needed to properly probe modifications of the Higgs boson self-coupling.

Therefore, to fully exploit the event kinematics and discriminate between SM and BSM Higgs boson production, first several categorization discriminants are constructed. Categorization closely follows that of Ref. [98].

For each category, discriminants are constructed, which enables for optimal discrimination between signal and alternative hypothesis (for example background) within a given category. These discriminants utilize Higgs boson decay products kinematics generally denoted as $\vec{\Omega}$ and/or kinematics of Higgs boson production in association with two jets ($\vec{\Omega}^{H+jj}$). Utilizing the MELA framework, the mentioned discriminants are constructed, in a general sense, as follows:
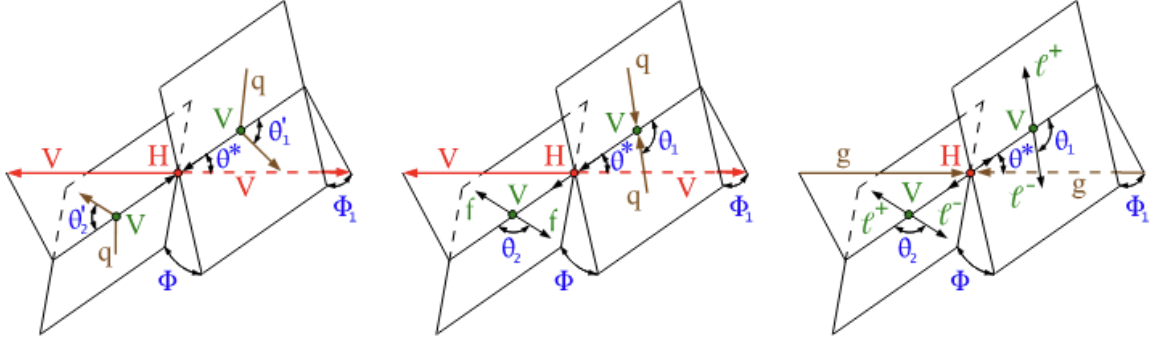
Figure 5.3. Three main processes of Higgs boson production. On the left a VBF $qq \rightarrow VV(qq) \rightarrow H(qq) \rightarrow VV(qq)$ is shown. In the middle associated production $qq \rightarrow V^* \rightarrow VH \rightarrow (\bar{f}f)H \rightarrow (\bar{f}f)VV$ is shown. On the right ggF $gg \rightarrow H \rightarrow VV \rightarrow 4l$ is shown. Initial state particles are shown in brown, the intermediate vector bosons (V) and their decay products are shown in green, whilst the Higgs boson and the vector bosons to which it decays to are shown in red. The angles that define the kinematics are shown in blue. Figure taken from Ref. [87].

$$\mathcal{D}_{\text{alt}}\left(\vec{\Omega}\right) = \frac{\mathcal{P}_{\text{sig}}\left(\vec{\Omega}\right)}{\mathcal{P}_{\text{sig}}\left(\vec{\Omega}\right) + \mathcal{P}_{\text{alt}}\left(\vec{\Omega}\right)}, \tag{5.12}$$

and

$$\mathcal{D}_{\text{int}}\left(\vec{\Omega}\right) = \frac{\mathcal{P}_{\text{int}}\left(\vec{\Omega}\right)}{2\sqrt{\mathcal{P}_{\text{sig}}\left(\vec{\Omega}\right)\,\mathcal{P}_{\text{alt}}\left(\vec{\Omega}\right)}}, \tag{5.13}$$

where $\mathcal{P}_{\text{alt}}$ is the probability that an event originates from an alternative scenario (alternative Higgs boson production mechanism, for example background or BSM processes), $\mathcal{P}_{\text{sig}}$ is the probability that an event originates from the process of interest (signal process) and $\mathcal{P}_{\text{int}}$ calculates the interference between the two models.

Based on Eq. (5.12) three discriminants are constructed: $\mathcal{D}_{\text{2jet}}^{\text{VBF}}$, $\mathcal{D}_{\text{2jet}}^{\text{WH}}$ and $\mathcal{D}_{\text{2jet}}^{\text{ZH}}$ which are defined as follows. In the the VBF (VH, $V = W, Z$) discriminant, $\mathcal{P}_{\text{sig}}$ is the signal probability for VBF (VH) production hypothesis, whilst the $\mathcal{P}_{\text{alt}}$ corresponds to probability of Higgs boson production in association with two jets via gluon-gluon fusion. In cases when more than two jets pass the selection criteria, two jets with the highest p_T are used in matrix element calculation. Thus, these three discriminants separate the VBF and VH production from ggF production using only the kinematics of Higgs boson and associated jets. Based on these discriminants, selected events are grouped into three categories:

- *VBF-2jet category*: Exactly four leptons must be present in the event. Additionally two or three jets must be present out of which one jet at most is a b-tagged jet, or four jets must be present where none is b-tagged jet [110]. Such event is categorized as VBF-2jet event if $\mathcal{D}_{\text{2jet}}^{\text{VBF}} > 0.5$ [110],

- *VH hadronic category*: Exactly four leptons must be present in the event. Additionally two or three jets must be present out of which no jets are b-tagged, or four jets must be present where none is a b-tagged jet. Such event is retained based on the selection criteria $\max(\mathcal{D}_{\text{2jet}}^{\text{VH}}, \mathcal{D}_{\text{2jet}}^{\text{VH}}) > 0.5$ [110].

- *Untagged category* is comprised of the remaining events.

Within each category, three discriminating variables are used to discriminate against the unwanted background contributions, $\{m_{4l}, \mathcal{D}_{bkg}, \mathcal{D}_{int}\}$. The two discriminants $\mathcal{D}_{bkg}$ and $\mathcal{D}_{int}$ are constructed differently based on the category under which the events fall. In case of VBF- and VH-tagged category, $\mathcal{P}_{bkg}$ represents the probability for EW and QCD background $4l + 2j$ processes, whilst $\mathcal{P}_{sig}$ represents the probability of the signal EW production for a given process (VBF or VH). These two probabilities are calculated using four-lepton and associated -jets kinematics. On the other hand in the untagged category, $\mathcal{P}_{bkg}$ is calculated for the dominant background process $q\bar{q} \to 4l$, where the signal and background probabilities are calculated for a given invariant mass of the four lepton final state system. Lastly, the discriminant $\mathcal{D}_{int}$ is calculated for a signal and background processes and it represents their interference. In the untagged category kinematics of the decay side of the process are used, whilst in the VBF- and VH-tagged category kinematics of production in association with two jets is used. Using $\mathcal{D}_{bkg}$ and $\mathcal{D}_{int}$, another matrix element based discriminant is constructed, nLD (non-Local Discriminant). It s constructed by convoluting $\mathcal{D}_{bkg}$ and $\mathcal{D}_{int}$. Resulting distributions, of m_{4l} (zoomed x-axis range) and nLD, are shown in Figures 5.4, 5.5, 5.6 for untagged, VBF tagged and VH tagged category, respectively. Background processes are shown in black, and they include ggZZ, qqZZ, VBS and $Z + X$ background processes. The SM LO signal process is shown in red, and it is entails ggF, EW and $t\bar{t}H$ production. The interference contribution, depicted in green, corresponds to the sum of the interference between LO ggF and ggZZ, and between LO electroweak production and VBS. Dashed lines indicate the effect of different values of κ_λ. It can be seen that the the discriminants provide discriminative power as shape changes are observed in the distributions. Fits performed on the data are 2-dimensional fits based on m_{4l} and nLD.

(a) (b)
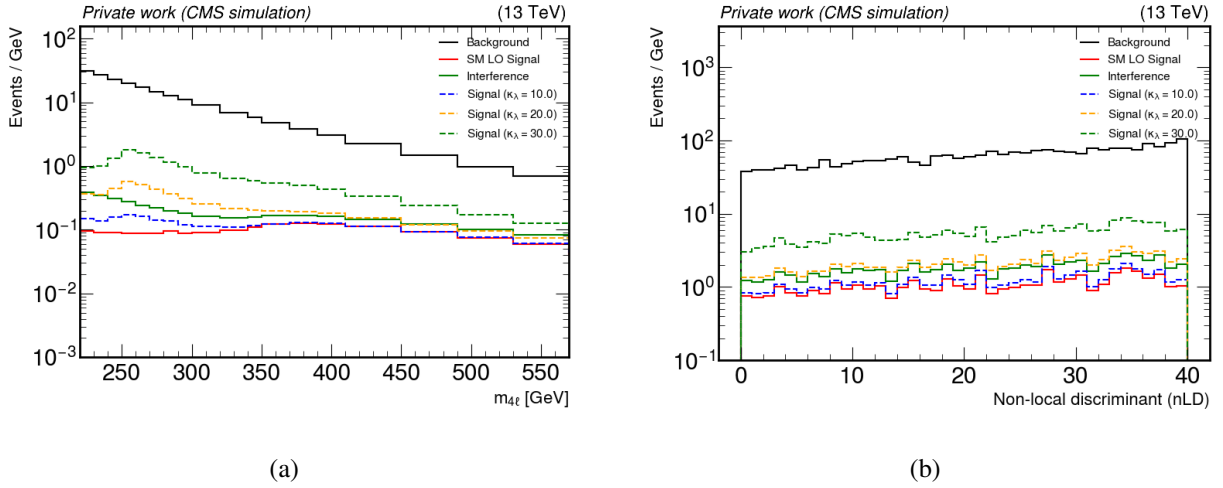
Figure 5.4. Distributions of m_{4l} (a) and nLD (b) show for SM LO signal, background, interference and for $\kappa_\lambda = 10, 20, 30$, for the untagged category. Courtesy of Andro Petković and his work.

5.3.5 Systematic uncertainties

Systematic uncertainties are classified into two categories, theoretical and experimental uncertainties. Template shapes are varied in each event category, while for sources that do not depend on m_{4l}, event kinematics or other quantities that are event-specific, normalization uncertainties are assigned.
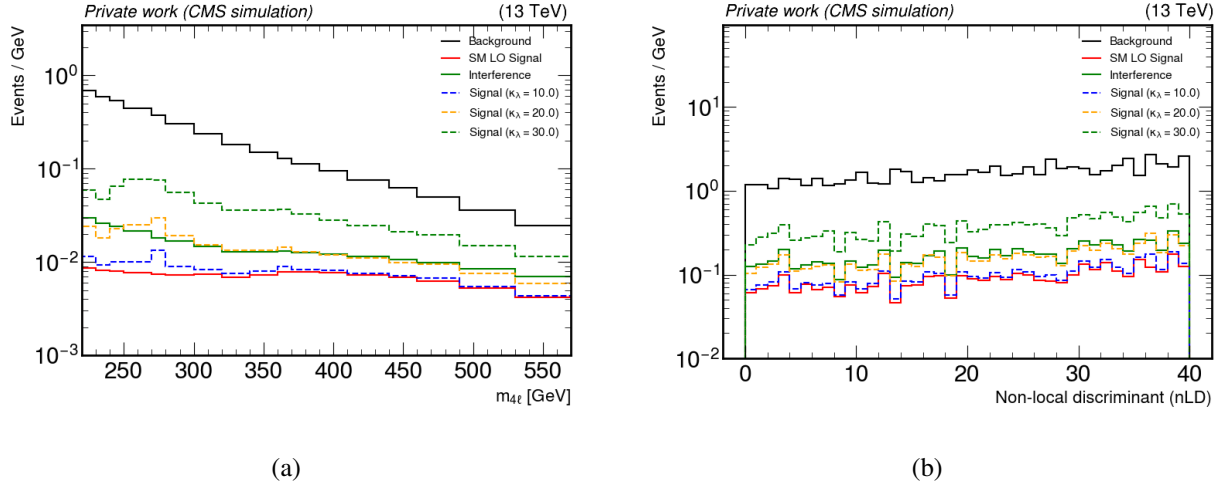
Figure 5.5. Distributions of m_{4l} (a) and nLD (b) show for SM LO signal, background, interference and for $\kappa_\lambda = 10, 20, 30$, for the VBF category. Courtesy of Andro Petković and his work.
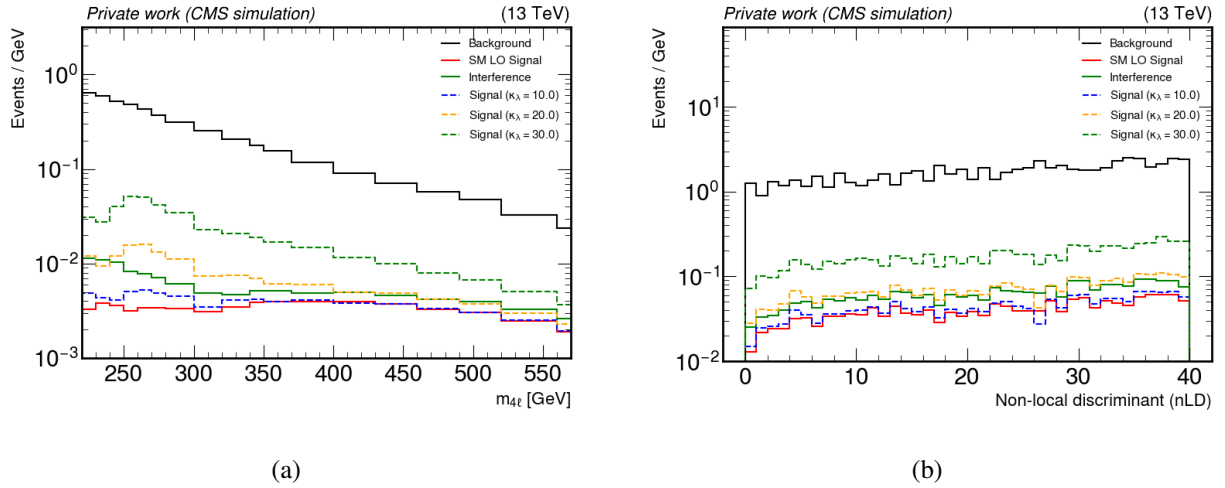
Figure 5.6. Distributions of m_{4l} (a) and nLD (b) show for SM LO signal, background, interference and for $\kappa_\lambda = 10, 20, 30$, for the VH category. Courtesy of Andro Petković and his work.

Theoretical uncertainties

A number of sources of theoretical uncertainty affect the yield, categorization of events and shapes of distributions of observables.

Uncertainties related to the applied K factors are extracted and applied to the signal processes. This includes both the QCD renormalization and factorization scales, α_s and PDF uncertainties. Beyond the impact on the total yield via K factors, also the shapes and yields per category are affected and the shape systematics is included in the analysis to account for the mentioned effects. Applied K factor to the $ggZZ$ background process introduces a 10% normalization uncertainty. The dominant background process $q\bar{q} \to 4l$ features an uncertainty due to applied NLO EW corrections to the simulation [244] and this is the dominant systematic uncertainty. Uncertainties related to renormalization and factorization scales are accounted for by varying the central scale by a factor of 2 or $1/2$, then the shape systematics are applied by considering alternative templates which include these variations.

Usage of PDFs also introduces uncertainty in the measurements, and it is evaluated by taking the envelope of 100 different PDF replicas (i.e. variations).

Considering PYTHIA, signal and interfering background processes can vary in terms of the multiplicity and kinematics of associated jets due to the hadronization scale and the underlying event variations (PYTHIA tune). PYTHIA scale uncertainties are estimated relying on the POWHEG high mass ggF sample. In case of EW Higgs boson production processes, scale uncertainty is extracted based on the JHUGen off-shell samples. Due to the observed weak dependence on variations a normalization systematics is assigned. Effects of PYTHIA UE tune are assessed by using samples with varied PYTHIA tunes for each category. For ggF production mode, the uncertainty was found the be up to 1%. For EW production mode, using on-shell samples it was found that the uncertainty is at most 2 % for the VH-tagged category.

Experimental uncertainties

The analysis focuses on Run 2 data taking period, with the three distinct four lepton final states. These final states are merged across all three data taking periods (2016, 2017, 2018), merging also the data taking periods. Luminosity is found to contribute 2.6% to the total systematic uncertainty.

Lepton reconstruction and identification efficiency uncertainties are included as normalization uncertainties. The uncertainties from each year and for each final state are combined into inclusive electron and muon reconstruction efficiency uncertainties. It was found that in case of electrons the reconstruction and identification efficiency uncertainty is 6.4%, whilst for muons it was found to be around 1%. Lepton energy resolution uncertainties were not considered as their impact on m_{4l} shape and width measurement is negligible.

As categorization relies also on jets, the jet uncertainties have to be considered. Related to jet reconstruction uncertainties, three sources are studied. These are jet energy and scale resolution, and the b-tagging efficiency. Up and down variational templates are constructed by considering alternative calculation of the categorization discriminants, for the observable discriminants and for the jet veto that considers number of b-tagged jets.

5.3.6 Statistical model

Keeping in mind the usage of binned templates, a specific statistical model is used, the *binned likelihood template model* (see Ref. [245] for deeper understanding of statistical methods and modeling).

Regarding the uncertainties, there are two prominent effects that may affect the measurement, i.e. two types of uncertainties. They are normalizations uncertainty and shape uncertainty. Shape uncertainties are included in measurement by constructing additional set of templates, i.e. the up and down variations of the original template, then the interpolation between them is done to assess the impact of the given shape uncertainty [246]. To parameterize the normalization uncertainties, a log-normal distribution is employed (instead of a Gaussian distribution). The general form of a log-normal distribution is give as:

$$p(x) = \frac{1}{\sqrt{2\pi}\ln k}\frac{1}{x}\exp\Big(-\frac{(\ln(x/x_m))^2}{x(\ln k)^2}\Big), \tag{5.14}$$

where x is an arbitrary variable whose logarithm is distributed with a mean $\ln x_m$ and with a standard deviation of $\ln k$. The log-normal distribution is used to model the impact of nuisance parameters (i.e. not those of interest) θ, and ensures a positive-definite normalization.

As the model employed is a binned template model, the per-bin yield is modeled with the Poisson distribution:

$$P_{\text{Poisson}} = \frac{\lambda^k e^{-\lambda}}{k!}, \tag{5.15}$$

where k is the observed and λ is the expected number of events.

Using these two distributions, a likelihood function is constructed:

$$\mathcal{L}(\kappa_\lambda, \vec{\theta}) = \prod_j \frac{\lambda_j^{k_j}(\kappa_\lambda, \mu) e^{-\lambda_j(\kappa_\lambda, \mu)}}{k_j!} \times P(\vec{\theta}), \tag{5.16}$$

where the expected number of events per bin depends on the Higgs boson self-coupling modifier and the signal strength μ, $\lambda_j(\kappa_\lambda, \mu)$, with the product running over each bin j, and k_j represents the observed number of events in the j-th bin of the template:

$$\lambda_j(\kappa_\lambda, \mu) = \left[\sum_i \mu_i f_i(\kappa_\lambda) H_i \right]_j. \tag{5.17}$$

Here the templates H_i are scaled differently based on whether the template corresponds to the SM signal case, BSM case, or else. In case of SM signal templates, it is scaled by signal strength μ. The BSM templates, containing $\mathcal{O}(\lambda)$ corrections, are scaled by polynomial functions $f_i(\kappa_\lambda)$ based on which corrections the template refers to (see next section). All remaining templates are scaled by 1. All of the nuisance parameters $\vec{\theta}$ are encompassed in a log-normal based distribution $P(\vec{\theta})$.

The fit is based on minimizing the negative log-likelihood function:

$$-2\Delta \ln \mathcal{L}(\kappa_\lambda) = -2 \ln \frac{\mathcal{L}(\kappa_\lambda, \hat{\hat{\vec{\theta}}})}{\mathcal{L}(\hat{\kappa_\lambda}, \hat{\vec{\theta}})}, \tag{5.18}$$

where κ_λ represents the parameter of interest. The denominator is built by first performing a 2D fit in the $\kappa_\lambda - \mu$ plane and extracting the best fit values, then by fitting all the nuisance parameters $\vec{\theta}$ simultaneously, thus obtaining $\mathcal{L}(\hat{\kappa_\lambda}, \hat{\vec{\theta}})$. In the numerator, the best fit value of nuisance parameters is taken, while scanning over a range of κ_λ values. The confidence interval limits on κ_λ are extracted based on where the negative log-likelihood function (Eq. (5.18)) intercepts 1 (4), which results in 1σ (2σ) confidence intervals.

5.3.7 Building templates for the statistical model

Templates used in the statistical model must be built from MC and data and parameterized as a function of κ_λ. The templates incorporate corrections to the SM ggF and EW production modes at the LO, which were discussed previously. Due to how c_6-related corrections are implemented, the c_6 coupling modifies only the loop diagrams (MC implementation itself is slightly different than Eq. (4.21) in that sense). Adopting the approximation $c_6 \approx \kappa_\lambda$, templates are built where production and decay scale linearly with κ_λ, while propagation scales quadratically.

The total amplitude for ggF mode of production includes several components, SM LO ggF production, ggZZ background, a combined production and decay correction term, and the propagation correction:

$$A^2 = |A_{\text{SM}_{\text{LO}}} + A_{\text{BKG}} + A_{\text{prod}}^{\text{tot}} + A_{\text{prop}}^{\text{tot}} + A_{\text{dec}}^{\text{tot}}|^2 =$$
$$= |A_{\text{SM}_{\text{LO}}} + A_{\text{BKG}} + A_{\text{prod}} + A_{\text{prod}}^{\delta Z_H} + A_{\text{prop}} + A_{\text{prop}}^{\delta Z_H} + A_{\text{dec}} + A_{\text{dec}}^{\delta Z_H}|^2 =$$
$$= |A_{\text{SM}_{\text{LO}}} + A_{\text{BKG}} + (A_{\text{prod}} + A_{\text{dec}}) + A_{\text{prop}}|^2 =$$
$$= A_{\text{SM}_{\text{LO}}}^2 + A_{\text{BKG}}^2 + (A_{\text{prod}} + A_{\text{dec}})^2 + A_{\text{prop}}^2$$
$$+ I(A_{\text{SM}_{\text{LO}}}, A_{\text{BKG}}) + I(A_{\text{SM}_{\text{LO}}}, A_{\text{prod}} + A_{\text{dec}}) + I(A_{\text{SM}_{\text{LO}}}, A_{\text{prop}})$$
$$+ I(A_{\text{BKG}}, A_{\text{prod}} + A_{\text{dec}}) + I(A_{\text{BKG}}, A_{\text{prop}}) + I(A_{\text{prod}} + A_{\text{dec}}, A_{\text{prop}}) \tag{5.19}$$

Each term in the total amplitude squared (A^2) has a distinct physical meaning. The first two components, $A_{SM_{LO}}^2$ and A_{BKG}^2 correspond to the leading–order SM Higgs boson signal process ($H \to ZZ \to 4l$, no loops) and the continuum $gg \to ZZ$ background process, respectively. Their interference is given with the term $I(A_{SM_{LO}}, A_{BKG})$. The term $(A_{prod} + A_{dec})^2$ represent the corrections to the Higgs boson production and decay vertices induced by the modified trilinear coupling, without the $A_{prod}^{\delta Z_H} + A_{dec}^{\delta Z_H}$ contribution as it exactly cancels out against $A_{prop}^{\delta Z_H}$. The term A_{prop}^2 accounts for the corrections to the propagator, without the δZ_h contribution (as it is canceled out). The remaining terms are the cross-interference terms $I(X, Y)$ between the different amplitude components. This decomposition thus provides the theoretical foundation for constructing the template parameterization used in the fit to extract sensitivity to the Higgs boson self-coupling.

Similarly, in case of EW Higgs boson production mode, the total amplitude can be decomposed as:

$$A^2 = |A_{\text{SM}_{\text{LO}}} + A_{\text{BKG}} + A_{\text{prod}}^{\text{tot}} + A_{\text{prop}}^{\text{tot}} + A_{\text{dec}}^{\text{tot}}|^2$$
$$= |A_{\text{SM}_{\text{LO}}} + A_{\text{BKG}} + A_{\text{prod}} + A_{\text{prod}}^{\delta Z_H} + A_{\text{prop}} + A_{\text{prop}}^{\delta Z_H} + A_{\text{dec}} + A_{\text{dec}}^{\delta Z_H}|^2$$
$$= |A_{\text{SM}_{\text{LO}}} + A_{\text{BKG}} + (A_{\text{prod}} + A_{\text{dec}}) + (A_{\text{prop}} + \delta Z_H)|^2$$
$$= A_{\text{SM}_{\text{LO}}}^2 + A_{\text{BKG}}^2 + (A_{\text{prod}} + A_{\text{dec}})^2 + (A_{\text{prop}} + \delta Z_H)^2$$
$$+ I(A_{\text{SM}_{\text{LO}}}, A_{\text{BKG}}) + I(A_{\text{SM}_{\text{LO}}}, A_{\text{prod}} + A_{\text{dec}}) + I(A_{\text{SM}_{\text{LO}}}, A_{\text{prop}} + \delta Z_H)$$
$$+ I(A_{\text{BKG}}, A_{\text{prod}} + A_{\text{dec}}) + I(A_{\text{BKG}}, A_{\text{prop}} + \delta Z_H) + I(A_{\text{prod}} + A_{\text{dec}}, A_{\text{prop}} + \delta Z_H) \tag{5.20}$$

with the big difference being when compared to Eq. (5.19) the presence of δZ_h term which encompasses all the relevant contributions related to the wave-function renormalization constant. As opposed to the case of ggF, these contributions do not cancel out (as discussed in the previous chapter). All the other terms have analogous meaning to the case of ggF.

The templates representing each term of Eqs. (5.19) and (5.20) are parametric 2-dimensional histograms of m_{4l} and nLD, built using the MELA framework. With access to all the necessary matrix elements, all the off-shell samples are reweighted to each of the components across a set of κ_λ values. With this a parametric description of templates is obtained, where such templates are built in such a way that they assume a constant normalization across the κ_λ values and the dependence on κ_λ is contained within a polynomial which multiplies the template normalization. Each signal templates has its own associated polynomial. The following scaling should be kept in mind:

- $A_{SM_{LO}}^2, A_{BKG}^2, I(A_{SM_{LO}}, A_{BKG}) \sim 1$ (i.e. no κ_λ dependence);

- $I(A_{SM_{LO}}, A_{prod} + A_{dec}), I(A_{BKG}, A_{prod} + A_{dec}) \sim \kappa_\lambda$;

- $(A_{prod} + A_{dec})^2 \sim \kappa_\lambda^2$;

- $I(A_{SM_{LO}}, A_{prop}), I(A_{SM_{LO}}, A_{prop}) \sim a\kappa_\lambda + b\kappa_\lambda^2$,

- $I(A_{prod} + A_{dec}, A_{prop}) \sim a\kappa_\lambda^2 + b\kappa_\lambda^3;$

- $A_{prop}^2 \sim a\kappa_\lambda^2 + b\kappa_\lambda^3 + c\kappa_\lambda^3;$

- $\delta Z_h \sim a\kappa_\lambda + b\kappa_\lambda^2,$

once again, stressing out the a priori different coefficients in the polynomial scaling for different templates.

With the templates built, and relying on reweighting features of MELA, it is now very simple to construct all templates, as all samples can be reweighted to $\kappa_\lambda = 1$ hypothesis and then parameterized by a polynomial function. This approach is efficient as it removes the need for building templates for each κ_λ value separately and thus modeling the shape variation with a huge number of templates.

5.3.8 Results

With the physics and statistical model built as explained above and using the CMS *Combine* software package [234, 246] a fit is performed to extract the expected value of κ_λ. The fit is performed in 2 dimensions, m_{4l} and convolution $D_{\text{bkg}}^{\text{kin}} * D_{\text{bsi}}$. Results are presented for three categories, and also for their combination. Scan of expected κ_λ in untagged category is presented in Figure 5.7, for VH tagged category in Figure 5.9, for VBF tagged category in Figure 5.8 and for their combination in Figure 5.10.

Expected scan of κ_λ across the three categories and their combined scan at 95% CL is:

$$
\begin{aligned}
\text{untagged category:} \quad & -19.26 < \kappa_\lambda < 21.49, \\
\text{VBF category:} \quad & -25.41 < \kappa_\lambda < 23.28, \\
\text{VH category:} \quad & -32.37 < \kappa_\lambda < 34.26, \\
\textbf{combined categories:} \quad & -18.53 < \kappa_\lambda < 19.64,
\end{aligned}
\tag{5.21}
$$

where it can be seen that the most sensitivity is carried in the untagged category, whilst the least in the VH tagged category. Combined scan over all three categories slightly increases the sensitivity above that of untagged category. The results of the *expected* scan of κ_λ demonstrate the feasibility of probing the Higgs boson self-coupling modifier using the off-shell regime of production in the $H \to ZZ \to 4l$ decay channel. Scans show that the current analysis achieves sensitivity to modifications of κ_λ from the value predicted by SM. The expected uncertainty, however, is large. The large uncertainty in the extracted κ_λ originates from several factors. By large, the dominant uncertainty is due to the statistical limitations, i.e. due to limited dataset owing to the rarity of the Higgs boson off-shell production (compared to the on-shell production). Contributing theoretical uncertainties are sizable, namely theoretical modeling of the off-shell signal and its interference with the continuum background, as well as uncertainty related to the applied K factors. Detector-related uncertainties, such as electron reconstruction and identification contribute non-negligibly to the total uncertainty. Non the less, the analysis establishes a methodological framework through the use of matrix elements which are employed in calculation of matrix element based discriminants and for building of likelihood templates.
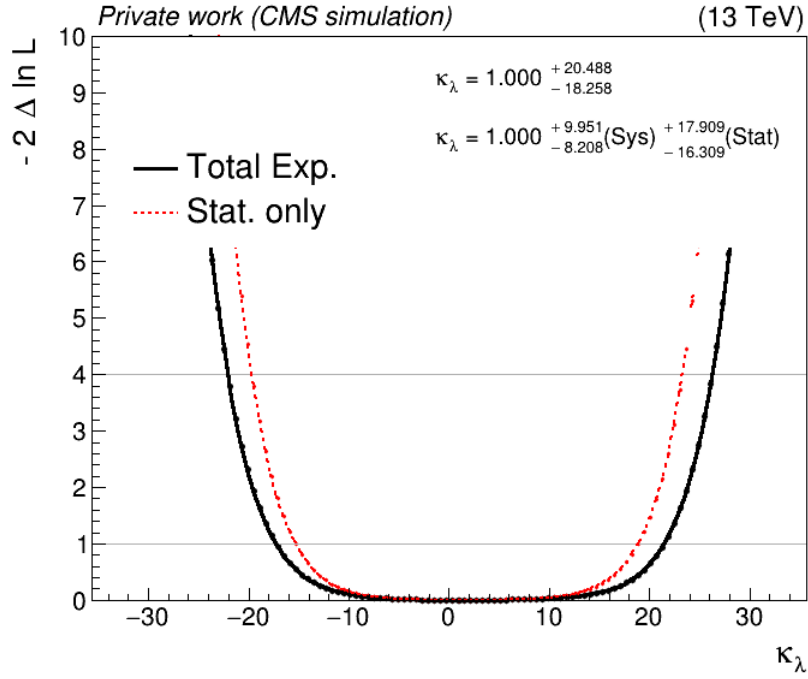
Figure 5.7. Expected scan of κ_λ in untagged category, where the scan with only statistical uncertainty included is shown in red and the scan including statistical and systematic uncertainty is shown in black. Courtesy of Andro Petković and his work.
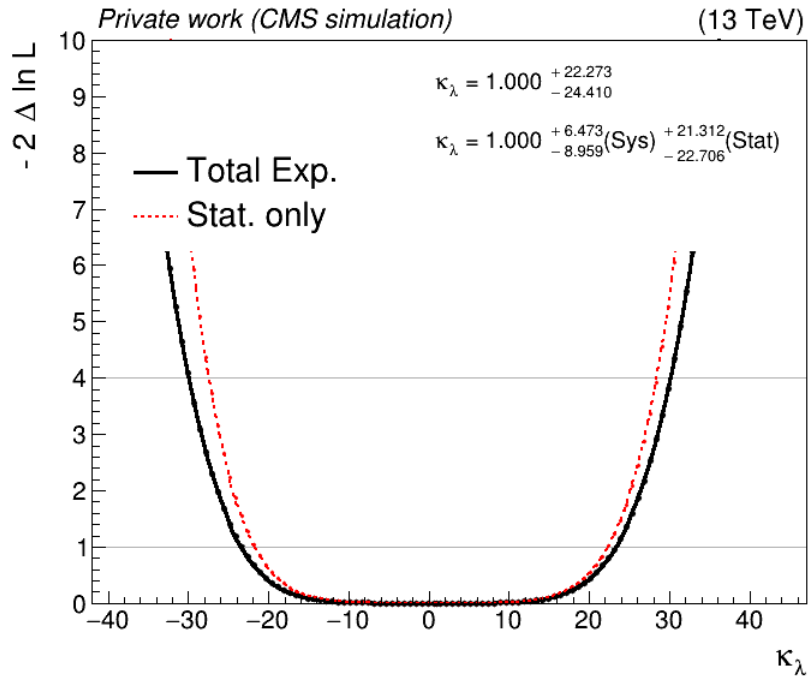
Figure 5.8. Expected scan of κ_λ in VBF tagged category, where the scan with only statistical uncertainty included is shown in red and the scan including statistical and systematic uncertainty is shown in black. Courtesy of Andro Petković and his work.
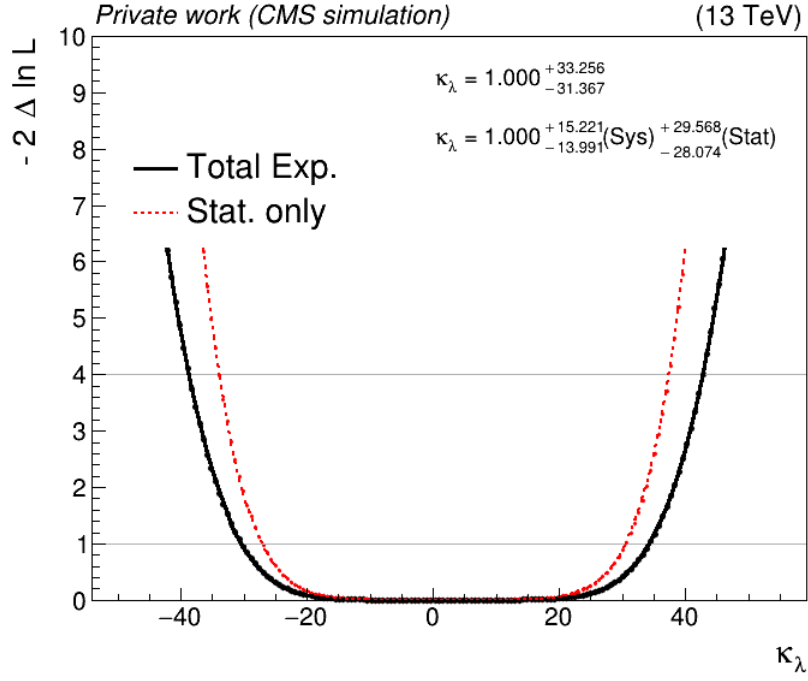
Figure 5.9. Expected scan of κ_λ in VH tagged category, where the scan with only statistical uncertainty included is shown in red and the scan including statistical and systematic uncertainty is shown in black. Courtesy of Andro Petković and his work.
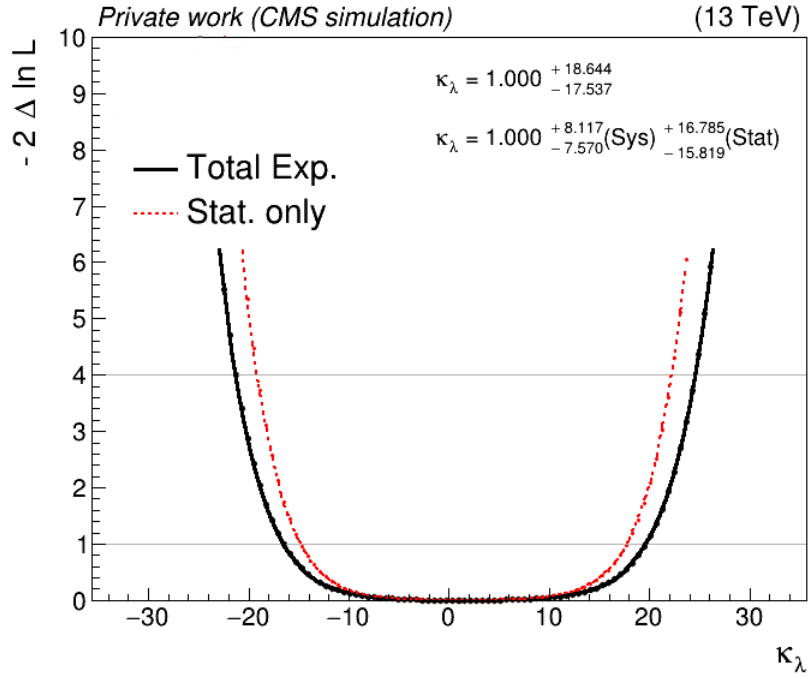
Figure 5.10. Expected combined scan of κ_λ from all three categories, where the scan with only statistical uncertainty included is shown in red and the scan including statistical and systematic uncertainty is shown in black. Courtesy of Andro Petković and his work.

Chapter 6

Discussion

Here the main outcomes of this work are summarized, spanning theoretical predictions, detector development, and Higgs boson-related measurements.

In view of the CMS detector upgrade for the High-Luminosity phase of the LHC, Ultra-Fast Silicon Detectors (UFSDs) are developed for timing measurements in the endcap region. The inter-pad region design study aimed to optimize the geometry and doping profile of UFSDs to achieve high fill-factor, fine segmentation, and stable electrical behavior without premature breakdown. It can be concluded (based on measurements performed on UFSD3.1 campaign) that low p-stop doping and small region A/B surface are the optimal characteristics to avoid early breakdown of a sensor. Inter-pad widths of ~ 25 μm are achievable. Overall, the elastomer setup allows for a measurement of total leakage current by contacting all of the single pads, although careful handling is needed for several experimental reasons, both mechanical and electrical. The trend of the expected voltage-current curves is reproduced well, although with a less precision for sensors with a deeper implant. Some of the measurements show higher current than the reported ones (by the manufacturer) indicating that the elastomer setup has room to improve, but is faithful in replicating the trend of current curves. Further studies are needed to confirm the exact reason as to why this is the case. Several things are to be considered: potential impact on measurement coming from elastomer-sensor contact, elastomer-copper contact, behavior of the mask under contact with the conducting material. The setup was tested under temperature change, where stability was observed for measurement of some sensors.

The MATRIX framework has proven to be a highly reliable tool for precision Standard Model predictions, particularly for di-vector boson production processes. The use of MATRIX at NNLO QCD accuracy (and including NLO EW corrections where available) enabled cross section calculation at a proton-proton center-of-mass of 13.6 TeV (LHC Run-3). The combination of NNLO QCD and NLO EW corrections was discussed and it was shown that percent-level theoretical precision is achieved. The results obtained with MATRIX serve as a cross check for various analysis within the CMS collaboration, which shows good agreement when comparing to results obtained with different MC generators.

The fiducial cross-section measurement of the $H \to ZZ \to 4l$ decay channel at 13.6 TeV presented in Section 5.2 demonstrates excellent agreement with the SM expectations. The measured fiducial value:

$$\sigma_{\text{fid}} = 2.89^{+0.53}_{-0.49} \text{ (stat)}^{+0.29}_{-0.21} \text{ (syst) fb.} \tag{6.1}$$

is consistent within uncertainties with the predicted value of $\sigma_{\text{expected}} = 3.09^{+0.27}_{-0.24}$ fb.

The strategy for Higgs boson self-coupling measurement from off-shell regime of production, presented in Chapters 4 and 5, shows that it is possible to probe the self-coupling in the $H \to ZZ \to 4l$

decay channel. The matrix elements, that entail c_6 corrections, were propagated from MCFM8.0 to JHUGen-MCFM. Further, the ggF production cross sections, where only one or all three of the contributions are turned on (production, propagation, decay), were calculated and compared between the two generator frameworks. A satisfactory matching between the cross section values was found. Another matrix element based test was carried out, i.e. reweighting test, which again shows satisfactory matching between the generated MC samples and those obtained by reweighting to corresponding c_6 hypothesis. The matrix element were also propagated to the EW modes of Higgs boson production, expanding the already existing parameterization for one (ggF) mode of production.

From a template-based statistical analysis, where all BSM effects are parameterized, was found that the greatest sensitivity to κ_λ modifications comes from the untagged category, whilst the sensitivity from the scan of combined categories is:

$$\textbf{combined categories:} \quad -18.53 < \kappa_\lambda < 19.64, \tag{6.2}$$

Comparing the scan between VBF and VH categories, it can be noted that the VBF tagged category carries better sensitivity, where the weakest sensitivity comes from the VH tagged category.

The methodology implemented in the off-shell regime serves a complementary purpose to the measurement from the on-shell regime as the measurement from the off-shell regime is sensitive to the higher-order loop-induced effects, whilst the on-shell regime measurement probes the effects of modified Higgs boson self-coupling near the resonance peak. The expected scan returns a best-fit κ_λ value compatible with the SM predictions, although with a large uncertainty. Even though the sensitivity to the Higgs boson self-coupling in off-shell is weaker than that of di-Higgs boson production, the analysis presented here demonstrates the potential of using the measurement in off-shell regime as an independent constraint in the future. At the HL-LHC the sensitivity to κ_λ is expected to improve significantly, as the leading uncertainty is the statistical one.

Appendix A

Leakage current and guard ring current measurement

Here a measurement of leakage current and guard ring currents are presented for 30 sensors which together with sensors presented in Section 2.5, make up the full set of tested sensors. Measurements of two mentioned currents are given side by side in the following figures, where the legends hold the information about the tested sensors.
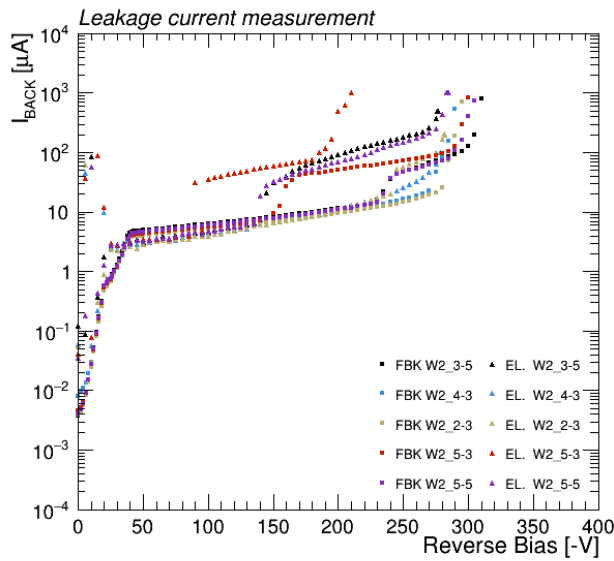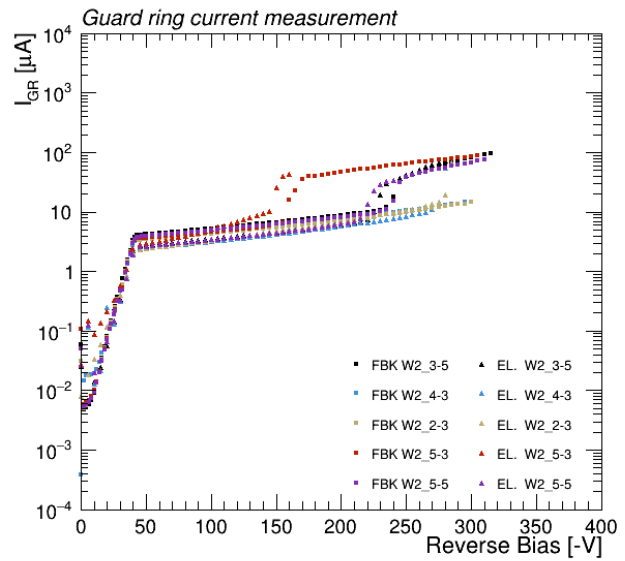
(a)   (b)

Figure A.1. Leakage current (a) and guard ring current (b) scan as a function of reverse bias. Elastomer measurements are labeled with triangles and the FBK measured values are labeled with squares.
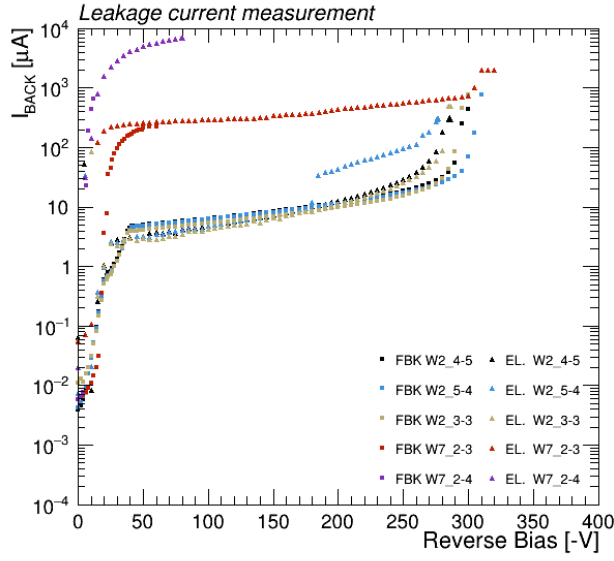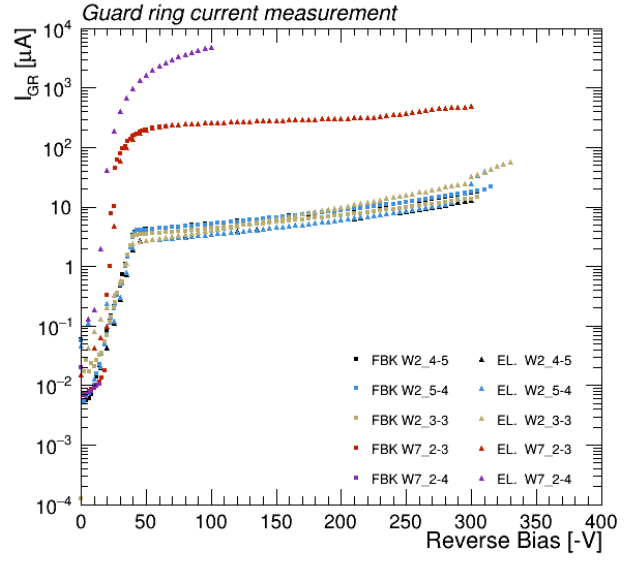
Figure A.2. Leakage current (a) and guard ring current (b) scan as a function of reverse bias. Elastomer measurements are labeled with triangles and the FBK measured values are labeled with squares.
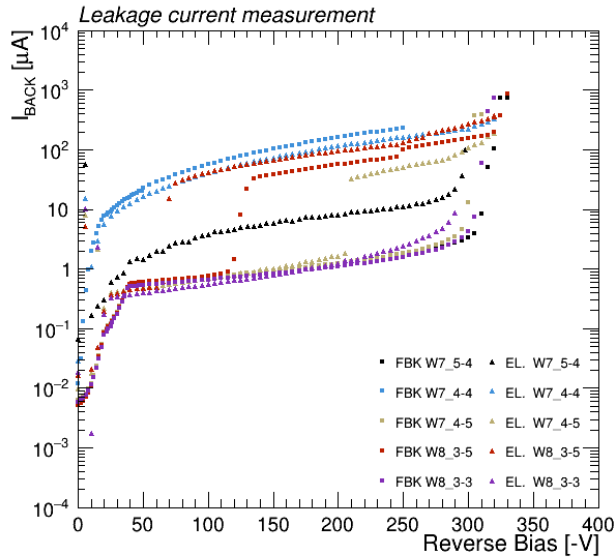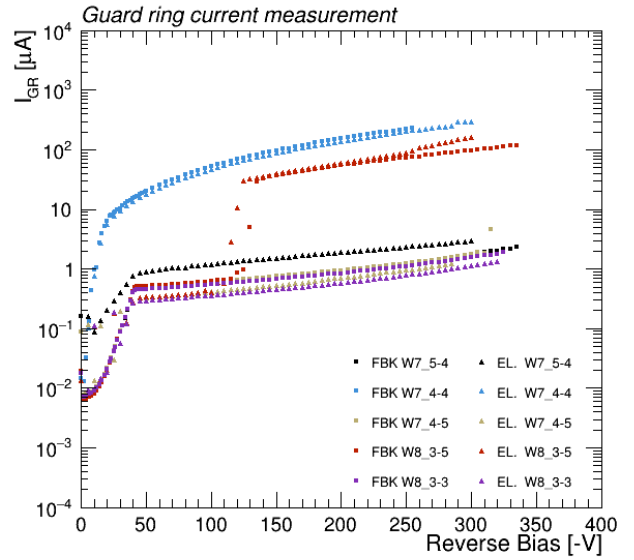
Figure A.3. Leakage current (a) and guard ring current (b) scan as a function of reverse bias. Elastomer measurements are labeled with triangles and the FBK measured values are labeled with squares.
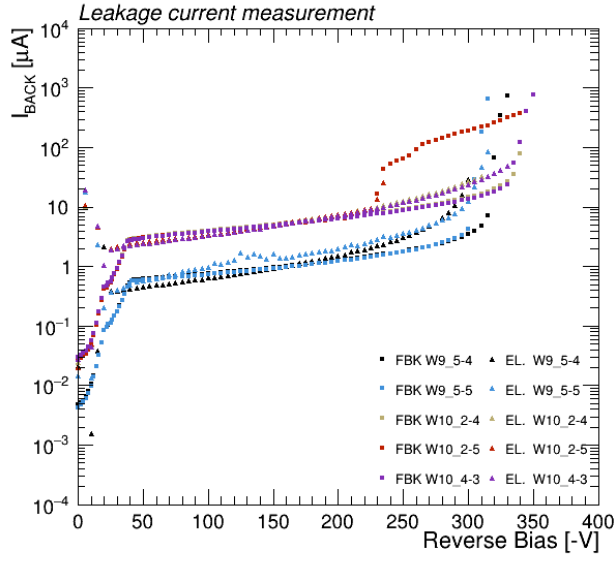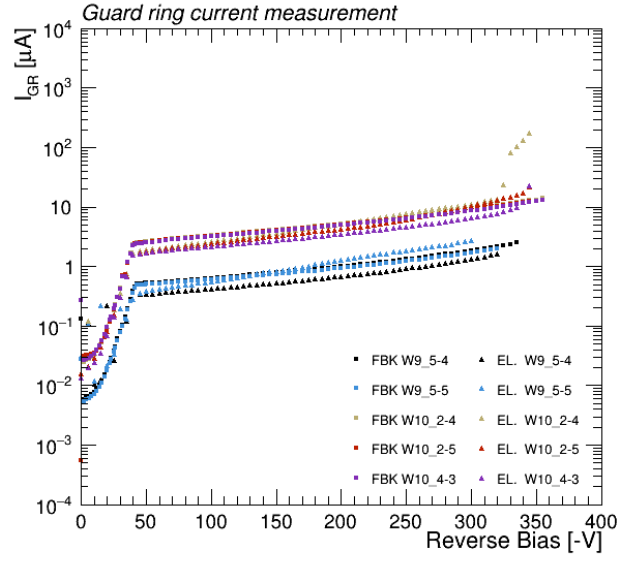
Figure A.4. Leakage current (a) and guard ring current (b) scan as a function of reverse bias. Elastomer measurements are labeled with triangles and the FBK measured values are labeled with squares.
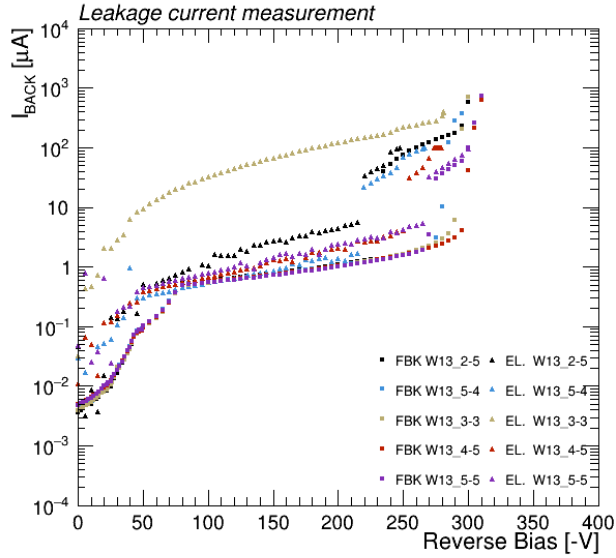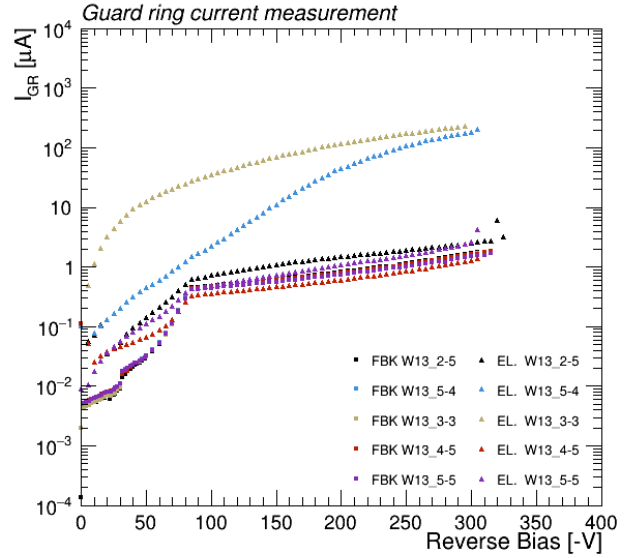
Figure A.5. Leakage current (a) and guard ring current (b) scan as a function of reverse bias. Elastomer measurements are labeled with triangles and the FBK measured values are labeled with squares.
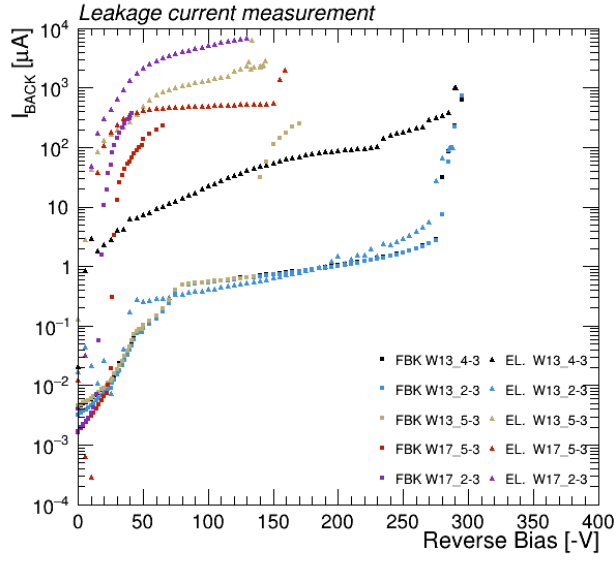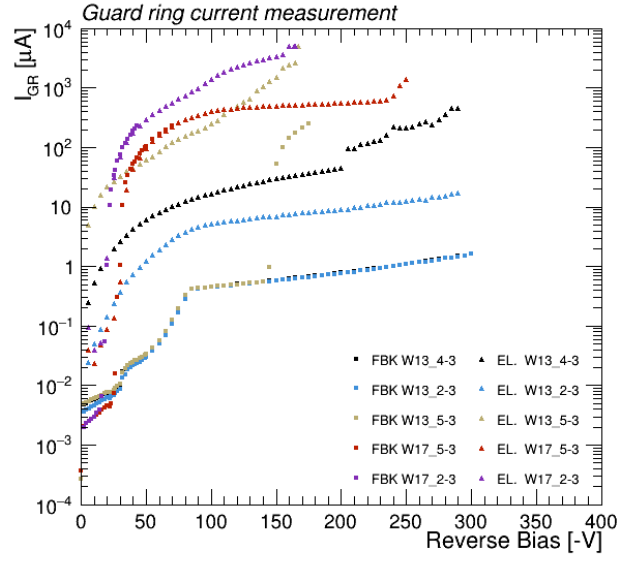
Figure A.6. Leakage current (a) and guard ring current (b) scan as a function of reverse bias. Elastomer measurements are labeled with triangles and the FBK measured values are labeled with squares.
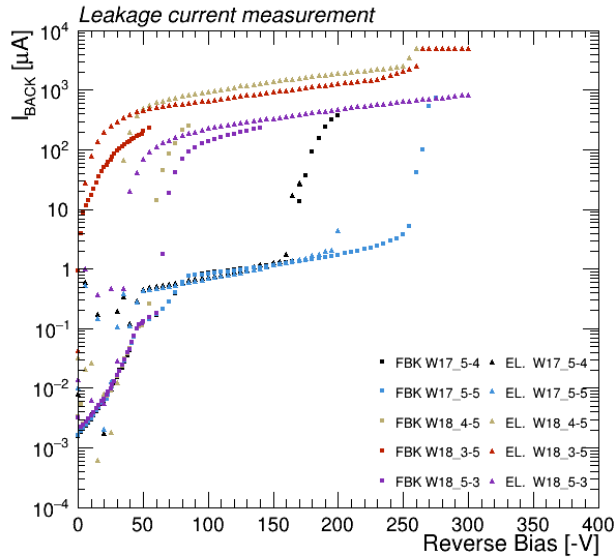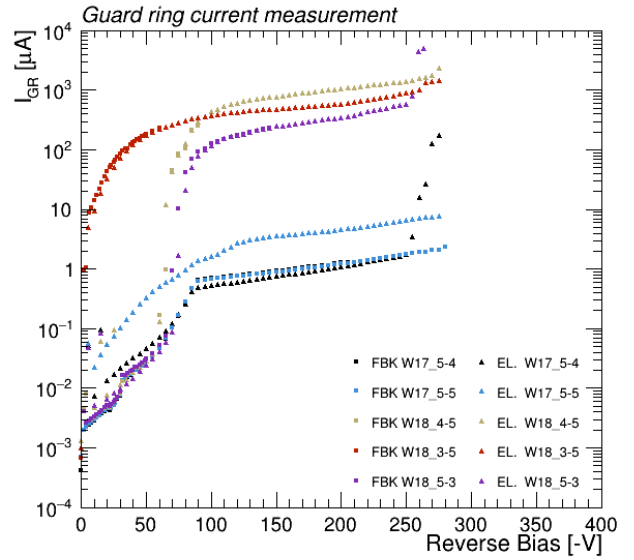
Figure A.7. Leakage current (a) and guard ring current (b) scan as a function of reverse bias. Elastomer measurements are labeled with triangles and the FBK measured values are labeled with squares.

Appendix B

BSM effects on various observables

In total 24 observables were tested against the change of c_6 coefficient. In chapter 4 five variables where presented, while here additional 19 are shown. Kinematical variables that define the Higgs boson decay (angles, discussed in Section 5.3.4) are shown in Figures B.1, B.2, B.3, B.5, B.4. Pseudorapidities of Higgs boson, leading lepton, sub-leading lepton (second highest p_T out of all leptons) and the difference between pseudorapidities of Higgs boson and the jet with the highest mass $\Delta\eta(H, j_1)$ are shown in Figures B.6, B.7, B.8, B.9 respectively. Distribution of transverse momentum of a Higgs boson in events where exactly one jet is produced, where exactly two jets are produced, where three or more jets are produced, distribution of transverse momentum of the jet with highest mass (in an event), of a Higgs boson inclusive in the number of jets produced in an event and masses of Z_1 and Z_2 candidates is shown in Figures B.10, B.11, B.12, B.13, B.14, B.15, B.16, respectively. Number of jets in event and the difference in azimuthal angle ϕ between a Higgs boson and a jet with the highest mass are shown in Figures B.17 and B.18 respectively. In all of the Figures the dominant contribution coming from $q\bar{q} \to ZZ \to 4l$ background was scaled down for shape comparison.

It can be observed that in general variation of c_6 induced changes in distributions in form of scaling, but not in form of shape change which vital for sensitivity exploration and measurement. Some variables like $p_T(l_1), p_T(l_2), p_T(Z_1), p_T(Z_2)$ exhibit some changes in shape looking at the ggF production alone. When studied together with the $ggZZ$ background and their interference, the changes fade away.
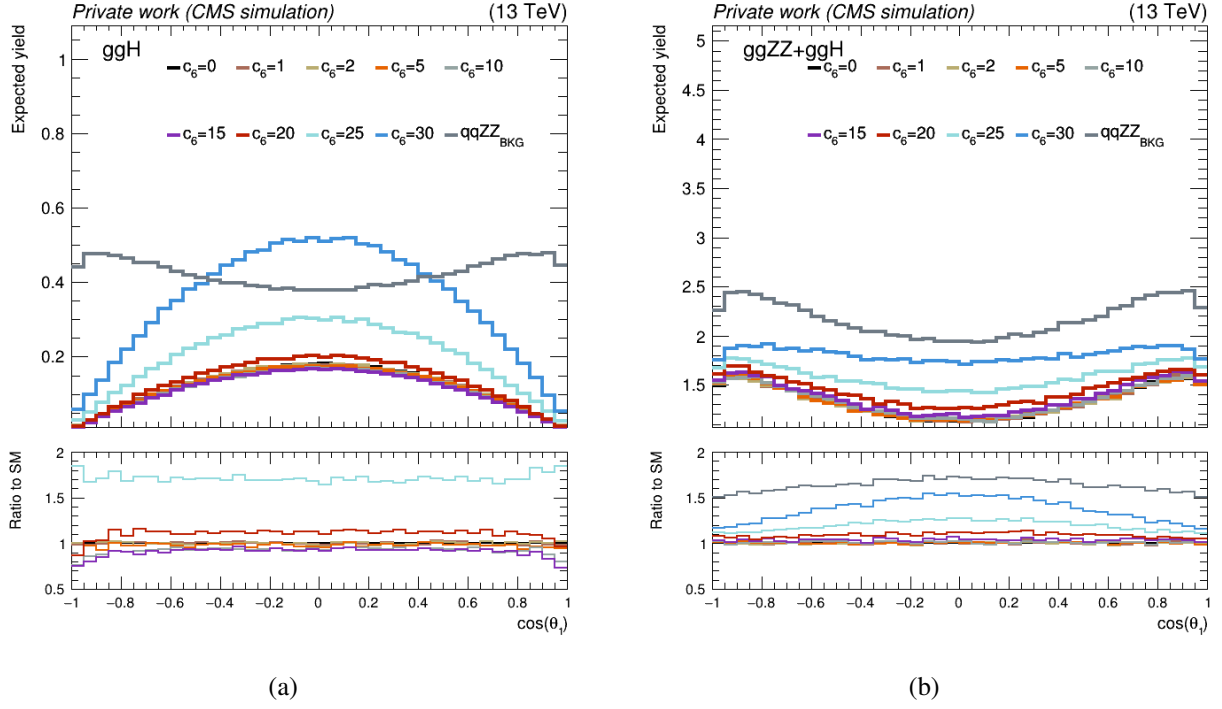
Figure B.1. Reconstruction level $cos(\theta_1)$ distributions for the processes $gg \rightarrow H^* \rightarrow ZZ \rightarrow 4l$ (a) and $gg \rightarrow ZZ \rightarrow 2e2\mu$ where the Higgs boson contribution is included (b). Lower panels present ratios of BSM distributions ($c_6 \neq 0$) to the LO SM distribution ($c_6 = 0$).
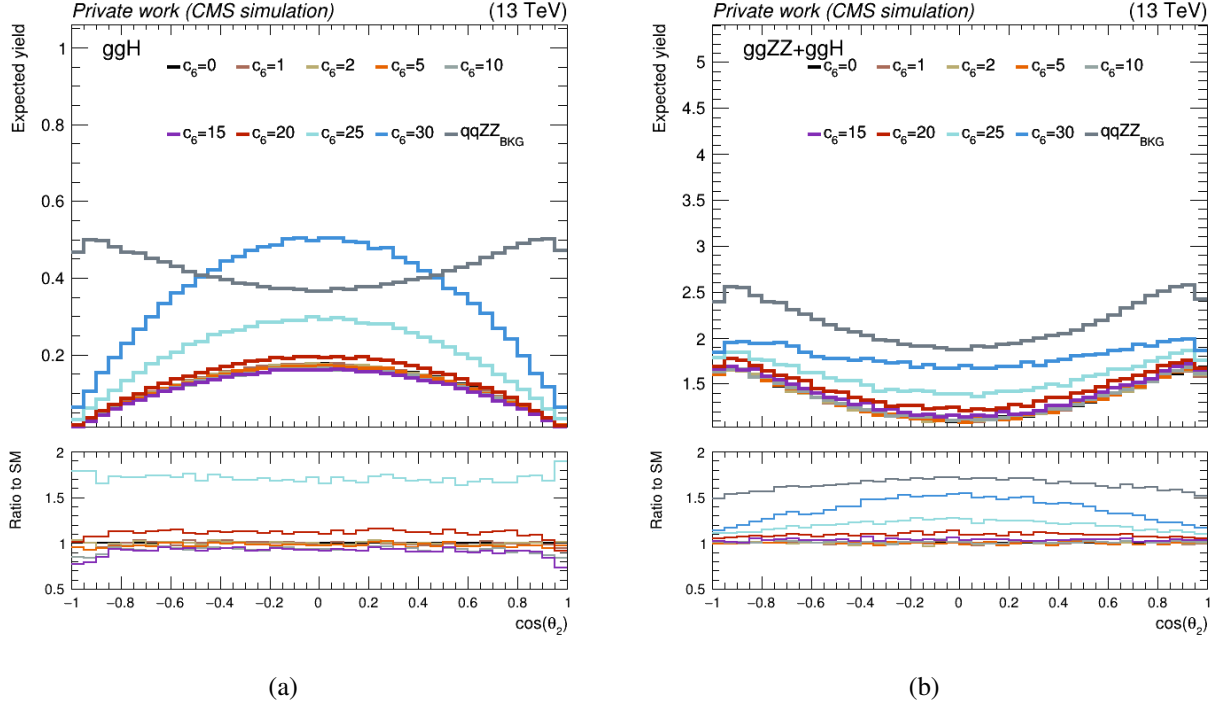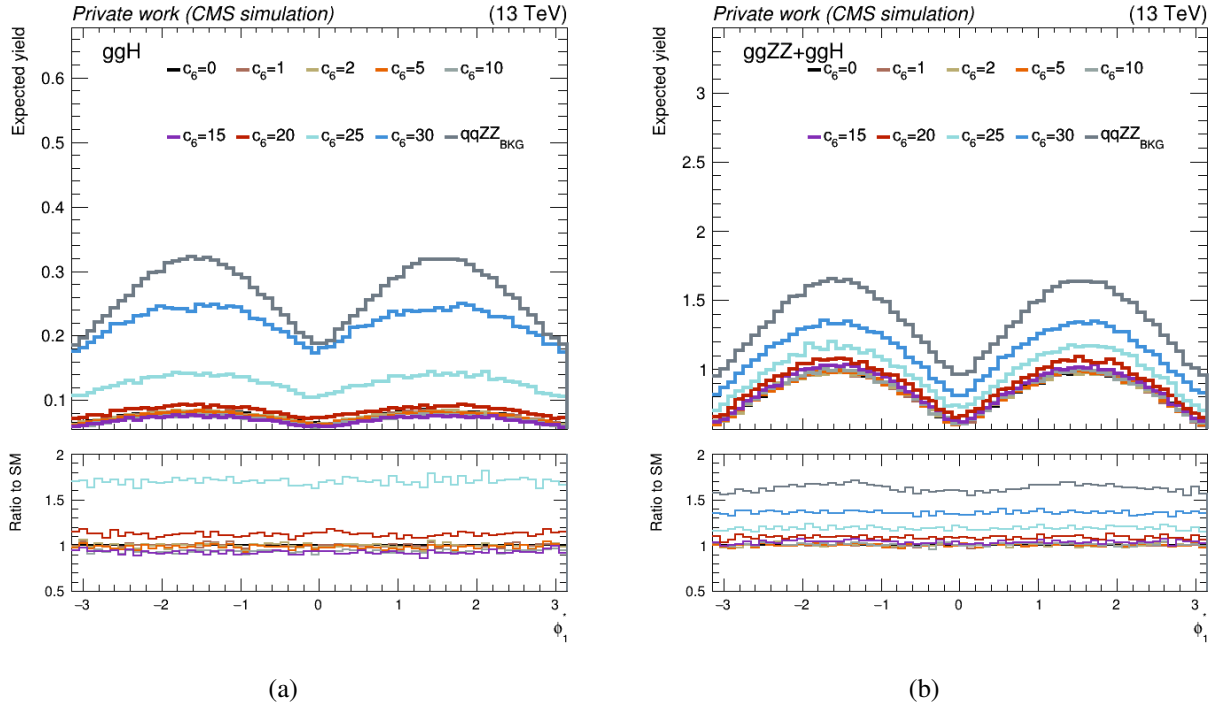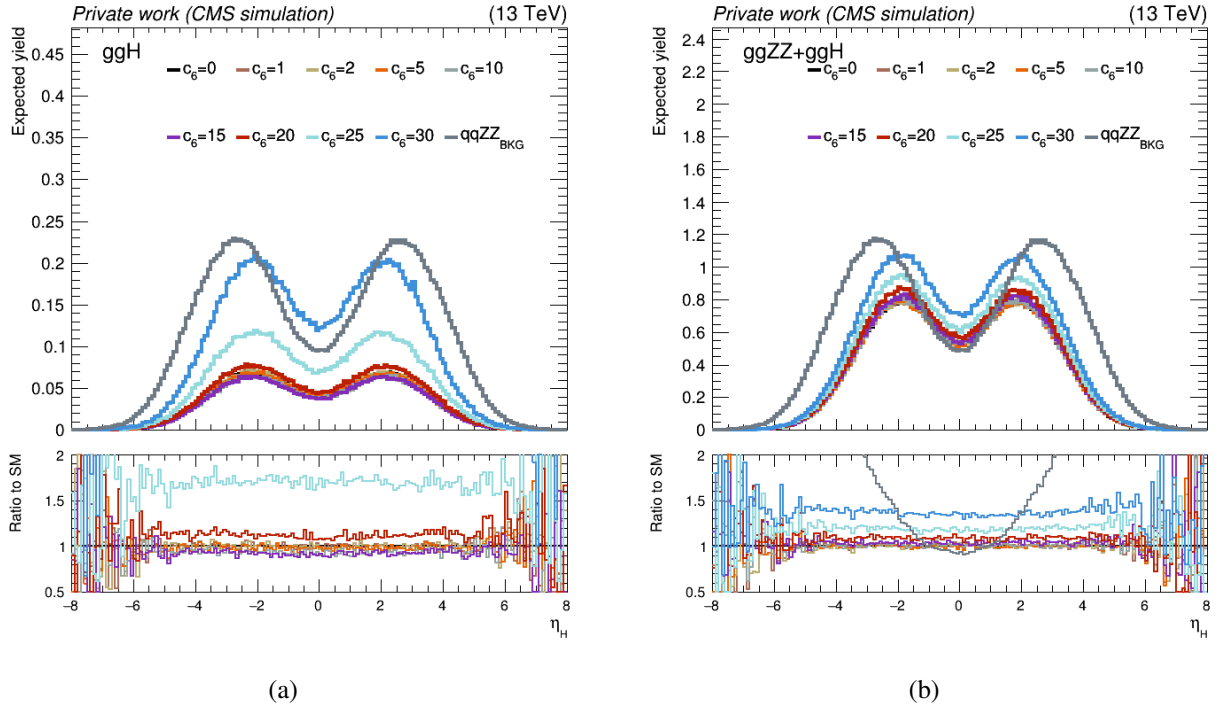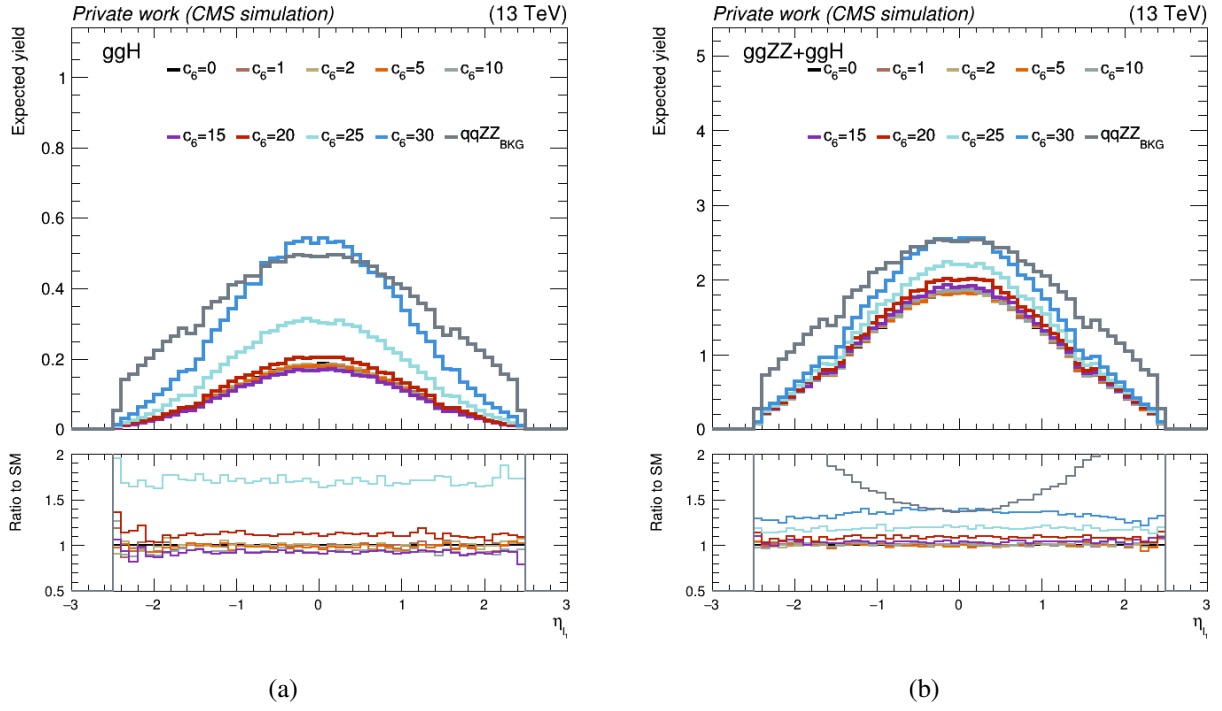

Figure B.2. Reconstruction level $cos(\theta_2)$ distributions for the processes $gg \rightarrow H^* \rightarrow ZZ \rightarrow 4l$ (a) and $gg \rightarrow ZZ \rightarrow 2e2\mu$ where the Higgs boson contribution is included (b). Lower panels present ratios of BSM distributions ($c_6 \neq 0$) to the LO SM distribution ($c_6 = 0$).
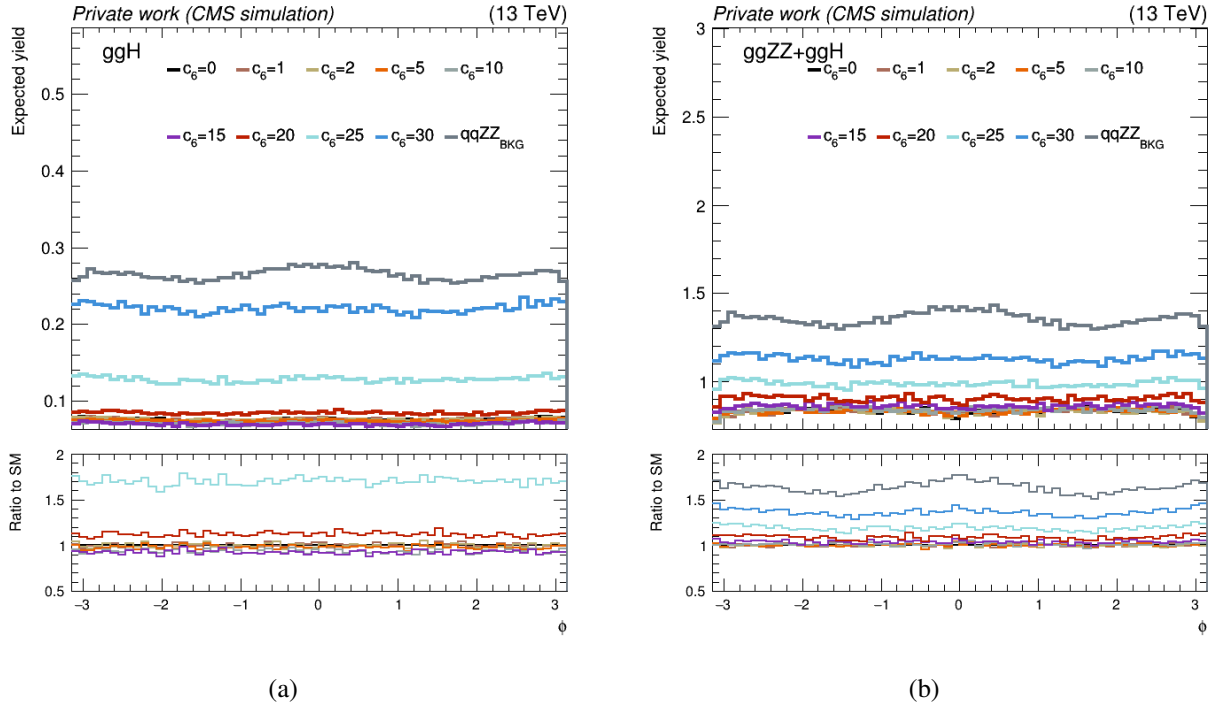
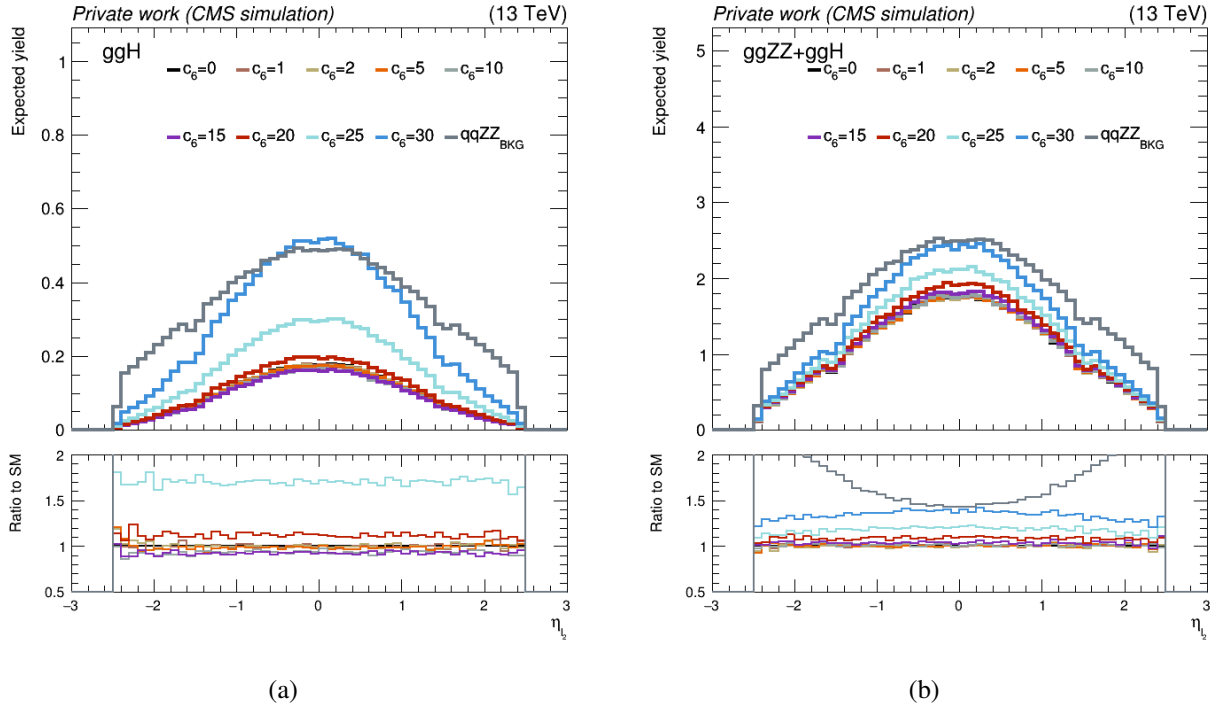**Figure B.3.** Reconstruction level Φ distributions for the processes $gg \rightarrow H^* \rightarrow ZZ \rightarrow 4l$ (a) and $gg \rightarrow ZZ \rightarrow 2e2\mu$ where the Higgs boson contribution is included (b). Lower panels present ratios of BSM distributions ($c_6 \neq 0$) to the LO SM distribution ($c_6 = 0$).
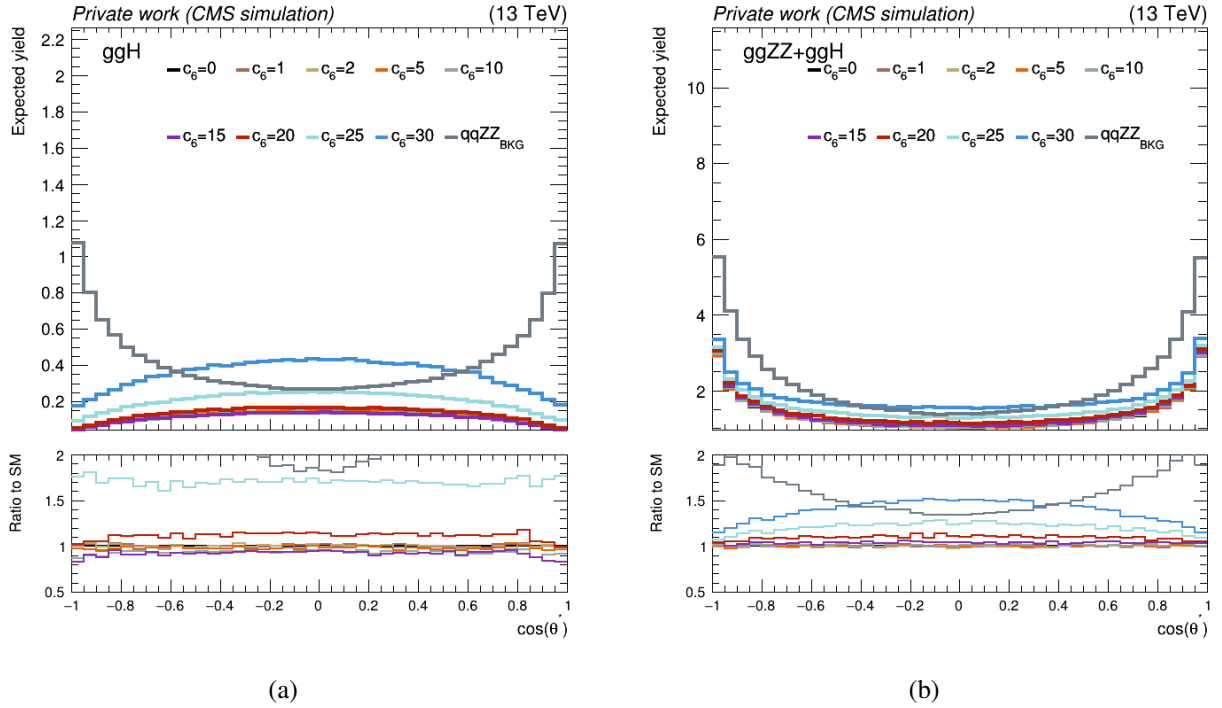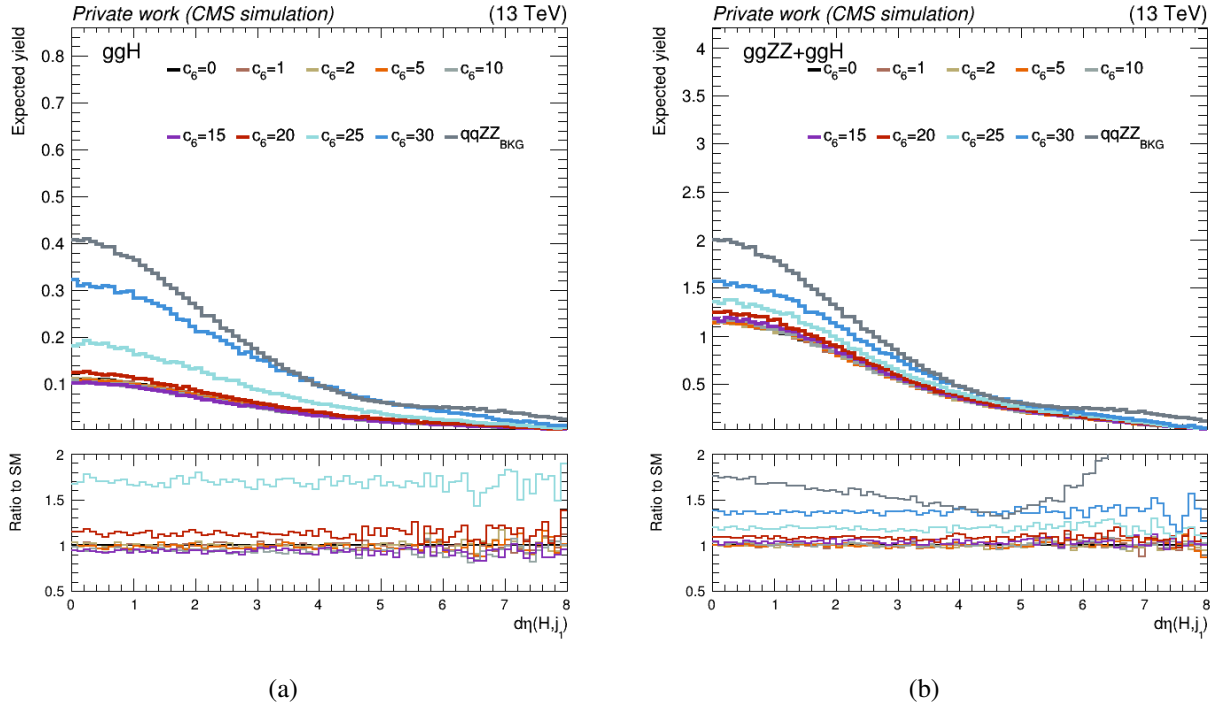

Figure B.4. Reconstruction level $cos(\theta^*)$ distributions for the processes $gg \rightarrow H^* \rightarrow ZZ \rightarrow 4l$ (a) and $gg \rightarrow ZZ \rightarrow 2e2\mu$ where the Higgs boson contribution is included (b). Lower panels present ratios of BSM distributions ($c_6 \neq 0$) to the LO SM distribution ($c_6 = 0$).

Figure B.5. Reconstruction level Φ^* distributions for the processes $gg \rightarrow H^* \rightarrow ZZ \rightarrow 4l$ (a) and $gg \rightarrow ZZ \rightarrow 2e2\mu$ where the Higgs boson contribution is included (b). Lower panels present ratios of BSM distributions ($c_6 \neq 0$) to the LO SM distribution ($c_6 = 0$).
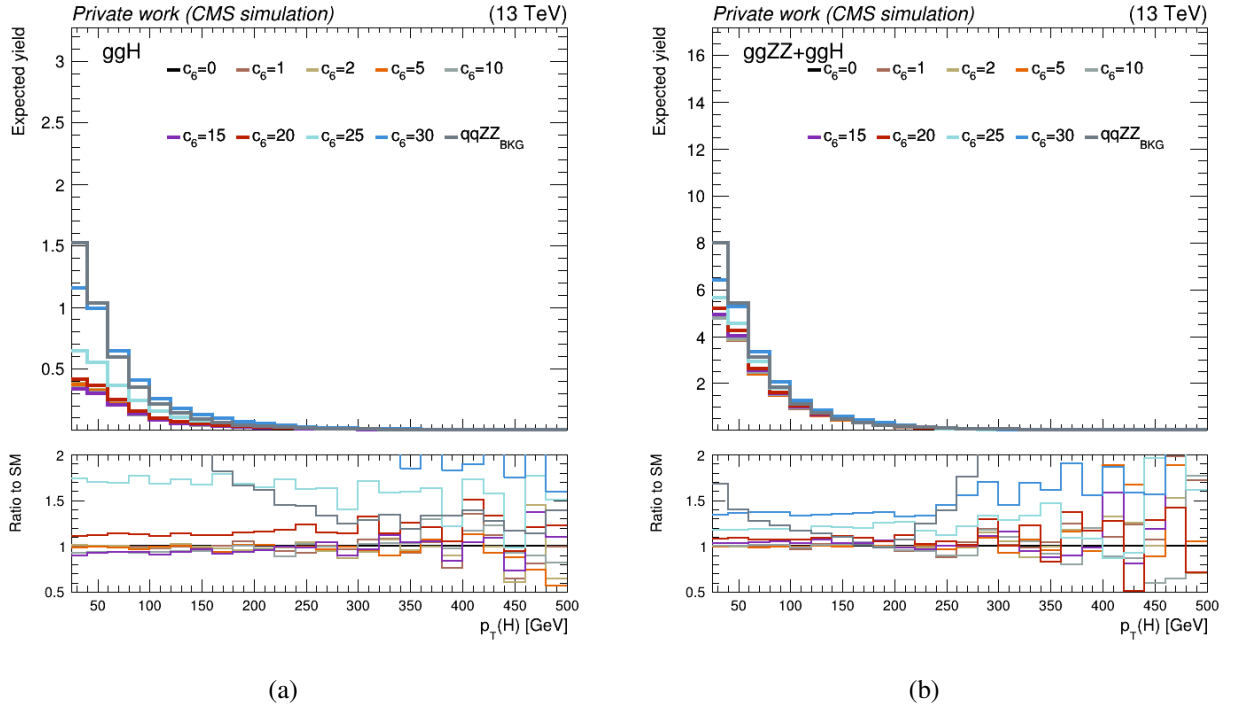

Figure B.6. Reconstruction level η_H distributions for the processes $gg \rightarrow H^* \rightarrow ZZ \rightarrow 4l$ (a) and $gg \rightarrow ZZ \rightarrow 2e2\mu$ where the Higgs boson contribution is included (b). Lower panels present ratios of BSM distributions ($c_6 \neq 0$) to the LO SM distribution ($c_6 = 0$).
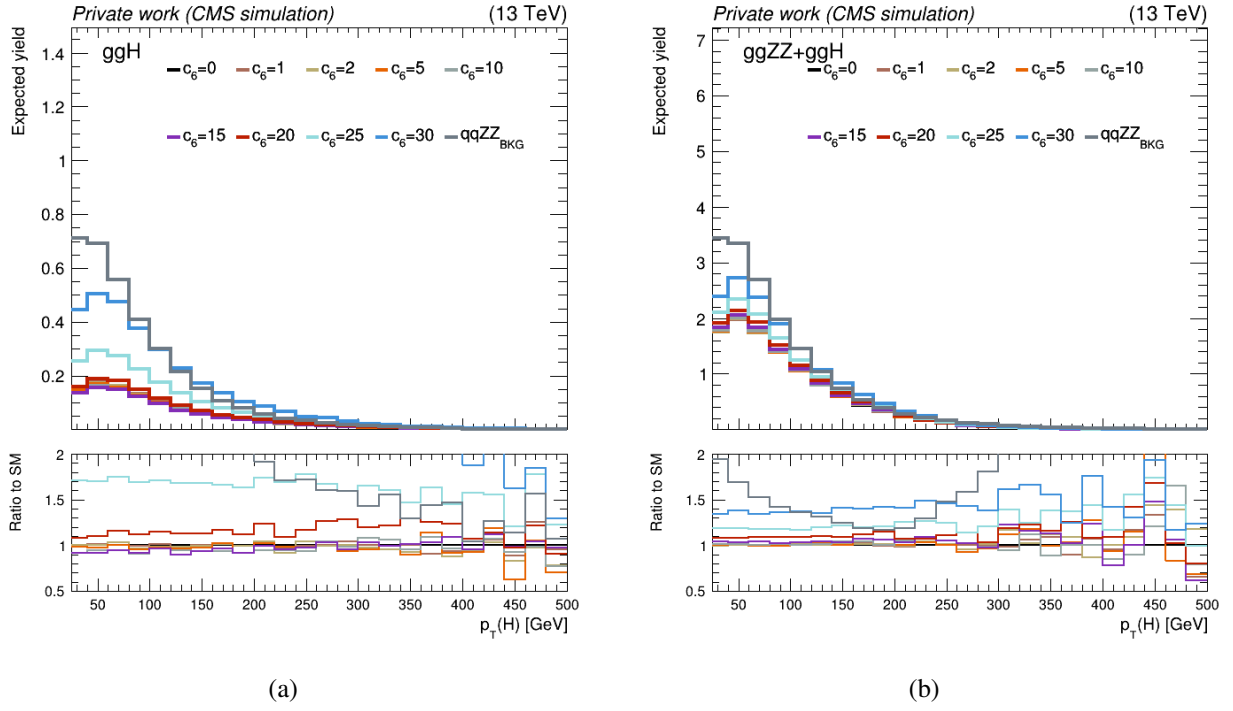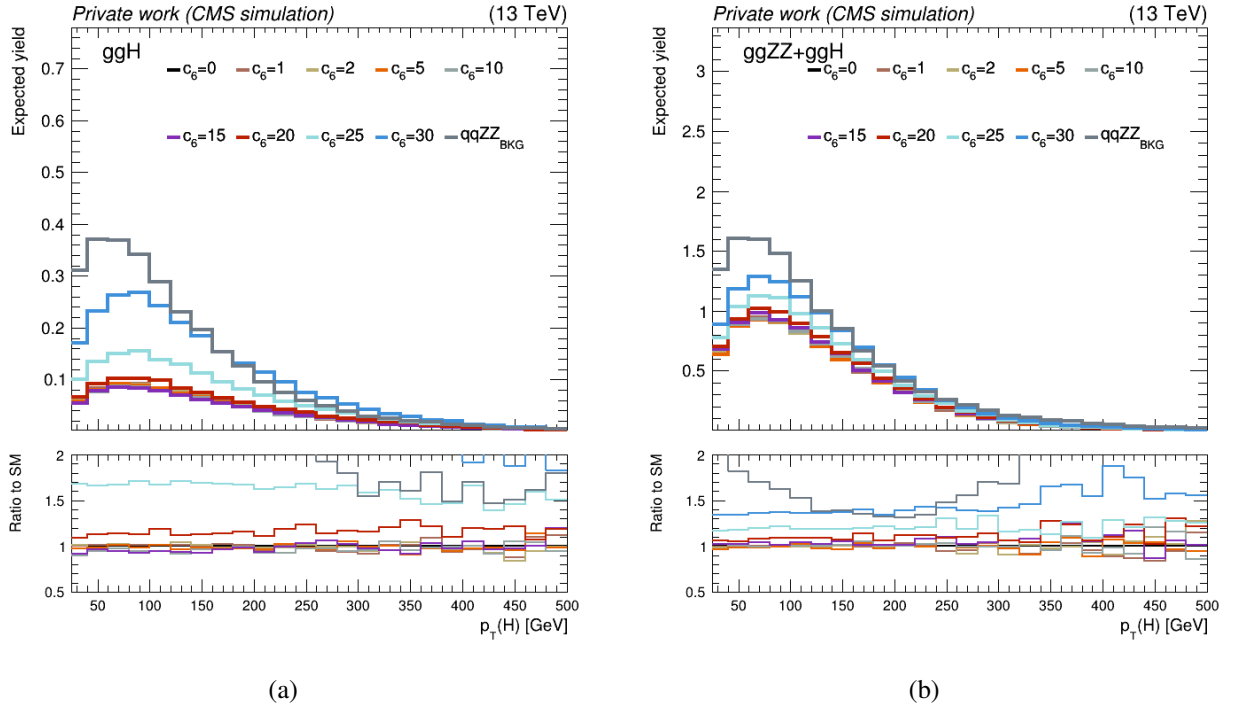
(a)   (b)

Figure B.7. Reconstruction level η_{l_1} distributions for the processes $gg \rightarrow H^* \rightarrow ZZ \rightarrow 4l$ (a) and $gg \rightarrow ZZ \rightarrow 2e2\mu$ where the Higgs boson contribution is included (b). Lower panels present ratios of BSM distributions ($c_6 \neq 0$) to the LO SM distribution ($c_6 = 0$).

(a)   (b)

Figure B.8. Reconstruction level η_{l_2} distributions for the processes $gg \rightarrow H^* \rightarrow ZZ \rightarrow 4l$ (a) and $gg \rightarrow ZZ \rightarrow 2e2\mu$ where the Higgs boson contribution is included (b). Lower panels present ratios of BSM distributions ($c_6 \neq 0$) to the LO SM distribution ($c_6 = 0$).
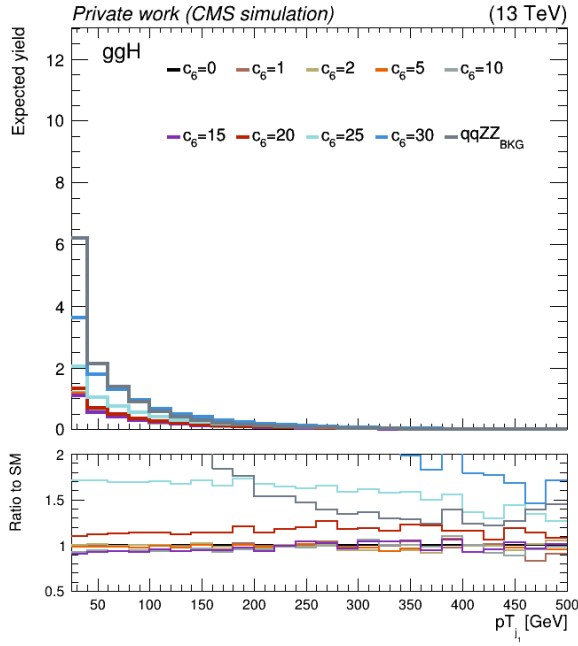
(a)   (b)

Figure B.9. Reconstruction level $\Delta\eta(H, j_1)$ distributions for the processes $gg \to H^* \to ZZ \to 4l$ (a) and $gg \to ZZ \to 2e2\mu$ where the Higgs boson contribution is included (b). Lower panels present ratios of BSM distributions ($c_6 \neq 0$) to the LO SM distribution ($c_6 = 0$).
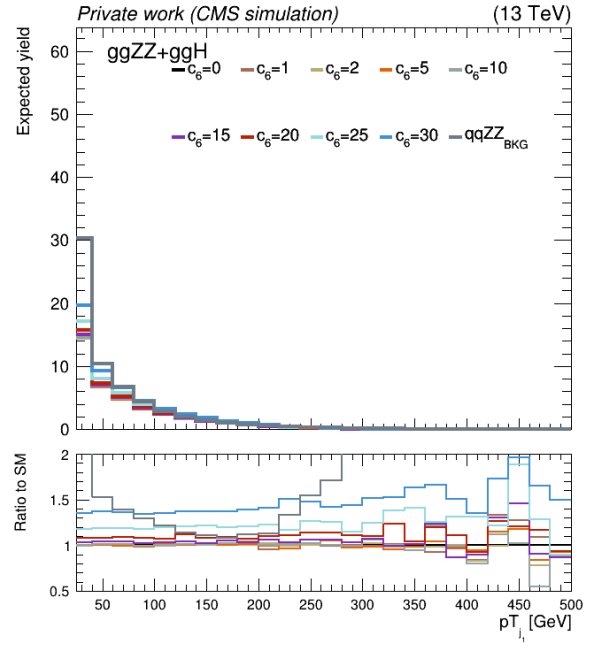

(a)   (b)

Figure B.10. Reconstruction level $p_T(H)$ distributions of events where exactly one jet is produced, for the processes $gg \to H^* \to ZZ \to 4l$ (a) and $gg \to ZZ \to 2e2\mu$ where the Higgs boson contribution is included (b). Lower panels present ratios of BSM distributions ($c_6 \neq 0$) to the LO SM distribution ($c_6 = 0$).

Figure B.11. Reconstruction level $p_T(H)$ distributions of events where exactly two jets are produced, for the processes $gg \to H^* \to ZZ \to 4l$ (a) and $gg \to ZZ \to 2e2\mu$ where the Higgs boson contribution is included (b). Lower panels present ratios of BSM distributions ($c_6 \neq 0$) to the LO SM distribution ($c_6 = 0$).

Figure B.12. Reconstruction level $p_T(H)$ distributions of events where three or more jets are produced, for the processes $gg \to H^* \to ZZ \to 4l$ (a) and $gg \to ZZ \to 2e2\mu$ where the Higgs boson contribution is included (b). Lower panels present ratios of BSM distributions ($c_6 \neq 0$) to the LO SM distribution ($c_6 = 0$).
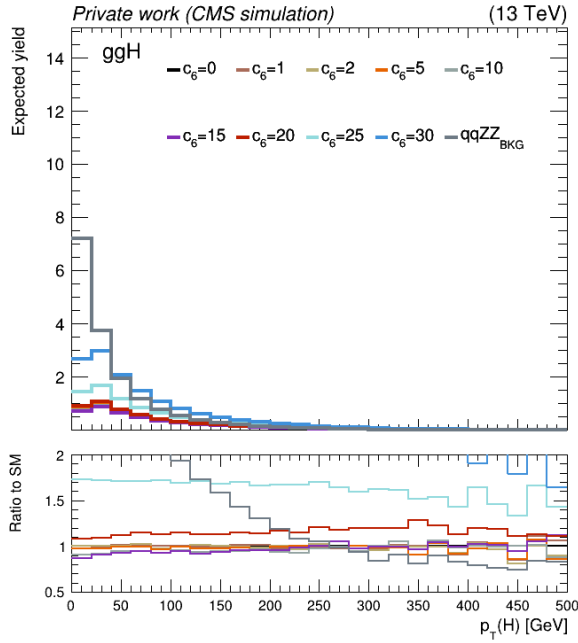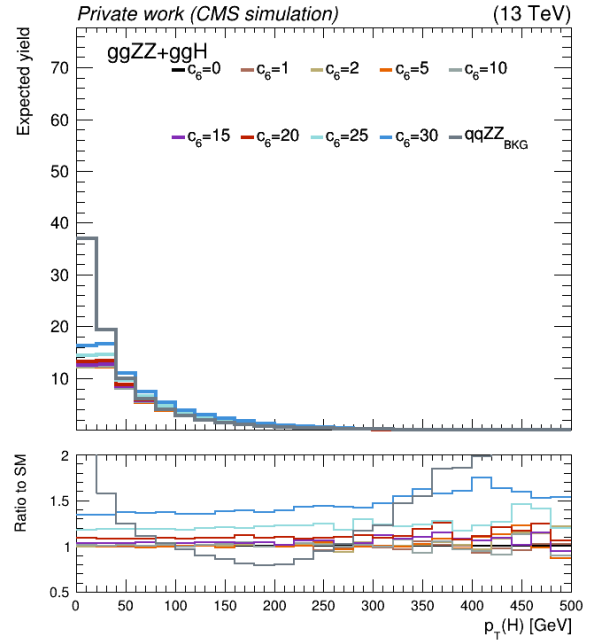
Figure B.13. Reconstruction level $p_T(j_1)$ distribution for the processes $gg \rightarrow H^* \rightarrow ZZ \rightarrow 4l$ (a) and $gg \rightarrow ZZ \rightarrow 2e2\mu$ where the Higgs boson contribution is included (b). Lower panels present ratios of BSM distributions ($c_6 \neq 0$) to the LO SM distribution ($c_6 = 0$).

Figure B.14. Reconstruction level $p_T(H)$ distribution for the processes $gg \rightarrow H^* \rightarrow ZZ \rightarrow 4l$ (a) and $gg \rightarrow ZZ \rightarrow 2e2\mu$ where the Higgs boson contribution is included (b). Lower panels present ratios of BSM distributions ($c_6 \neq 0$) to the LO SM distribution ($c_6 = 0$).
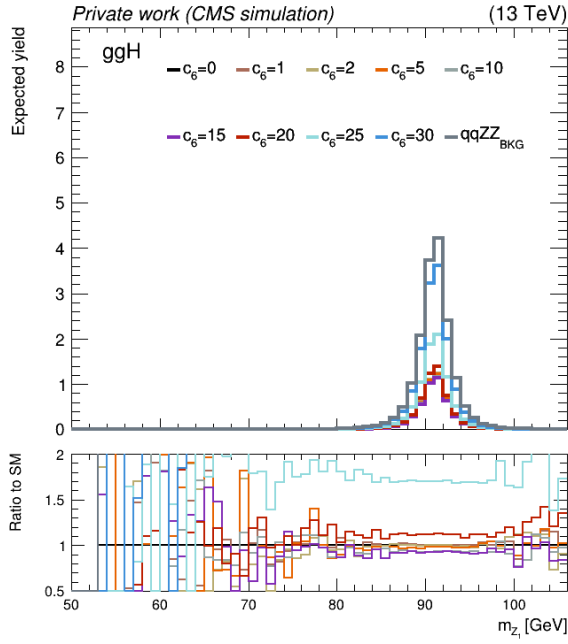
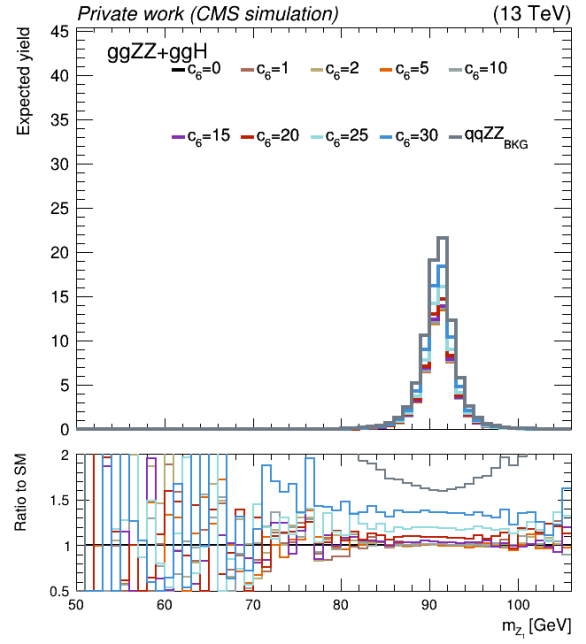**Figure B.15.** Reconstruction level m_{Z_1} distribution for the processes $gg \rightarrow H^* \rightarrow ZZ \rightarrow 4l$ (a) and $gg \rightarrow ZZ \rightarrow 2e2\mu$ where the Higgs boson contribution is included (b). Lower panels present ratios of BSM distributions ($c_6 \neq 0$) to the LO SM distribution ($c_6 = 0$).
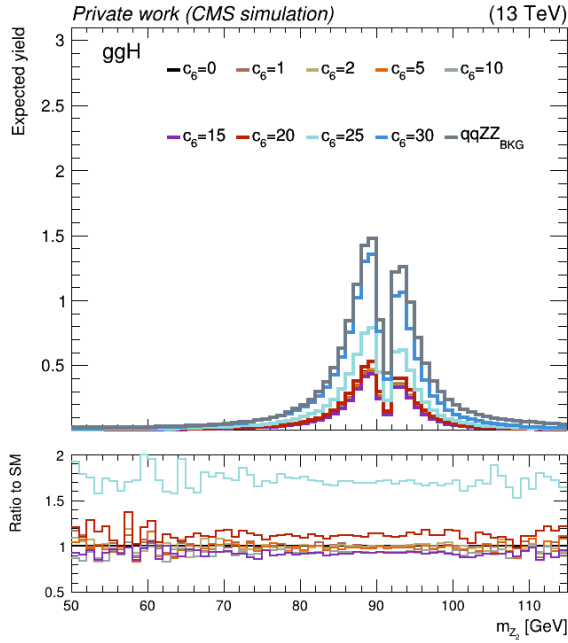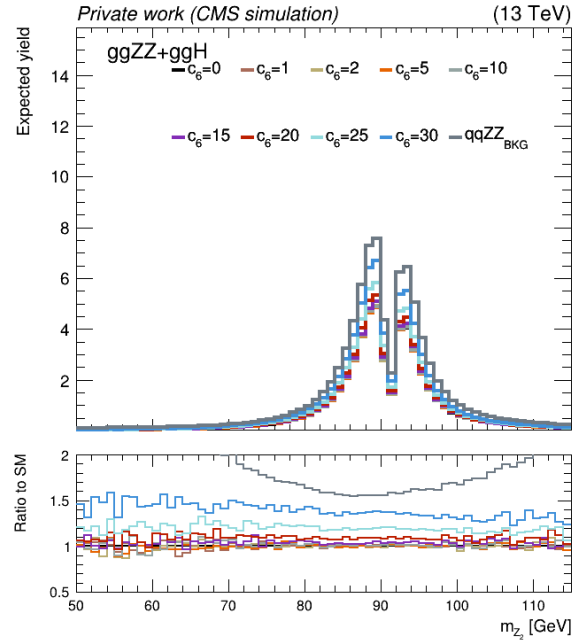

Figure B.16. Reconstruction level m_{Z_1} distribution for the processes $gg \rightarrow H^* \rightarrow ZZ \rightarrow 4l$ (a) and $gg \rightarrow ZZ \rightarrow 2e2\mu$ where the Higgs boson contribution is included (b). Lower panels present ratios of BSM distributions ($c_6 \neq 0$) to the LO SM distribution ($c_6 = 0$).
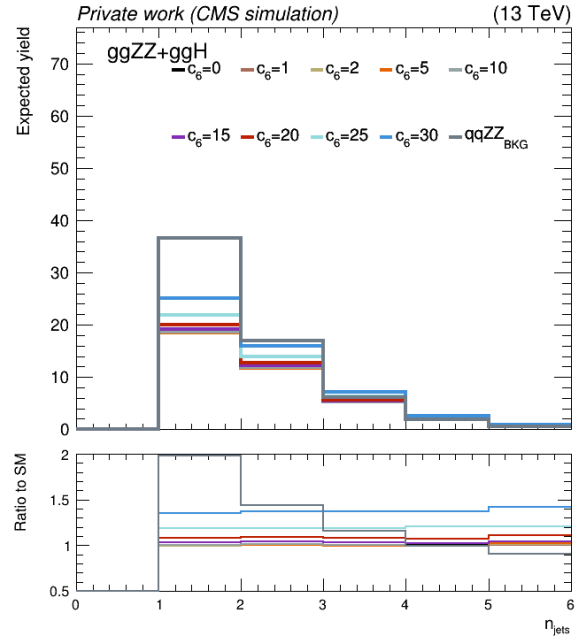
Figure B.17. Reconstruction level n_j distribution for the processes $gg \rightarrow H^* \rightarrow ZZ \rightarrow 4l$ (a) and $gg \rightarrow ZZ \rightarrow 2e2\mu$ where the Higgs boson contribution is included (b). Lower panels present ratios of BSM distributions ($c_6 \neq 0$) to the LO SM distribution ($c_6 = 0$).
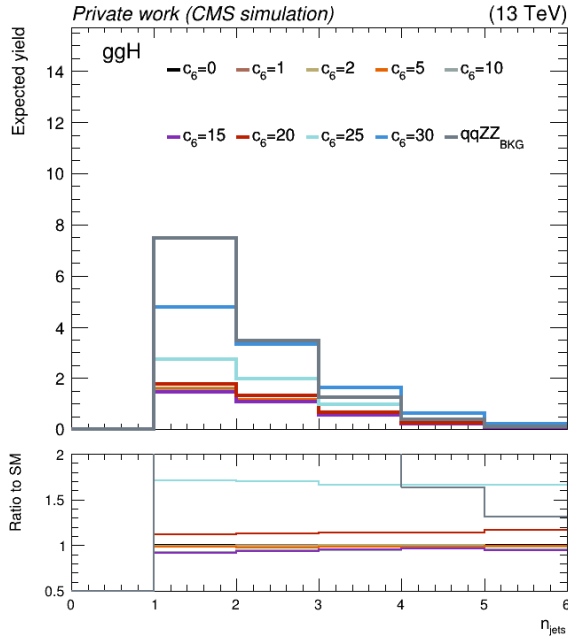

Figure B.18. Reconstruction level $\Delta\phi(H, j_1)$ distribution for the processes $gg \rightarrow H^* \rightarrow ZZ \rightarrow 4l$ (a) and $gg \rightarrow ZZ \rightarrow 2e2\mu$ where the Higgs boson contribution is included (b). Lower panels present ratios of BSM distributions ($c_6 \neq 0$) to the LO SM distribution ($c_6 = 0$).

Appendix C
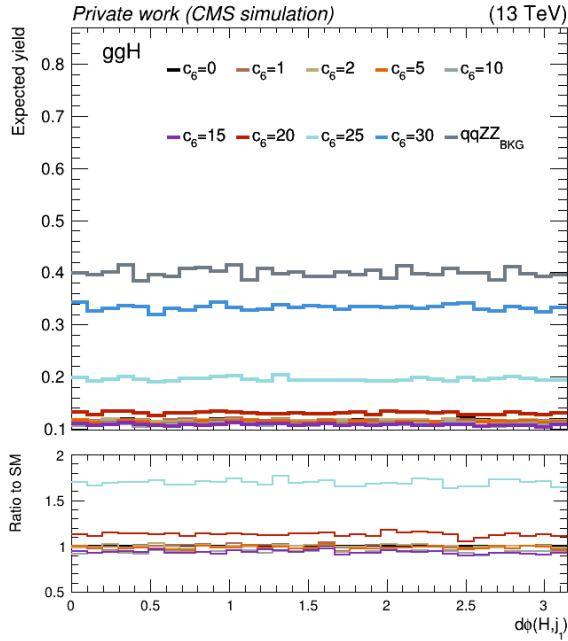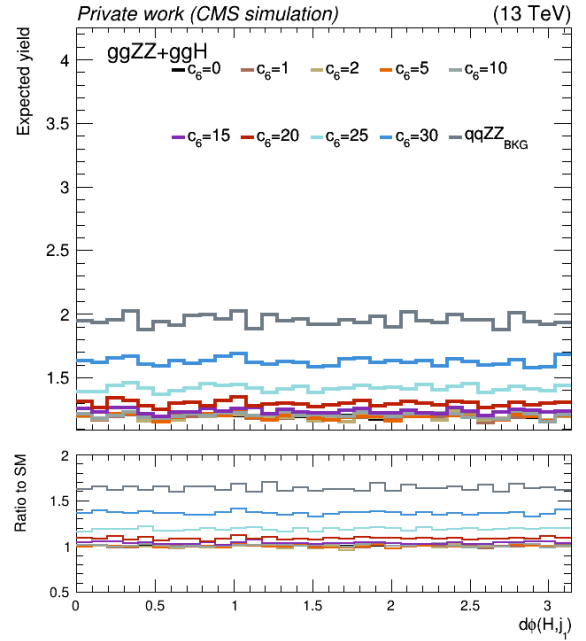
Production cross sections obtained with MATRIX

In this appendix the production cross section results obtained with MATRIX v2.0.1 and v2.1.0. releases are presented. In this was a direct comparison between the two MATRIX releases is available, as well as as an overview of the production cross section for a selection of single- and di-boson production processes. With these results, a reliable reference point in cross section calculation within the CMS collaboration is established.

C.1 Imposed kinematical cuts

The fiducial cuts imposed, within MATRIX v2.1.0, for $W^{\pm}$, Z, $W^{\pm}/Z + \gamma$ production are shown in Tables C.1 and C.2, while the only cut imposed for W^+W^-, ZZ, W^+W^-/ZZ production is $m_{OSSF} > 4$ GeV. Between the two MATRIX releases used there's one differences in setups. Namely, in MATRIX v2.0.1 constraints on dR separation between leptons and a photon were not used, rather they were used in MATRIX v2.1.0 to better control the convergence and the size of the cross section.

Table C.1. Fiducial cuts used for $W^{\pm}/Z$ boson production processes. A slash (/) stand for no explicit requirements.

	$pp \to e^+e^-$	$pp \to e^-\bar{\nu}_e$ / $pp \to e^+\nu_e$	$pp \to \nu_e\bar{\nu}_e$
lepton cuts	$m_{ll} > 50$ GeV	/	/
jet cuts	/	$p_T > 0.01$ GeV, $|\eta| < 5$	/
jet definition		anti-kT algorithm with $R = 0.4$,	

C.2 Results with MATRIX v2.0.1

The production cross section values obtained with MATRIX v2.0.1 are summarized in Tables C.3, C.4, C.5 and C.6.

Table C.2. Fiducial cuts used for $W^{\pm}/Z + \gamma$ production processes. A slash (/) stand for no explicit requirements.

	$pp \to e^+ e^- \gamma$	$pp \to e^- \bar{\nu}_e \gamma$ / $pp \to e^+ \nu_e \gamma$
lepton cuts	$m_{ll} > 30$ GeV, $p_T > 15$ GeV	$|\eta| < 2.5$
jet cuts	/	$p_T > 0.01$ GeV, $|\eta| < 5$
jet definition	anti-kT algorithm with $R = 0.4$	
photon definition	$n = 1$, $\epsilon_\gamma = 1$, $\delta_0 = 0.05$	$n = 1$, $\epsilon_\gamma = 1$, $\delta_0 = 0.4$
photon cuts	$p_T > 15$ GeV, $|\eta| < 2.6$	$p_T > 10$ GeV, $|\eta| < 2.5$
dR separation	$l\gamma > 0.7$	$jj > 0.001$, $j\gamma > 0.05$, $l\gamma > 0.05$

Table C.3. Cross section values at different orders in perturbative expansion of QCD and EW and their combinations for $pp \to W^{\pm}/Z$ production at COM energy of 13.6 TeV.

	Cross section values at 13.6 TeV [nb]			
σ_{ORDER}/process $pp \to$	$pp \to e^+ e^-$	$pp \to e^- \bar{\nu}_e$	$pp \to e^+ \nu_e$	$pp \to \nu_e \bar{\nu}_e$
σ_{LO}	$1.86^{+11.6\%}_{-12.6\%} \pm 0.2\%$	$8.08^{+12.5\%}_{-13.5\%} \pm 0.2\%$	$10.7^{+12.2\%}_{-13.2\%} \pm 0.2\%$	$3.53^{+11.6\%}_{-12.5\%} \pm 0.2\%$
σ_{NLO_QCD}	$2.13^{+2.9\%}_{-4.7\%} \pm 0.2\%$	$9.22^{+3.2\%}_{-5.3\%} \pm 0.2\%$	$12.3^{+3.3\%}_{-5.3\%} \pm 0.2\%$	$4.03^{+2.9\%}_{-4.8\%} \pm 0.2\%$
σ_{NLO_EW}	$1.85^{+11.7\%}_{-12.6\%} \pm 0.2\%$	$8.05^{+12.7\%}_{-13.7\%} \pm 0.2\%$	$10.7^{+12.3\%}_{-13.3\%} \pm 0.2\%$	$3.55^{+11.7\%}_{-12.6\%} \pm 0.2\%$
$\sigma_{NLO\_QCD+NLO\_EW}$	$2.11^{+0.5\%}_{-0.8\%} \pm 0.2\%$	$9.19^{+3.3\%}_{-5.3\%} \pm 0.2\%$	$12.3^{+3.3\%}_{-5.3\%} \pm 0.2\%$	$4.05^{+3.1\%}_{-4.8\%} \pm 0.2\%$
$\sigma_{NLO\_QCD \times NLO\_EW}$	$2.11^{+3.0\%}_{-4.8\%} \pm 0.2\%$	$9.19^{+3.3\%}_{-5.4\%} \pm 0.2\%$	$12.3^{+3.4\%}_{-5.4\%} \pm 0.2\%$	$4.06^{+3.0\%}_{-4.8\%} \pm 0.2\%$
σ_{NNLO_QCD}	$2.09^{+1.0\%}_{-0.9\%} \pm 1.1\%$	$8.86^{+1.3\%}_{-1.0\%} \pm 0.9\%$	$12.2^{+0.5\%}_{-1.2\%} \pm 1.2\%$	$3.93^{+1.0\%}_{-1.0\%} \pm 0.9\%$
$\sigma_{NNLO\_QCD+NLO\_EW}$	$2.07^{+1.0\%}_{-0.9\%} \pm 1.1\%$	$8.82^{+1.3\%}_{-1.0\%} \pm 0.9\%$	$12.1^{+0.6\%}_{-1.2\%} \pm 1.2\%$	$3.95^{+1.1\%}_{-1.1\%} \pm 0.9\%$
$\sigma_{NNLO\_QCD \times NLO\_EW}$	$2.07^{+1.1\%}_{-1.0\%} \pm 1.1\%$	$8.82^{+1.4\%}_{-1.1\%} \pm 0.9\%$	$12.1^{+0.6\%}_{-1.6\%} \pm 1.2\%$	$3.95^{+1.1\%}_{-1.0\%} \pm 0.9\%$

C.3 Results with MATRIX v2.1.0

The production cross section values obtained with MATRIX v2.0.1 are summarized in Tables C.7, C.8, C.9 and C.10.

C.4 Discussion and Comparison

Several conclusions can be drawn based on comparison of the results obtained with two different MATRIX releases.

The gluon-gluon loop induced contribution shows greater stability in the release MATRIX v.2.1.0,

Table C.4. Cross section values at different orders in perturbative expansion of QCD and EW and their combinations for $pp \to W^{\pm}/Z + \gamma$ production at COM energy of 13.6 TeV.

σ_{ORDER}/process $pp \to$	Cross section values at 13.6 TeV [pb]		
	$e^+e^-\gamma$	$e^-\bar{\nu}_e\gamma$	$e^+\nu_e\gamma$
σ_{LO}	$50^{+11.7\%}_{-12.7\%} \pm 6.3\%$	$59.0^{+13.0\%}_{-14.0\%} \pm 0.2\%$	$78.7^{+12.7\%}_{-13.7\%} \pm 0.2\%$
σ_{NLO_QCD}	$65^{+3.6\%}_{-5.3\%} \pm 6.6\%$	$73.5^{+3.1\%}_{-5.1\%} \pm 0.4\%$	$97^{+3.1\%}_{-5.1\%} \pm 0.7\%$
σ_{NNLO_QCD}	$382^{+16.9\%}_{-12.1\%} \pm 18.2\%$	$79^{+1.4\%}_{-1.7\%} \pm 1.7\%$	$103^{+1.2\%}_{-1.7\%} \pm 2.2\%$
σ_{LO_gg}	$34.0^{+23.0\%}_{-17.0\%} \pm 0.3\%$	/	/

Table C.5. Cross section values at different orders in perturbative expansion of QCD and EW and their combinations for $pp \to W^{\pm}Z$ production at COM energy of 13.6 TeV.

σ_{ORDER}/process $pp \to$	Cross section values at 13.6 TeV [fb]			
	$pp \to e^-\mu^-e^+\bar{\nu}_\mu$	$pp \to e^-e^+e^-\bar{\nu}_e$	$pp \to e^-\mu^+e^+\nu_\mu$	$pp \to e^-e^+e^+\nu_e$
σ_{LO}	$173.0^{+8.7\%}_{-9.6\%} \pm 0.1\%$	$169.8^{+8.6\%}_{-9.5\%} \pm 0.2\%$	$244.3^{+8.1\%}_{-9.0\%} \pm 0.2\%$	$240.4^{+8.0\%}_{-8.9\%} \pm 0.2\%$
σ_{NLO_QCD}	$229.0^{+2.6\%}_{-3.4\%} \pm 0.2\%$	$225.1^{+2.6\%}_{-3.1\%} \pm 0.2\%$	$328.2^{+2.7\%}_{-3.3\%} \pm 0.2\%$	$323.4^{+2.7\%}_{-3.3\%} \pm 0.2\%$
σ_{NLO_EW}	$171.0^{+8.8\%}_{-9.7\%} \pm 0.2\%$	$167.4^{+8.7\%}_{-9.6\%} \pm 0.2\%$	$241.5^{+8.2\%}_{-9.1\%} \pm 0.2\%$	$237.2^{+8.1\%}_{-9.0\%} \pm 0.2\%$
$\sigma_{NLO\_QCD+NLO\_EW}$	$227.0^{+2.6\%}_{-3.5\%} \pm 0.2\%$	$222.7^{+2.6\%}_{-3.4\%} \pm 0.3\%$	$325.5^{+2.7\%}_{-3.4\%} \pm 0.2\%$	$320.1^{+2.7\%}_{-3.3\%} \pm 0.2\%$
$\sigma_{NLO\_QCD \times NLO\_EW}$	$226.4^{+2.6\%}_{-3.5\%} \pm 0.2\%$	$221.9^{+2.6\%}_{-3.5\%} \pm 0.3\%$	$324.5^{+2.7\%}_{-3.4\%} \pm 0.2\%$	$319.0^{+2.7\%}_{-3.4\%} \pm 0.2\%$
σ_{NNLO_QCD}	$244^{+1.1\%}_{-1.2\%} \pm 1.1\%$	$238^{+0.4\%}_{-0.7\%} \pm 1.3\%$	$353^{+1.2\%}_{-1.3\%} \pm 1.1\%$	$346.6^{+1.4\%}_{-1.4\%} \pm 0.2\%$
$\sigma_{NNLO\_QCD+NLO\_EW}$	$241^{+1.1\%}_{-1.2\%} \pm 1.1\%$	$235^{+0.4\%}_{-0.7\%} \pm 1.4\%$	$350^{+1.3\%}_{-1.4\%} \pm 1.1\%$	$343^{+1.5\%}_{-1.5\%} \pm 1.4\%$
$\sigma_{NNLO\_QCD \times NLO\_EW}$	$242^{+1.1\%}_{-1.2\%} \pm 1.1\%$	$234^{+0.4\%}_{-0.8\%} \pm 1.4\%$	$349^{+1.2\%}_{-1.3\%} \pm 1.1\%$	$342^{+1.4\%}_{-1.4\%} \pm 1.3\%$

which can be seen when comparing the results from Tables C.6 and C.10. It is worth noting that for example $\sigma_{\mathrm{LO\_gg}}$ varies a lot with the change of PDF replica of the given set when using MATRIX v2.0.1.

Comparing W^+ and W^- (w/o γ) production, processes involving W^+ production are found to have higher cross section value, which is majorly attributed to the composition of the proton where it is assumed to be comprised of 2 up and 1 down (valence) quarks.

Cross sections at NNLO and nNNLO differ (where applicable) by the difference $\sigma_{\mathrm{NLO\_gg}} - \sigma_{\mathrm{LO\_gg}}$ which is in line with how these contributions are defined and added (see Subsection 5.1.3).

When using MATRIX v2.0.1, a 5FS was used in calculation of production cross section of processes which involve W^+W^- bosons. In setup which relies on MATRIX v.2.1.0 a switch was made to 4FS which eliminates the top quark contribution which is evidently overwhelming

Table C.6. Cross section values at different orders in perturbative expansion of QCD and EW and their combinations for $pp \to W^+W^-/ZZ$ production at COM energy of 13.6 TeV.

σ_{ORDER}/process $pp \to$	$pp \to e^-\mu^-e^+\mu^+$	$pp \to e^-e^+e^-e^+$	$pp \to e^-e^+\nu_\mu\bar{\nu}_\mu$	$pp \to e^-\mu^+\nu_\mu\bar{\nu}_e$	$pp \to e^-e^+\nu_e\bar{\nu}_e$
			Cross section values at 13.6 TeV [fb]		
σ_{LO}	$266.3^{+14.5\%}_{-14.6\%} \pm 0.2\%$	$120.2^{+12.0\%}_{-12.7\%} \pm 0.2\%$	$94.7^{+5.0\%}_{-5.9\%} \pm 0.1\%$	$1012^{+3.5\%}_{-4.2\%} \pm 0.1\%$	$1105^{+3.6\%}_{-4.4\%} \pm 0.2\%$
σ_{NLO_QCD}	$323.0^{+4.3\%}_{-7.1\%} \pm 0.3\%$	$144.9^{+3.6\%}_{-5.7\%} \pm 0.2\%$	$115.5^{+1.8\%}_{-2.2\%} \pm 0.2\%$	$2019^{+4.9\%}_{-4.1\%} \pm 0.2\%$	$2131^{+4.7\%}_{-3.9\%} \pm 0.2\%$
σ_{NLO_EW}	$262.2^{+14.6\%}_{-14.7\%} \pm 0.2\%$	$118.1^{+12.2\%}_{-12.8\%} \pm 0.2\%$	$93.2^{+5.2\%}_{-6.0\%} \pm 0.1\%$	$1000^{+3.6\%}_{-4.4\%} \pm 0.1\%$	$1091^{+3.8\%}_{-4.5\%} \pm 0.2\%$
$\sigma_{NLO\_QCD+NLO\_EW}$	$319.1^{+4.3\%}_{-7.0\%} \pm 0.3\%$	$142.9^{+3.6\%}_{-5.7\%} \pm 0.2\%$	$114.0^{+1.8\%}_{-2.2\%} \pm 0.2\%$	$2007^{+4.9\%}_{-4.1\%} \pm 0.2\%$	$2118^{+4.8\%}_{-4.0\%} \pm 0.2\%$
$\sigma_{NLO\_QCD\times NLO\_EW}$	$318.2^{+4.4\%}_{-7.2\%} \pm 0.3\%$	$142.5^{+3.7\%}_{-5.8\%} \pm 0.2\%$	$113.7^{+1.8\%}_{-2.3\%} \pm 0.2\%$	$1996^{+4.9\%}_{-4.1\%} \pm 0.2\%$	$2105^{+4.7\%}_{-3.9\%} \pm 0.2\%$
σ_{NNLO_QCD}	$373^{+4.4\%}_{-5.1\%} \pm 1.1\%$	$160^{+2.4\%}_{-3.0\%} \pm 1.3\%$	$129^{+2.0\%}_{-1.7\%} \pm 0.8\%$	$7754^{+19.3\%}_{-14.3\%} \pm 0.4\%$	$7807^{+19.0\%}_{-14.1\%} \pm 0.5\%$
σ_{nNNLO_QCD}	$438^{+9.7\%}_{-8.5\%} \pm 1.0\%$	$172^{+4.0\%}_{-3.8\%} \pm 1.3\%$	$136^{+2.5\%}_{-2.2\%} \pm 0.8\%$	$7842^{+19.3\%}_{-14.3\%} \pm 0.4\%$	$7897^{+18.9\%}_{-14.0\%} \pm 0.5\%$
$\sigma_{nNNLO\_QCD+NLO\_EW}$	$435^{+9.8\%}_{-8.5\%} \pm 1.0\%$	$170^{+4.1\%}_{-3.8\%} \pm 1.3\%$	$135^{+2.5\%}_{-2.2\%} \pm 0.8\%$	$7830^{+19.3\%}_{-14.3\%} \pm 0.4\%$	$7884^{+18.9\%}_{-14.0\%} \pm 0.5\%$
$\sigma_{nNNLO\_QCD\times NLO\_EW}$	$432^{+9.7\%}_{-8.6\%} \pm 1.0\%$	$169^{+4.0\%}_{-3.9\%} \pm 1.3\%$	$134^{+2.5\%}_{-2.2\%} \pm 0.8\%$	$7750^{+19.1\%}_{-14.2\%} \pm 0.4\%$	$7800^{+18.7\%}_{-13.9\%} \pm 0.5\%$
σ_{LO_gg}	$27.5^{+32.7\%}_{-28.9\%} \pm 0.3\%$	$7.7^{+29.8\%}_{-21.7\%} \pm 0.6\%$	$6.9^{+21.7\%}_{-16.3\%} \pm 0.3\%$	$75.8^{+22.4\%}_{-16.7\%} \pm 0.3\%$	$80.3^{+22.3\%}_{-16.6\%} \pm 0.3\%$
σ_{NLO_gg}	$93^{+38.1\%}_{-28.2\%} \pm 2.2\%$	$19.4^{+28.4\%}_{-19.4\%} \pm 5.2\%$	$13.8^{+16.5\%}_{-13.3\%} \pm 0.5\%$	$163^{+18.2\%}_{-14.3\%} \pm 1.3\%$	$170.8^{+17.8\%}_{-14.1\%} \pm 0.5\%$

Table C.7. Cross section values at different orders in perturbative expansion of QCD and EW and their combinations for $pp \to W^\pm/Z$ production at COM energy of 13.6 TeV.

σ_{ORDER}/process $pp \to$	$pp \to e^-\bar{\nu}_e$	$pp \to e^+\nu_e$	$pp \to \nu_e\bar{\nu}_e$	
			Cross section values at 13.6 TeV [nb]	
σ_{LO}	$1.86^{+11.6\%}_{-12.6\%} \pm 0.2\%$	$8.09^{+12.5\%}_{-13.5\%} \pm 0.2\%$	$10.7^{+12.2\%}_{-13.2\%} \pm 0.2\%$	$3.53^{+11.6\%}_{-12.5\%} \pm 0.2\%$
σ_{NLO_QCD}	$2.13^{+3.0\%}_{-4.8\%} \pm 0.2\%$	$9.23^{+3.2\%}_{-5.3\%} \pm 0.2\%$	$12.3^{+3.3\%}_{-5.2\%} \pm 0.2\%$	$4.03^{+3.0\%}_{-4.8\%} \pm 0.2\%$
σ_{NLO_EW}	$1.85^{+11.7\%}_{-12.7\%} \pm 0.2\%$	$8.05^{+12.7\%}_{-13.7\%} \pm 0.2\%$	$10.7^{+12.3\%}_{-13.3\%} \pm 0.2\%$	$3.55^{+11.7\%}_{-12.6\%} \pm 0.2\%$
$\sigma_{NLO\_QCD+NLO\_EW}$	$2.11^{+3.0\%}_{-4.8\%} \pm 0.2\%$	$9.20^{+3.3\%}_{-5.3\%} \pm 0.2\%$	$12.3^{+3.3\%}_{-5.3\%} \pm 0.2\%$	$4.05^{+3.1\%}_{-4.8\%} \pm 0.2\%$
$\sigma_{NLO\_QCD\times NLO\_EW}$	$2.11^{+3.1\%}_{-4.9\%} \pm 0.2\%$	$9.19^{+3.3\%}_{-5.4\%} \pm 0.2\%$	$12.3^{+3.4\%}_{-5.4\%} \pm 0.2\%$	$4.06^{+3.0\%}_{-4.8\%} \pm 0.2\%$
σ_{NNLO_QCD}	$2.11^{+0.7\%}_{-1.2\%} \pm 1.0\%$	$9.05^{+1.2\%}_{-1.1\%} \pm 0.8\%$	$12.2^{+1.0\%}_{-1.3\%} \pm 0.7\%$	$3.93^{+1.0\%}_{-1.0\%} \pm 0.7\%$
$\sigma_{NNLO\_QCD+NLO\_EW}$	$2.09^{+0.7\%}_{-1.1\%} \pm 1.0\%$	$9.01^{+1.3\%}_{-1.1\%} \pm 0.8\%$	$12.1^{+1.1\%}_{-1.4\%} \pm 0.7\%$	$3.95^{+1.1\%}_{-1.1\%} \pm 0.7\%$
$\sigma_{NNLO\_QCD\times NLO\_EW}$	$2.09^{+0.8\%}_{-1.3\%} \pm 1.0\%$	$9.01^{+1.4\%}_{-1.2\%} \pm 0.8\%$	$12.1^{+1.1\%}_{-1.4\%} \pm 0.7\%$	$3.96^{+1.1\%}_{-1.1\%} \pm 0.7\%$

Table C.8. Cross section values at different orders in perturbative expansion of QCD and EW and their combinations for $pp \to W^\pm/Z + \gamma$ production at COM energy of 13.6 TeV.

σ_{ORDER}/process $pp \to$	Cross section values at 13.6 TeV [pb]		
	$e^+e^-\gamma$	$e^-\bar{\nu}_e\gamma$	$e^+\nu_e\gamma$
σ_{LO}	$5.7^{+10.9\%}_{-11.8\%} \pm 0.2\%$	$58.9^{+13.0\%}_{-14.0\%} \pm 0.2\%$	$78.6^{+12.7\%}_{-13.7\%} \pm 0.2\%$
σ_{NLO_QCD}	$7.2^{+2.8\%}_{-4.3\%} \pm 0.2\%$	$73.3^{+3.1\%}_{-5.1\%} \pm 0.2\%$	$96.5^{+3.0\%}_{-5.0\%} \pm 0.2\%$
σ_{NNLO_QCD}	$7.7^{+1.1\%}_{-1.2\%} \pm 0.9\%$	$76^{+0.7\%}_{-1.3\%} \pm 0.9\%$	$99^{+0.4\%}_{-1.1\%} \pm 0.7\%$
σ_{LO_gg}	$0.032^{+23.0\%}_{-17.0\%} \pm 0.3\%$	/	/

Table C.9. Cross section values at different orders in perturbative expansion of QCD and EW and their combinations for $pp \to W^\pm Z$ production at COM energy of 13.6 TeV.

σ_{ORDER}/process $pp \to$	Cross section values at 13.6 TeV [fb]			
	$pp \to e^-\mu^-e^+\bar{\nu}_\mu$	$pp \to e^-e^+e^-\bar{\nu}_e$	$pp \to e^-\mu^+e^+\nu_\mu$	$pp \to e^-e^+e^+\nu_e$
σ_{LO}	$173.0^{+8.7\%}_{-9.6\%} \pm 0.1\%$	$170.1^{+8.6\%}_{-9.6\%} \pm 0.1\%$	$244.8^{+8.1\%}_{-9.0\%} \pm 0.2\%$	$240.6^{+8.0\%}_{-8.9\%} \pm 0.2\%$
σ_{NLO_QCD}	$229.1^{+2.6\%}_{-3.4\%} \pm 0.2\%$	$225.7^{+2.6\%}_{-3.5\%} \pm 0.2\%$	$328.7^{+2.7\%}_{-3.4\%} \pm 0.2\%$	$323.4^{+2.7\%}_{-3.4\%} \pm 0.2\%$
σ_{NLO_EW}	$171.3^{+8.8\%}_{-9.7\%} \pm 0.2\%$	$168.0^{+8.7\%}_{-9.7\%} \pm 0.2\%$	$242.2^{+8.2\%}_{-9.1\%} \pm 0.2\%$	$237.7^{+8.1\%}_{-9.0\%} \pm 0.2\%$
$\sigma_{NLO\_QCD+NLO\_EW}$	$227.4^{+2.6\%}_{-3.5\%} \pm 0.2\%$	$223.5^{+2.6\%}_{-3.5\%} \pm 0.2\%$	$326.0^{+2.7\%}_{-3.4\%} \pm 0.2\%$	$320.4^{+2.7\%}_{-3.4\%} \pm 0.2\%$
$\sigma_{NLO\_QCD\times NLO\_EW}$	$226.9^{+2.6\%}_{-3.5\%} \pm 0.2\%$	$222.8^{+2.6\%}_{-3.6\%} \pm 0.2\%$	$325.1^{+2.7\%}_{-3.5\%} \pm 0.2\%$	$319.4^{+2.7\%}_{-3.5\%} \pm 0.2\%$
σ_{NNLO_QCD}	$241^{+0.5\%}_{-0.8\%} \pm 1.0\%$	$240^{+1.6\%}_{-1.1\%} \pm 1.0\%$	$351^{+1.2\%}_{-1.3\%} \pm 1.0\%$	$350^{+1.1\%}_{-1.2\%} \pm 1.3\%$
$\sigma_{NNLO\_QCD+NLO\_EW}$	$239^{+0.6\%}_{-0.8\%} \pm 1.1\%$	$2385^{+1.6\%}_{-1.1\%} \pm 1.0\%$	$349^{+1.2\%}_{-1.3\%} \pm 1.0\%$	$347^{+1.1\%}_{-1.2\%} \pm 1.3\%$
$\sigma_{NNLO\_QCD\times NLO\_EW}$	$239^{+0.5\%}_{-0.8\%} \pm 1.0\%$	$237^{+1.6\%}_{-1.1\%} \pm 1.0\%$	$347^{+1.2\%}_{-1.3\%} \pm 1.0\%$	$346^{+1.1\%}_{-1.2\%} \pm 1.3\%$

Table C.10. Cross section values at different orders in perturbative expansion of QCD and EW and their combinations for $pp \to W^+W^-/ZZ$ production at COM energy of 13.6 TeV.

	Cross section values at 13.6 TeV [fb]				
σ_{ORDER}/process $pp \to$	$e^-\mu^-e^+\mu^+$	$e^-e^+e^-e^+$	$e^-e^+\nu_\mu\bar{\nu}_\mu$	$e^-\mu^+\nu_\mu\bar{\nu}_e$	$e^-e^+\nu_e\bar{\nu}_e$
σ_{LO}	$266.4^{+14.4\%}_{-14.6\%} \pm 0.2\%$	$120.2^{+12.0\%}_{-12.7\%} \pm 0.2\%$	$94.7^{+5.0\%}_{-5.9\%} \pm 0.1\%$	$1002^{+3.5\%}_{-4.3\%} \pm 0.1\%$	$1096^{+3.7\%}_{-4.4\%} \pm 0.1\%$
σ_{NLO_QCD}	$322.9^{+4.3\%}_{-7.1\%} \pm 0.3\%$	$144.8^{+3.6\%}_{-5.7\%} \pm 0.3\%$	$115.4^{+1.8\%}_{-2.2\%} \pm 0.2\%$	$1313^{+2.4\%}_{-2.0\%} \pm 0.1\%$	$1428^{+2.4\%}_{-2.0\%} \pm 0.1\%$
σ_{NLO_EW}	$262.9^{+14.6\%}_{-14.7\%} \pm 0.2\%$	$118.3^{+12.2\%}_{-12.8\%} \pm 0.2\%$	$93.3^{+5.2\%}_{-6.0\%} \pm 0.1\%$	$990.7^{+3.7\%}_{-4.4\%} \pm 0.1\%$	$1083^{+3.8\%}_{-4.5\%} \pm 0.1\%$
$\sigma_{NLO\_QCD+NLO\_EW}$	$319.4^{+4.3\%}_{-7.1\%} \pm 0.3\%$	$142.9^{+3.6\%}_{-5.7\%} \pm 0.3\%$	$114.0^{+1.8\%}_{-2.3\%} \pm 0.2\%$	$1303^{+2.4\%}_{-2.0\%} \pm 0.1\%$	$1415^{+2.4\%}_{-2.0\%} \pm 0.1\%$
$\sigma_{NLO\_QCD\times NLO\_EW}$	$318.7^{+4.4\%}_{-7.2\%} \pm 0.3\%$	$142.5^{+3.7\%}_{-5.8\%} \pm 0.3\%$	$113.7^{+1.9\%}_{-2.4\%} \pm 0.2\%$	$1299^{+2.4\%}_{-2.0\%} \pm 0.1\%$	$1411^{+2.4\%}_{-2.0\%} \pm 0.1\%$
σ_{NNLO_QCD}	$375^{+4.0\%}_{-5.0\%} \pm 0.9\%$	$160^{+2.6\%}_{-3.1\%} \pm 1.2\%$	$127.9^{+2.2\%}_{-1.9\%} \pm 0.6\%$	$1498^{+2.9\%}_{-2.5\%} \pm 0.9\%$	$1610^{+2.3\%}_{-2.0\%} \pm 0.7\%$
σ_{nNNLO_QCD}	$392^{+3.1\%}_{-4.5\%} \pm 0.9\%$	$166^{+2.7\%}_{-3.1\%} \pm 1.2\%$	$134.8^{+2.6\%}_{-2.3\%} \pm 0.6\%$	$1576^{+3.4\%}_{-2.9\%} \pm 0.8\%$	$1694^{+2.9\%}_{-2.5\%} \pm 0.7\%$
$\sigma_{nNNLO\_QCD+NLO\_EW}$	$388.6^{+3.1\%}_{-4.5\%} \pm 0.9\%$	$164^{+2.7\%}_{-3.0\%} \pm 1.2\%$	$133.3^{+2.7\%}_{-3.0\%} \pm 0.6\%$	$1565^{+3.5\%}_{-3.0\%} \pm 0.8\%$	$1681^{+3.0\%}_{-2.6\%} \pm 0.7\%$
$\sigma_{nNNLO\_QCD\times NLO\_EW}$	$387.0^{+3.1\%}_{-4.6\%} \pm 0.9\%$	$163^{+2.7\%}_{-3.2\%} \pm 1.2\%$	$132.7^{+2.6\%}_{-2.3\%} \pm 0.6\%$	$1559^{+3.4\%}_{-2.9\%} \pm 0.8\%$	$1674^{+2.9\%}_{-2.5\%} \pm 0.7\%$
σ_{LO_gg}	$27.3^{+32.7\%}_{-28.8\%} \pm 2.2\%$	$7.6^{+29.8\%}_{-21.8\%} \pm 0.6\%$	$6.9^{+21.7\%}_{-16.3\%} \pm 0.4\%$	$71.0^{+23.4\%}_{-17.2\%} \pm 0.7\%$	$75.9^{+23.3\%}_{-17.2\%} \pm 0.4\%$
σ_{NLO_gg}	$44.3^{+13.4\%}_{-16.1\%} \pm 4.1\%$	$13.3^{+18.3\%}_{-14.9\%} \pm 6.0\%$	$13.7^{+16.1\%}_{-13.1\%} \pm 1.4\%$	$150.7^{+18.4\%}_{-14.5\%} \pm 1.1\%$	$160.2^{+18.5\%}_{-14.5\%} \pm 0.8\%$

Acknowledgments

Bibliography

[1] E. Lyndon (ed) and B. Philip (ed), *LHC Machine*, *JINST* **3** (2008) S08001.

[2] K. Hubner, *Designing and building LEP*, *Phys. Rept.* **403-404** (2004) 177–188.

[3] C. E. Gerber, *LHC Highlights and Prospects*, *CERN Yellow Rep. School Proc.* **2** (2021) 161, [arXiv:1909.10919].

[4] **ATLAS** Collaboration, G. Aad et al., *Observation of a new particle in the search for the Standard Model Higgs boson with the ATLAS detector at the LHC*, *Phys. Lett. B* **716** (2012) 1–29, [arXiv:1207.7214].

[5] **CMS** Collaboration, S. Chatrchyan et al., *Observation of a New Boson at a Mass of 125 GeV with the CMS Experiment at the LHC*, *Phys. Lett. B* **716** (2012) 30–61, [arXiv:1207.7235].

[6] I. Zurbano Fernandez et al., *High-Luminosity Large Hadron Collider (HL-LHC): Technical design report*, *CERN-2020-010* **10/2020** (12, 2020).

[7] **CMS** Collaboration, G. L. Bayatian et al., *CMS Physics: Technical Design Report Volume 1: Detector Performance and Software*, *CERN-LHCC-2006-001, CMS-TDR-8-1* (2006).

[8] **CMS** Collaboration, G. Acquistapace et al., *CMS, the magnet project: Technical design report*, *CERN-LHCC-97-10, CMS-TDR-1* (1997).

[9] **CMS** Collaboration, V. Karimäki et al., *The CMS tracker system project: Technical Design Report*, *CERN-LHCC-98-006, CMS-TDR-5* (1997).

[10] **CMS** Collaboration, , *The CMS electromagnetic calorimeter project: Technical Design Report*, *CERN-LHCC-97-033, CMS-TDR-4* (1997).

[11] **CMS** Collaboration, , *The CMS hadron calorimeter project: Technical Design Report*, *CERN-LHCC-97-031, CMS-TDR-2* (1997).

[12] **CMS** Collaboration, , *The CMS muon project: Technical Design Report*, *CERN-LHCC-97-032, CMS-TDR-3* (1997).

[13] **CMS** Collaboration, A. M. Sirunyan et al., *Particle-flow reconstruction and global event description with the CMS detector*, *JINST* **12** (2017), no. 10 P10003, [arXiv:1706.04965].

[14] S. Ghosh, *Highlights from the Compact Muon Solenoid (CMS) Experiment*, *Universe* **5** (01, 2019) 28.

[15] V. Halyo, A. Hunt, P. Jindal, P. LeGresley, and P. Lujan, *GPU Enhancement of the Trigger to Extend Physics Reach at the LHC*, *JINST* **8** (2013) P10005, [arXiv:1305.4855].

[16] **CMS** Collaboration, S. Chatrchyan et al., *Description and Performance of Track and Primary-Vertex Reconstruction with the CMS Tracker*, *JINST* **9** (2014), no. 10 P10009, [arXiv:1405.6569].

[17] A. Benaglia, *The cms ecal performance with examples*, *Journal of Instrumentation* **9** (2014), no. 02 C02008.

[18] **CMS** Collaboration, S. Chatrchyan et al., *Energy Calibration and Resolution of the CMS Electromagnetic Calorimeter in pp Collisions at $\sqrt{s} = 7$ TeV*, *JINST* **8** (2013) P09009, [arXiv:1306.2016].

[19] **CMS** Collaboration, A. Hayrapetyan et al., *Performance of the CMS electromagnetic calorimeter in pp collisions at $\sqrt{s}$ = 13 TeV*, *JINST* **19** (2024), no. 09 P09004, [arXiv:2403.15518].

[20] Baur, Gerhard and others, *Heavy ion physics programme in cms*, *European Physical Journal C* **32** (2004) s69–s202.

[21] **CMS HCAL/ECAL** Collaboration, , *The cms barrel calorimeter response to particle beams from 2 to* 350 *GeV/c*, *European Physical Journal C* **60** (2009) 359.

[22] H. Seo, *Rpc hit contribution to cms muon reconstruction at lhc*, *Nuclear Instruments and Methods in Physics Research Section A Accelerators Spectrometers Detectors and Associated Equipment* **718** (2013) 437–439.

[23] **CMS** Collaboration, A. M. Sirunyan et al., *Performance of the CMS muon detector and muon reconstruction with proton-proton collisions at $\sqrt{s} = 13$ TeV*, *JINST* **13** (2018), no. 06 P06015, [arXiv:1804.04528].

[24] **CMS** Collaboration, V. Khachatryan et al., *The CMS trigger system*, *JINST* **12** (2017), no. 01 P01020, [arXiv:1609.02366].

[25] T. Speer, W. Adam, R. Fruhwirth, A. Strandlie, T. Todorov, and M. Winkler, *Track reconstruction in the CMS tracker*, *Nucl. Instrum. Meth. A* **559** (2006) 143–147.

[26] Billoir, Pierre and Qian, S., *Simultaneous pattern recognition and track fitting by the Kalman filtering method*, *Nucl. Instrum. Meth. A* **294** (1990) 219–228.

[27] W. Adam, R. Frühwirth, A. Strandlie, and T. Todorov, *Reconstruction of electrons with the gaussian-sum filter in the cms tracker at the lhc*, *Journal of Physics G: Nuclear and Particle Physics* **31** (2005) N9–N20.

[28] M. Cacciari, G. P. Salam, and G. Soyez, *The anti-k_t jet clustering algorithm*, *JHEP* **04** (2008) 063, [arXiv:0802.1189].

[29] G. Apollinari, O. Brüning, T. Nakamoto, and L. Rossi, *High Luminosity Large Hadron Collider HL-LHC*, *CERN Yellow Rep.* (2015), no. 5 1–19, [arXiv:1705.08830].

[30] O. Brüning, H. Gray, K. Klein, M. Lamont, M. Narain, R. Polifka, and L. Rossi, *The scientific potential and technological challenges of the high-luminosity large hadron collider program*, *Reports on Progress in Physics* **85** (03, 2022).

[31] **CMS** Collaboration, A. Tumasyan et al., *The Phase-2 Upgrade of the CMS Tracker*, (6, 2017).

[32] **CMS** Collaboration, , *The Phase-2 Upgrade of the CMS Endcap Calorimeter*, (2017).

[33] **CMS** Collaboration, , *The Phase-2 Upgrade of the CMS Barrel Calorimeters*, (2017).

[34] **CMS** Collaboration, T. Hebbeker and A. Korytov, *The Phase-2 Upgrade of the CMS Muon Detectors*, (9, 2017).

[35] **CMS** Collaboration, A. Zabi, J. W. Berryhill, E. Perez, and A. D. Tapper, *The Phase-2 Upgrade of the CMS Level-1 Trigger*, (2020).

[36] C. Collaboration, *The Phase-2 Upgrade of the CMS Data Acquisition and High Level Trigger*, (2021).

[37] **CMS** Collaboration, J. N. Butler and T. Tabarelli de Fatis, *A MIP Timing Detector for the CMS Phase-2 Upgrade*, (2019).

[38] S. Gundacker, E. Auffray, B. Frisch, P. Jarron, A. Knapitsch, T. Meyer, M. Pizzichemi, and P. Lecoq, *Time of flight positron emission tomography towards* 100 *ps resolution with L(Y)SO: an experimental and theoretical analysis*, *JINST* **8** (2013) P07014.

[39] D. Anderson, A. Apreysan, A. Bornheim, J. Duarte, H. Newman, C. Pena, A. Ronzhin, M. Spiropulu, J. Trevor, S. Xie, and R.-Y. Zhu, *Precision timing measurements for high energy photons*, *Nucl. Inst. Meth. A* **787** (2015) 94–97.

[40] E. Albuquerque et al., *TOFHIR2: the readout ASIC of the CMS barrel MIP Timing Deector*, *JINST* **19** (2024), no. 05 P05048.

[41] G. Pellegrini, P. Fernández-Martínez, M. Baselga, C. Fleta, D. Flores, V. Greco, S. Hidalgo, I. Mandić, G. Kramberger, D. Quirion, and M. Ullan, *Technology developments and first measurements of low gain avalanche detectors (LGAD) for high energy physics applications*, *Nucl. Inst. Meth. A* **765** (2014) 12–16.

[42] H. Sun et al., *Characterization of the CMS Endcap Timing Layer readout chip prototype with charge injection*, *JINST* **16** (2021), no. 06 P06038, [`arXiv:2106.00174`].

[43] H. Sun et al., *A radiation tolerant clock generator for the CMS Endcap Timing Layer readout chip*, *JINST* **17** (2022) C03038, [`arXiv:2110.12625`].

[44] P. Barria, *Precision Timing with the CMS MIP Timing Detector*, *XI International Conference on New Frontiers in Physics* (2022).

[45] M. Tornago, *Characterisation of UFSD4 production by FBK*, *17th "Trento" Workshop in Advanced Silicon Radiation Detectors* (2022).

[46] S. Ramo, *Currents induced by electron motion*, *Proceedings of the IRE* **27** (1939), no. 9 584–585.

[47] W. Shockley, *Currents induced by electron motion*, *Appl. Phys.* **9** (1938), no. 10 635–636.

[48] V. O. R. Maes W., De Meyer K., *Impact ionization in silicon: A review and update*, *Solid-State Electronics* **33** (1999), no. 10 705–718.

[49] M. Ferrero et al., *Radiation resistant LGAD design*, *Nucl. Instrum. Meth. A* **919** (2019) 16–26, [arXiv:1802.01745].

[50] Y. Shimizu, H. Takamizawa, K. Inoue, F. Yano, S. Kudo, A. Nishida, T. Toyama, and Y. Nagai, *Impact of carbon co-implantation on boron distribution and activation in silicon studied by atom probe tomography and spreading resistance measurements*, *Japanese Journal of Applied Physics* **55** (Feb., 2016).

[51] R. Wunstorf, W. Bugg, J. Walter, F. Garber, and D. Larson, *Investigations of donor and acceptor removal and long term annealing in silicon with different boron/phosphorus ratios*, *Nucl. Inst. Meth. A* **377** (1996), no. 2 228–233.

[52] G. Paternoster, *New developments in ultra fast silicon detectors at FBK*, *31th RD50 Workshop* **CERN, Geneva** (2017).

[53] M. Ferrero and et al., *Ultra-fast silicon detectors : design, tests, and performances*, *Boca Raton: CRC Press* (2021).

[54] R. Mulargia et al., *Temperature dependence of the response of ultra fast silicon detectors*, *Journal of Instrumentation* **11** (dec, 2016) C12013.

[55] V. Sola et al., *Ultra-fast silicon detectors for 4D tracking*, *Journal of Instrumentation* **12** (feb, 2017) C02072.

[56] N. Cartiglia et al., *Beam test results of a 16ps timing system based on ultra-fast silicon detectors*, *Nucl. Instrum. Meth. A* **850** (2017) 83–88.

[57] N. Cartiglia et al., *Timing capabilities of ultra-fast silicon detectors*, *Acta Physica Polonica B Proceedings Supplement* **7** (03, 2014).

[58] F. Siviero et al., *Design optimization of the UFSD inter-pad region*, *Nucl. Instrum. Meth. A* **1061** (2024) 169153.

[59] M. Printz, *P-stop isolation study of irradiated n-in-p type silicon strip sensors for harsh radiation environments*, *Nucl. Instrum. Meth. A* **831** (2016) 38–43. Proceedings of the 10th International "Hiroshima" Symposium on the Development and Application of Semiconductor Tracking Detectors.

[60] E. N. Ramos, *CRadiation tolerance study of LGADs for the CMS Endcap Timing Layer detector*, *18th "Trento" Workshop in Advanced Silicon Radiation Detectors* (2023).

[61] K. Technologies, *Keysight technologies b1505a power device analyzer/curve tracer*, .

[62] K. Huang, *Quarks, Leptons and Gauge Fields*. World Scientific, 1992.

[63] E. Leader and E. Predazzi, *An Introduction to Gauge Theories and Modern Particle Physics, Volume 1*. Cambridge University Press, 1996.

[64] F. Halzen and A. D. Martin, *Quarks and Leptons: An Introductory Course in Modern Particle Physics*. John Wiley & Sons, 1991.

[65] F. Mandl and G. Shaw, *Quantum Field Theory*. John Wiley & Sons, 2 ed., 2010.

[66] L. H. Ryder, *Quantum Field Theory*. Cambridge University Press, 2 ed., 1996.

[67] M. E. Peskin and D. V. Schroeder, *An Introduction to Quantum Field Theory*. CRC Press, 2018.

[68] G. 't Hooft and M. J. G. Veltman, *Regularization and Renormalization of Gauge Fields*, *Nucl. Phys. B* **44** (1972) 189–213.

[69] J. Goldstone, *Field Theories with Superconductor Solutions*, *Nuovo Cim.* **19** (1961) 154–164.

[70] J. Goldstone, A. Salam, and S. Weinberg, *Broken Symmetries*, *Phys. Rev.* **127** (1962) 965–970.

[71] P. W. Higgs, *Broken Symmetries and the Masses of Gauge Bosons*, *Phys. Rev. Lett.* **13** (1964) 508–509.

[72] F. Englert and R. Brout, *Broken Symmetry and the Mass of Gauge Vector Mesons*, *Phys. Rev. Lett.* **13** (1964) 321–323.

[73] W. J. Marciano and H. Pagels, *Quantum Chromodynamics: A Review*, *Phys. Rept.* **36** (1978) 137.

[74] S. L. Glashow, *Partial-symmetries of weak interactions*, *Nuclear Physics* **22** (1961) 579–588.

[75] A. Salam, *Weak and Electromagnetic Interactions*, *Conf. Proc. C* **680519** (1968) 367–377.

[76] S. Weinberg, *A Model of Leptons*, *Phys. Rev. Lett.* **19** (1967) 1264–1266.

[77] C. Grosse-Knetter and R. Kogerler, *Unitary gauge, Stuckelberg formalism and gauge invariant models for effective lagrangians*, *Phys. Rev. D* **48** (1993) 2865–2876, [hep-ph/9212268].

[78] **Super-Kamiokande** Collaboration, Y. Fukuda et al., *Evidence for oscillation of atmospheric neutrinos*, *Phys. Rev. Lett.* **81** (1998) 1562–1567, [hep-ex/9807003].

[79] **NOvA** Collaboration, M. A. Acero et al., *First Measurement of Neutrino Oscillation Parameters using Neutrinos and Antineutrinos by NOvA*, *Phys. Rev. Lett.* **123** (2019), no. 15 151803, [arXiv:1906.04907].

[80] C. Giunti and C. W. Kim, *Fundamentals of Neutrino Physics and Astrophysics*. Oxford university press, 2007.

[81] R. Szafron and M. Zralek, *Neutrino oscillation beyond the Standard Model*, *Prog. Part. Nucl. Phys.* **64** (2010) 210–212.

[82] M. Kobayashi and T. Maskawa, *CP Violation in the Renormalizable Theory of Weak Interaction*, *Prog. Theor. Phys.* **49** (1973) 652–657.

[83] L. Wolfenstein, *Parametrization of the kobayashi-maskawa matrix*, *Phys. Rev. Lett.* **51** (1983) 1945–1947.

[84] P. D. Group, W. R. L, et al., *Review of particle physics*, *Progress of Theoretical and Experimental Physics* **2022** (2022) 083C01.

[85] **Particle Data Group** Collaboration, M. Tanabashi and E. al., *Review of particle physics*, *Phys. Rev. D* **98** (Aug, 2018) 030001.

[86] **LHC Higgs Cross Section Working Group** Collaboration, D. de Florian et al., *Handbook of LHC Higgs Cross Sections: 4. Deciphering the Nature of the Higgs Sector*, *CERN Yellow Rep. Monogr.* **2** (2017) 1–869, [`arXiv:1610.07922`].

[87] **CMS** Collaboration, A. Hayrapetyan et al., *Measurements of inclusive and differential cross sections for the Higgs boson production and decay to four-leptons in proton-proton collisions at $\sqrt{s} = 13$ TeV*, *JHEP* **08** (2023) 040, [`arXiv:2305.07532`].

[88] **CMS** Collaboration, V. Khachatryan et al., *Measurement of differential and integrated fiducial cross sections for Higgs boson production in the four-lepton decay channel in pp collisions at $\sqrt{s} = 7$ and 8 TeV*, *JHEP* **04** (2016) 005, [`arXiv:1512.08377`].

[89] N. Berger et al., *Simplified Template Cross Sections – Stage 1.1 and 1.2*, *LHCHXSWG-2019-003, DESY 19-070, LHCHWG-INT-2025-001* (6, 2019) [`arXiv:1906.02754`].

[90] **CMS** Collaboration, S. Chatrchyan et al., *Search for the Standard Model Higgs Boson in the Decay Channel H to ZZ to 4 Leptons in pp Collisions at $\sqrt{s} = 7$ TeV*, *Phys. Rev. Lett.* **108** (2012) 111804, [`arXiv:1202.1997`].

[91] **CMS** Collaboration, S. Chatrchyan et al., *Search for the Standard Model Higgs Boson Decaying into Two Photons in pp Collisions at $\sqrt{s} = 7$ TeV*, *Phys. Lett. B* **710** (2012) 403–425, [`arXiv:1202.1487`].

[92] **ATLAS, CMS** Collaboration, G. Aad et al., *Measurements of the Higgs boson production and decay rates and constraints on its couplings from a combined ATLAS and CMS analysis of the LHC pp collision data at $\sqrt{s} = 7$ and 8 TeV*, *JHEP* **08** (2016) 045, [`arXiv:1606.02266`].

[93] **CMS** Collaboration, , *Combined Higgs boson production and decay measurements with up to 137 fb^{-1} of proton-proton collision data at $\sqrt{s} = 13$ TeV*, *CMS-PAS-HIG-19-005* (2020).

[94] **CMS** Collaboration, A. M. Sirunyan et al., *Combined measurements of Higgs boson couplings in proton–proton collisions at $\sqrt{s} = 13$ TeV*, *Eur. Phys. J. C* **79** (2019), no. 5 421, [`arXiv:1809.10733`].

[95] **CMS** Collaboration, A. Tumasyan et al., *A portrait of the Higgs boson by the CMS experiment ten years after the discovery.*, *Nature* **607** (2022), no. 7917 60–68, [`arXiv:2207.00043`]. [Erratum: Nature 623, (2023)].

[96] **ATLAS** Collaboration, G. Aad et al., *Combined measurements of Higgs boson production and decay using up to 80 fb^{-1} of proton-proton collision data at $\sqrt{s} = 13$ TeV collected with the ATLAS experiment*, *Phys. Rev. D* **101** (2020), no. 1 012002, [`arXiv:1909.02845`].

[97] **ATLAS** Collaboration, G. Aad et al., *A detailed map of Higgs boson interactions by the ATLAS experiment ten years after the discovery*, *Nature* **607** (2022), no. 7917 52–59, [`arXiv:2207.00092`]. [Erratum: Nature 612, E24 (2022)].

[98] **CMS** Collaboration, A. Hayrapetyan et al., *Measurement of the Higgs boson mass and width using the four-lepton final state in proton-proton collisions at $\sqrt{s} = 13$ TeV, Phys. Rev. D* **111** (2025), no. 9 092014, [arXiv:2409.13663].

[99] **CMS** Collaboration, S. Chatrchyan et al., *Measurement of the Properties of a Higgs Boson in the Four-Lepton Final State, Phys. Rev. D* **89** (2014), no. 9 092007, [arXiv:1312.5353].

[100] **CMS** Collaboration, S. Chatrchyan et al., *Study of the Mass and Spin-Parity of the Higgs Boson Candidate Via Its Decays to Z Boson Pairs, Phys. Rev. Lett.* **110** (2013), no. 8 081803, [arXiv:1212.6639].

[101] **CMS** Collaboration, V. Khachatryan et al., *Constraints on the spin-parity and anomalous HVV couplings of the Higgs boson in proton collisions at 7 and 8 TeV, Phys. Rev. D* **92** (2015), no. 1 012004, [arXiv:1411.3441].

[102] **ATLAS** Collaboration, G. Aad et al., *Measurements of Higgs boson production and couplings in the four-lepton channel in pp collisions at center-of-mass energies of 7 and 8 TeV with the ATLAS detector, Phys. Rev. D* **91** (2015), no. 1 012006, [arXiv:1408.5191].

[103] **ATLAS** Collaboration, G. Aad et al., *Study of the spin and parity of the Higgs boson in diboson decays with the ATLAS detector, Eur. Phys. J. C* **75** (2015), no. 10 476, [arXiv:1506.05669]. [Erratum: Eur.Phys.J.C 76, 152 (2016)].

[104] **CMS** Collaboration, V. Khachatryan et al., *Constraints on the Higgs Boson Width from Off-Shell Production and Decay to Z-Boson Pairs, Phys. Lett. B* **736** (2014) 64–85, [arXiv:1405.3455].

[105] **CMS** Collaboration, V. Khachatryan et al., *Limits on the Higgs boson lifetime and width from its decay to four charged leptons, Phys. Rev. D* **92** (2015), no. 7 072010, [arXiv:1507.06656].

[106] **ATLAS** Collaboration, G. Aad et al., *Constraints on the off-shell Higgs boson signal strength in the high-mass ZZ and WW final states with the ATLAS detector, Eur. Phys. J. C* **75** (2015), no. 7 335, [arXiv:1503.01060].

[107] **LHC Higgs Cross Section Working Group** Collaboration, J. R. Andersen et al., *Handbook of LHC Higgs Cross Sections: 3. Higgs Properties*, (7, 2013) [arXiv:1307.1347].

[108] **CMS** Collaboration, A. Hayrapetyan et al., *Constraints on the Higgs boson self-coupling from the combination of single and double Higgs boson production in proton-proton collisions at $\sqrt{s} = 13$ TeV, Phys. Lett. B* **861** (2025) 139210, [arXiv:2407.13554].

[109] **ATLAS** Collaboration, G. Aad et al., *Constraints on the Higgs boson self-coupling from single- and double-Higgs production with the ATLAS detector using pp collisions at $\sqrt{s} = 13$ TeV, Phys. Lett. B* **843** (2023) 137745, [arXiv:2211.01216].

[110] **CMS** Collaboration, A. M. Sirunyan et al., *Measurements of production cross sections of the Higgs boson in the four-lepton final state in proton–proton collisions at $\sqrt{s} = 13$ TeV, Eur. Phys. J. C* **81** (2021), no. 6 488, [arXiv:2103.04956].

[111] **CMS** Collaboration, A. M. Sirunyan et al., *Measurements of Higgs boson production cross sections and couplings in the diphoton decay channel at $\sqrt{s}$ = 13 TeV*, *JHEP* **07** (2021) 027, [arXiv:2103.06956].

[112] **CMS** Collaboration, A. M. Sirunyan et al., *Search for nonresonant Higgs boson pair production in final states with two bottom quarks and two photons in proton-proton collisions at $\sqrt{s}$ = 13 TeV*, *JHEP* **03** (2021) 257, [arXiv:2011.12373].

[113] **CMS** Collaboration, A. Tumasyan et al., *Measurements of the Higgs boson production cross section and couplings in the W boson pair decay channel in proton-proton collisions at $\sqrt{s} = 13$ TeV*, *Eur. Phys. J. C* **83** (2023), no. 7 667, [arXiv:2206.09466].

[114] **CMS** Collaboration, A. M. Sirunyan et al., *Measurement of the Higgs boson production rate in association with top quarks in final states with electrons, muons, and hadronically decaying tau leptons at $\sqrt{s}$ = 13 TeV*, *Eur. Phys. J. C* **81** (2021), no. 4 378, [arXiv:2011.03652].

[115] **CMS** Collaboration, A. M. Sirunyan et al., *Inclusive search for highly boosted Higgs bosons decaying to bottom quark-antiquark pairs in proton-proton collisions at $\sqrt{s}$ = 13 TeV*, *JHEP* **12** (2020) 085, [arXiv:2006.13251].

[116] **CMS** Collaboration, A. M. Sirunyan et al., *Observation of Higgs boson decay to bottom quarks*, *Phys. Rev. Lett.* **121** (2018), no. 12 121801, [arXiv:1808.08242].

[117] **CMS** Collaboration, A. M. Sirunyan et al., *Search for $t\bar{t}H$ production in the $H \to b\bar{b}$ decay channel with leptonic $t\bar{t}$ decays in proton-proton collisions at $\sqrt{s} = 13$ TeV*, *JHEP* **03** (2019) 026, [arXiv:1804.03682].

[118] **CMS** Collaboration, A. Tumasyan et al., *Measurements of Higgs boson production in the decay channel with a pair of τ leptons in proton–proton collisions at $\sqrt{s} = 13$ TeV*, *Eur. Phys. J. C* **83** (2023), no. 7 562, [arXiv:2204.12957].

[119] **CMS** Collaboration, A. M. Sirunyan et al., *Evidence for Higgs boson decay to a pair of muons*, *JHEP* **01** (2021) 148, [arXiv:2009.04363].

[120] **CMS** Collaboration, A. M. Sirunyan et al., *Search for nonresonant Higgs boson pair production in final states with two bottom quarks and two photons in proton-proton collisions at $\sqrt{s}$ = 13 TeV*, *JHEP* **03** (2021) 257, [arXiv:2011.12373].

[121] **CMS** Collaboration, A. Tumasyan et al., *Search for nonresonant Higgs boson pair production in final state with two bottom quarks and two tau leptons in proton-proton collisions at $\sqrt{s} = 13$ TeV*, *Phys. Lett. B* **842** (2023) 137531, [arXiv:2206.09401].

[122] **CMS** Collaboration, A. Tumasyan et al., *Search for Higgs Boson Pair Production in the Four b Quark Final State in Proton-Proton Collisions at $\sqrt{s} = 13$ TeV*, *Phys. Rev. Lett.* **129** (2022), no. 8 081802, [arXiv:2202.09617].

[123] **CMS** Collaboration, A. Tumasyan et al., *Search for Nonresonant Pair Production of Highly Energetic Higgs Bosons Decaying to Bottom Quarks*, *Phys. Rev. Lett.* **131** (2023), no. 4 041803, [arXiv:2205.06667].

[124] **CMS** Collaboration, A. Hayrapetyan et al., *Search for Higgs boson pair production with one associated vector boson in proton-proton collisions at $\sqrt{s}$ = 13 TeV*, JHEP **10** (2024) 061, [arXiv:2404.08462].

[125] **CMS** Collaboration, A. Tumasyan et al., *Search for Higgs boson pairs decaying to WW^*WW^*, $WW^*\tau\tau$, and $\tau\tau\tau\tau$ in proton-proton collisions at $\sqrt{s}$ = 13 TeV*, JHEP **07** (2023) 095, [arXiv:2206.10268].

[126] **CMS** Collaboration, A. Hayrapetyan et al., *Search for Higgs boson pair production in the $b\bar{b}W^+W^-$ decay mode in proton-proton collisions at $\sqrt{s}$ = 13 TeV*, JHEP **07** (2024) 293, [arXiv:2403.09430].

[127] **ATLAS** Collaboration, G. Aad et al., *Measurement of the properties of Higgs boson production at $\sqrt{s} = 13$ TeV in the $H \to \gamma\gamma$ channel using $139\,fb^{-1}$ of pp collision data with the ATLAS experiment*, JHEP **07** (2023) 088, [arXiv:2207.00348].

[128] **ATLAS** Collaboration, G. Aad et al., *Higgs boson production cross-section measurements and their EFT interpretation in the 4ℓ decay channel at $\sqrt{s} = 13$ TeV with the ATLAS detector*, Eur. Phys. J. C **80** (2020), no. 10 957, [arXiv:2004.03447]. [Erratum: Eur.Phys.J.C 81, 29 (2021), Erratum: Eur.Phys.J.C 81, 398 (2021)].

[129] **ATLAS** Collaboration, G. Aad et al., *Measurements of Higgs boson production cross-sections in the $H \to \tau^+\tau^-$ decay channel in pp collisions at $\sqrt{s}$ = 13 TeV with the ATLAS detector*, JHEP **08** (2022) 175, [arXiv:2201.08269].

[130] **ATLAS** Collaboration, G. Aad et al., *Measurements of Higgs boson production by gluon-gluon fusion and vector-boson fusion using $H \to WW^* \to e\nu\mu\nu$ decays in pp collisions at $\sqrt{s} = 13$ TeV with the ATLAS detector*, Phys. Rev. D **108** (2023) 032005, [arXiv:2207.00338].

[131] **ATLAS** Collaboration, G. Aad et al., *Measurements of WH and ZH production in the $H \to b\bar{b}$ decay channel in pp collisions at 13 TeV with the ATLAS detector*, Eur. Phys. J. C **81** (2021), no. 2 178, [arXiv:2007.02873].

[132] **ATLAS** Collaboration, G. Aad et al., *Measurements of Higgs bosons decaying to bottom quarks from vector boson fusion production with the ATLAS experiment at $\sqrt{s} = 13$ TeV*, Eur. Phys. J. C **81** (2021), no. 6 537, [arXiv:2011.08280].

[133] **ATLAS** Collaboration, G. Aad et al., *Measurement of Higgs boson decay into b-quarks in associated production with a top-quark pair in pp collisions at $\sqrt{s} = 13$ TeV with the ATLAS detector*, JHEP **06** (2022) 097, [arXiv:2111.06712].

[134] **ATLAS** Collaboration, G. Aad et al., *Search for Higgs boson pair production in the two bottom quarks plus two photons final state in pp collisions at $\sqrt{s} = 13$ TeV with the ATLAS detector*, Phys. Rev. D **106** (2022), no. 5 052001, [arXiv:2112.11876].

[135] **ATLAS** Collaboration, G. Aad et al., *Search for resonant and non-resonant Higgs boson pair production in the $b\bar{b}\tau^+\tau^-$ decay channel using 13 TeV pp collision data from the ATLAS detector*, JHEP **07** (2023) 040, [arXiv:2209.10910].

[136] **ATLAS** Collaboration, G. Aad et al., *Search for nonresonant pair production of Higgs bosons in the bb̄bb̄ final state in pp collisions at $\sqrt{s} = 13$ TeV with the ATLAS detector*, *Phys. Rev. D* **108** (2023), no. 5 052003, [arXiv:2301.03212].

[137] U. Haisch and G. Koole, *Off-shell Higgs production at the LHC as a probe of the trilinear Higgs coupling*, *JHEP* **02** (2022) 030, [arXiv:2111.12589].

[138] R. Batterman, ed., *The Oxford Handbook of Philosophy of Physics*. OUP, Oxford, 2013.

[139] H. Georgi, *Effective field theory*, *Ann. Rev. Nucl. Part. Sci.* **43** (1993) 209–252.

[140] F. Jegerlehner, *The Standard model as a low-energy effective theory: what is triggering the Higgs mechanism?*, *Acta Phys. Polon. B* **45** (2014), no. 6 1167, [arXiv:1304.7813].

[141] M. E. Peskin, *Beyond the standard model*, in *The 1996 European School of High-Energy Physics (formerly CERN / JINR School of Physics)*, pp. 49–142, 5, 1997. hep-ph/9705479.

[142] G. 't Hooft, *Renormalizable Lagrangians for Massive Yang-Mills Fields*, *Nucl. Phys. B* **35** (1971) 167–188.

[143] C. G. Bollini and J. J. Giambiagi, *Dimensional Renormalization: The Number of Dimensions as a Regularizing Parameter*, *Nuovo Cim. B* **12** (1972) 20–26.

[144] E. Fermi, *Tentativo di una teoria dell'emissione dei raggi beta*, *Ric. Sci.* **4** (1933) 491–495.

[145] I. Brivio and M. Trott, *The Standard Model as an Effective Field Theory*, *Phys. Rept.* **793** (2019) 1–98, [arXiv:1706.08945].

[146] S. Weinberg, *Baryon and Lepton Nonconserving Processes*, *Phys. Rev. Lett.* **43** (1979) 1566–1570.

[147] B. Grzadkowski, M. Iskrzynski, M. Misiak, and J. Rosiek, *Dimension-Six Terms in the Standard Model Lagrangian*, *JHEP* **10** (2010) 085, [arXiv:1008.4884].

[148] E. E. Jenkins, A. V. Manohar, and M. Trott, *Renormalization Group Evolution of the Standard Model Dimension Six Operators I: Formalism and lambda Dependence*, *JHEP* **10** (2013) 087, [arXiv:1308.2627].

[149] E. E. Jenkins, A. V. Manohar, and M. Trott, *Renormalization Group Evolution of the Standard Model Dimension Six Operators II: Yukawa Dependence*, *JHEP* **01** (2014) 035, [arXiv:1310.4838].

[150] R. Alonso, E. E. Jenkins, A. V. Manohar, and M. Trott, *Renormalization Group Evolution of the Standard Model Dimension Six Operators III: Gauge Coupling Dependence and Phenomenology*, *JHEP* **04** (2014) 159, [arXiv:1312.2014].

[151] C. Grojean, E. E. Jenkins, A. V. Manohar, and M. Trott, *Renormalization Group Scaling of Higgs Operators and \Gamma(h -> \gamma \gamma)*, *JHEP* **04** (2013) 016, [arXiv:1301.2588].

[152] R. Alonso, H.-M. Chang, E. E. Jenkins, A. V. Manohar, and B. Shotwell, *Renormalization group evolution of dimension-six baryon number violating operators*, *Phys. Lett. B* **734** (2014) 302–307, [arXiv:1405.0486].

[153] J. F. Nieves and P. B. Pal, *Generalized Fierz identities*, *Am. J. Phys.* **72** (2004) 1100–1108, [hep-ph/0306087].

[154] G. F. Giudice, C. Grojean, A. Pomarol, and R. Rattazzi, *The Strongly-Interacting Light Higgs*, *JHEP* **06** (2007) 045, [hep-ph/0703164].

[155] G. Buchalla, O. Cata, and C. Krause, *A Systematic Approach to the SILH Lagrangian*, *Nucl. Phys. B* **894** (2015) 602–620, [arXiv:1412.6356].

[156] Q.-H. Cao, Y. Liu, and S.-R. Yuan, *Unitarity Bounds and Basis Transformations in SMEFT: An Analysis of Warsaw and SILH Bases*, *test* (9, 2023) [arXiv:2309.14079].

[157] G. Degrassi, P. P. Giardino, F. Maltoni, and D. Pagani, *Probing the Higgs self coupling via single Higgs production at the LHC*, *JHEP* **12** (2016) 080, [arXiv:1607.04251].

[158] M. Gorbahn and U. Haisch, *Indirect probes of the trilinear Higgs coupling: $gg \to h$ and $h \to \gamma\gamma$*, *JHEP* **10** (2016) 094, [arXiv:1607.03773].

[159] T. Hahn and M. Perez-Victoria, *Automatized one loop calculations in four-dimensions and D-dimensions*, *Comput. Phys. Commun.* **118** (1999) 153–165, [hep-ph/9807565].

[160] M. Gorbahn and U. Haisch, *Two-loop amplitudes for Higgs plus jet production involving a modified trilinear Higgs coupling*, *JHEP* **04** (2019) 062, [arXiv:1902.05480].

[161] W. Bizoń, U. Haisch, and L. Rottoli, *Constraints on the quartic Higgs self-coupling from double-Higgs production at future hadron colliders*, *JHEP* **10** (2019) 267, [arXiv:1810.04665].

[162] S. Borowka, C. Duhr, F. Maltoni, D. Pagani, A. Shivaji, and X. Zhao, *Probing the scalar potential via double Higgs boson production at hadron colliders*, *JHEP* **04** (2019) 016, [arXiv:1811.12366].

[163] W. Bizon, M. Gorbahn, U. Haisch, and G. Zanderighi, *Constraints on the trilinear Higgs coupling from vector boson fusion and associated Higgs production at the LHC*, *JHEP* **07** (2017) 083, [arXiv:1610.05771].

[164] R. Boughezal, J. M. Campbell, R. K. Ellis, C. Focke, W. Giele, X. Liu, F. Petriello, and C. Williams, *Color singlet production at NNLO in MCFM*, *Eur. Phys. J. C* **77** (2017), no. 1 7, [arXiv:1605.08011].

[165] J. M. Campbell, R. K. Ellis, and C. Williams, *Bounding the Higgs Width at the LHC Using Full Analytic Results for $gg \to e^- e^+ \mu^- \mu^+$*, *JHEP* **04** (2014) 060, [arXiv:1311.3589].

[166] J. M. Campbell and R. K. Ellis, *MCFM for the Tevatron and the LHC*, *Nucl. Phys. B Proc. Suppl.* **205-206** (2010) 10–15, [arXiv:1007.3492].

[167] J. M. Campbell, R. K. Ellis, and C. Williams, *Vector Boson Pair Production at the LHC*, *JHEP* **07** (2011) 018, [arXiv:1105.0020].

[168] J. M. Campbell and R. K. Ellis, *Higgs Constraints from Vector Boson Fusion and Scattering*, *JHEP* **04** (2015) 030, [arXiv:1502.02990].

[169] Y. Gao, A. V. Gritsan, Z. Guo, K. Melnikov, M. Schulze, and N. V. Tran, *Spin determination of single-produced resonances at hadron colliders*, *Phys. Rev. D* **81** (Apr, 2010) 075022.

[170] S. Bolognesi, Y. Gao, A. V. Gritsan, K. Melnikov, M. Schulze, N. V. Tran, and A. Whitbeck, *Spin and parity of a single-produced resonance at the lhc*, *Phys. Rev. D* **86** (Nov, 2012) 095031.

[171] I. Anderson et al., *Constraining Anomalous HVV Interactions at Proton and Lepton Colliders*, *Phys. Rev. D* **89** (2014), no. 3 035007, [arXiv:1309.4819].

[172] A. V. Gritsan, R. Röntsch, M. Schulze, and M. Xiao, *Constraining anomalous Higgs boson couplings to the heavy flavor fermions using matrix element techniques*, *Phys. Rev. D* **94** (2016), no. 5 055023, [arXiv:1606.03107].

[173] A. V. Gritsan, J. Roskes, U. Sarica, M. Schulze, M. Xiao, and Y. Zhou, *New features in the JHU generator framework: constraining Higgs boson properties from on-shell and off-shell production*, *Phys. Rev. D* **102** (2020), no. 5 056022, [arXiv:2002.09888].

[174] S. Dulat, T.-J. Hou, J. Gao, M. Guzzi, J. Huston, P. Nadolsky, J. Pumplin, C. Schmidt, D. Stump, and C. P. Yuan, *New parton distribution functions from a global analysis of quantum chromodynamics*, *Phys. Rev. D* **93** (2016), no. 3 033006, [arXiv:1506.07443].

[175] J. Pumplin, D. R. Stump, J. Huston, H. L. Lai, P. M. Nadolsky, and W. K. Tung, *New generation of parton distributions with uncertainties from global QCD analysis*, *JHEP* **07** (2002) 012, [hep-ph/0201195].

[176] M. Grazzini, S. Kallweit, and M. Wiesemann, *Fully differential NNLO computations with MATRIX*, *Eur. Phys. J. C* **78** (2018), no. 7 537, [arXiv:1711.06631].

[177] S. Kallweit, J. M. Lindert, P. Maierhöfer, S. Pozzorini, and M. Schönherr, *NLO electroweak automation and precise predictions for W+multijet production at the LHC*, *JHEP* **04** (2015) 012, [arXiv:1412.5157].

[178] S. Kallweit, J. M. Lindert, P. Maierhofer, S. Pozzorini, and M. Schönherr, *NLO QCD+EW predictions for V + jets including off-shell vector-boson decays and multijet merging*, *JHEP* **04** (2016) 021, [arXiv:1511.08692].

[179] F. Cascioli, P. Maierhofer, and S. Pozzorini, *Scattering Amplitudes with Open Loops*, *Phys. Rev. Lett.* **108** (2012) 111601, [arXiv:1111.5206].

[180] F. Buccioni, S. Pozzorini, and M. Zoller, *On-the-fly reduction of open loops*, *Eur. Phys. J. C* **78** (2018), no. 1 70, [arXiv:1710.11452].

[181] A. Denner, S. Dittmaier, and L. Hofer, *COLLIER - A fortran-library for one-loop integrals*, *PoS* **LL2014** (2014) 071, [arXiv:1407.0087].

[182] A. Denner, S. Dittmaier, and L. Hofer, *Collier: a fortran-based Complex One-Loop LIbrary in Extended Regularizations*, *Comput. Phys. Commun.* **212** (2017) 220–238, [arXiv:1604.06792].

[183] G. Ossola, C. G. Papadopoulos, and R. Pittau, *CutTools: A Program implementing the OPP reduction method to compute one-loop amplitudes*, *JHEP* **03** (2008) 042, [arXiv:0711.3596].

[184] A. van Hameren, *OneLOop: For the evaluation of one-loop scalar functions*, *Comput. Phys. Commun.* **182** (2011) 2427–2438, [arXiv:1007.4716].

[185] S. Catani and M. H. Seymour, *A General algorithm for calculating jet cross-sections in NLO QCD*, *Nucl. Phys. B* **485** (1997) 291–419, [hep-ph/9605323]. [Erratum: Nucl.Phys.B 510, 503–504 (1998)].

[186] S. Catani and M. Grazzini, *An NNLO subtraction formalism in hadron collisions and its application to Higgs boson production at the LHC*, *Phys. Rev. Lett.* **98** (2007) 222002, [hep-ph/0703012].

[187] T. Gehrmann, A. von Manteuffel, and L. Tancredi, *The two-loop helicity amplitudes for* $q\bar{q}' \to V_1 V_2 \to 4$ *leptons*, *JHEP* **09** (2015) 128, [arXiv:1503.04812].

[188] T. Gehrmann, A. von Manteuffel, and L. Tancredi, *The VVamp project*, http://vvamp.hepforge.org.

[189] M. Grazzini, S. Kallweit, J. M. Lindert, S. Pozzorini, and M. Wiesemann, *NNLO QCD + NLO EW with Matrix+OpenLoops: precise predictions for vector-boson pair production*, *JHEP* **02** (2020) 087, [arXiv:1912.00068].

[190] C. W. Bauer, A. Frink, and R. Kreckel, *Introduction to the GiNaC framework for symbolic computation within the C++ programming language*, *J. Symb. Comput.* **33** (2002) 1–12, [cs/0004015].

[191] A. Buckley, J. Ferrando, S. Lloyd, K. Nordström, B. Page, M. Rüfenacht, M. Schönherr, and G. Watt, *LHAPDF6: parton density access in the LHC precision era*, *Eur. Phys. J. C* **75** (2015) 132, [arXiv:1412.7420].

[192] **NNPDF** Collaboration, V. Bertone, S. Carrazza, N. P. Hartland, and J. Rojo, *Illuminating the photon content of the proton within a global PDF analysis*, *SciPost Phys.* **5** (2018), no. 1 008, [arXiv:1712.07053].

[193] T. Gehrmann, M. Grazzini, S. Kallweit, P. Maierhöfer, A. von Manteuffel, S. Pozzorini, D. Rathlev, and L. Tancredi, W^+W^- *Production at Hadron Colliders in Next to Next to Leading Order QCD*, *Phys. Rev. Lett.* **113** (2014), no. 21 212001, [arXiv:1408.5243].

[194] **NNPDF** Collaboration, R. D. Ball et al., *Parton distributions from high-precision collider data*, *Eur. Phys. J. C* **77** (2017), no. 10 663, [arXiv:1706.00428].

[195] **NNPDF** Collaboration, R. D. Ball et al., *Parton distributions for the LHC Run II*, *JHEP* **04** (2015) 040, [arXiv:1410.8849].

[196] **NNPDF** Collaboration, R. D. Ball, V. Bertone, F. Cerutti, L. Del Debbio, S. Forte, A. Guffanti, J. I. Latorre, J. Rojo, and M. Ubiali, *Unbiased global determination of parton distributions and their uncertainties at NNLO and at LO*, *Nucl. Phys. B* **855** (2012) 153–221, [arXiv:1107.2652].

[197] **CMS** Collaboration, , *Open source project CMS Software*,
https://github.com/cms-sw/cmssw?tab=readme-ov-file.

[198] CERN, *CERN Batch Service*, https://batchdocs.web.cern.ch/index.html.

[199] HTCSS, *HTCondor Software Suite (HTCSS) for automating and managing High Throughput workloads and computing capacity*, https://research.cs.wisc.edu/htcondor/.

[200] **Particle Data Group** Collaboration, C. Patrignani et al., *Review of Particle Physics*, *Chin. Phys. C* **40** (2016), no. 10 100001.

[201] **CMS** Collaboration, A. M. Sirunyan et al., *Measurements of* $\text{pp} \rightarrow \text{ZZ}$ *production cross sections and constraints on anomalous triple gauge couplings at* $\sqrt{s} = 13\,TeV$, *Eur. Phys. J. C* **81** (2021), no. 3 200, [arXiv:2009.01186].

[202] **ATLAS** Collaboration, G. Aad et al., *Fiducial and differential cross sections of Higgs boson production measured in the four-lepton decay channel in* pp *collisions at* $\sqrt{s}$=8 *TeV with the ATLAS detector*, *Phys. Lett. B* **738** (2014) 234–253, [arXiv:1408.3226].

[203] **ATLAS** Collaboration, M. Aaboud et al., *Measurement of inclusive and differential cross sections in the* $H \rightarrow ZZ^* \rightarrow 4\ell$ *decay channel in* pp *collisions at* $\sqrt{s} = 13$ *TeV with the ATLAS detector*, *JHEP* **10** (2017) 132, [arXiv:1708.02810].

[204] **ATLAS** Collaboration, G. Aad et al., *Measurements of the Higgs boson inclusive and differential fiducial cross sections in the* 4ℓ *decay channel at* $\sqrt{s} = 13$ *TeV*, *Eur. Phys. J. C* **80** (2020), no. 10 942, [arXiv:2004.03969].

[205] **CMS** Collaboration, , *Luminosity measurement in proton-proton collisions at* $13.6\,\text{TeV}$ *in 2022 at CMS*, .

[206] **CMS** Collaboration, V. Chekhovsky et al., *Measurements of the Higgs boson production cross section in the four-lepton final state in proton-proton collisions at* $\sqrt{s}$ = 13.6 *TeV*, *JHEP* **05** (2025) 079, [arXiv:2501.14849].

[207] P. Nason, *A New method for combining NLO QCD with shower Monte Carlo algorithms*, *JHEP* **11** (2004) 040, [hep-ph/0409146].

[208] S. Frixione, P. Nason, and C. Oleari, *Matching NLO QCD computations with Parton Shower simulations: the POWHEG method*, *JHEP* **11** (2007) 070, [arXiv:0709.2092].

[209] S. Alioli, P. Nason, C. Oleari, and E. Re, *A general framework for implementing NLO calculations in shower Monte Carlo programs: the POWHEG BOX*, *JHEP* **06** (2010) 043, [arXiv:1002.2581].

[210] S. Alioli, P. Nason, C. Oleari, and E. Re, *NLO Higgs boson production via gluon fusion matched with shower in POWHEG*, *JHEP* **04** (2009) 002, [arXiv:0812.0578].

[211] P. Nason and C. Oleari, *NLO Higgs boson production via vector-boson fusion matched with shower in POWHEG*, *JHEP* **02** (2010) 037, [arXiv:0911.5299].

[212] G. Luisoni, P. Nason, C. Oleari, and F. Tramontano, $HW^{\pm}/HZ$ + *0 and 1 jet at NLO with the POWHEG BOX interfaced to GoSam and their merging within MiNLO*, *JHEP* **10** (2013) 083, [arXiv:1306.2542].

[213] H. B. Hartanto, B. Jager, L. Reina, and D. Wackeroth, *Higgs boson production in association with top quarks in the POWHEG BOX*, *Phys. Rev. D* **91** (2015), no. 9 094003, [arXiv:1501.04498].

[214] K. Hamilton, P. Nason, E. Re, and G. Zanderighi, *NNLOPS simulation of Higgs boson production*, *JHEP* **10** (2013) 222, [arXiv:1309.0017].

[215] A. Karlberg et al., *Ad interim recommendations for the Higgs boson production cross sections at $\sqrt{s} = 13.6$ TeV*, arXiv:2402.09955.

[216] T. Melia, P. Nason, R. Rontsch, and G. Zanderighi, *W^+W^-, WZ and ZZ production in the POWHEG BOX*, *JHEP* **11** (2011) 078, [arXiv:1107.5051].

[217] A. Bierweiler, T. Kasprzik, and J. H. Kühn, *Vector-boson pair production at the LHC to $\mathcal{O}(\alpha^3)$ accuracy*, *JHEP* **12** (2013) 071, [arXiv:1305.5402].

[218] M. Bonvini, F. Caola, S. Forte, K. Melnikov, and G. Ridolfi, *Signal-background interference effects for $gg \to H \to W^+W^-$ beyond leading order*, *Phys. Rev. D* **88** (2013), no. 3 034032, [arXiv:1304.3053].

[219] K. Melnikov and M. Dowling, *Production of two Z-bosons in gluon fusion in the heavy top quark approximation*, *Phys. Lett. B* **744** (2015) 43–47, [arXiv:1503.01274].

[220] C. S. Li, H. T. Li, D. Y. Shao, and J. Wang, *Soft gluon resummation in the signal-background interference process of $gg \to h^* \to ZZ$*, *JHEP* **08** (2015) 065, [arXiv:1504.02388].

[221] G. Passarino, *Higgs CAT*, *Eur. Phys. J. C* **74** (2014) 2866, [arXiv:1312.2397].

[222] **CMS** Collaboration, A. M. Sirunyan et al., *Measurements of properties of the Higgs boson decaying into the four-lepton final state in pp collisions at $\sqrt{s} = 13$ TeV*, *JHEP* **11** (2017) 047, [arXiv:1706.09936].

[223] J. Alwall, R. Frederix, S. Frixione, V. Hirschi, F. Maltoni, O. Mattelaer, H. S. Shao, T. Stelzer, P. Torrielli, and M. Zaro, *The automated computation of tree-level and next-to-leading order differential cross sections, and their matching to parton shower simulations*, *JHEP* **07** (2014) 079, [arXiv:1405.0301].

[224] **CMS** Collaboration, A. M. Sirunyan et al., *Extraction and validation of a new set of CMS PYTHIA8 tunes from underlying-event measurements*, *Eur. Phys. J. C* **80** (2020), no. 1 4, [arXiv:1903.12179].

[225] **GEANT4** Collaboration, S. Agostinelli et al., *GEANT4 - A Simulation Toolkit*, *Nucl. Instrum. Meth. A* **506** (2003) 250–303.

[226] J. Allison et al., *Geant4 developments and applications*, *IEEE Trans. Nucl. Sci.* **53** (2006) 270.

[227] **CMS** Collaboration, A. M. Sirunyan et al., *Measurements of the Higgs boson width and anomalous HVV couplings from on-shell and off-shell production in the four-lepton final state*, *Phys. Rev. D* **99** (2019), no. 11 112003, [arXiv:1901.00174].

[228] **CMS** Collaboration, A. M. Sirunyan et al., *Constraints on anomalous Higgs boson couplings using production and decay information in the four-lepton final state*, *Phys. Lett. B* **775** (2017) 1–24, [arXiv:1707.00541].

[229] **CMS** Collaboration, A. M. Sirunyan et al., *Electron and photon reconstruction and identification with the CMS experiment at the CERN LHC*, *JINST* **16** (2021), no. 05 P05014, [arXiv:2012.06888].

[230] **Particle Data Group** Collaboration, S. Navas et al., *Review of particle physics*, *Phys. Rev. D* **110** (2024), no. 3 030001.

[231] J. E. Gaiser, *Charmonium Spectroscopy From Radiative Decays of the J/ψ and ψ'*, other thesis, , 8, 1982.

[232] M. Oreglia, *A Study of the Reactions $\psi' \to \gamma\gamma\psi$*, other thesis, SLAC, 12, 1980.

[233] T. Skwarnicki, *A study of the radiative CASCADE transitions between the Upsilon-Prime and Upsilon resonances*. PhD thesis, Cracow, INP, 1986.

[234] **ATLAS, CMS, LHC Higgs Combination Group** Collaboration, , *Procedure for the LHC Higgs boson search combination in Summer 2011*, .

[235] G. Cowan, K. Cranmer, E. Gross, and O. Vitells, *Asymptotic formulae for likelihood-based tests of new physics*, *Eur. Phys. J. C* **71** (2011) 1554, [arXiv:1007.1727]. [Erratum: Eur.Phys.J.C 73, 2501 (2013)].

[236] **CMS** Collaboration, A. Hayrapetyan et al., *The CMS Statistical Analysis and Combination Tool: Combine*, *Comput. Softw. Big Sci.* **8** (2024), no. 1 19, [arXiv:2404.06614].

[237] A. Ballestrero, A. Belhouari, G. Bevilacqua, V. Kashkan, and E. Maina, *PHANTOM: A Monte Carlo event generator for six parton final states at high energy colliders*, *Comput. Phys. Commun.* **180** (2009) 401–417, [arXiv:0801.3359].

[238] M. Grazzini, *NNLO predictions for the Higgs boson signal in the $H \to WW \to l\nu l\nu$ and $H \to ZZ \to 4l$ decay channels*, *JHEP* **02** (2008) 043, [arXiv:0801.3232].

[239] M. Grazzini and H. Sargsyan, *Heavy-quark mass effects in Higgs boson production at the LHC*, *JHEP* **09** (2013) 129, [arXiv:1306.4581].

[240] F. Caola, K. Melnikov, R. Röntsch, and L. Tancredi, *QCD corrections to ZZ production in gluon fusion at the LHC*, *Phys. Rev. D* **92** (2015), no. 9 094028, [arXiv:1509.06734].

[241] J. M. Campbell, R. K. Ellis, M. Czakon, and S. Kirchner, *Two loop correction to interference in $gg \to ZZ$*, *JHEP* **08** (2016) 011, [arXiv:1605.01380].

[242] F. Caola, M. Dowling, K. Melnikov, R. Röntsch, and L. Tancredi, *QCD corrections to vector boson pair production in gluon fusion including interference effects with off-shell Higgs at the LHC*, *JHEP* **07** (2016) 087, [arXiv:1605.04610].

[243] **CMS** Collaboration, A. M. Sirunyan et al., *Identification of heavy-flavour jets with the CMS detector in pp collisions at 13 TeV*, *JINST* **13** (2018), no. 05 P05011, [arXiv:1712.07158].

[244] S. Gieseke, T. Kasprzik, and J. H. Kühn, *Vector-boson pair production and electroweak corrections in HERWIG++*, *Eur. Phys. J. C* **74** (2014), no. 8 2988, [arXiv:1401.3964].

[245] G. Cowan, *Statistical data analysis*. Oxford University Press, 1998.

[246] **CMS** Collaboration, A. Hayrapetyan et al., *The CMS Statistical Analysis and Combination Tool: Combine*, *Comput. Softw. Big Sci.* **8** (2024), no. 1 19, [arXiv:2404.06614].

Biografija

Lazar Marković was born on August 6, 1996, in Belgrade. He graduated from the Zemun Gymnasium in 2015. He completed his undergraduate studies at the Faculty of Physics, University of Belgrade, in the program of Theoretical and Experimental Physics in 2020, with an average grade of 9.59 (nine point fifty-nine out of 10).

He obtained his Master's degree in Physics at the same faculty in 2021, also in the program of Theoretical and Experimental Physics, with an average grade of 10 (ten). During his Master's studies, Lazar joined the CMS Collaboration at CERN. His Master's thesis, titled "Search for New Phenomena in the Production and Decay of the Higgs Boson Using the Effective Field Theory Approach," was defended under the supervision of Prof. Dr. Predrag Milenović at the Faculty of Physics, with the highest grade (10). Simultaneously, as a member of the ATLAS Collaboration at CERN, Lazar attended CERN's Summer School, where he conducted research and prepared a final report on supersymmetry, titled "Gluino Pair Production at the LHC."

Lazar Marković enrolled in the PhD program in Physics in the academic year 2021/2022, in the field of Nuclear and High Energy Physics, at the Faculty of Physics, University of Belgrade, and the Department of Physics, University of Turin. From January 2022 to August 2023, he spent most of his time in Turin conducting research and professional training, working in the Laboratory for Innovative Silicon Detectors. From August 2023 to August 2024, Lazar spent most of his time at CERN, engaged in research and development in Monte Carlo simulations of proton–proton collisions and in developing techniques and methods for measuring the Higgs boson self-coupling. Based on his work and acquired expertise, Lazar became the CMS Collaboration contact person for the MATRIX Monte Carlo event generator and the HZZ MC contact person within CMS, thus becoming a collaboration-level expert responsible for simulations of all processes relevant for measurements processes and internal reviews within the HZZ group. At both universities, Lazar passed all required examinations, achieving an average grade of 10 (ten) at the University of Belgrade.

Lazar has attended three major CERN schools dedicated to high-energy physics, statistical data analysis methods, and experimental technologies. He has also participated in several workshops and conferences, presenting the results of his research.

Since March 2021, Lazar has been teaching computer-based exercises in the Elementary Particle Physics course, and since November 2021, he has been involved in the Advanced Course in Elementary Particle Physics 1. He is one of the co-authors of the laboratory manual for these courses and is currently contributing to the preparation of an accompanying problem book. Since October 2024, Lazar has been conducting problem-solving and laboratory exercises in two courses: (1) Nuclear and Particle Physics and (2) Nuclear Physics. For the course Nuclear Physics, he is one of the co-authors of the laboratory manual.

Since March 2022, Lazar has been employed at the Faculty of Physics, University of Belgrade, as a Research Assistant Trainee, and since October 2024, he has been employed as a Teaching Assistant in the field of Nuclear Physics.

Statement of Authorship

Author's name and surname: *Lazar Marković*
Student ID number: **8011/2021**

I hereby declare

that the doctoral dissertation titled

Measurement of triple self-coupling of the Higgs boson in the four lepton decay channel with the CMS experiment

- is the result of my own research work;

- that this dissertation, in whole or in part, has not been submitted for the award of any other degree at any higher education institution;

- that all results have been correctly presented i

- that I have not violated copyright or used the intellectual property of others.

Date   **Author's signature**

17.11.2025.   _____

Statement on the Identity of the Printed and Electronic Versions of the Doctoral Dissertation

Author's name and surname: *Lazar Marković*
Student ID number: **8011/2021**
Study program: *Nuclear and High Energy Physics*
Thesis title: *Measurement of triple self-coupling of the Higgs boson in the four lepton decay channel with the CMS experiment*
Supervisors: *Prof. Dr. Predrag Milenović (University of Belgrade), Prof. Dr. Roberto Covarelli (University of Turin)*

I hereby declare that the printed version of my doctoral dissertation is identical to the electronic version submitted for archiving in the **Digital Repository of the University of Belgrade.**.

I authorize the publication of my personal data related to the award of the academic title Doctor of Science, including my name, surname, year and place of birth, and date of thesis defense.

These personal data may be published on the websites of the digital library, in the electronic catalog, and in University of Belgrade publications.

Date   **Author's signature**

17.11.2025.   _____

Statement on the Use of the Doctoral Dissertation

I authorize the University Library Svetozar Marković to include my doctoral dissertation titled

Measurement of triple self-coupling of the Higgs boson in the four lepton decay channel with the CMS experiment

in the Digital Repository of the University of Belgrade, as my original work.

I have submitted the dissertation, along with all appendices, in electronic format suitable for permanent archiving

The dissertation stored in the University of Belgrade Digital Repository and made available in open access may be used by anyone who complies with the provisions of the selected Creative Commons license indicated below:

1. Attribution (CC BY)

2. Attribution – NonCommercial (CC BY-NC)

3. Attribution – NonCommercial – NoDerivatives (CC BY-NC-ND)

4. Attribution – NonCommercial – ShareAlike (CC BY-NC-SA)

5. Attribution – NoDerivatives (CC BY-ND)

6. Attribution – ShareAlike (CC BY-SA)

(Please circle only one of the six offered licenses. A brief description of each license is attached to this statement.)

Date   **Author's signature**

17.11.2025.   _____

1. Attribution. You allow reproduction, distribution, public communication of the work, and adaptations, provided that the name of the author is indicated in the manner specified by the author or the licensor, even for commercial purposes. This is the most open of all licenses.

2. Attribution – NonCommercial. You allow reproduction, distribution, and public communication of the work, and adaptations, provided that the name of the author is indicated in the manner specified by the author or the licensor. This license does not permit commercial use of the work.

3. Attribution – NonCommercial – NoDerivatives. You allow reproduction, distribution, and public communication of the work, without modifications, transformations, or use of the work within another work, provided that the name of the author is indicated in the manner specified by the author or the licensor. This license does not permit commercial use of the work. Compared to all other licenses, this license imposes the greatest restriction on the scope of rights to use the work.

4. Attribution – NonCommercial – ShareAlike. You allow reproduction, distribution, and public communication of the work, and adaptations, provided that the name of the author is indicated in the manner specified by the author or the licensor, and that any adaptation is distributed under the same or a similar license. This license does not permit commercial use of the work or of its adaptations.

5. Attribution – NoDerivatives. You allow reproduction, distribution, and public communication of the work, without modifications, transformations, or use of the work within another work, provided that the name of the author is indicated in the manner specified by the author or the licensor. This license permits commercial use of the work.

6. Attribution – ShareAlike. You allow reproduction, distribution, and public communication of the work, and adaptations, provided that the name of the author is indicated in the manner specified by the author or the licensor, and that any adaptation is distributed under the same or a similar license. This license permits commercial use of the work and of its adaptations. It is similar to software or open-source licenses.

Biografija

Lazar Marković je rodjen 06.08.1996. u Beogradu. Zemunsku gimnaziju je završio 2015. godine. Osnovne studije na Fizičkom fakultetu, smer teorijska i eksperimentalna fizika, je završio 2020. godine sa prosečnom ocenom 9.59 (devet i 59/100).

Master studije fizike na istom fakultetu, na smeru teorijska i eksperimentalna fizika, završio je 2021. godine sa prosečnom ocenom 10 (deset). U toku master studija Lazar postaje član kolaboracije CMS u CERN-u. Master rad "Potraga za novim fenomenima u produkciji i raspadu Higsovog bozona koristecí metod efektivnih teorija polja", pod mentorstvom prof. dr Predraga Milenovića, odbranio je na Fizičkom fakultetu sa prosečnom ocenom 10 (deset). Uporedo sa master studijama Lazar je, kao član kolaboracije ATLAS u CERN-u, bio polaznik CERN-ove letnje škole, gde je istraživanje i završni rad uradio iz oblasti supersimetrija na temu "Proizvodnja parova gluina na LHC-u".

Doktorske studije fizike u okviru uže naučne oblasti Nuklearna fizika i fizika visokih energija Lazar Marković je upisao školske 2021/2022. godine na Fizičkom fakultetu Univerziteta u Beogradu i na Departmanu za fiziku Univerziteta u Torinu. Od januara 2022. do avgusta 2023. godine Lazar veći deo vremena provodi u Torinu radi istraživanja i stručnog usavršavanja, gde je radio u laboratoriji za inovativne silikonske detektore. U periodu od avgusta 2023. do avgusta 2024. godine veći deo vremena Lazar provodi u CERN-u radi istraživanja i stručnog usavršavanja, gde se bavio Monte Karlo simulacijama proton-proton sudara i gde je razvijao tehnike i metode za merenje samointerkacije Higsovog bozona. Na osnovu rada i stečene ekspertize, Lazar postaje kontakt osoba kolaboracije CMS za Monte Karlo (MK) generator dogadjaja MATRIX i HZZ MC kontakt osoba u kolaboraciji CMS, čime postaje ekspert na nivou kolaboracije zadužen za simulacije svih procesa relevantnih za sva merenja koja se obavljaju i recenziraciju u okviru HZZ grupe. Na oba Univerziteta Lazar je položio sve ispite, a na Univerzitetu u Beogradu posebno sa prosečnom ocenom 10 (deset).

Lazar Marković je pohadjao tri velike CERN-ove škole posvećene fizici visokih energija, metodama statističke obrade podataka i eksperimentalnim tehnologijama. Takodje, Lazar je učestvovao na nekoliko radionica i konferencija gde je prezentovao rezultate svog rada.

Od marta 2021. godine, Lazar drži kompjuterske vežbe na kursu fizika elementarnih čestica (FEČ), a od novembra 2021. godine i na kursu Viši kurs fizike elementarnih čestica 1 (vkFEČ1). Lazar je jedan od koautora praktikuma napisanog za pomenute kurseve i trenutno učestvuje u pripremi zbirke zadataka. Od oktobra 2024. godine, Lazar drži računske i laboratorijske vežbe na dva predmeta: 1. Fizika jezgra i čestica, 2. Nuklearna fizika. Za kurs Nuklearne fizike Lazar je jedan od koautora praktikuma za laboratorijske vežbe.

Od marta 2022. godine Lazar je zaposlen na Fizičkom fakultetu Univerziteta u Beogradu u zvanju istrazhivač-pripravnik, a od oktobra 2024. godine Lazar je zaposlen u zvanju asistent za užu naučnu oblast nuklearna fizika.

Izjava o autorstvu

Ime i prezime autora: *Lazar Marković*
Broj indeksa: **8011/2021**

Izjavljujem

da je doktorska disertacija pod naslovom

Merenje trostruke samointerakcije Higsovog bozona u kanalu raspada na četiri leptona eksperimentom CMS

- rezultat sopstvenog istraživačkog rada;

- da disertacija u celini ni u delovima nije bila predložena za sticanje druge diplome prema studijskim programima drugih visokoškolskih institucija;

- da su rezultati korektno navedeni i

- da nisam kršio autorska prava i koristio intelektualnu svojinu drugih lica.

Datum   **Potpis autora**

17.11.2025.   _____

Izjava o istovetnosti štampane i elektronske verzije doktorskog rada

Ime i prezime autora: *Lazar Marković*
Broj indeksa: **8011/2021**
Studijski program: *Nuklearna fizika i fizika visokih energija*
Naslov rada: *Merenje trostruke samointerakcije Higsovog bozona u kanalu raspada na četiri leptona eksperimentom CMS*
Mentori: *prof. dr Predrag Milenović (Univerzitet u Beogradu), prof. dr Roberto Kovareli (Univerzitet u Torinu*

Izjavljujem da je štampana verzija mog doktorskog rada istovetna elektronskoj verziji koju sam predao radi pohranjivanja u **Digitalnom repozitorijumu Univerziteta u Beogradu**.

Dozvoljavam da se objave moji lični podaci vezani za dobijanje akademskog naziva doktora nauka, kao što su ime i prezime, godina i mesto rođenja i datum odbrane rada.

Ovi lični podaci mogu se objaviti na mrežnim stranicama digitalne biblioteke, u elektronskom katalogu i u publikacijama Univerziteta u Beogradu.

Datum   **Potpis autora**

17.11.2025.   _____

Izjava o korišćenju

Ovlašćujem Univerzitetsku biblioteku Svetozar Marković da u Digitalni repozitorijum Univerziteta u Beogradu unese moju doktorsku disertaciju pod naslovom:

Merenje trostruke samointerakcije Higsovog bozona u kanalu raspada na četiri leptona eksperimentom CMS

koja je moje autorsko delo.

Disertaciju sa svim prilozima predao sam u elektronskom formatu pogodnom za trajno arhiviranje.

Moju doktorsku disertaciju pohranjenu u Digitalnom repozitorijumu Univerziteta u Beogradu i dostupnu u otvorenom pristupu mogu da koriste svi koji poštuju odredbe sadržane u odabranom tipu licence Kreativne zajednice (Creative Commons) za koju sam se odlučio.

1. Autorstvo (CC BY)

2. Autorstvo – nekomercijalno (CC BY-NC)

3. Autorstvo – nekomercijalno – bez prerada (CC BY-NC-ND)

4. Autorstvo – nekomercijalno – deliti pod istim uslovima (CC BY-NC-SA)

5. Autorstvo – bez prerada (CC BY-ND)

6. Autorstvo – deliti pod istim uslovima (CC BY-SA)

(Molimo da zaokružite samo jednu od šest ponuđenih licenci. Kratak opis licenci je sastavni deo ove izjave).

Datum   **Potpis autora**

17.11.2025.   _____

1. Autorstvo. Dozvoljavate umnožavanje, distribuciju i javno saopštavanje dela, i prerade, ako se navede ime autora na način određen od strane autora ili davaoca licence, čak i u komercijalne svrhe. Ovo je najslobodnija od svih licenci.

2. Autorstvo – nekomercijalno. Dozvoljavate umnožavanje, distribuciju i javno saopštavanje dela, i prerade, ako se navede ime autora na način određen od strane autora ili davaoca licence. Ova licenca ne dozvoljava komercijalnu upotrebu dela.

3. Autorstvo – nekomercijalno – bez prerada. Dozvoljavate umnožavanje, distribuciju i javno saopštavanje dela, bez promena, preoblikovanja ili upotrebe dela u svom delu, ako se navede ime autora na način određen od strane autora ili davaoca licence. Ova licenca ne dozvoljava komercijalnu upotrebu dela. U odnosu na sve ostale licence, ovom licencom se ograničava najveći obim prava korišćenja dela.

4. Autorstvo – nekomercijalno – deliti pod istim uslovima. Dozvoljavate umnožavanje, distribuciju i javno saopštavanje dela, i prerade, ako se navede ime autora na način određen od strane autora ili davaoca licence i ako se prerada distribuira pod istom ili sličnom licencom. Ova licenca ne dozvoljava komercijalnu upotrebu dela i prerada.

5. Autorstvo – bez prerada. Dozvoljavate umnožavanje, distribuciju i javno saopštavanje dela, bez promena, preoblikovanja ili upotrebe dela u svom delu, ako se navede ime autora na način određen od strane autora ili davaoca licence. Ova licenca dozvoljava komercijalnu upotrebu dela.

6. Autorstvo – deliti pod istim uslovima. Dozvoljavate umnožavanje, distribuciju i javno saopštavanje dela, i prerade, ako se navede ime autora na način određen od strane autora ili davaoca licence i ako se prerada distribuira pod istom ili sličnom licencom. Ova licenca dozvoljava komercijalnu upotrebu dela i prerada. Slična je softverskim licencama, odnosno licencama otvorenog koda.